# ELECTRONIC AND VIBRATIONAL EXCITATION

# IN ATOM / MOLECULE COLLISIONS

Thesis

Submitted by

ELEANOR ELIZABETH BRYCE CAMPBELL

For the Degree of

DOCTOR OF PHILOSOPHY

University of Edinburgh

OCTOBER, 1985.

## ABSTRACT

A time of flight, crossed beams technique has been used to study the narrow angle scattering of a fast beam of potassium atoms by two small molecules, $CH_3I$ and $N_2$. Results are reported for a number of collision energies in the range 100-250 eV LAB.

The data show a number of peaks in the scattered time of flight spectra indicating inelastic processes taking place. The excitations are interpreted as electronic excitation of the atom or molecule. All of the atomic excitation processes and some of the molecular ones are accompanied by vibrational excitation due to the involvement of intermediate potential surfaces with equilibrium geometries different from the ground state.

A simple classical model involving ground and excited ion pair states is shown to account very well for the 14 exit channels for which data is available in the $CH_3I$ system (including ion pair formation). The ground ionic intermediate accounts for the observed A state excitation in $CH_3I$ as well as the production of excited alkali atoms. Other, more highly excited, processes can be understood on the basis of an electron harpoon to form one of a sequence of strongly ionic doorway states.

A similar model is developed to account for the alkali excitation in the $N_2^-$ system. The molecular vibrational excitation which accompanies the atomic excitation is shown to depend strongly on the phase of the $N_2^-$ motion.

The final chapter is concerned with the construction and performance of a location sensitive scattered atom/ion detector.

## DECLARATION

I hereby declare that this thesis has been composed by myself and that I made a substantial contribution to the results reported whilst working in the Molecular Beam Group. All members of the group participated in data collection. I analysed all the data presented in this thesis and developed the modelling program (Chapter 4). I made improvements to the design of the particle detector discussed in Chapter 7 and characterised its performance. The interpretation of the results presented in Chapters 5 and 6 was developed in discussions with Dr. Malcolm Fluendy.

September, 1985.

# C O N T E N T S

C O N T E N T S (Contd.)

# CHAPTER 1

## INTRODUCTION

Understanding of collisions between atoms and/or molecules is fundamental to chemistry. Chemical and thermal equilibria are maintained by collisions while rates of chemical reaction and energy transfer are controlled by the frequency and dynamics of molecular collisions.

Chemical experiments, usually performed on bulk samples in thermal equilibrium with their surroundings, assume a Boltzmann distribution of molecules among the available states and, if the measured property is a function of the quantum state of the molecule, only an ensemble average can be obtained. The information has to be interpreted by means of theories relating statistical models of the bulk with the dynamics of a single collision.

Molecular beam scattering techniques, where a single quantum state or range of states can be selected for measurement, allow the dynamics of the collision as well as the angular and energy dependence of the associated scattering to be explored. Direct molecular information can be obtained without relying on theories relating molecular properties to non-equilibrium bulk properties.

Such techniques were first used to study elastic scattering in order to determine intermolecular potentials from the total scattering cross sections. A number of review articles exist (BUC 75, PAU 78).

Reactive scattering experiments followed, representing the

progression into chemical applications (KIN 72, GRI 75). Early studies involved reactions of alkali atoms with halogen containing molecules (HER 61). This work led to the revival and refinement (GIS 79) of the harpoon model, first developed by Polanyi and Magee (MAG 40) to explain the large reactive cross sections observed for alkali atoms and halogen molecules in flame experiments (POL 32).

This picture of collisions involving alkali atoms has proved to be a very useful one. The reaction is initiated by an electron transfer from the metal atom to the molecule. The two ions then combine to form the metallic halide leaving behind a free radical. The electron jump occurs at the point where the covalent potential energy surface crosses the ionic surface. At infinite separation these surfaces differ by an energy:

$$E = IP - EA \qquad (1.1)$$

where IP is the ionisation potential of the metal and EA the electron affinity of the molecule. This is a physically plausible, intuitively attractive picture of such reactions and, most importantly, it agrees with experimental observations.

Technological advances in the 1960's made superthermal crossed beam experiments possible with collision energies in the range 10 - 1000eV. These experiments have the advantage of allowing the experimenter to separate the dynamics of the collision from the electronic motion thus simplifying the analysis and understanding of the collisions. The velocity of the colliding partners is too great to allow reaction to occur - the main exit channels will be electronically

excited states with vibrational and rotational excitation of the molecule and ion pair formation.

If interest is confined to the narrow scattering angle region in these superthermal experiments the chemically important well region of the potentials can be investigated. With these glancing collisions, several electronic states may be involved in the collision.

The more excited states that are accessed in an experiment the more important it becomes to find a simple model capable of reproducing the key features in the data with a minimum of adjustable parameters. Not only to help gain an intuitive insight into the collision processes but also to help in the assignment of the experimentally observed processes.

Chapter 2 of this thesis describes such a superthermal scattering experiment used to determine the angular dependence of the inelastically scattered potassium atoms in collisions with small molecules. It has also been used to detect molecular ions formed in the collisions.

The experimental results for potassium colliding with methyl iodide and nitrogen are given in Chapter 3. The data is illustrated in the form of time of flight profiles for the alkali atom from which discrete energy loss processes can be picked out. The relative differential cross sections are shown as a function of reduced scattering angle for the observed processes.

In these systems, where the molecules have a negative vertical electron affinity, non-adiabatic effects are expected to occur at ranges shorter than those observed in the more widely studied halogens (LAC 80). Consequently the ionic exit channel can only

be reached after a sequence of avoided crossings with excited state potential surfaces. A large number of exit channels including electronic, vibrational and ion production channels are accessible via curve crossings and can yield information on the dynamics of the collision.

A simple classical trajectory surface hopping model used to account for the observed exit channels in the collision is described in detail in Chapter 4. This extends the use of the harpoon model to more complex situations with an ion pair state(s) providing the gateway to the observed electronically excited states.

The motion of any molecular system is described by the solution of the Schroedinger equation

$$(H - E)\psi = 0 \tag{1.2}$$

where $H$ is the total Hamiltonian for the system. The electronic and nuclear coordinates can be separated into two groups, internal coordinates, $q$, and external coordinates, $Q$. Normally the $q$ are chosen to be the electronic coordinates, $\mathbf{r}$, and the $Q$ are taken as the nuclear coordinates, $R$ (KLE 82). The total Hamiltonian for the system can then be written

$$H = T_Q + H_q \tag{1.3}$$

Here $T_Q$ is the kinetic energy operator for the external coordinates and $H_q$ is the internal Hamiltonian. Normally $H_q = H_{el}$ where $H_{el}$ is the usual electronic Hamiltonian.

The Born-Oppenheimer approximation then allows the internal and external degrees of freedom to be separated. The total wavefunction $\psi(q,Q)$ is expanded in a complete, orthonormal set of internal wave-

functions, $\phi_k(q;Q)$, which depend parametrically on $Q$.

$$\psi(q,Q) = \sum_k \phi_k(q;Q)\chi_k(Q) \tag{1.4}$$

where $\phi_k$ is an electronic wavefunction and $\chi_k(Q)$ is the external (i.e. nuclear) wavefunction on the potential energy surface associated with state $k$. Substituting this into the Schroedinger equation (eq. 1.2) and using the orthonormality of the $\phi_k$'s the following equation is obtained:

$$(T_Q + H_{kk} - E)\chi_k = -\sum_{k'\neq k} (t_{kk'} + H_{kk'})\chi_{k'} \tag{1.5}$$

Here $t_{kk'}$, the nonadiabatic interaction term, depends upon the rate of change of the $\phi_k$ with changes in the external coordinates, $Q$. The matrix element $H_{kk'}$, is given by

$$H_{kk'}(Q) = \langle\phi_k|H_q|\phi_{k'}\rangle \tag{1.6}$$

The brackets denote an integration over the $q$ coordinates.

The internal problem is formally solved by choosing the functions $\phi_k(q;Q)$ and evaluating the matrix elements $H_{kk'}$ and $t_{kk'}$. The external problem can be solved by finding solutions to equation 1.5.

There are two common representations used in selecting the internal basis functions.

The first is the adiabatic representation which uses the eigenfunctions of $H_q$ as the basis functions. Thus the $\phi_k$'s satisfy $(H_q - E_k)\phi_k = 0$ at each value of $Q$ and the matrix elements, $H_{kk'}$, are given by

$$H_{kk'}(Q) = E_k(Q)\delta_{kk'} \tag{1.7}$$

where $\delta_{kk'}$ is the Kronecker delta function., The functions $E_k(Q)$ are the potential energy surfaces which govern the motion of the external coordinates. The coupling between different states, k and k', is then caused by the nonadiabatic interaction term, $t_{kk'}$.

The diabatic representation is the other common choice for the basis functions. The $\phi_k$'s are determined at a fixed value of Q, say $Q_o$, and then do not change as Q varies

$$\phi_k^d(q;Q) \equiv \phi_k(q;Q_o) \equiv \phi_k(q) \quad . \tag{1.8}$$

Since the functions $\phi_k(q)$ do not vary with Q, the nonadiabatic interaction terms, $t_{kk'}$, are zero. Transitions between two diabatic surfaces $H_{kk}(Q)$ and $H_{\ell\ell}(Q)$ are induced by the off-diagonal matrix element $H_{k\ell}(Q)$.

Diabatic potential surfaces are used in the model - a good approximation at the collision energies involved - and the Landau-Zener theory (ZEN 32) is used to calculate the probability of crossing between surfaces.

Chapters 5 and 6 discuss the experimental data in the light of the modelling results.

The K-$CH_3I$ collision system (Chapter 5) is known to be a good example of electron harpooning (HER 79) and this is confirmed here with the model successfully predicting the fourteen exit channels for which data is available.

Nitrogen (Chapter 6) is not such a clear cut example. The negative ion has only been observed as a short-lived resonance in electron scattering experiments (SCH 73) and there is some debate

as to the validity of an ion pair coupling ground and excited states (HER 81). However the modelling shows that at superthermal collision energies this still provides a useful picture for the collisions.

The final chapter is concerned with the construction of a multi-angle atom/ion detector. Such a detector makes a number of experiments possible which would otherwise be too time consuming.

# CHAPTER 2

# EXPERIMENTAL

## 2.1 General

The results reported in Chapter 3 of this thesis were obtained on a molecular beam apparatus designed to investigate the dynamics of collisions between alkali atoms and various target molecules in the superthermal energy range from about 50 eV to 1000 eV.

A time of flight technique is used which allows observation of any electronic and/or vibrational excitation occurring during the collision. This makes an assignment of the final states of the collision system possible. The relative differential cross sections were calculated from measurements taken in the narrow scattering angle region about the main beam line - up to about 4° in the lab. frame of reference. By confining interest to this region the model calculations are considerably simplified with the use of a small angle formula (see Chapter 4) and the chemically important part of the atom-molecule potential surfaces can be probed.

The construction of the apparatus has been described in detail by Duchart (DUC 71) with various modifications described by Reddington (RED 73), Kerr (KER 75) and Black (BLA 81). The most recent addition to the apparatus, to enable positive molecular ions formed in the collision to be detected, has been briefly described by Brunetti et al. (BRU 84) and will be given in a little more detail here.

The apparatus is shown schematically in Fig. 2.1. There are four main sections; the alkali beam production, the target beam

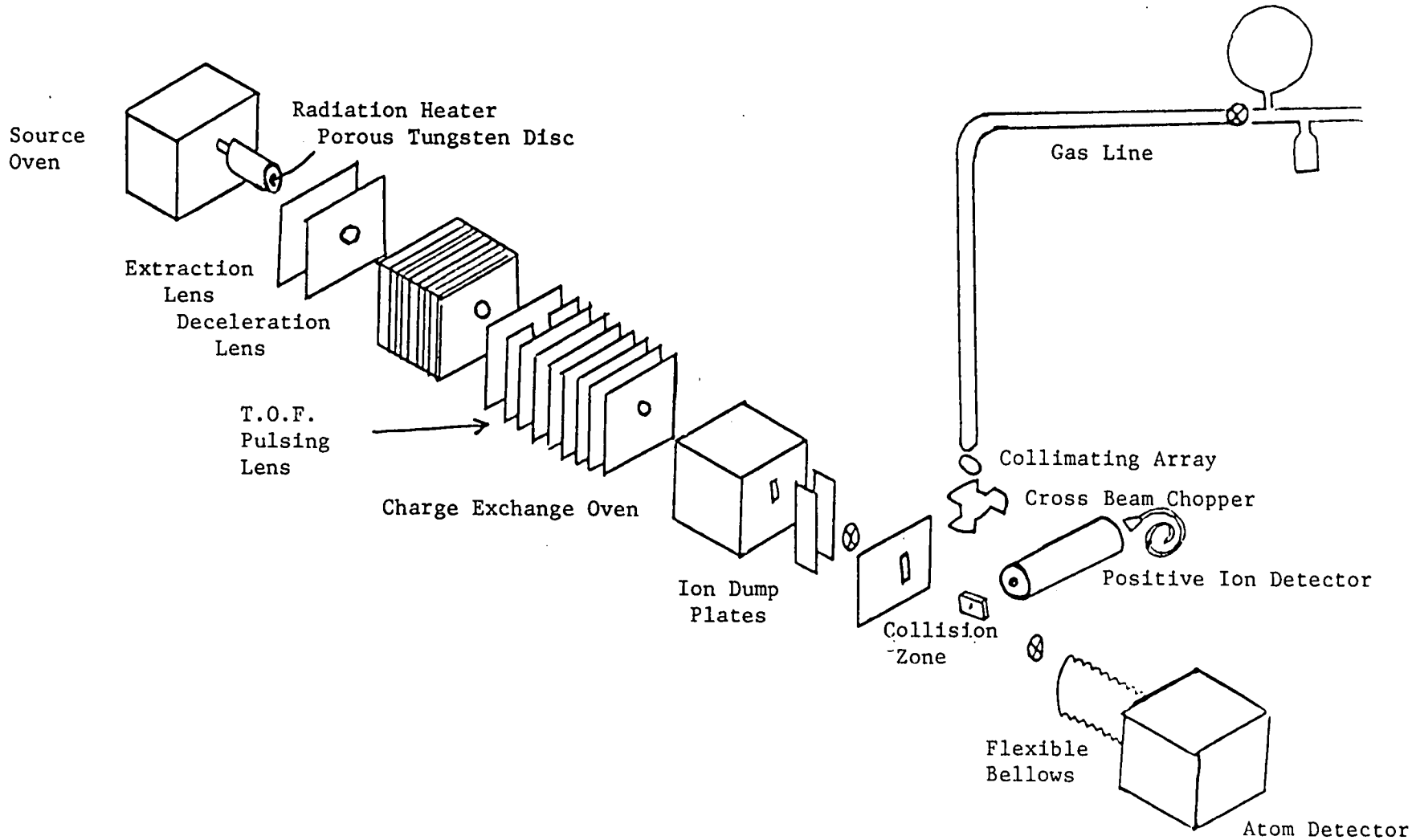


Fig. 2.1: Schematic Diagram of Apparatus.

formation, the detection of the scattered alkali atoms and the detection of positive molecular ions.

## 2.2 Vacuum System

The apparatus is made up of four differentially pumped chambers containing the main beam source, the cross beam unit, the scattering region and positive ion detector and the alkali atom detector.

The beam production chambers and the scattering chamber are pumped by oil diffusion pumps with liquid nitrogen cryogenic baffles backed up by three rotary pumps on a single roughing line. Liquid nitrogen cold traps are used to catch any stray condensibles thus preventing any build-up causing poor scattered beam intensities and higher background noise. Pressures to be expected in the alkali beam production chamber and the collision chamber are $10^{-5}$ and $10^{-6}$ torr. respectively. A gate valve separates these two chambers. The cross beam source chamber maintains a pressure of around $10^{-5}$ to $10^{-6}$ torr.

The alkali detection chamber is connected to the bulk of the apparatus by flexible bellows with a gate valve providing entry from the collision chamber. The detection chamber is initially pumped out through this slit until a low enough pressure is achieved to allow the ion pump to operate. It provides the main pumping power, running continuously with a titanium sublimation pump to handle occasional heavy contamination. The pressure in this chamber is normally about $10^{-7}$ torr.

## 2.3 Alkali Beam Production

Potassium ions are produced by surface ionisation on a porous tungsten disc heated radiatively to about 1500K and bathed to the rear in potassium vapour from a reservoir oven maintained at a temperature of about 250°C. The oven is kept at a positive voltage corresponding to the desired beam energy. The ions are extracted by a two element grid and accelerator electrostatic lens which focusses the ions into the Lindholm-Gustaffson deceleration lens assembly. This lens focusses the ion beam by means of an electrostatic field which drops exponentially in strength over the length of the lens system. Several of the lens elements are split to allow steering of the ion flux so that misalignments in the source may be compensated for.

After the deceleration lens the focussed ion beam enters the pulsing lens where it is first pulsed by applying a voltage across its path. After a suitable delay, velocity compression is applied to the slice of beam passed by the pulsing plates. A voltage gradient is set up along the beam path such that those ions to the rear of the pulse experience a greater acceleration than those to the front so the original pulse is compressed to a much narrower pulse at the detector, thus making time of flight studies possible (McC 78).

The pulsed beam is neutralised by charge exchange on passing through a second oven containing potassium at about 166°C by the resonant process:

$$K^{+} \text{ (fast)} + K^{\circ} \text{ (slow)} \rightarrow K^{\circ} \text{ (fast)} + K^{+} \text{ (slow)}.$$

The charge exchange oven is kept as near as possible to the optimum temperature, since the intensity of the final neutral beam is sensitive to changes at this point. Below about 160°C the vapour is too diffuse to achieve any useful degree of neutralisation while above about 170°C the vapour pressure is too high and the intensity is badly diminished by multiple collisions.

The neutral pulsed flux passes between dump plates, where a transverse voltage deflects any residual ions out of the beam path, and is collimated on entering the collision chamber.

## 2.4 Cross Beam Production

The cross beam reservoir is set up in a gas line external to the main apparatus enabling a variety of target beams to be investigated in a single experimental run without lengthy change-overs. From the gas line, the slow, thermal cross beam is let into the collision chamber by effusion through a glass capillary array. It is mechanically chopped at 47Hz to allow signal plus noise and noise alone to be differentiated. The cross beam chopper also interrupts light from a bulb falling on a photocell, with the light off when the cross beam is off. By monitoring the output from the photocell, each arrival at either detector can be labelled according to whether the cross beam was on or off when the atom/molecule passed through the collision zone. The target beam intensity is continuously monitored by a barostat attached to the gas line.

## 2.5 Alkali Atom Detector

The beam of scattered potassium atoms enters the detector and is ionised on a warm tungsten/platinum filament (Fig. 2.2). The ions so formed are accelerated towards a well defined spot on the aluminised surface directly opposite the scintillator and photomultiplier housing. The secondary electrons emitted at the aluminised surface are accelerated onto the scintillator. Photons produced by the electron pulse are detected by the photomultiplier and the output pulse is passed to a computer interface. The arrival of the scattered atom is recorded (arrivals at the detector stop a 50 MHz crystal clock running in synchronism with the pulse modulation) and a time of flight spectrum is built up for each scattering angle. The detector is mounted on a turntable and can measure over the range 0° - 12° in the laboratory frame of reference.

Due to the low count rates, especially at wider angles, an experiment can take about five days.

## 2.6 Positive Molecular Ion Detection

Positive molecular ions formed in the collision zone are extracted by a cylindrical Einzel lens into a quadropole mass spectrometer (Fig. 2.3). Ions with the selected mass to charge ratio are detected using a channel electron multiplier and counted into a dual scalar gated in synchronism with the target beam modulation to enable signal plus noise and noise alone to be differentiated. With the present mass spectrometer the best resolution available is 2 atomic mass units.

To calibrate the apparatus an electron beam, of known energy,

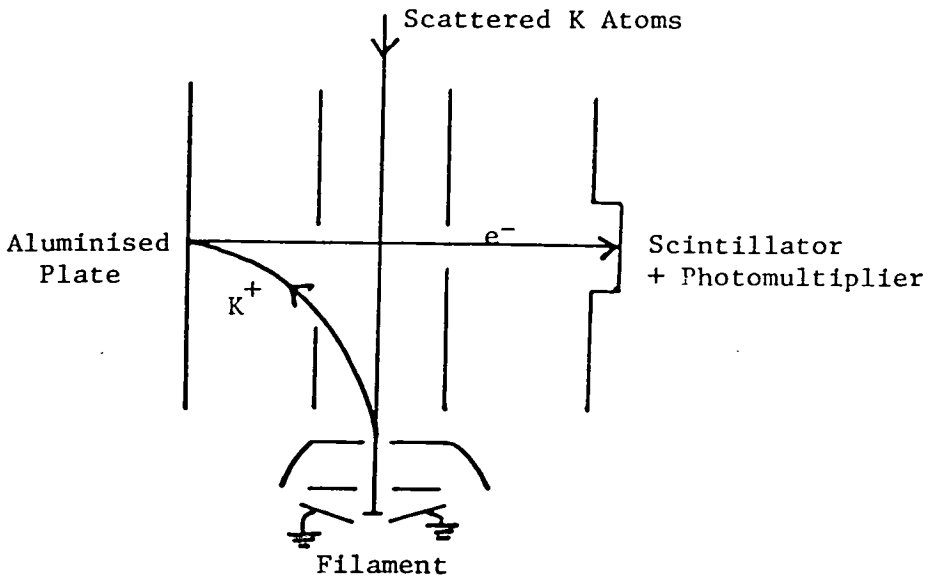


Fig. 2.2: Alkali Atom Detector.

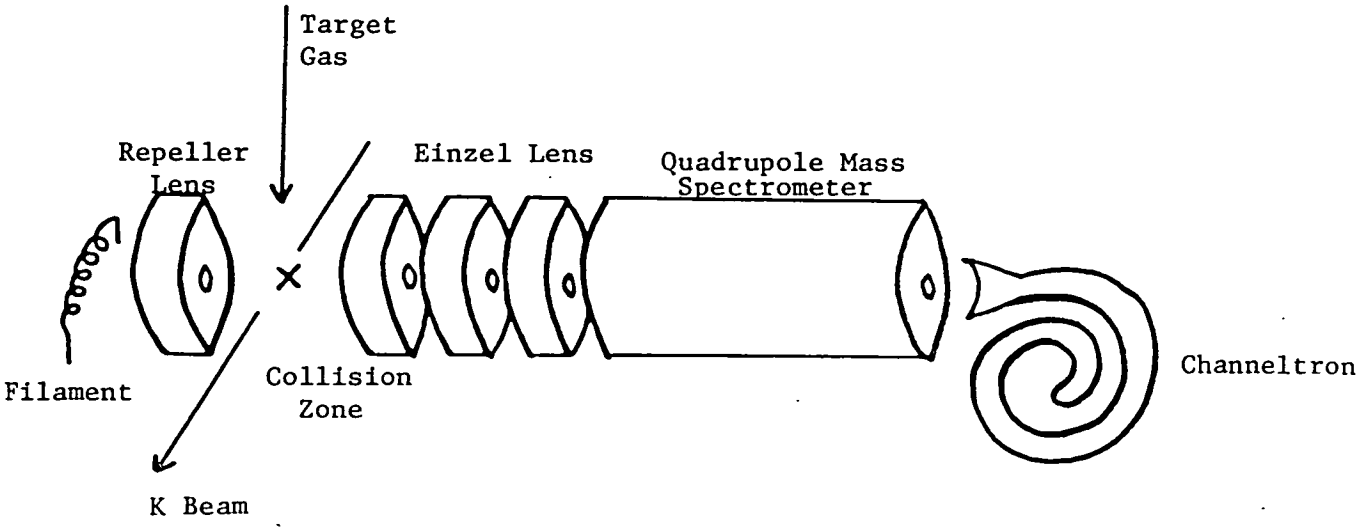


Fig. 2.3: Positive Ion Detection.

from a heated tungsten filament is used to bombard the target molecules with no alkali atoms present in the collision zone. The strong mass dependent transmission of the quadropole and the multiplier response can then be corrected for by comparing the electron impact ion yields with published data.

For these rather preliminary experiments the alkali beam pulsing and computer control are not required.

It is hoped in the future to do experiments where coincidences between the scattered alkali atoms and the positive molecular ions are detected. These experiments will help to identify the processes involved in producing the autoionising states of the molecule which give rise to the positive ions.

## 2.7 Data Collection and Analysis for Time of Flight Experiments

This has been described at length in Black's thesis (BLA 81) and only minor changes have been made since then which will be mentioned here.

### 2.7.1 Collection

The collection of experimental data is handled by an on-line DEC PDP11/45 computer which displays the accumulating data and provides the electronic counting for the experiments. Experimental conditions are defined at the start of a run by 32 experimental variables read into the collection program, e.g. beam energy, target beam mass and details of the apparatus geometry.

The detected signal stops a 50 MHz clock counting into a 10 bit scalar in the interface to record the flight time. With four separate scalars, 4 arrivals can be registered in the interface before an interrupt to the computer transfers their readings together with the time since the previous transfer and other experimental values. Every ten minutes the collected data is written to disc. If experimental conditions change, e.g. if the alkali beam intensity falls significantly, data collection is stopped and the experimenter informed.

It is possible to alter the experimental situation via a set of manual flags which communicate with the data collection program.

### 2.7.2 Analysis

The results accumulated on disc in the PDP11/45 computer are reviewed and edited after the run is completed. Appropriate reference profiles (i.e. undeflected beam) are chosen for the experimental angles and blocks collected at the same time are examined and merged if necessary to improve the quality of the data. The files are then transferred to the Edinburgh Regional Computing Centre's EMAS system where the raw data is analysed on the Centre's ICL 2972 computer.

The data is then transferred to the centre of mass frame of reference and a five-point polynomial filter applied to each spectrum. The scattering data is then deconvoluted with reference spectra using the H.P. Van Crittert method (JAN 70) to enhance the peaks and troughs. The program which does this now also outputs the standard deviation of the intensity of each data point as the error involved in the measurement and normalises to constant total scattering

intensity at each deflection angle. At this stage a check is made to ensure that peaks in the filtered data are also present in the raw data.

Another program sets up an array of data points suitable for the easy extraction of time-of-flight profiles, differential cross sections and contour maps. It can be used to 'smooth' the data over a narrow angular range to make process assignment easier. This array can be normalised to the total inelastic scattering data of Reddington (RED 73) to allow comparison of the differential cross sections for various processes at a range of collision energies. Standard graphics routines, available on EMAS, are used to display the analysed data.

# CHAPTER 3

# EXPERIMENTAL RESULTS

## 3.1 Systems Studied

Energy transfer processes occurring in collisions between fast moving potassium atoms and two small molecules - methyl iodide and nitrogen - were investigated using the crossed molecular beam apparatus described in Chapter 2. Time of flight profiles of the scattered potassium atoms were collected at a number of deflection angles and, from these, energy losses and differential cross sections were inferred for a range of collision energies.

The data was collected by Dr. Stuart Lunt with help from myself and Ms. Rona Ryall. I carried out the analysis for the data described here.

The energy resolution is given by $\Delta E/E \sim 0.01$ so that at the higher collision energies two or three peaks may be merged into one on the time of flight spectra. The angular range covered was from 0° to about 9° cm. At larger scattering angles the experiments become very time consuming.

Table 3.1 shows the collision energies studied by the Edinburgh group for these two systems over a number of years. References are given for the results that have already been reported.

There are a large number of exit channels open to these systems. Table 3.2 details them for a general collision system, A + BC.

TABLE 3.1

SYSTEMS STUDIED

| SYSTEM | cm COLLISION ENERGY/eV | REFERENCE |
|---|---|---|
| $K + CH_3I$ | 81 | SUT 80 |
| $K + CH_3I$ | 106 | |
| $K + CH_3I$ | 164 | SUT 80 |
| $K + CH_3I$ | 218 | |
| $K + N_2$ | 43 | |
| $K + N_2$ | 58 | |
| $K + N_2$ | 86 | BLA 81 |
| $K + N_2$ | 106 | |

TABLE 3.2

EXIT CHANNELS

1) $A + BC \rightarrow A + BC \quad (A + BC(v))$ ELASTIC (VIBRATIONAL)

2) $A + BC \rightarrow AB + C$ REACTION

3) $A + BC \rightarrow A^+ + BC^-$ CHEMI-IONISATION (INC. e.g. ELECTRON DETACHMENT)

4) $A + BC \rightarrow A^* + BC$
   $A + BC \rightarrow A + BC^*$ ELECTRONIC EXCITATION

5) $A + BC \rightarrow A + B + C$ DISSOCIATION

## 3.2 K - $CH_3I$ Scattering

Alkali metal - alkyl halide reactions have played an important part in the development of chemical reaction dynamics (MAG 40, HER 79) and a large amount of data concerning the reaction channel at thermal energies is available (HER 66). It has been fairly well established that the reaction process is an example of electron harpooning involving donation of an electron by the metal atom. However, the relatively short range encounters required for harpooning in these systems destroy the simplicity of near spectator stripping dynamics found in the otherwise analogous alkali metal - halogen molecule reactions (LAC 80). The position of the ion-pair potential, dependent upon the ionisation potential of the atom and the electron affinity of the molecule, is such that many more states are accessible via harpooning in the alkyl halide systems. The description of the reactive process is thus particularly dependent upon the potential surfaces and non-adiabatic effects at short ranges where information on these properties is scant.

At collisions in the eV range the differential cross sections for the wide range of exit channels available, including elastic scattering, vibrational excitation, electronic excitation and ion production can all yield information on these non-adiabatic effects.

Total cross sections for ion production in alkali metal - methyl halide systems over a range of collision energies are available (MOU 74). More recently, differential cross sections for ion production in these systems have been made available (SPA 81, PRA 83).

Elastic differential cross sections for the neutral exit channels (vibronic excitation) have been measured in Edinburgh at four collision energies. The results for two of these collision energies have been published (FLU 79). The energy losses observed for all collision energies will be presented here for completeness but only the previously unpublished data will be presented in the form of time of flight profiles and contour maps. This, more recent, data was intended to confirm the model predictions based on the more intensive data already collected and was not meant to give detailed differential cross sections.

### 3.2.1 Observations

As can be seen from the contour maps in Fig. 3.1, which show scattering intensity times the square of the scattering angle against final atom velocity and scattering angle, a large number of energy losses are observed even at fairly narrow scattering angles.

Any observed energy loss below 1.6 eV - the first possible electronic excitation - must be due to vibrational excitation of the molecule. The only electronically excited state of potassium to be observed is the $4^2P$ state. This is seen with differing amounts of vibrational excitation depending upon whether an early or late crossing onto the ion-pair intermediate has occurred. Higher states may be present with low intensity but will be obscured by the molecular electronic excitations.

All other energy losses observed can be attributed to excited molecular electronic states, although it is possible to envisage

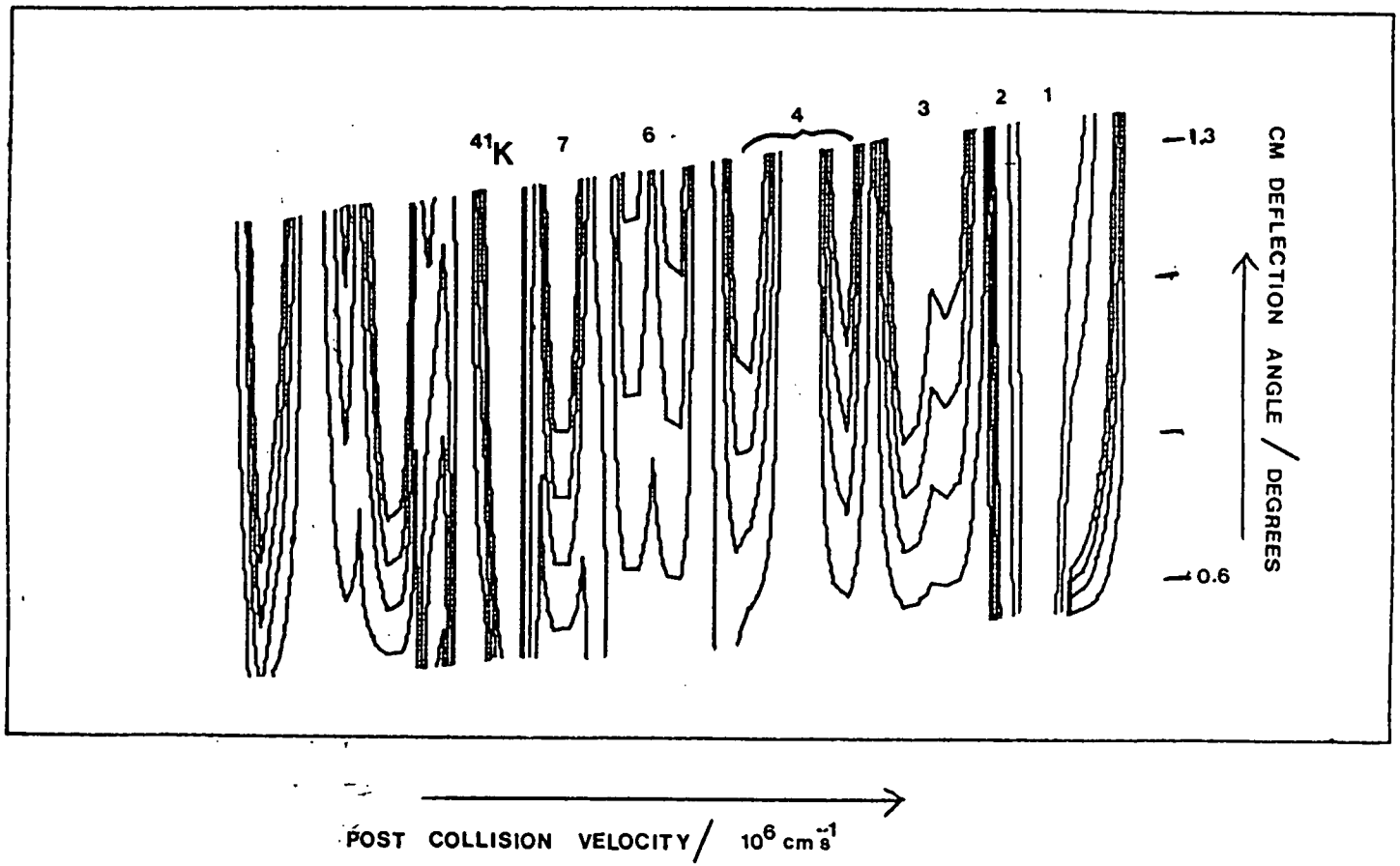


Fig. 3.1: K + $CH_3I$ Contour Maps

Contour Levels: 1%, 3%, 5%, 7%, 10%, 30% of elastic peak intensity.

Process numbers from Table 3.3 are shown.

109 eV cm Collision Energy.

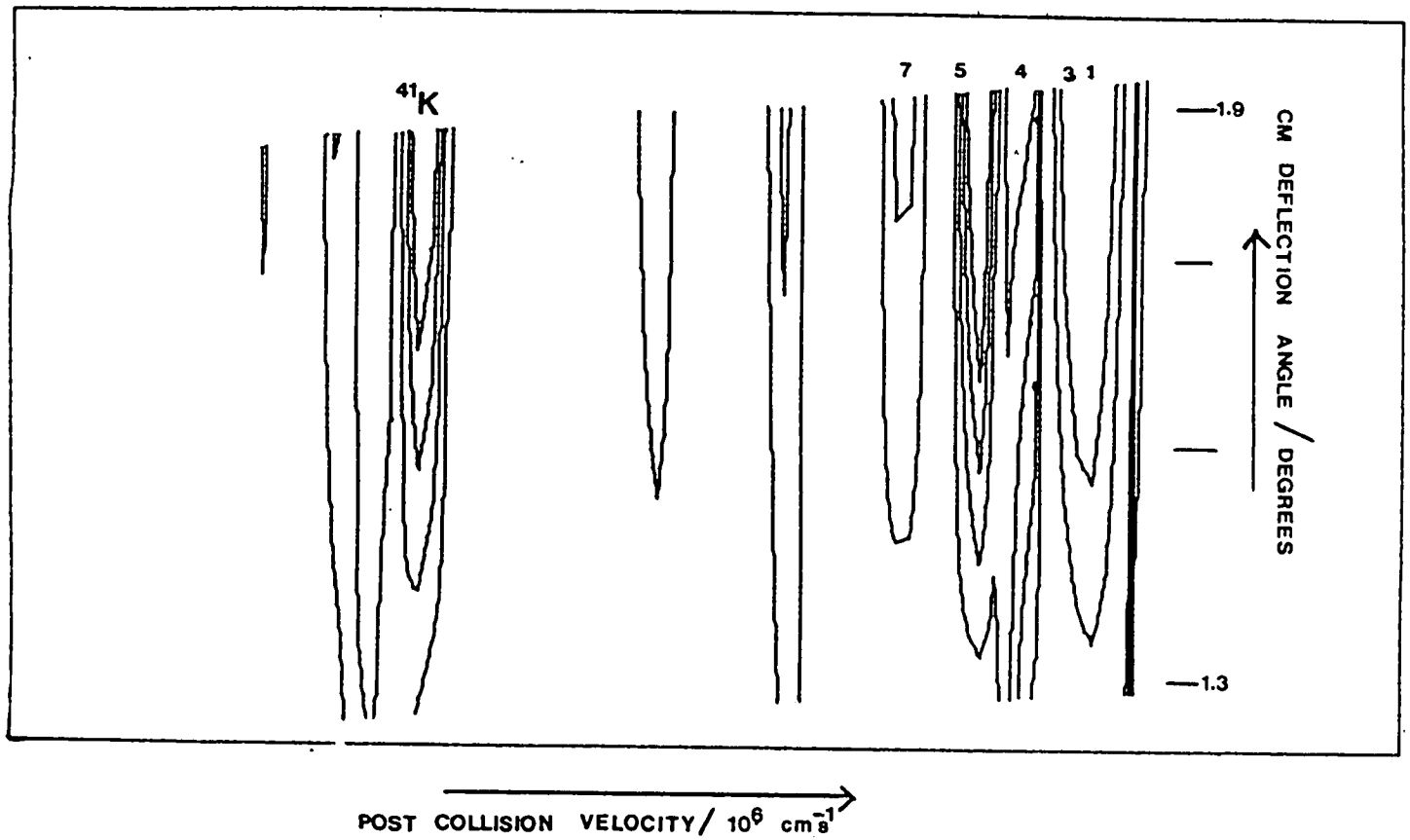


Fig. 3.1 continued

222 eV cm Collision Energy.

double electronic excitation (i.e. both the atom and the molecule being electronically excited) contributing to the higher energy losses observed.

The average energy losses measured for each collision process at the different collision energies are shown in Table 3.3 along with the proposed assignments and electronic excitation energies of these assigned states.

Time of flight profiles at different scattering angles for collisions at 109 eV and 222 eV cm are shown in Figs. 3.2 and 3.3. The data has been normalised to give the same total scattering intensity at each deflection angle. Higher inelastic processes can be observed more readily at the higher collision energy but the resolution is not so good.

## 3.3 K - $N_2$ Scattering

The quenching of alkali atoms as a result of collisions with diatomic molecules has been of interest for a considerable time (MAS 73, HER 81). The Na - $N_2$ system has been of particular interest both experimentally (HER 77, REI 82) and theoretically (BOT 75, BAU 69, FIS 72, BOT 77, GIS 81). The inverse process, atomic excitation as a result of energetic collisions has also been investigated (KEM 75, BLA 80). Kempter (MAR 79) has investigated the differential cross section for excitation of $K(4^2P)$ in potassium nitrogen collisions using an atom-photon coincidence technique to detect the inelastic process unambiguously.

Most of the above assumed an ionic intermediate was responsible

TABLE 3.3

OBSERVED ENERGY LOSSES, K + $CH_3I$

| Collision energy cm/eV | | 81 | 109 | 164 | 222 | Proposed Assignment based on model results (Chap. 5) | Predicted electronic energy loss/ev. |
|---|---|---|---|---|---|---|---|
| Process No. | 1 | 0.0 | 0.0 | 0.0 | 0.0 | Elastic | 0.0 |
| | 2 | 0.6<br>1.3 | 1.2 | 1.0 | | vib. energy in C-I bond | 0.0 |
| | 3a | 2.0 | 1.9 | 1.7 | (1.4) | 4s → 4p | 1.6 (BAC 32) |
| | 3b | 3.1 | 3.1 | 2.8 | | | |
| | 4 | 4.0 | 4.0 | 4.2 | | | |
| | | 4.3 | | 4.8 | (5.0) | n(I) → $\sigma^*$(C - I) | 3.5-5.5 (HER 66) |
| | | 5.0 | | 5.5 | | | |
| | | 5.6 | 5.6 | | | | |
| | 5 | 6.4 | | 6.4 | (7.0) | n(I) → 6s Rydberg | 6.5 (BOS 72) |
| | 6 | 8.0 | 8.6 | 8.4 | | n(I) → 7s Rydberg | 8.2 (BOS 72) |
| | 7 | | 10.5 | 10.4 | (10.2) | $\sigma_p$(C-H) → 6s Rydberg | 11.0 (BOS 74) |
| | 8 | | | 12.4 | | $\sigma_p$(C-H) → 7s Rydberg | 12.9 (BOS 74) |
| | 9 | 6-7.2 in range 40-220 eV° | | 6.4-9.0 in range 60-900 eV° | | n(I) → $\sigma^*$(C-H) | ∿ 6.0 (HIT 78) |

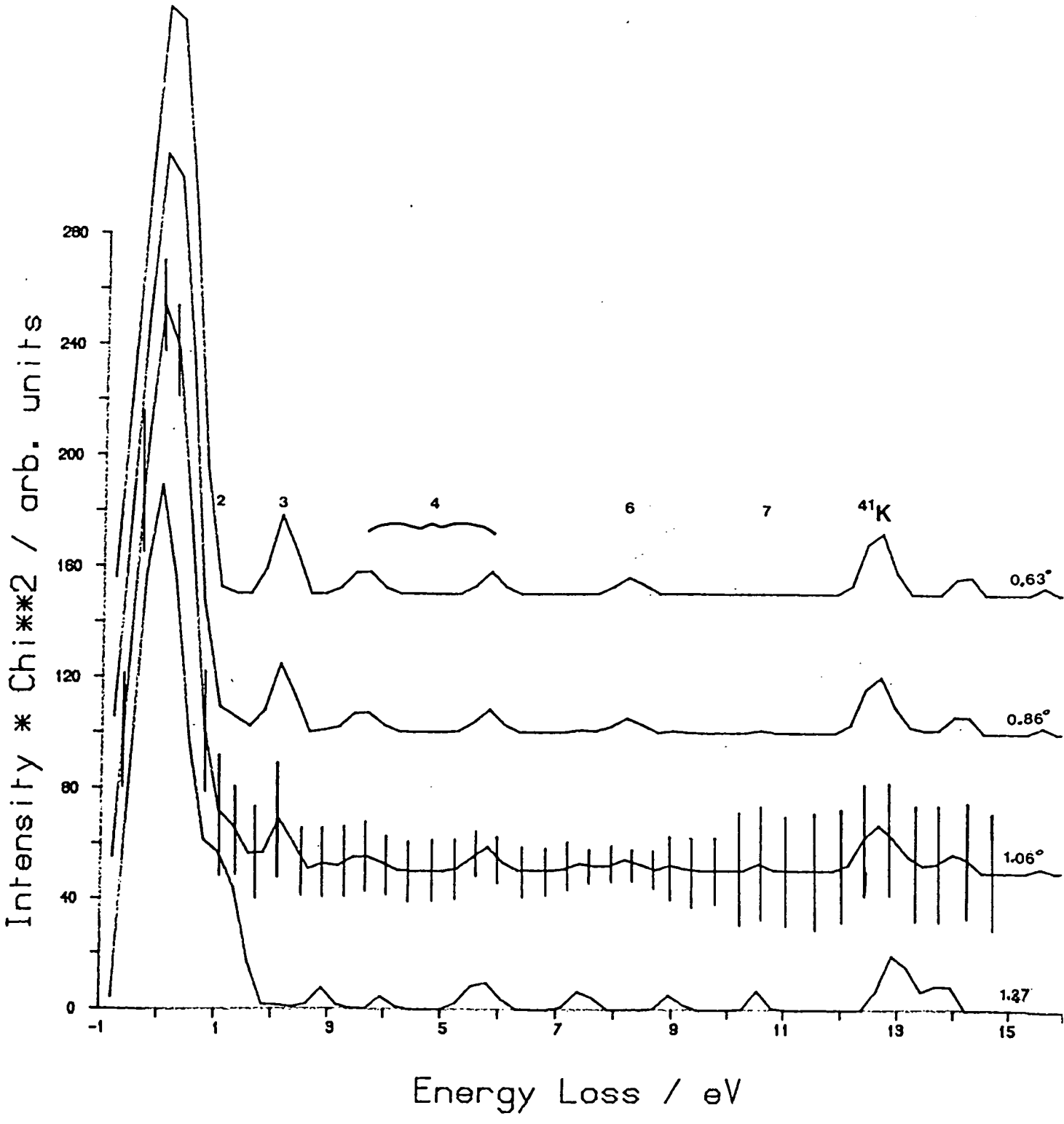


Fig. 3.2: K + $CH_3I$ Time of Flight Profiles at 109 eV CM Collision Energy.

Process numbers are indicated and typical error bars shown.

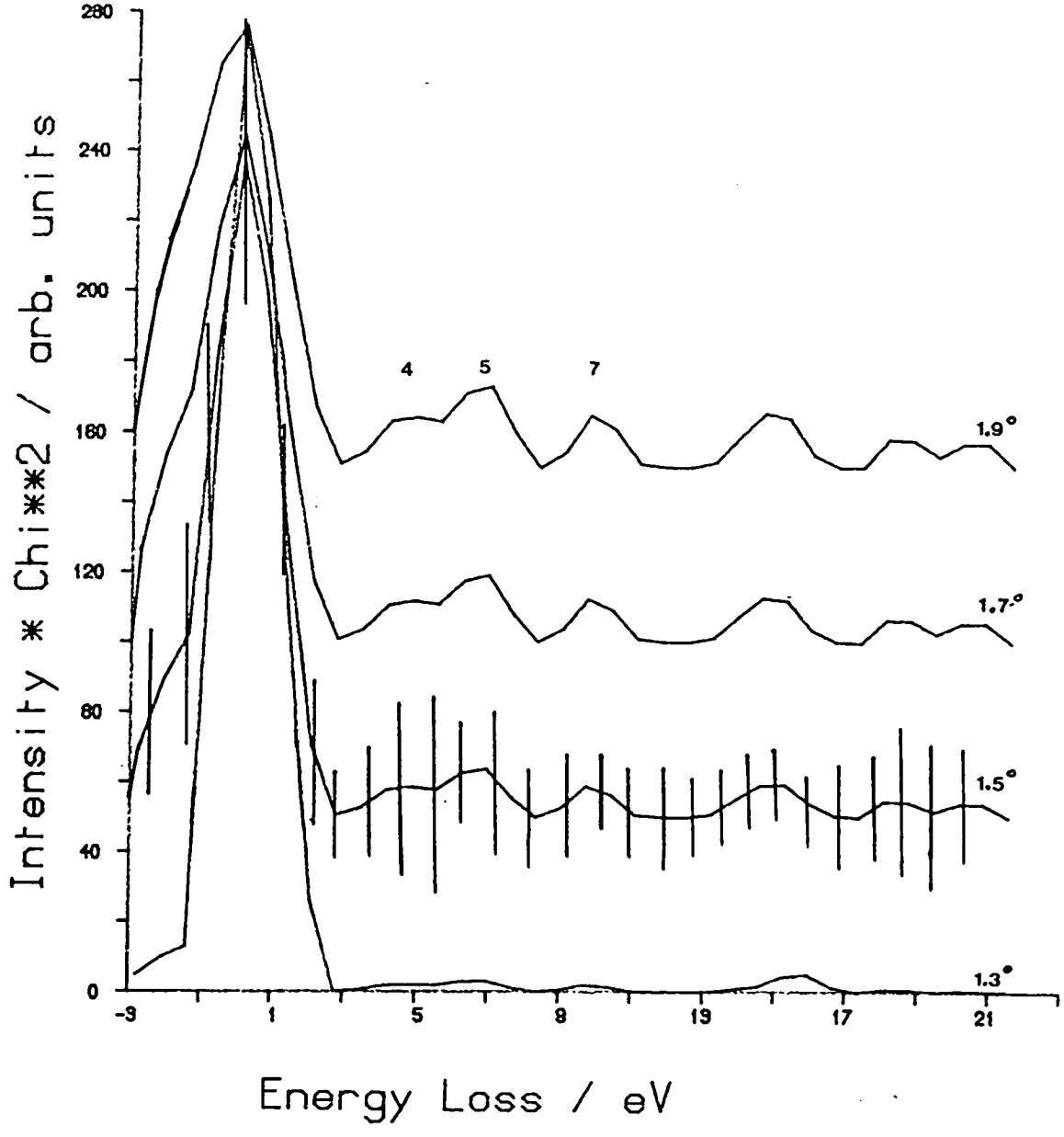


Fig. 3.3: K + $CH_3I$ Time of Flight Profiles at 222 eV CM Collision Energy

Process numbers are indicated and typical error bars shown.

for the quenching and/or excitation. However calculations of the adiabatic potential energy surfaces for sodium-nitrogen (HAB 80) suggest otherwise. These calculations show that the energy transfer for $Na(3^2P)$ excitation/quenching can be interpreted by a "bond stretch attraction" mechanism without invoking the ionic intermediate. This will be discussed in more detail in Chapter 6.

The results presented here, involving the excitation of many more electronic states of the atom and molecule than the above work, will again assume the intervention of some form of ionic intermediate in an attempt to push the simple diabatic picture of these collisions to its limits.

Inelastic differential cross sections have been obtained for all the observed vibronic excitations occurring in collisions between fast moving potassium atoms and nitrogen molecules at four collision energies: 43.3, 58.1, 85.6 and 106.7 eV cm. Data at one of these energies has already been dealt with rigorously (BLA 81) and will not be presented here in the form of individual time of flight plots or differential cross sections although it will be included, for completeness, in Table 3.4 which details the energy losses observed, and Fig. 3.5 which shows the angle averaged time of flight profiles for each collision energy.

### 3.3.1 Observations

The contour maps for three collision energies, 43.3, 58.1 and 106.7 eV cm are shown in Fig. 3.4. Although these plots are useful in identifying the behaviour of energy loss processes with angle,

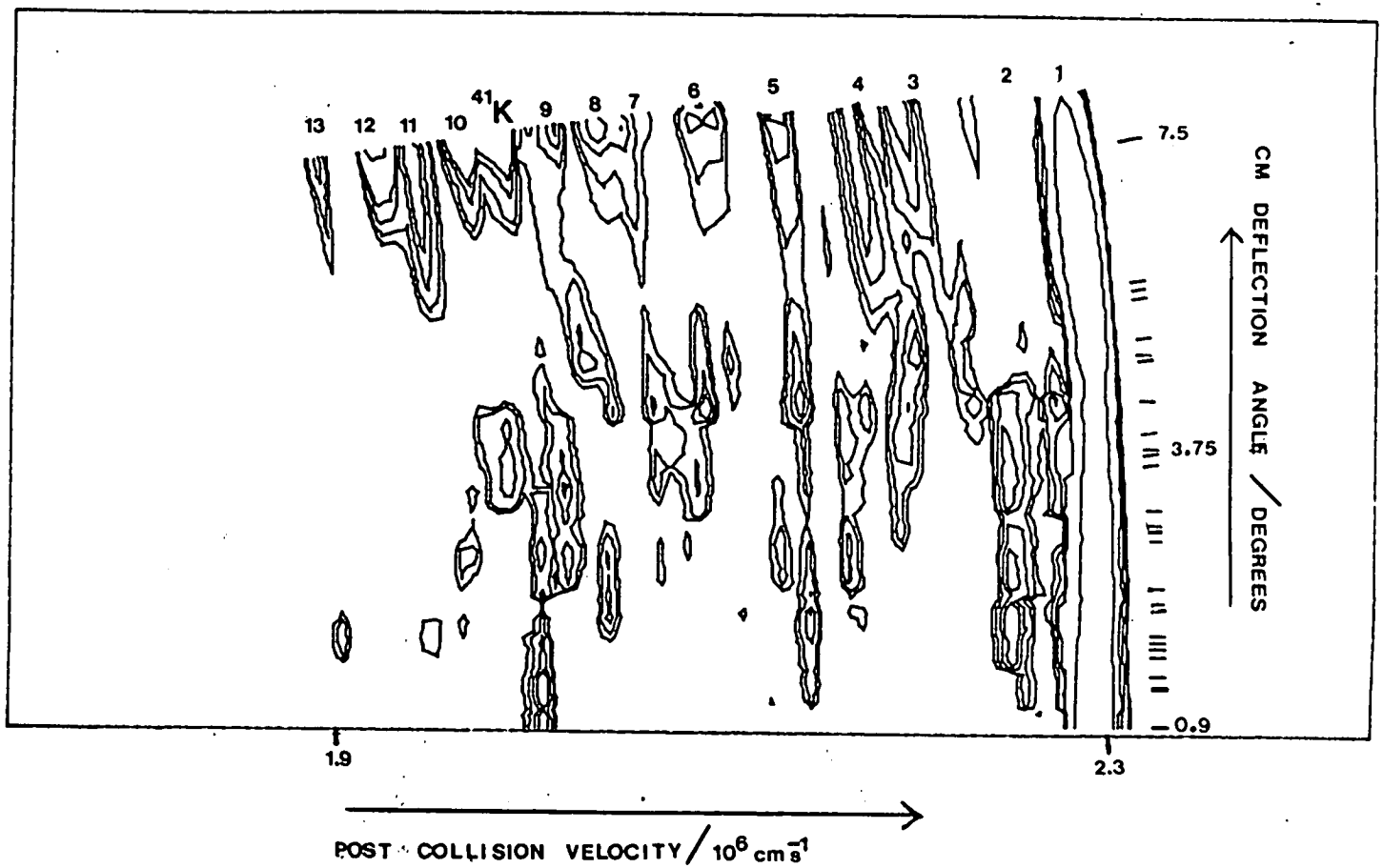


Fig. 3.4: $K + N_2$ Contour Maps.

Contour levels 1%, 3%, 5%, 7%, 30% of elastic peak intensity.

Process numbers from Table 3.4 are shown.

43.3 eV CM Collision Energy.

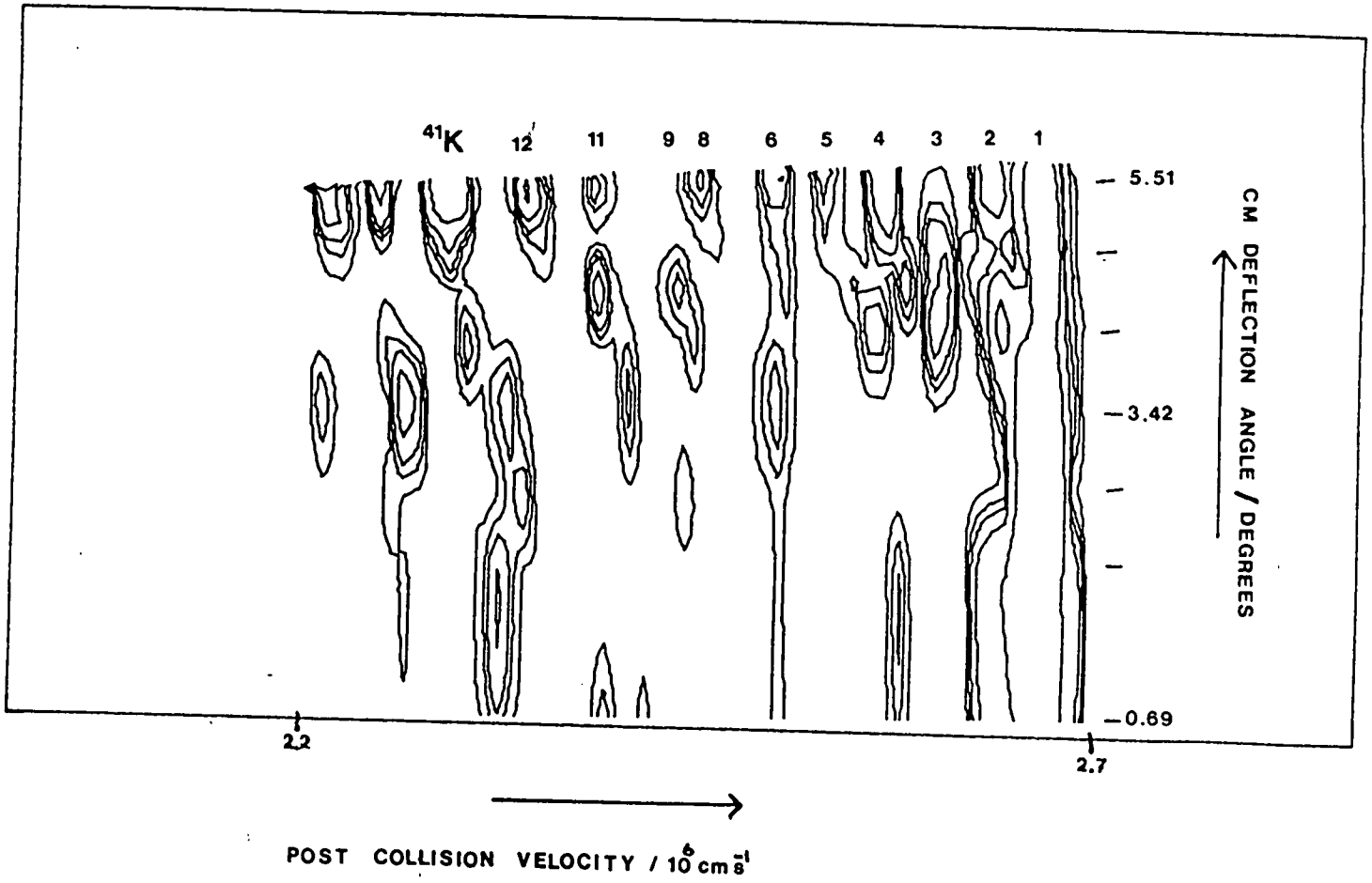


Fig. 3.4 continued.
58.1 eV CM Collision Energy.

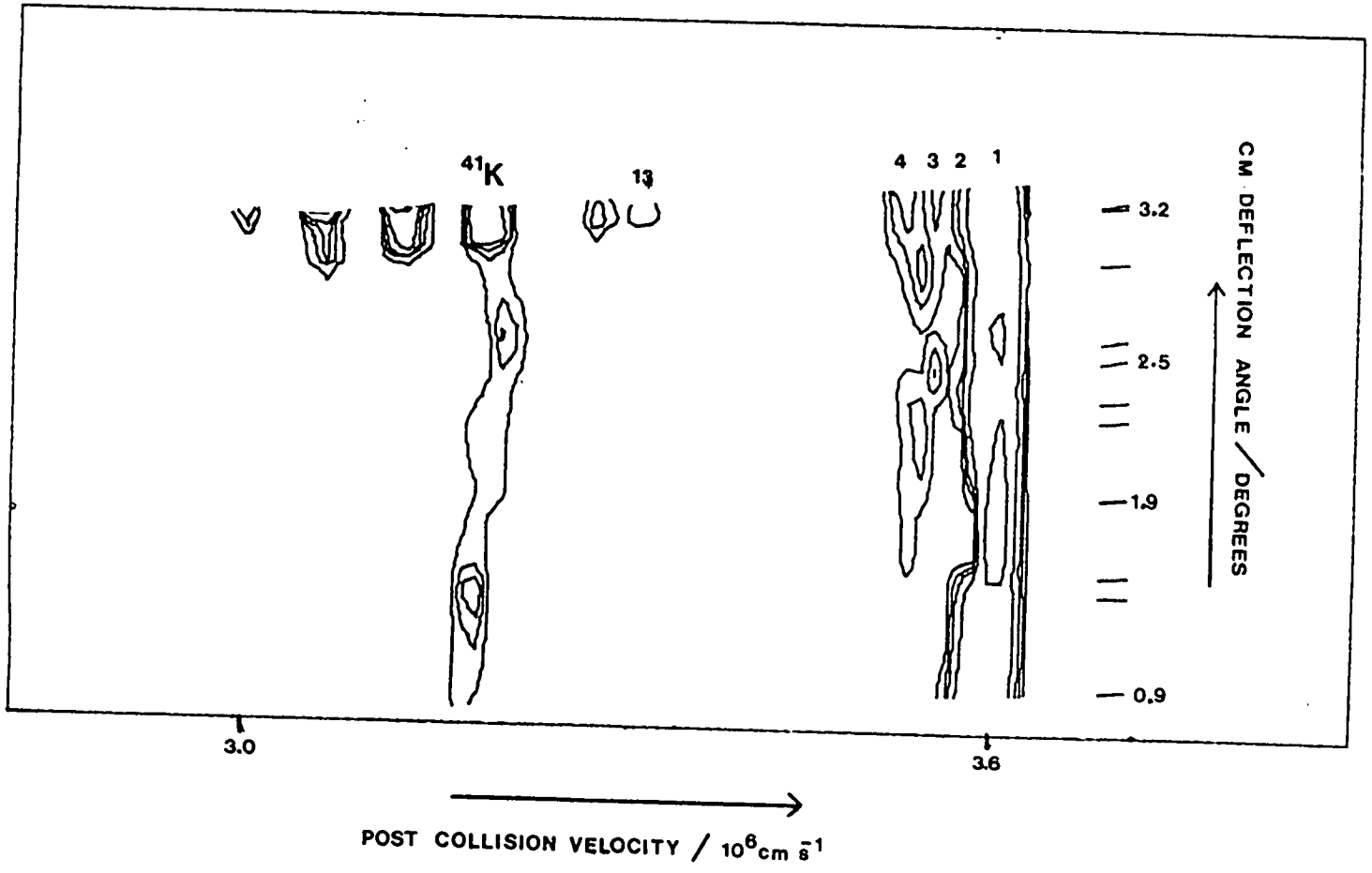


Fig. 3.4 continued.

106.7 eV CM Collision Energy.

most of the data is taken from the time of flight profiles which display in a more accessible way, the intensity of the different energy loss processes observed for a range of angles. Fig. 3.5 shows such time of flight profiles averaged over all scattering angles for all the collision energies investigated. The data has been normalised to the same elastic peak intensity and shifted for clarity.

Figs. 3.6 - 3.8 show similar profiles but for different scattering angles. This data has been normalised to the differential cross sections for total inelastic scattering measured in Edinburgh by Kerr (KER 75). In this way we can obtain the relative differential cross sections for all the processes observed. These are shown in Figs. 3.9 - 3.42 for the assigned processes.

As can be seen from the time of flight profiles and differential cross sections, elastic scattering is by far the most intense process observed, even at the highest collision energy. Its intensity falls off at about 300-360 eV°, corresponding to the onset at the associated impact parameter of the inelastic processes. Unfortunately this is the limit of the observations for three out of the four collision energies for which data is available. The fact that the other processes are observed to onset at reduced scattering angles less than this is indicative of an attractive intermediate potential surface, e.g. of an ionic nature.

The shapes of the differential cross sections for some of the energy loss processes are less well defined due to their low intensity.

Table 3.4 summarises the energy loss information by giving the

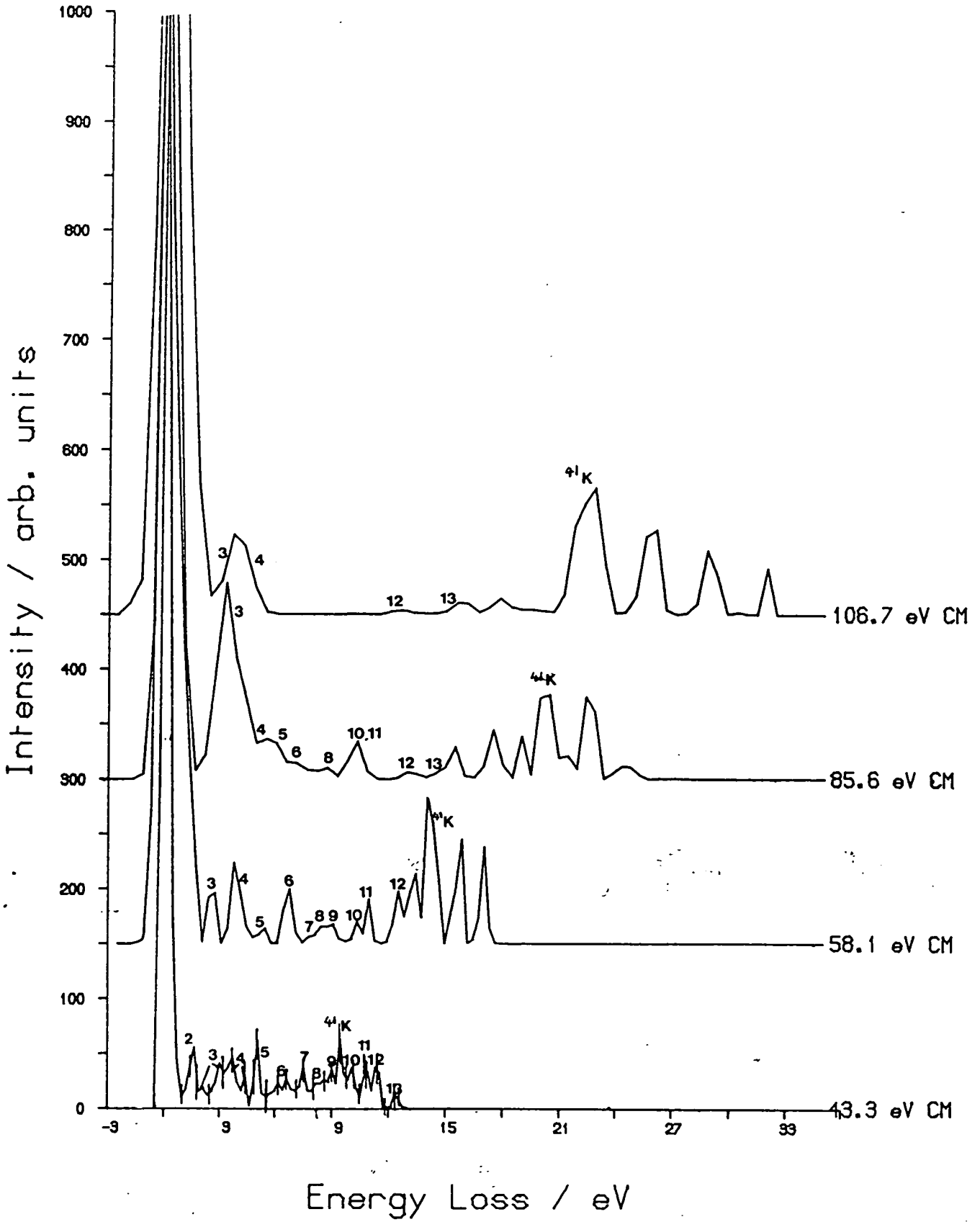


Fig. 3.5: K + $N_2$ Angle Averaged Time of Flight Profiles
Process numbers are given and error bars are shown for the lowest collision energy. All profiles are normalised to the same elastic peak intensity and shifted for clarity.

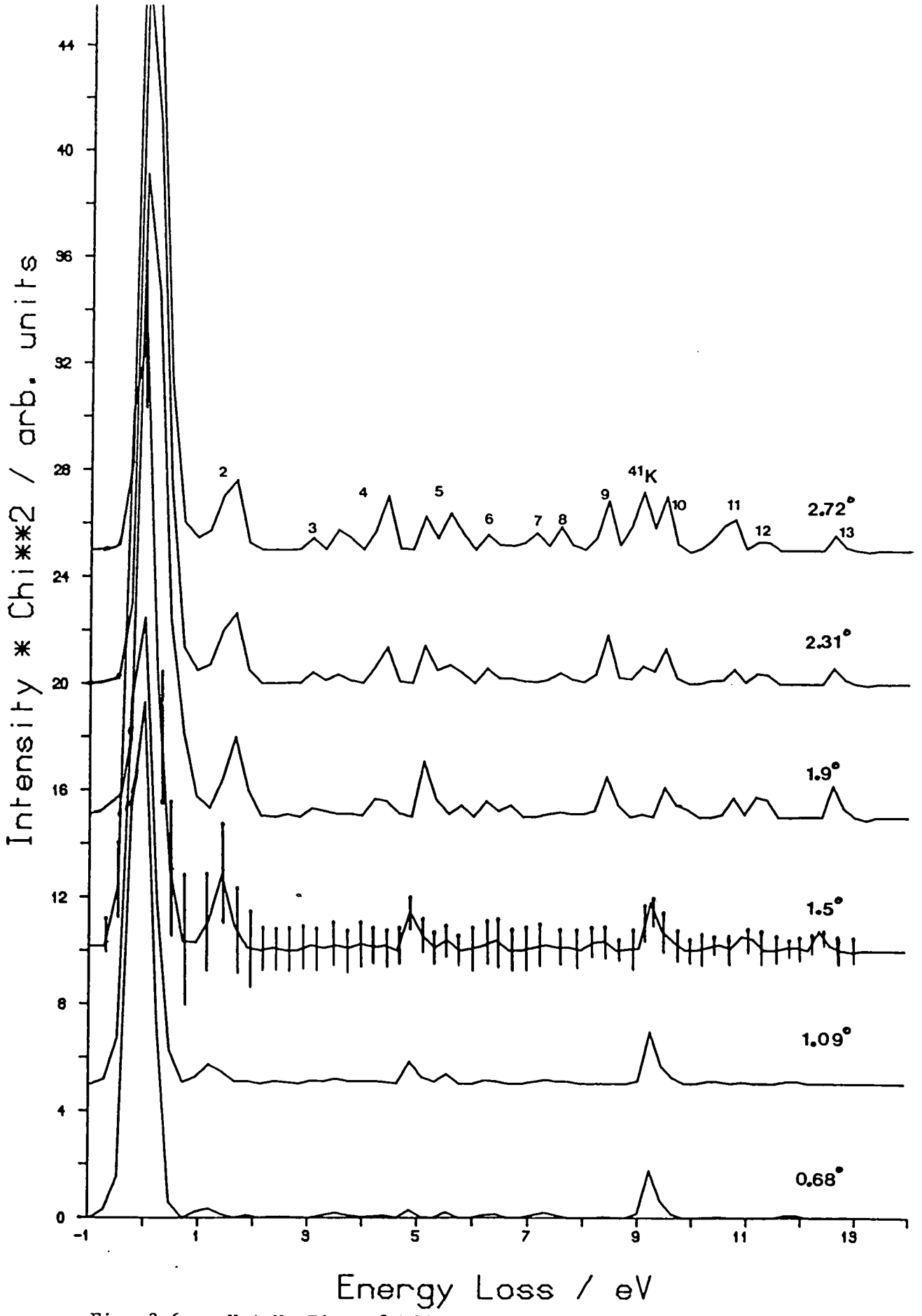


Fig. 3.6: $K + N_2$ Time of Flight Profiles at 43.3 eV CM Collision Energy
Process numbers are indicated and typical error bars shown
$0.68^{\circ} - 2.72^{\circ}$ CM.

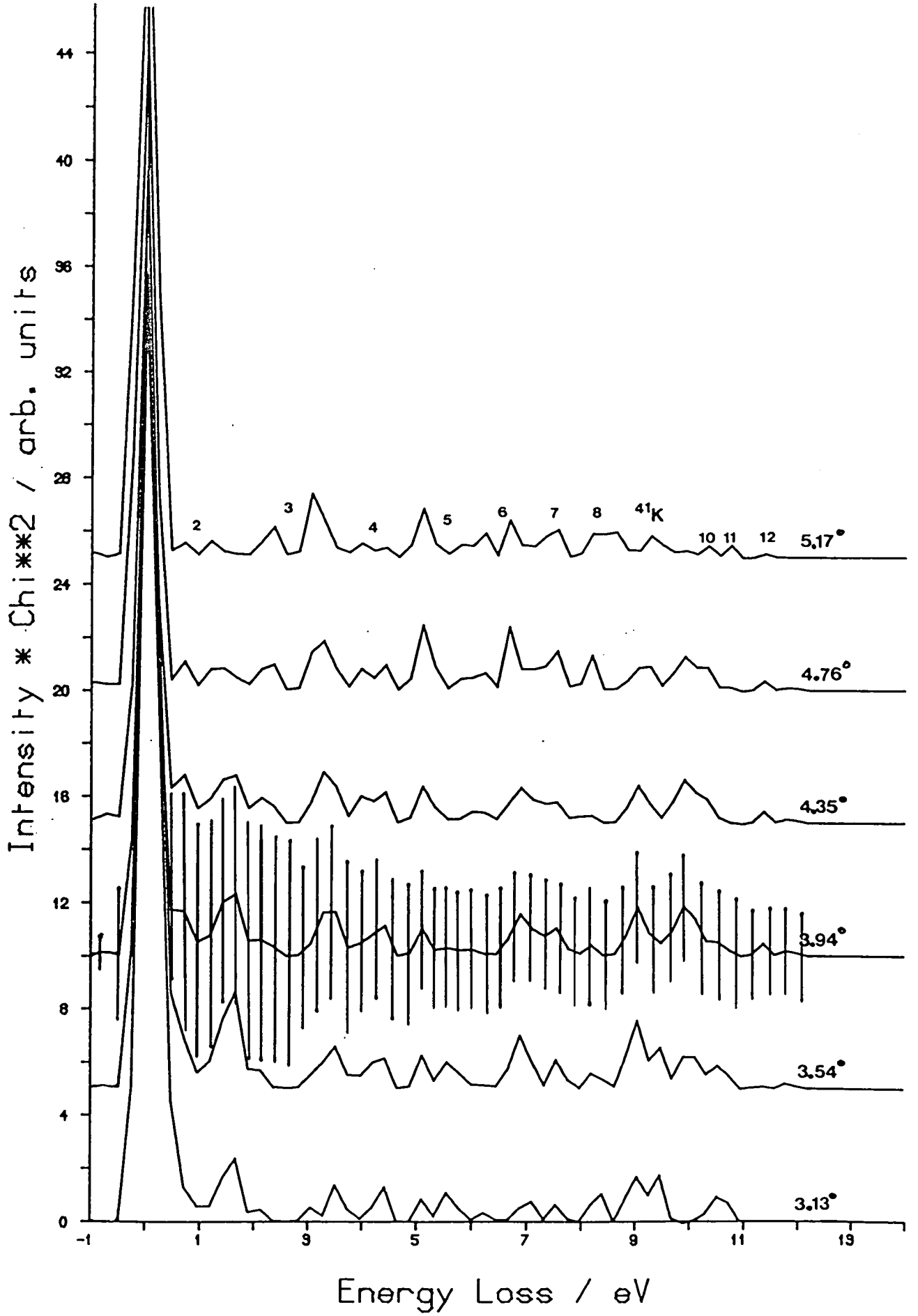


Fig. 3.6 continued.

3.13° - 5.17° CM

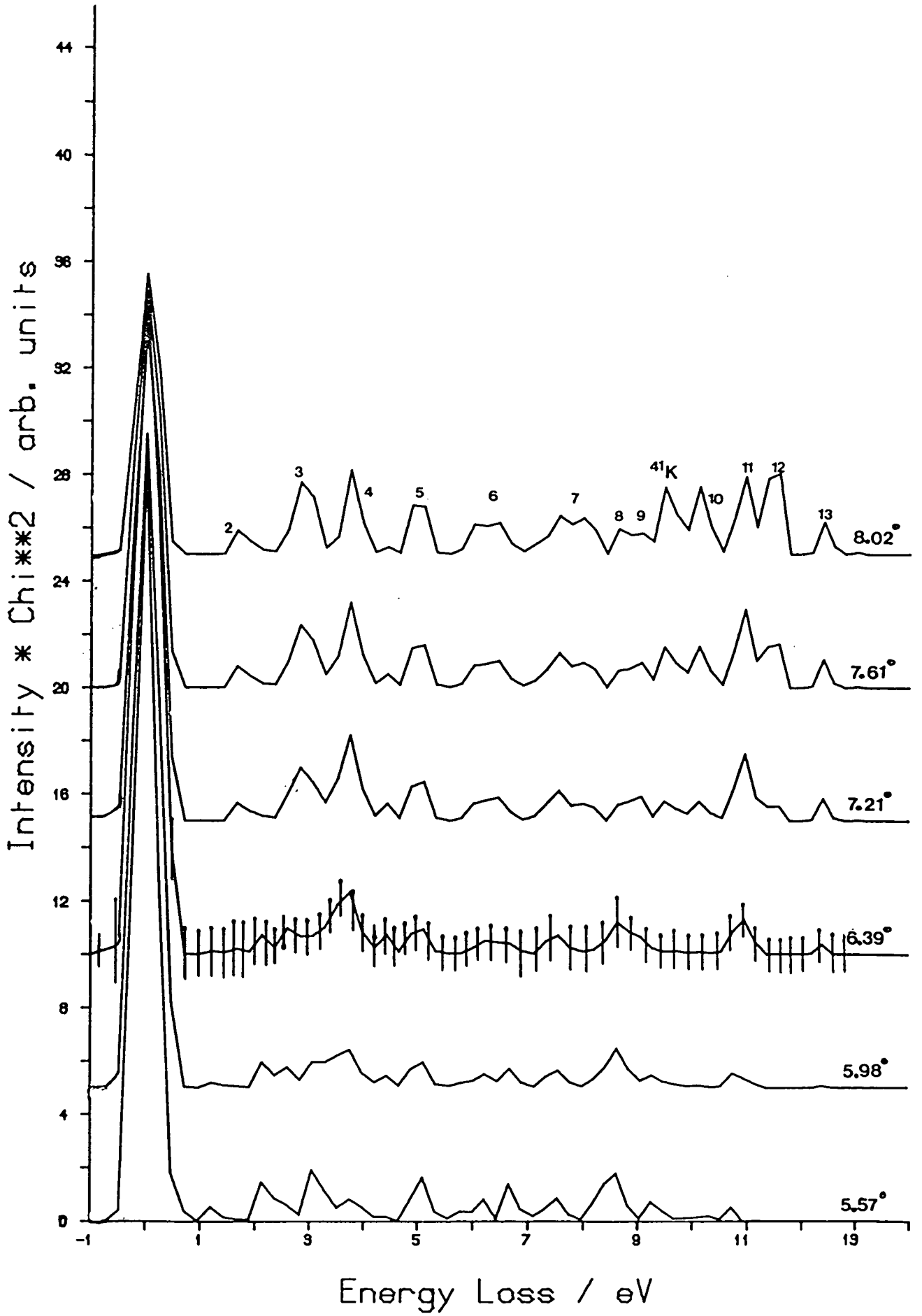


Fig. 3.6 continued.

5.57° - 8.02° CM.

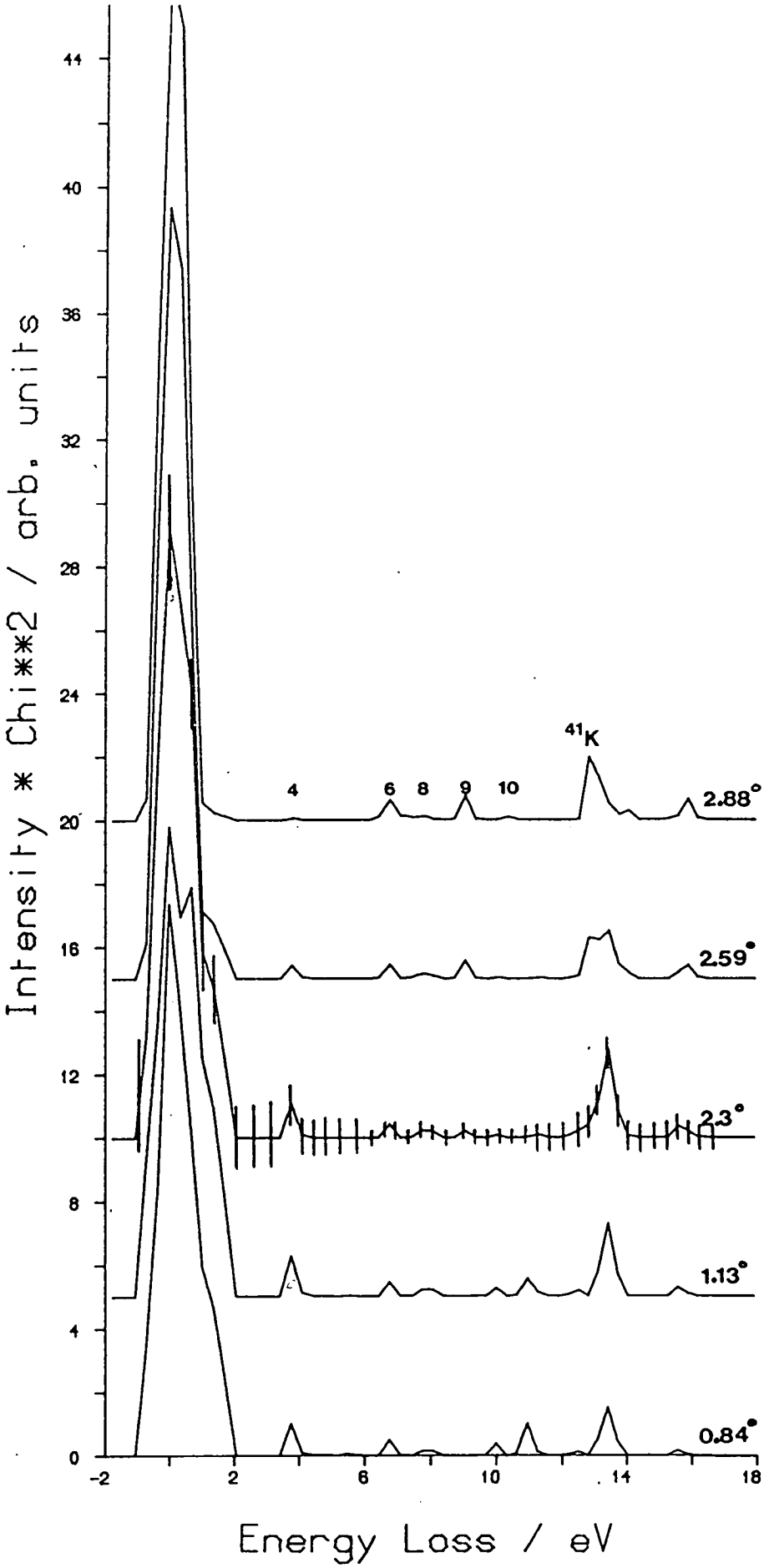


Fig. 3.7: $K + N_2$ Time of Flight Profiles at 58.1 eV CM Collision Energy.

Process numbers are indicated and typical error bars shown.

$0.84^{\circ}$ - $2.88^{\circ}$ CM.

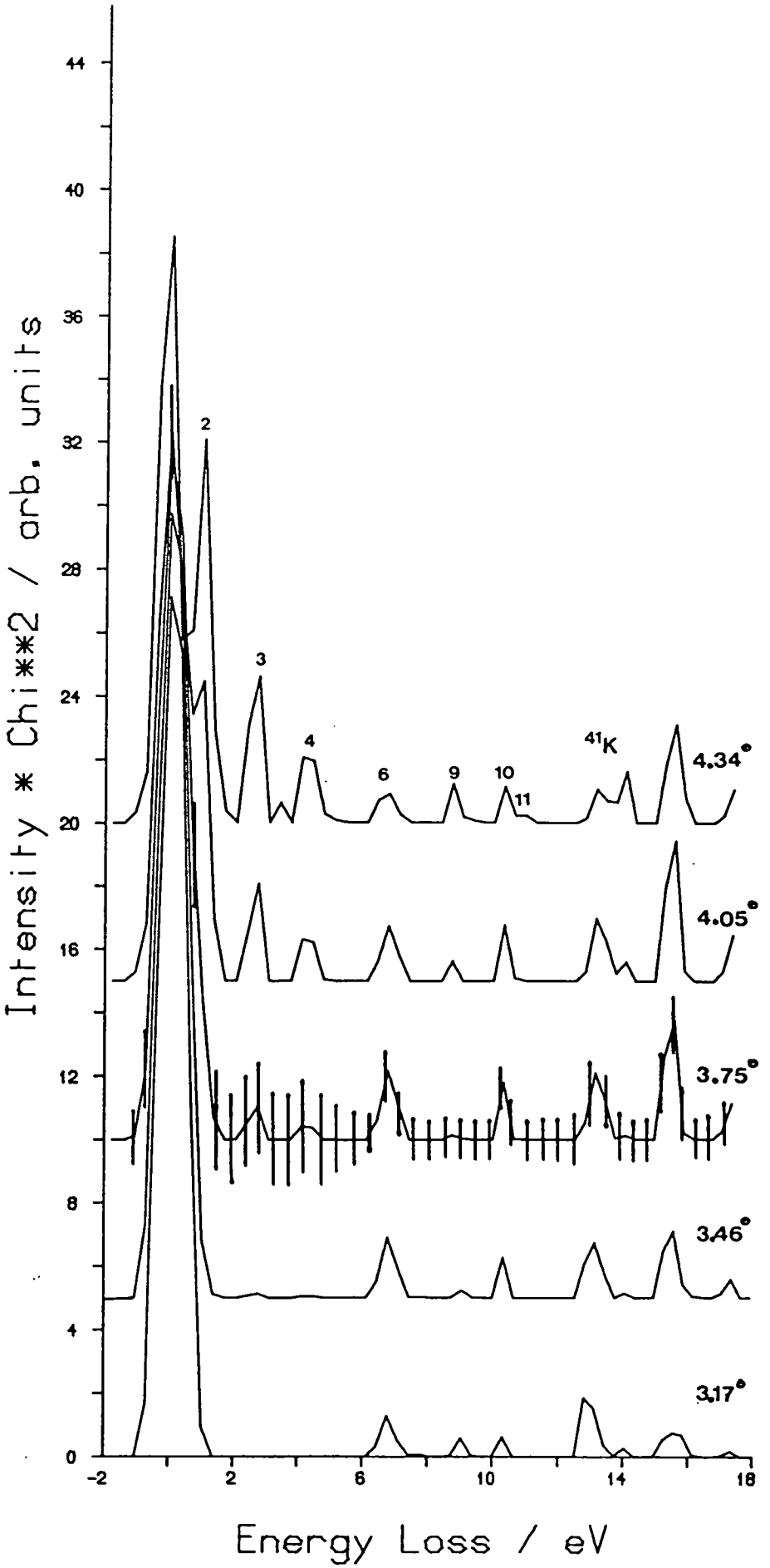


Fig. 3.7 continued.
3.17° - 4.34° CM.

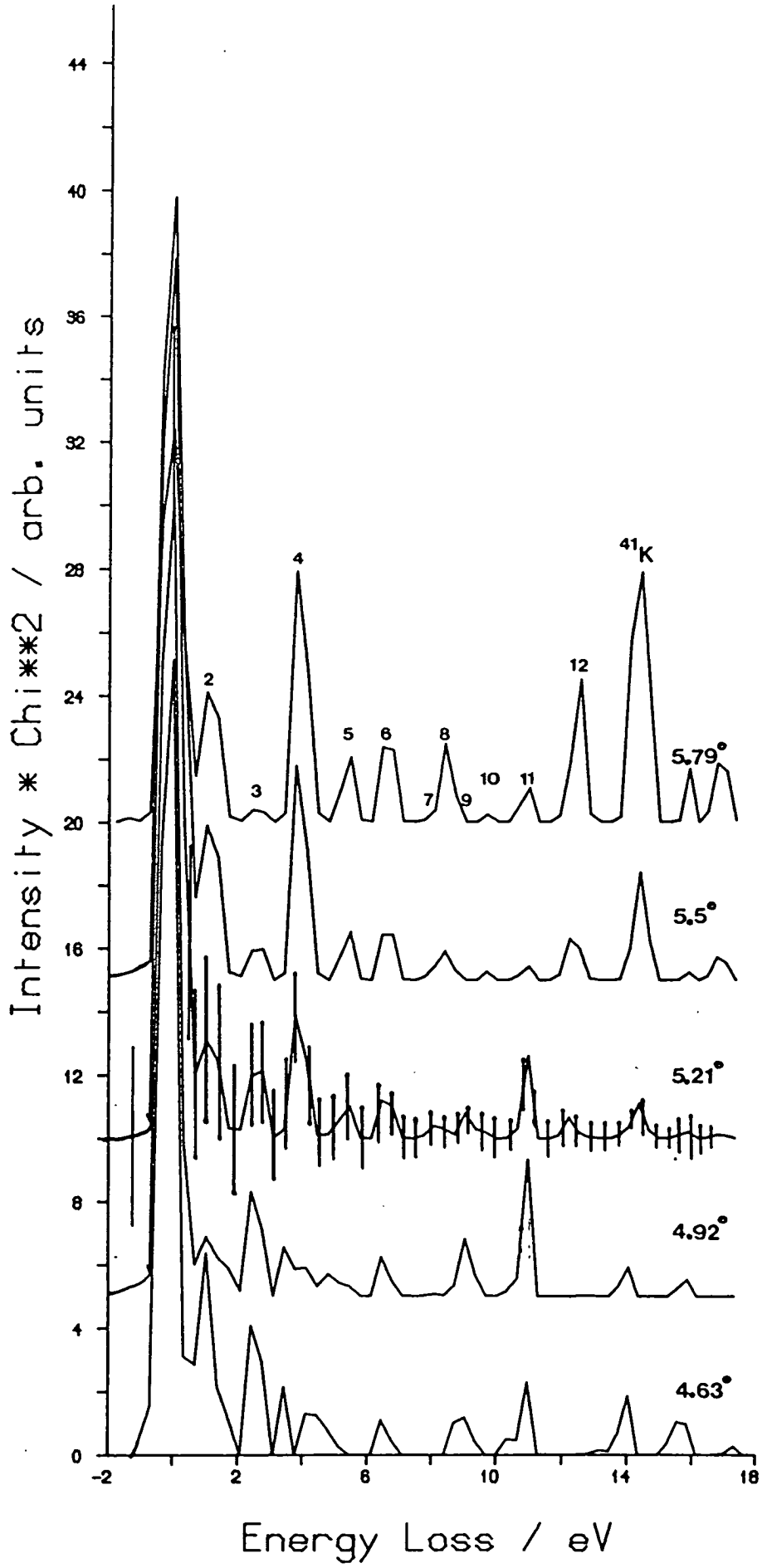


Fig. 3.7 continued.
4.63° - 5.79° CM.

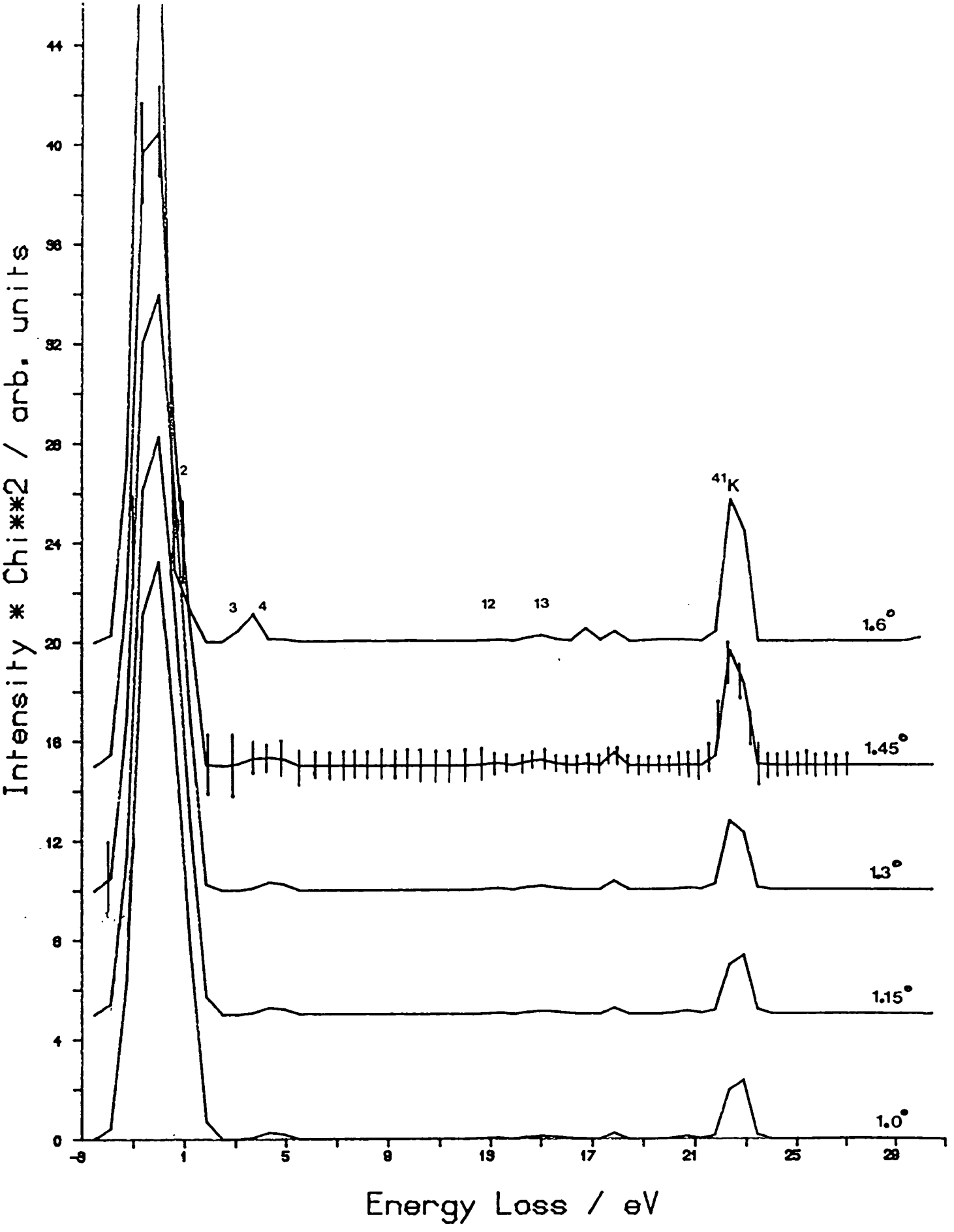


Fig. 3.8: $K + N_2$ Time of Flight Profiles at 106.7 eV CM Collision Energy.

Process numbers are indicated and typical error bars shown.

$1.0^\circ - 1.6^\circ$ CM.

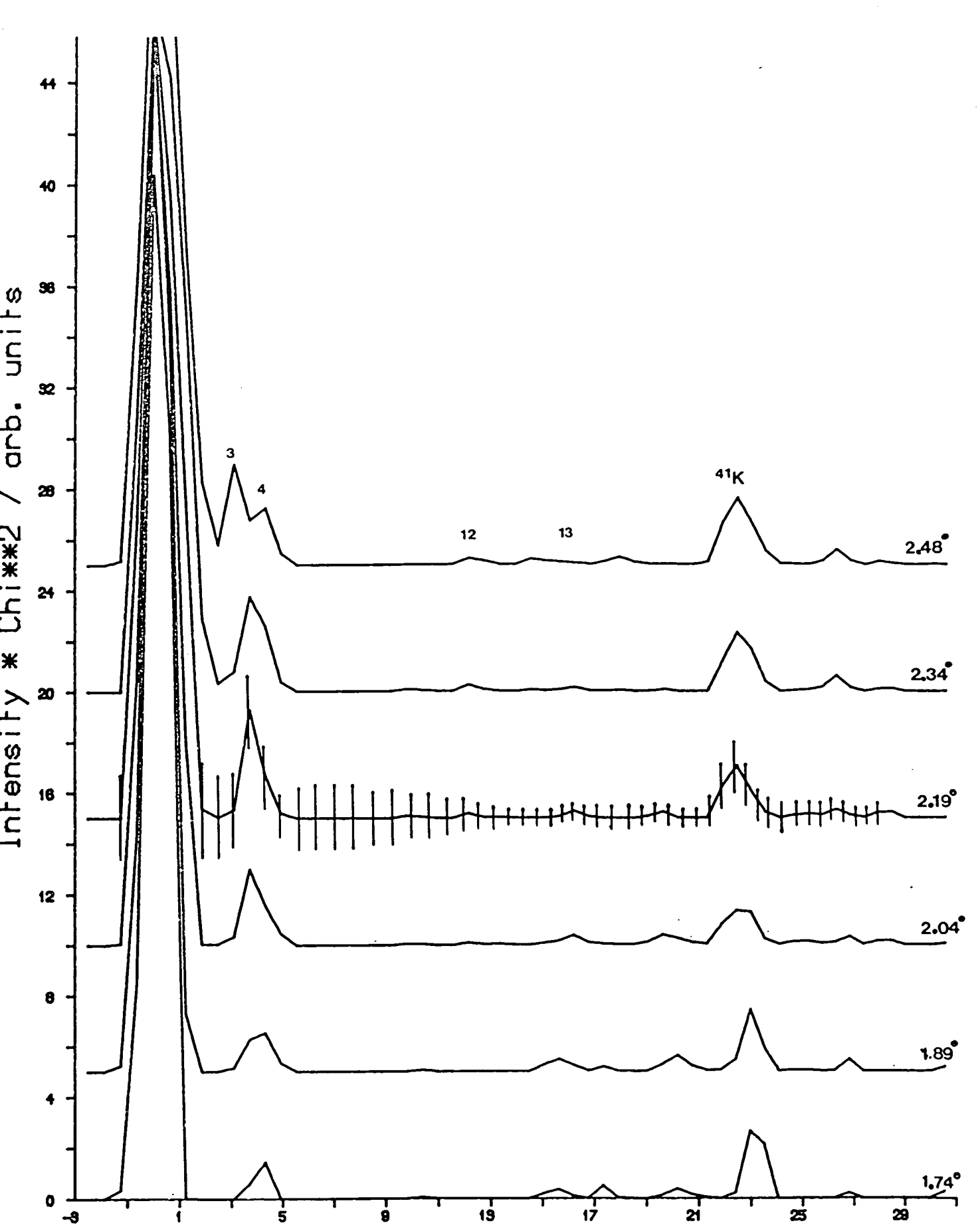


Fig. 3.8 continued.
1.74° - 2.48° CM.

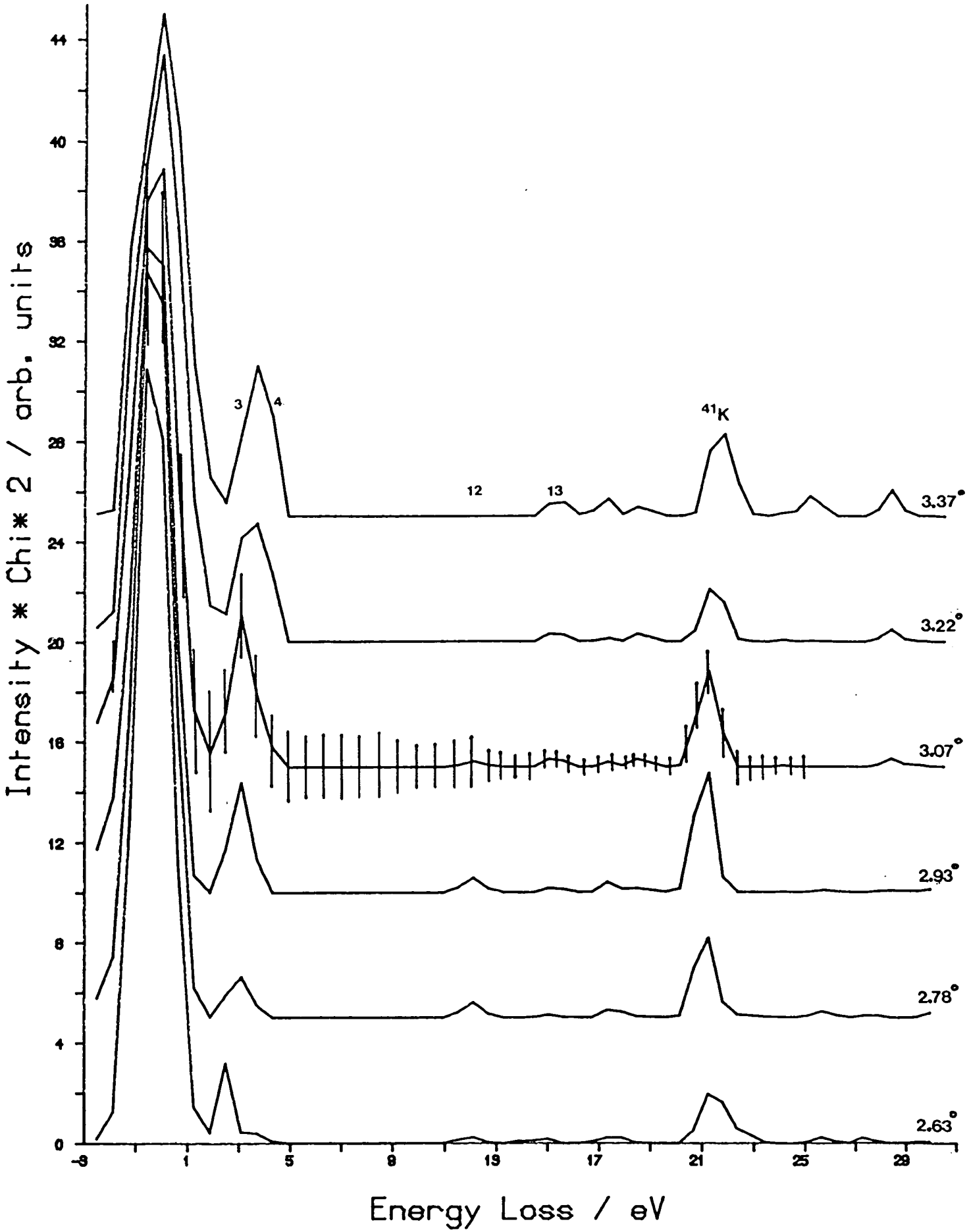


Fig. 3.8 continued.
2.63° - 3.37° CM.

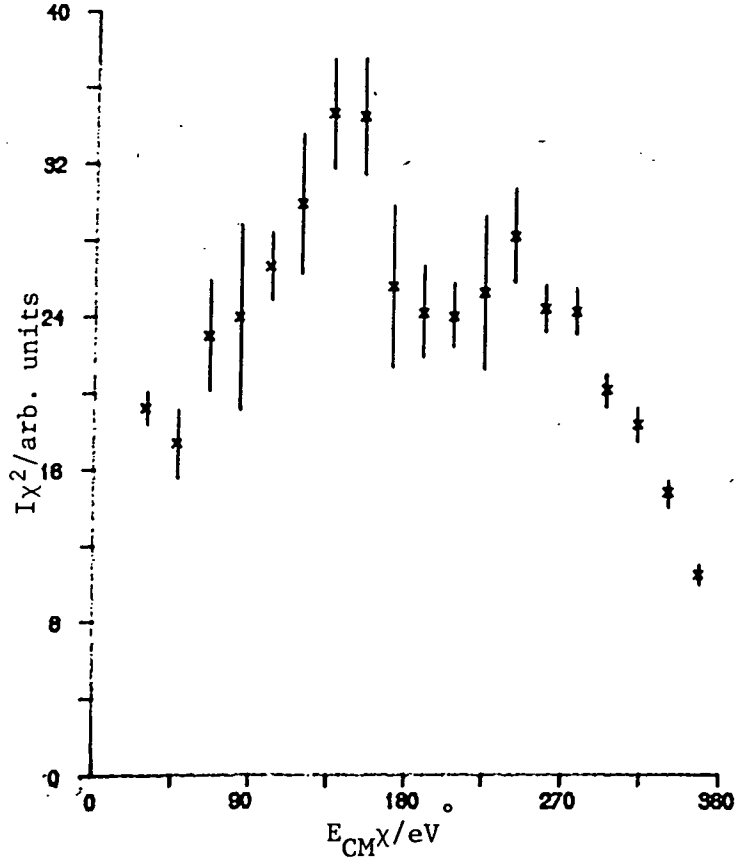


Fig. 3.9: 43.3eV CM, Process 1
Elastic

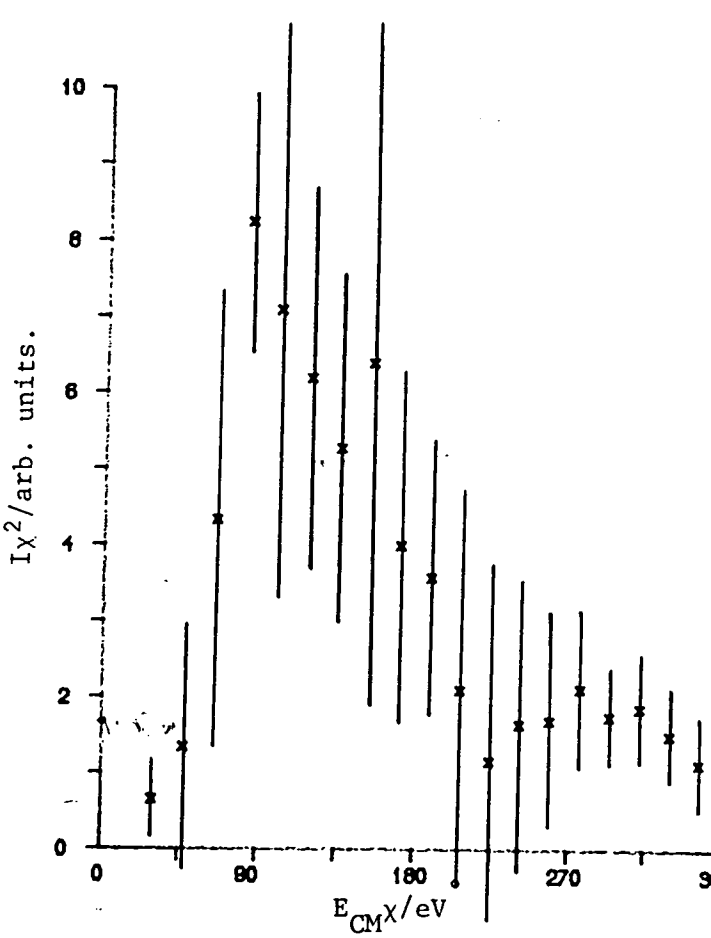


Fig. 3.10: 43.3eV CM, Process 2
Vib. excitation in N-N

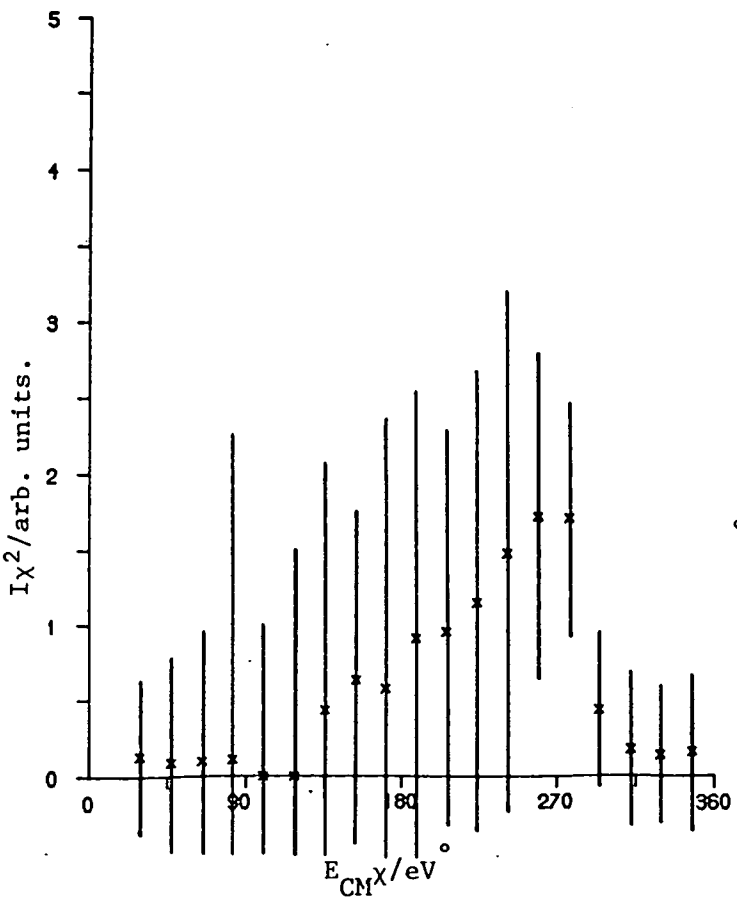


Fig. 3.11: 43.3eV CM Process 3a
K(4p) crossing early

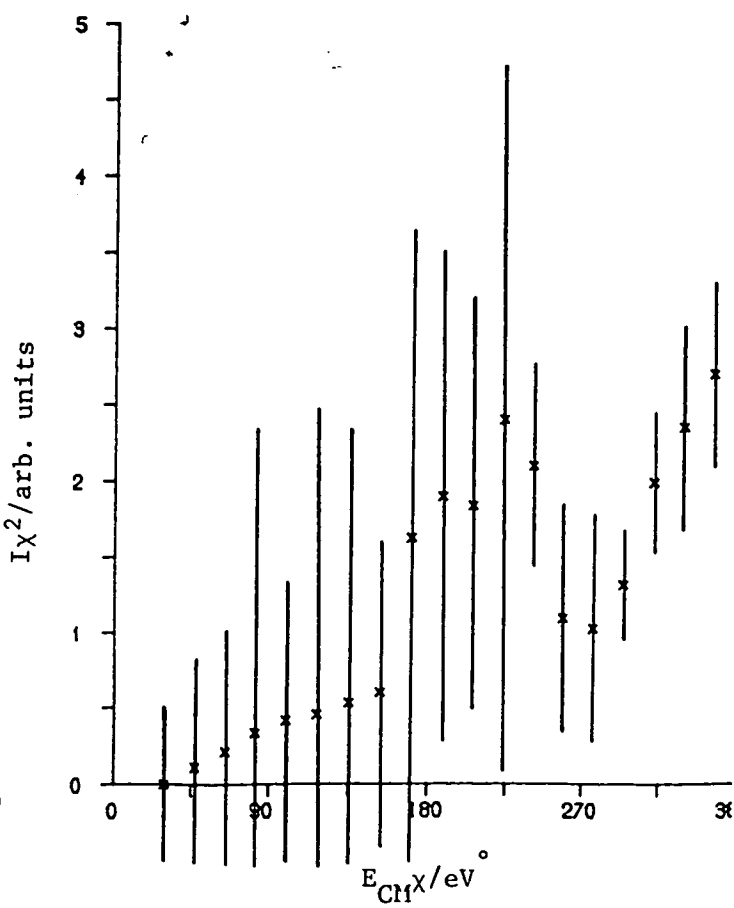


Fig. 3.12: 43.3eV CM Process 3b
K(4p), crossing late.

All error bars are 2 standard deviations long.

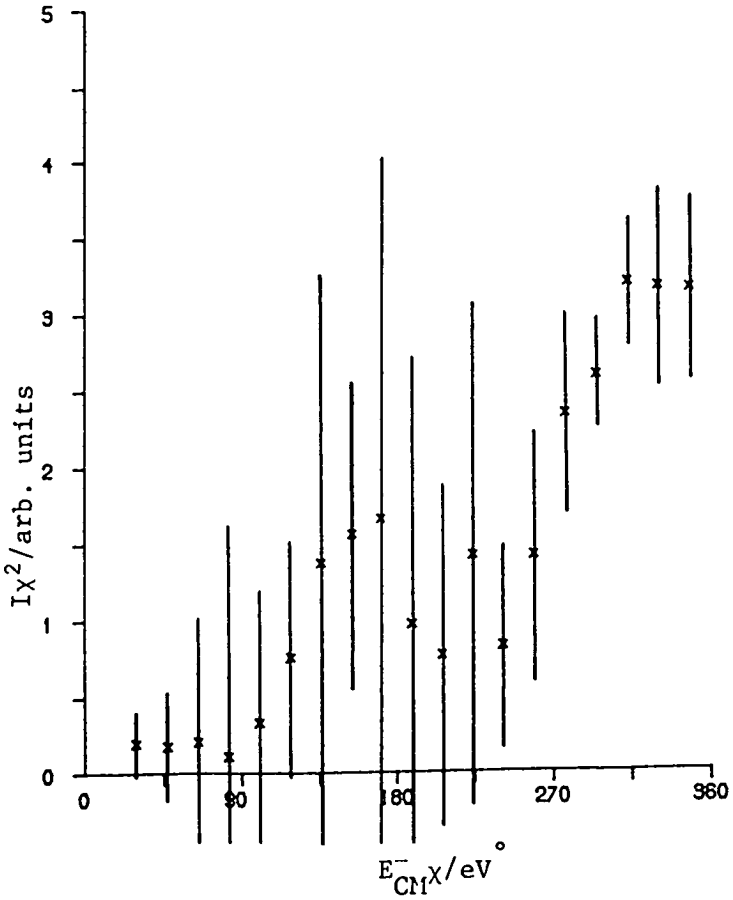


Fig. 3.13: 43.3eV CM, Process 4a
K(5s), early crossing

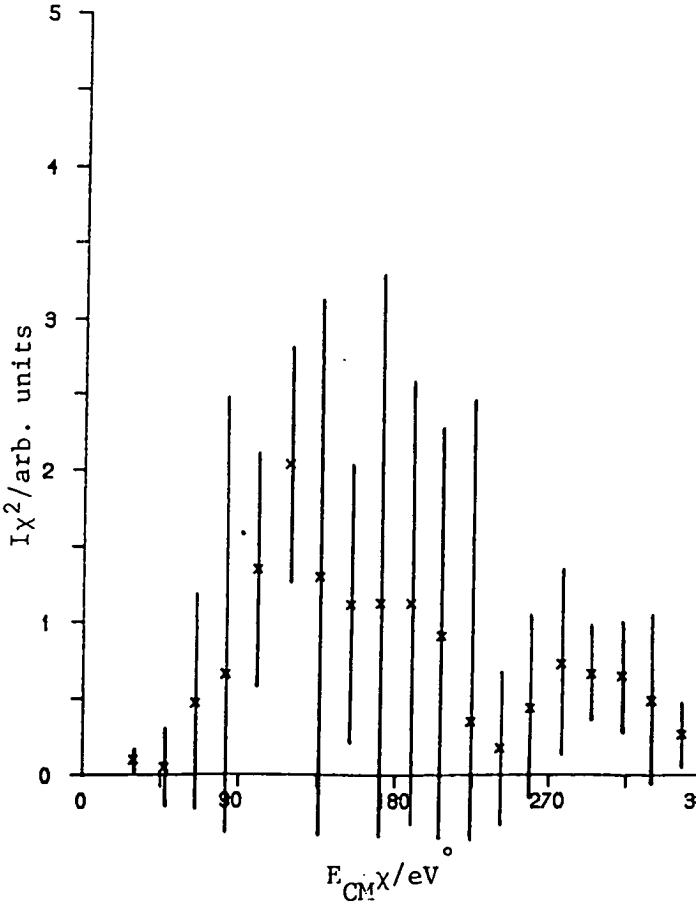


Fig. 3.14: 43.3eV CM, Process 4b
K(5s), late crossing

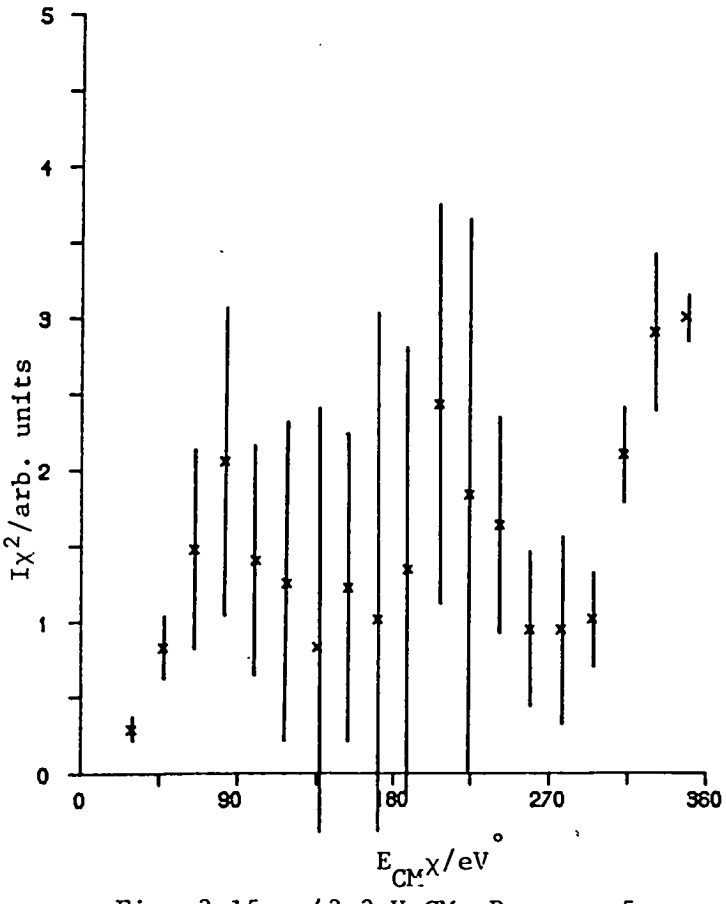


Fig. 3.15: 43.3eV CM, Process 5a
K(5p), early crossing

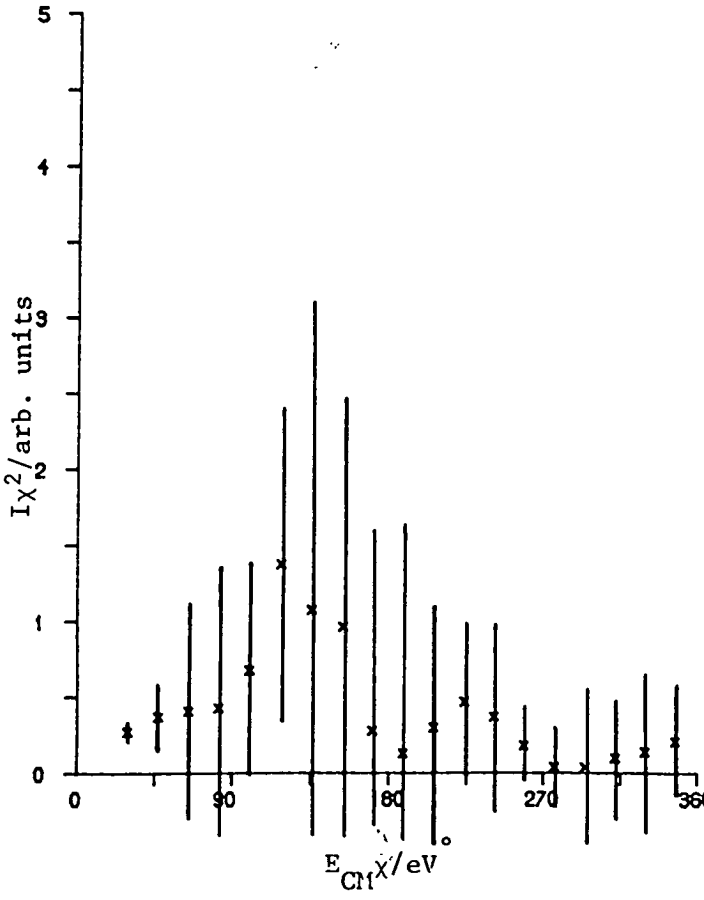


Fig. 3.16: 43.3eV CM, Process 5b
K(5p), late crossing

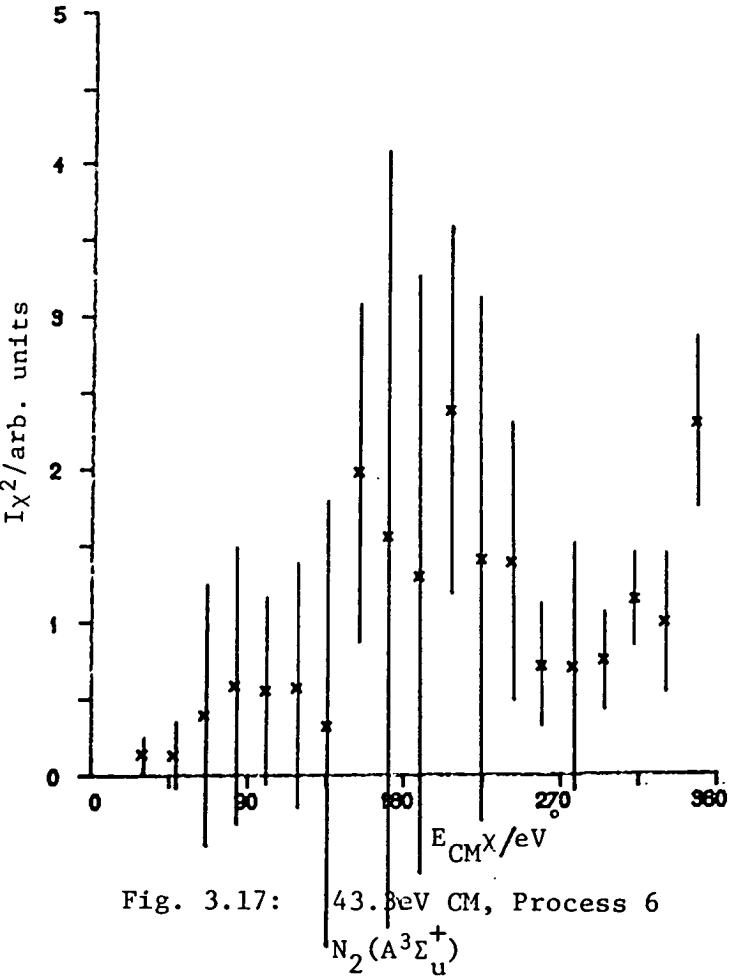


Fig. 3.17: 43.3eV CM, Process 6
$N_2(A^3\Sigma_u^+)$

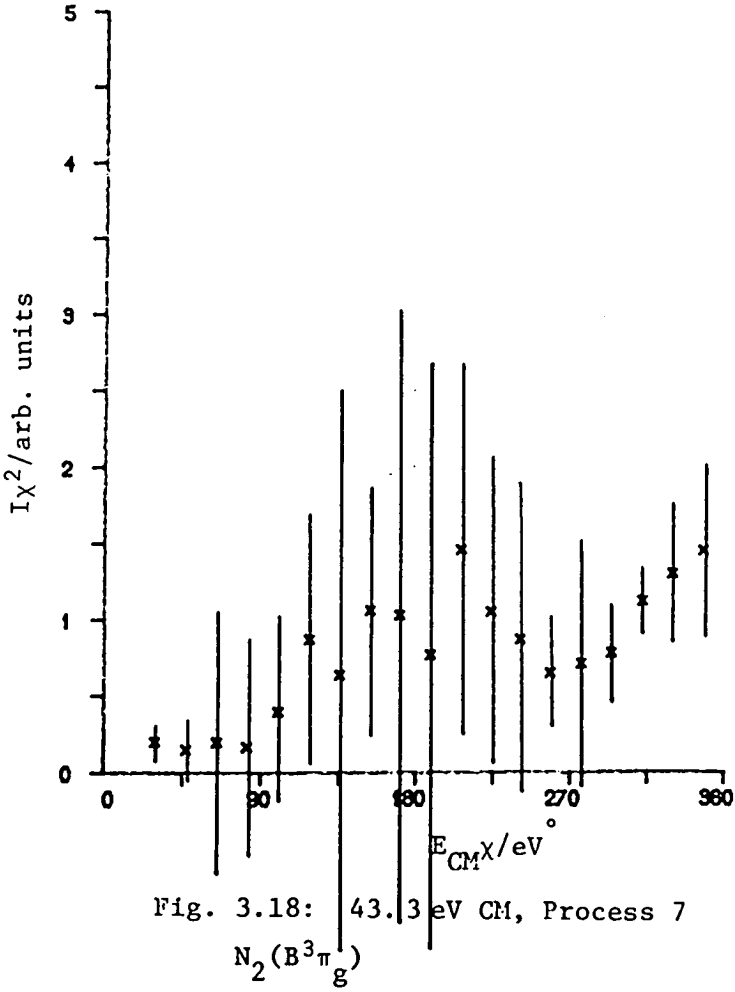


Fig. 3.18: 43.3 eV CM, Process 7
$N_2(B^3\pi_g)$

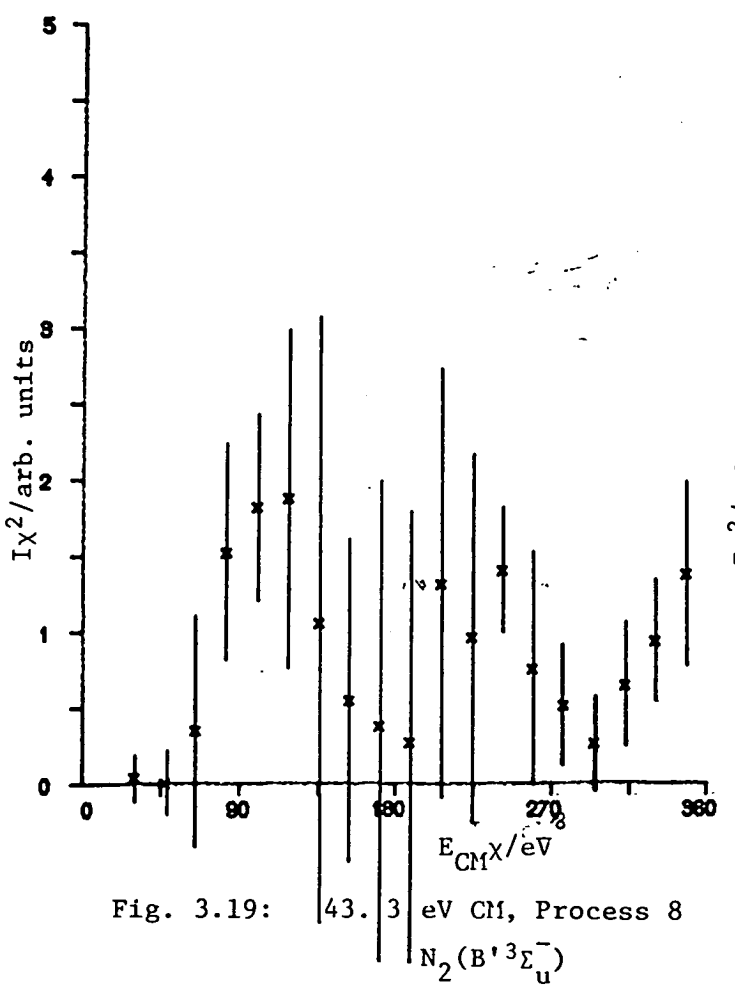


Fig. 3.19: 43.3 eV CM, Process 8
$N_2(B'^3\Sigma_u^-)$

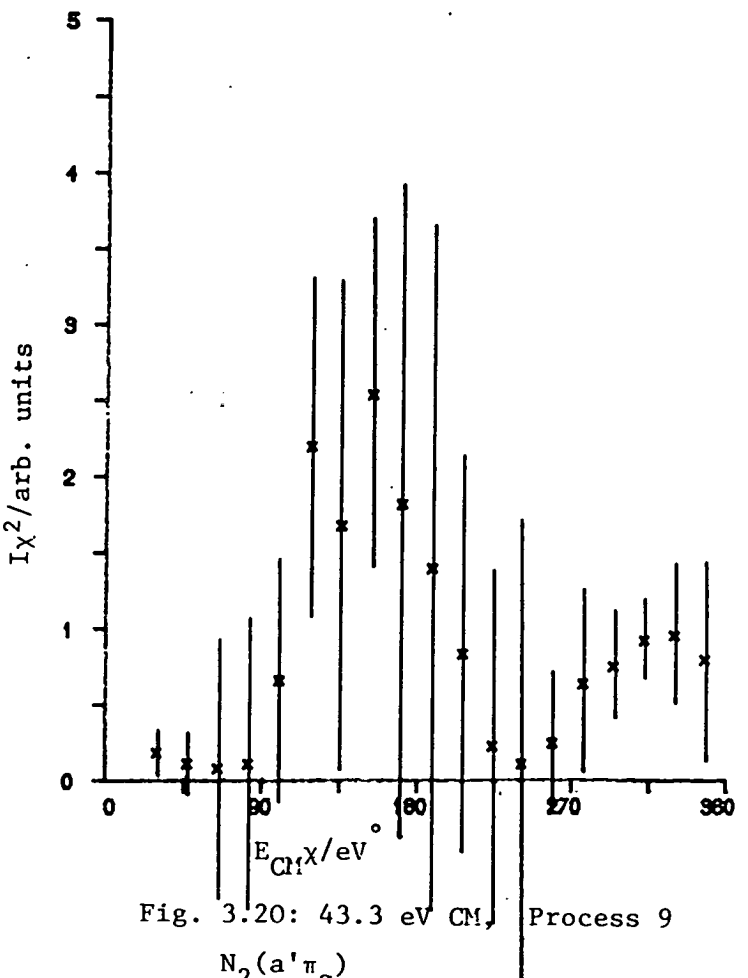


Fig. 3.20: 43.3 eV CM, Process 9
$N_2(a'^1\pi_g)$

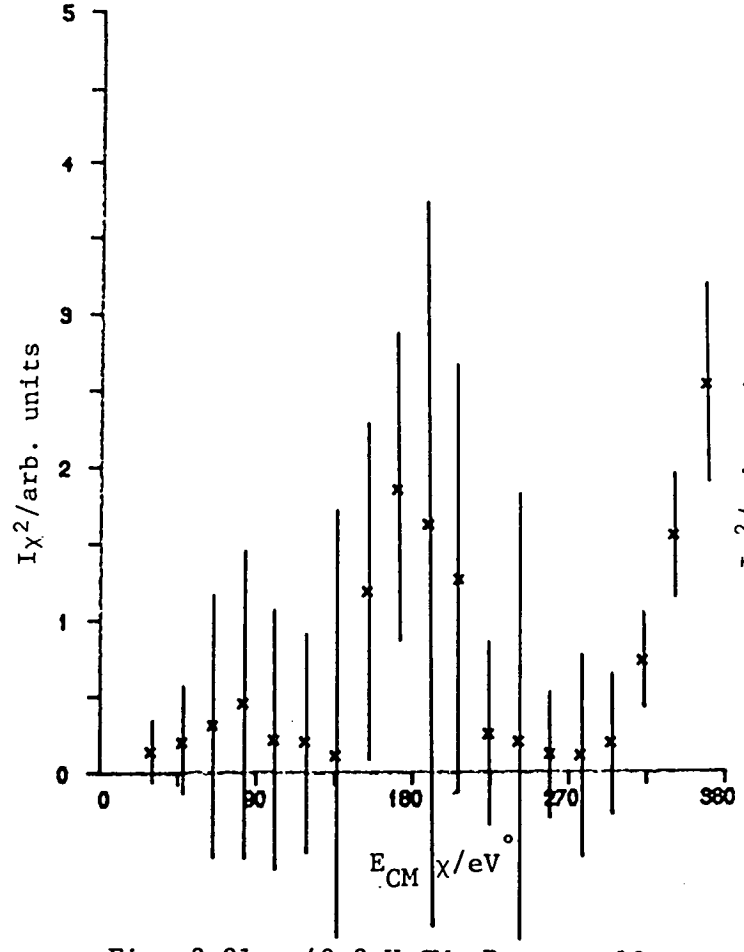


Fig. 3.21: 43.3eV CM, Process 10
$N_2(^5\Sigma^+_g)$

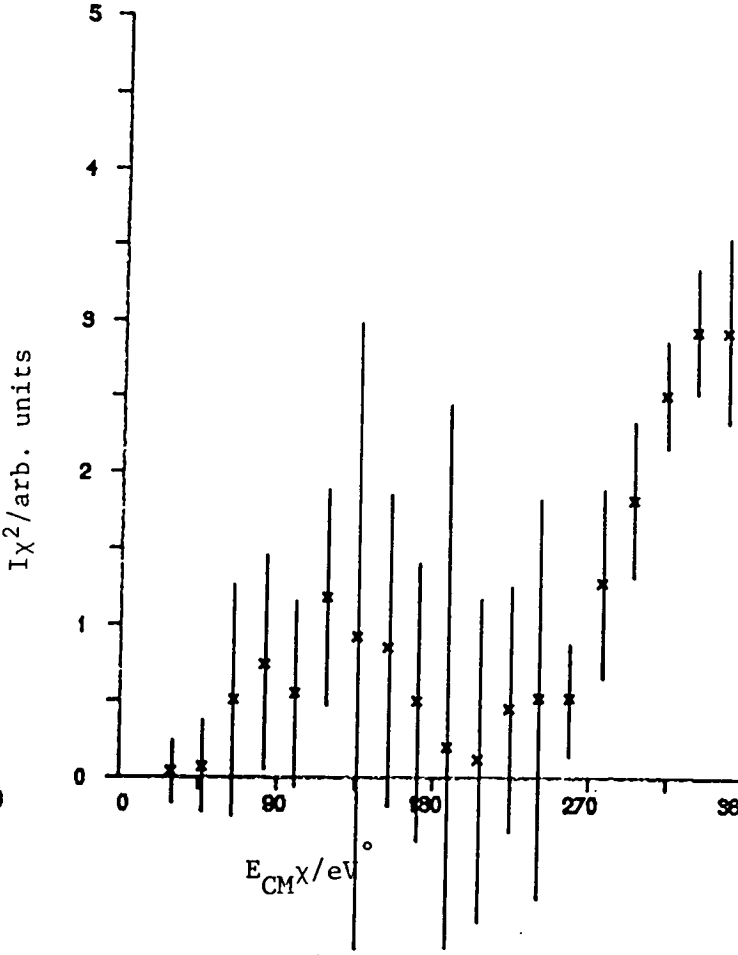


Fig. 3.22: 43.3eV CM, Process 11
$N_2(^1\Sigma^+_g)$

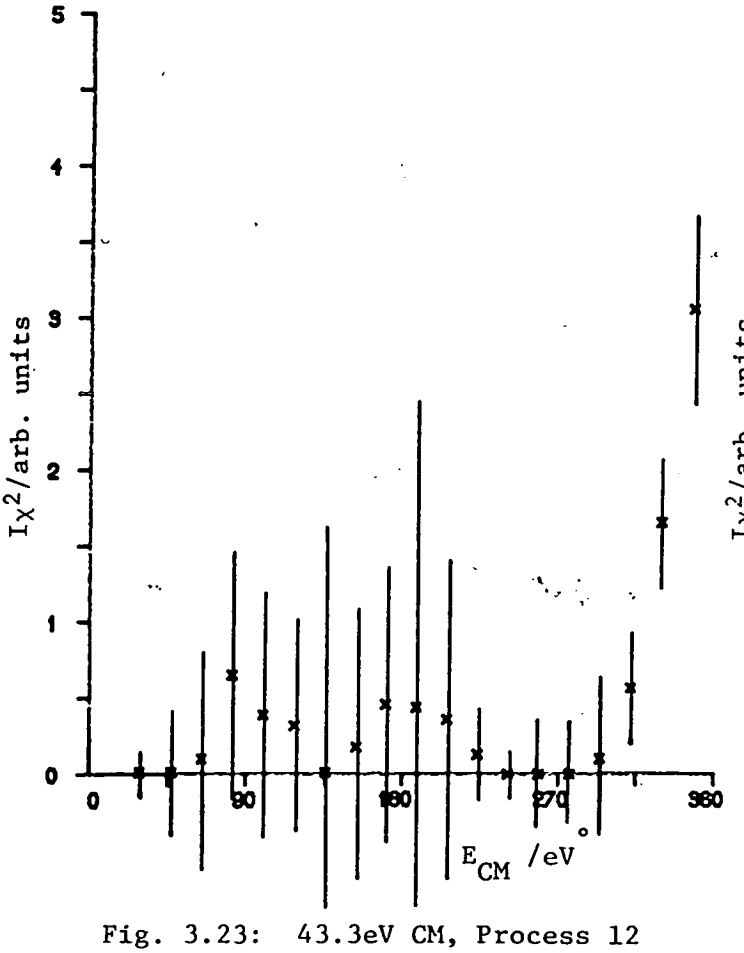


Fig. 3.23: 43.3eV CM, Process 12
$N_2(C^3\pi_u)$

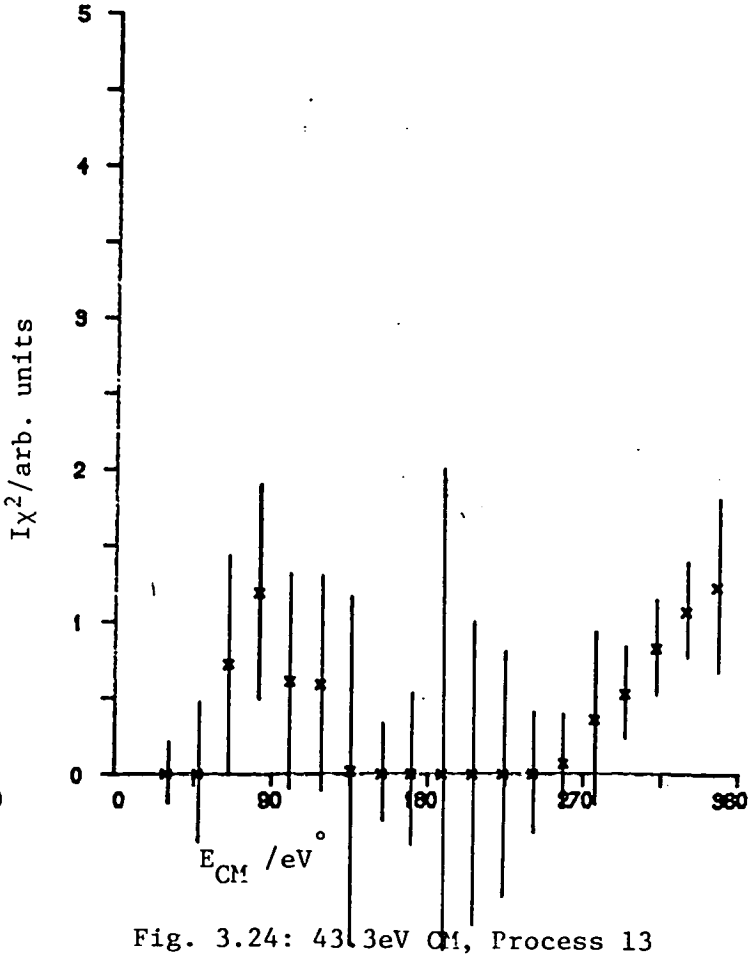


Fig. 3.24: 43.3eV CM, Process 13
$N(E^3\Sigma^+_g)$

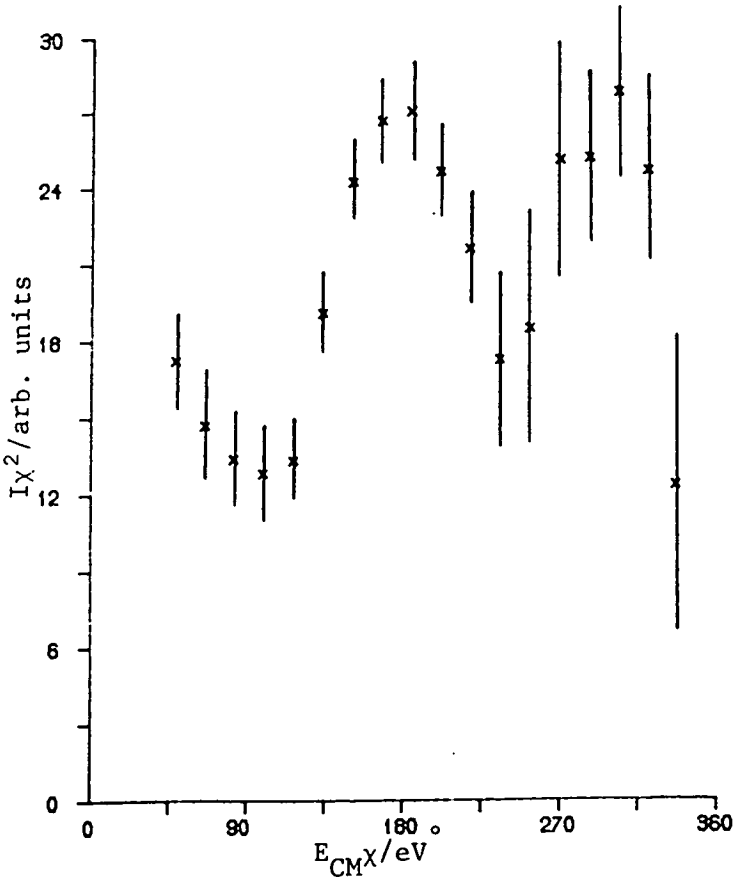


Fig. 3.25: 58.1eV CM, Process 1
Elastic

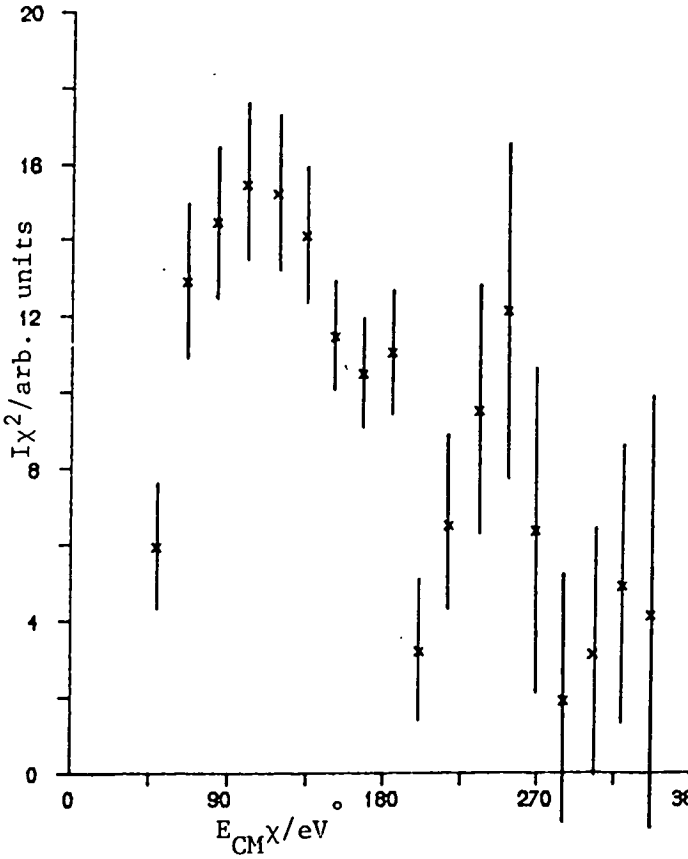


Fig. 3.26: 58.1eV CM, Process 2
Vib. excitation in N-N

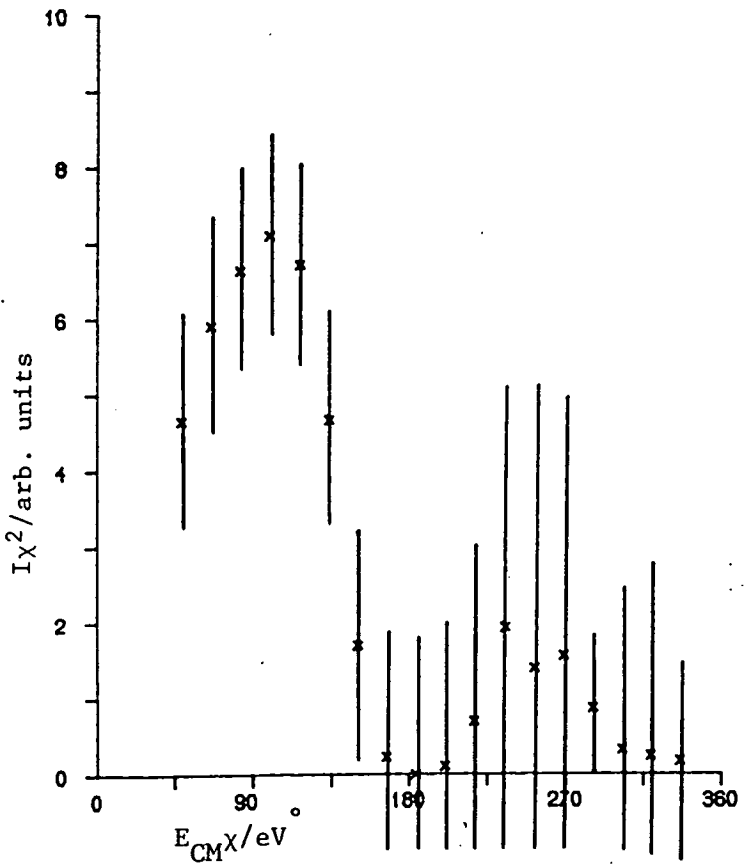


Fig. 3.27: 58.1eV CM, Process 3
K(4p) early and late

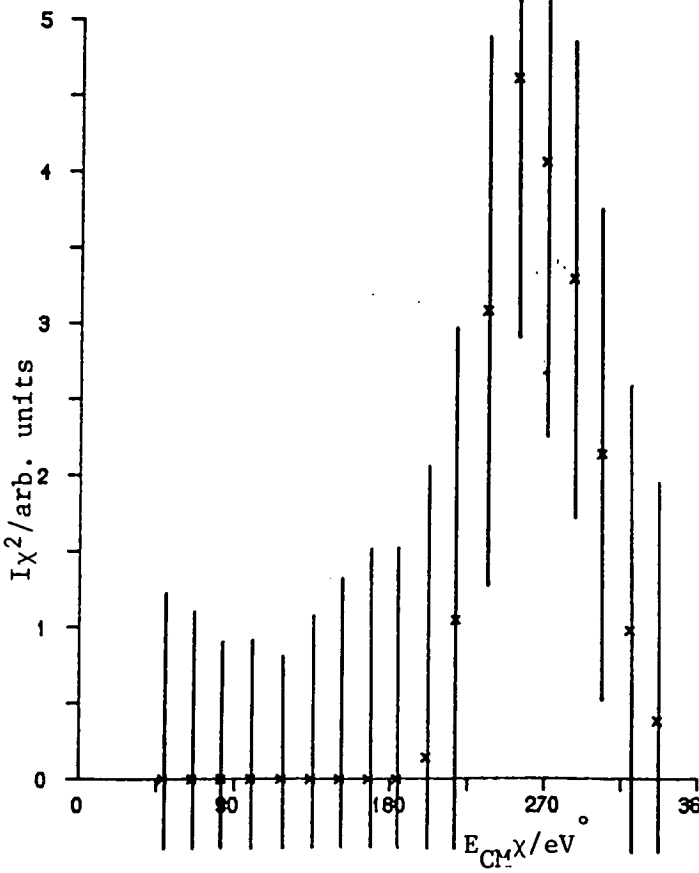


Fig. 3.28: 58.1eV CM, Process 4
K(5s) early and late.

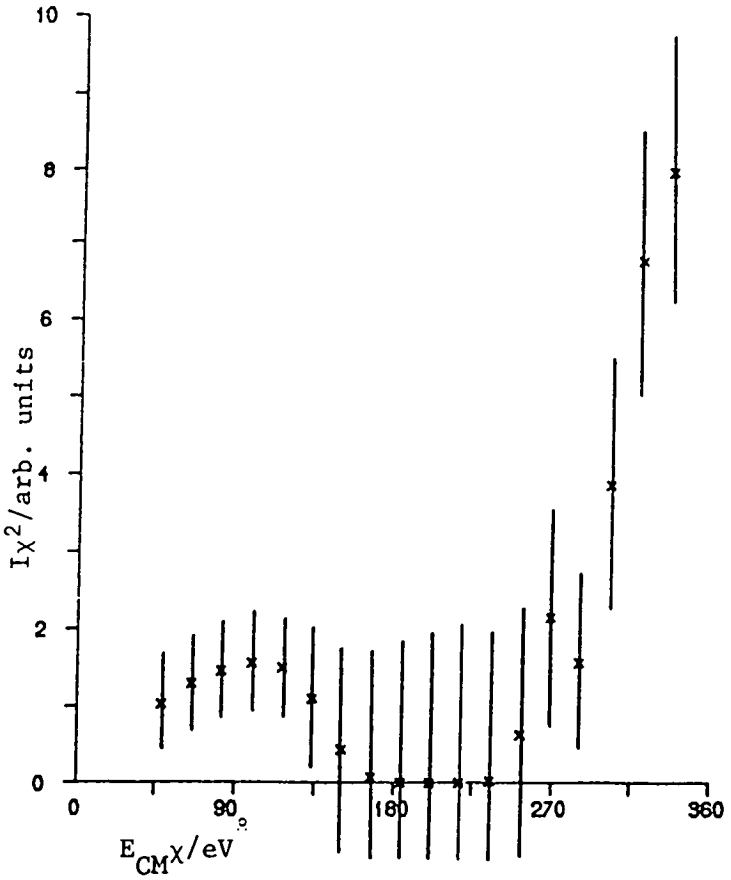


Fig. 3.29: 58.1eV CM, Process 5
K(5p) early and late

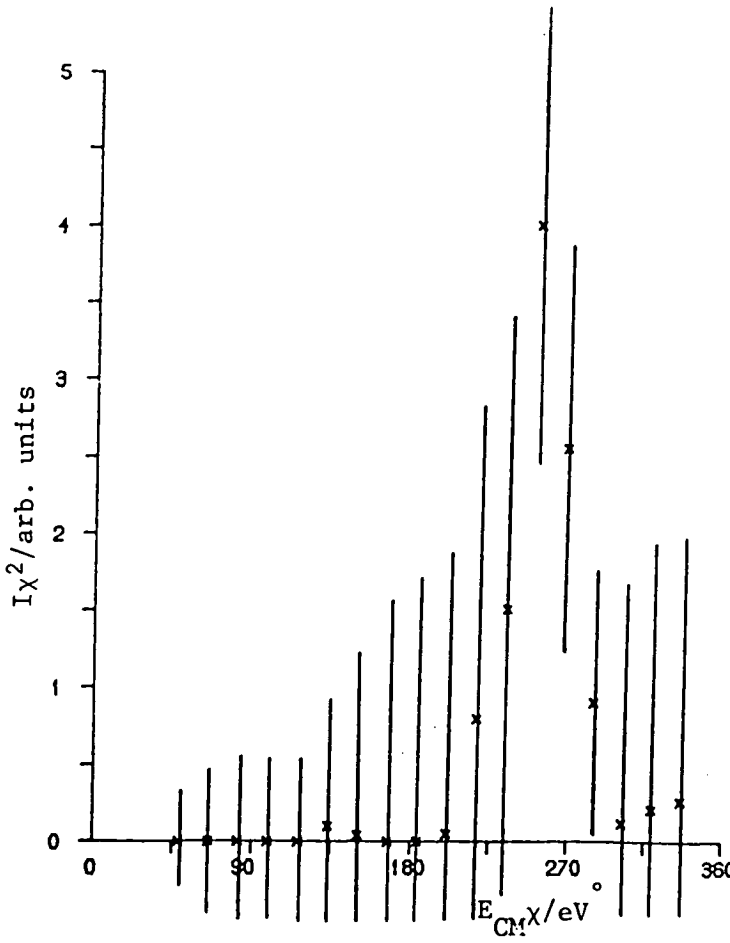


Fig. 3.30: 58.1eV CM, Process 6
$N_2(A^3\Sigma_u^+)$

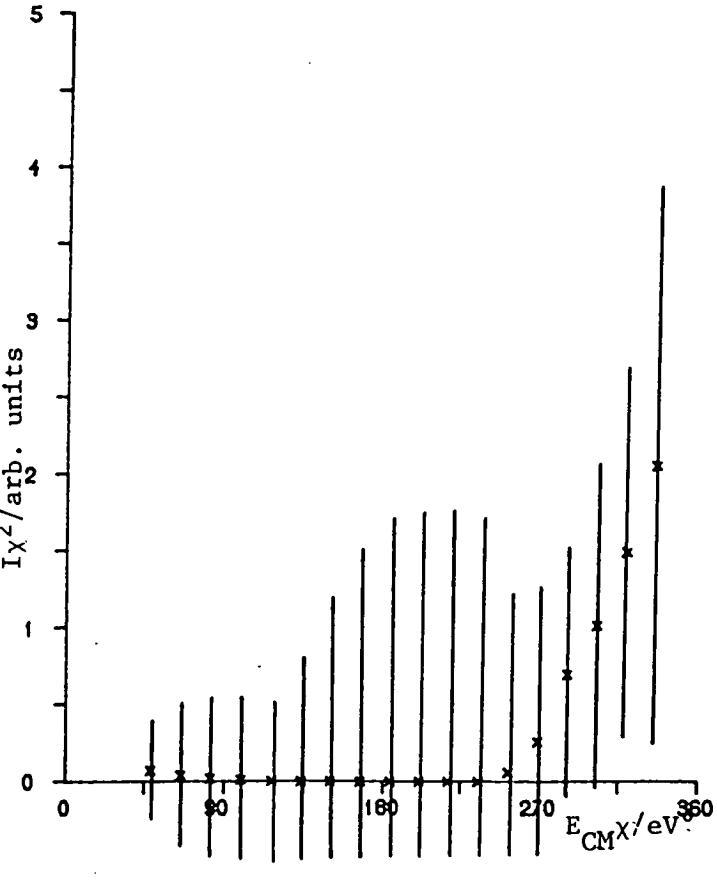


Fig. 3.31: 58.1eV CM, Process 7
$N_2(B^3\pi_g)$

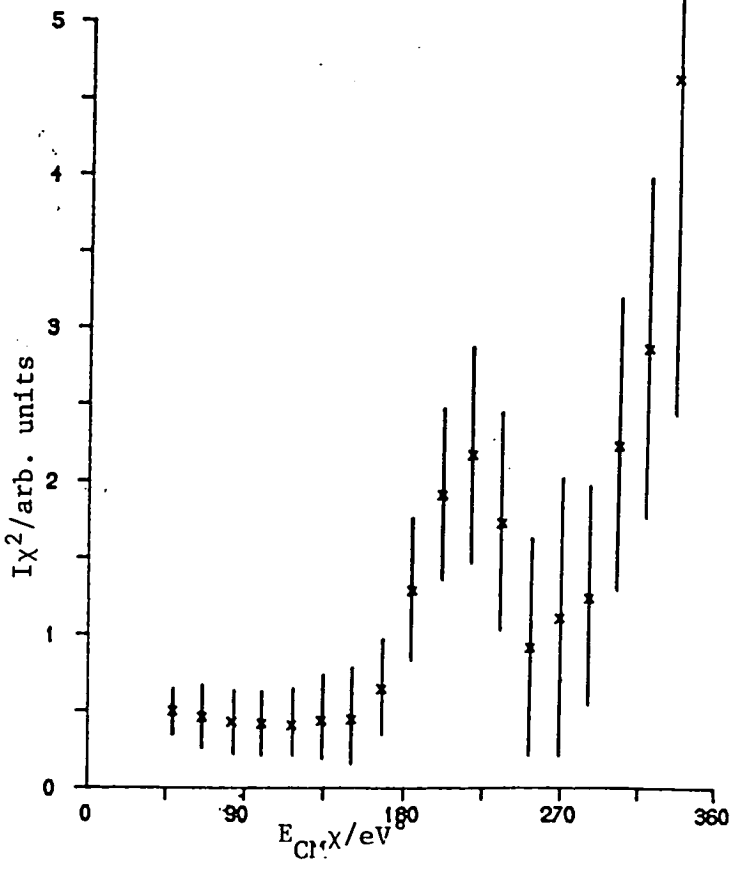


Fig. 3.32: 58.1eV CM, Process 8
$N_2(B'^3\Sigma_u^-)$

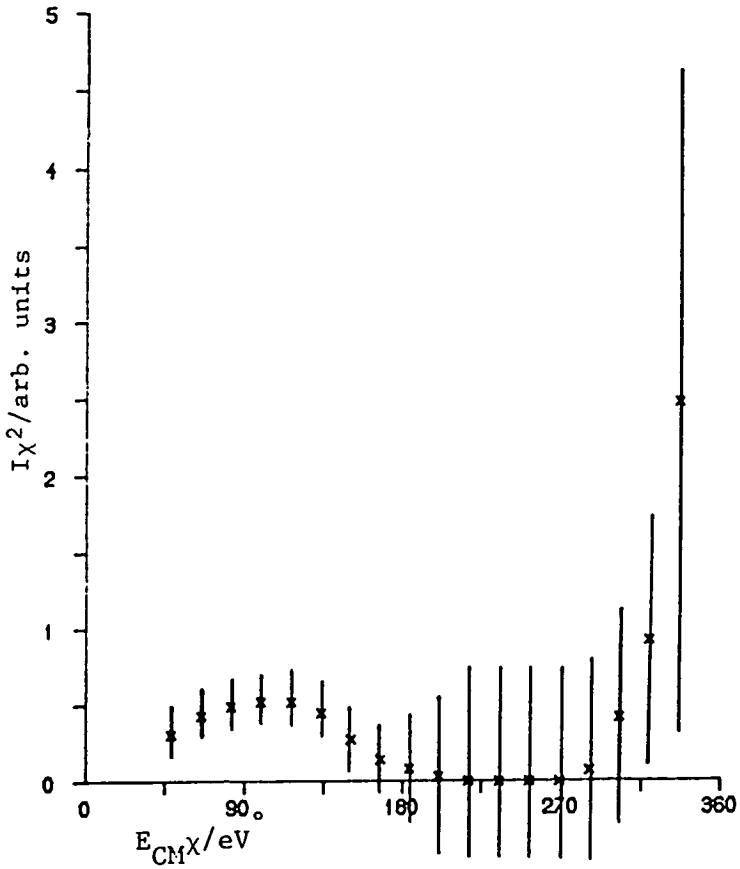


Fig. 3.33: 58.1eV CM, Process 9

$N_2(a'\pi_g)$

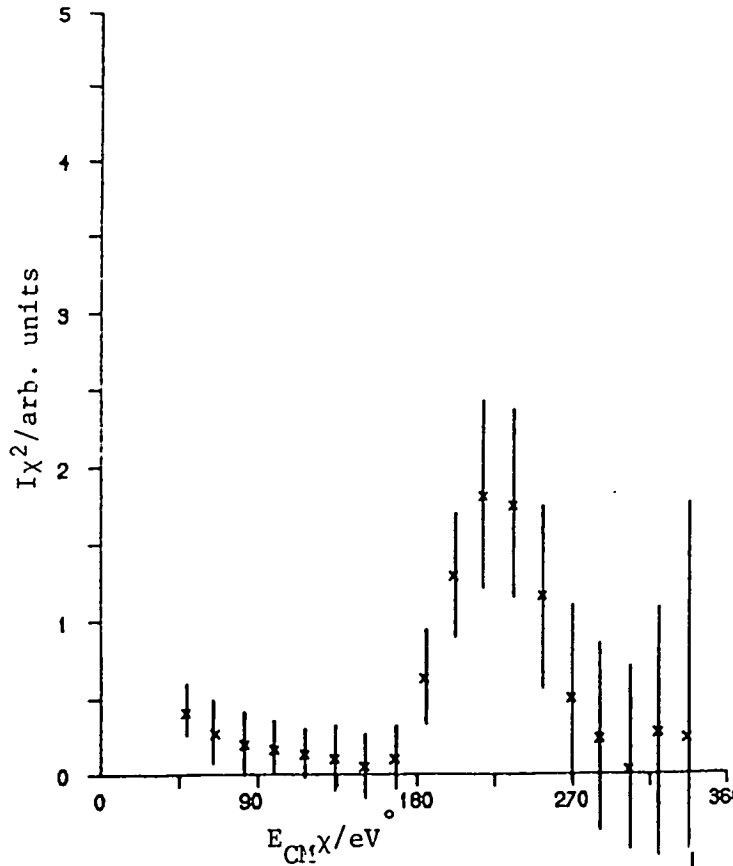


Fig. 3.34: 58.1eV CM, Process 10

$N_2(^5\Sigma_g^+)$

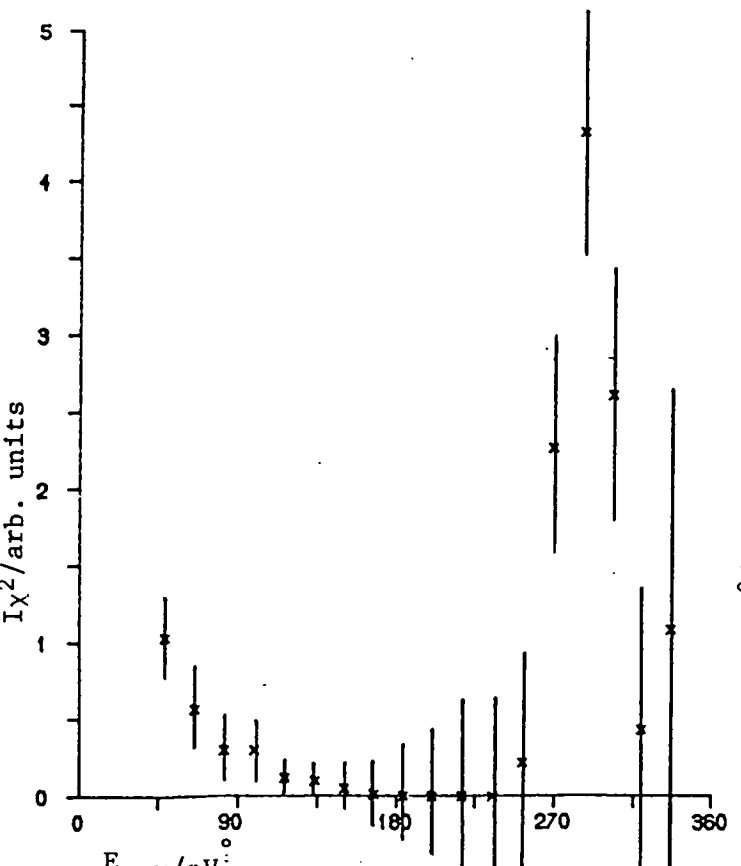


Fig. 3.35: 58.1eV CM, Process 11

$N_2(^1\Sigma_g^+)$

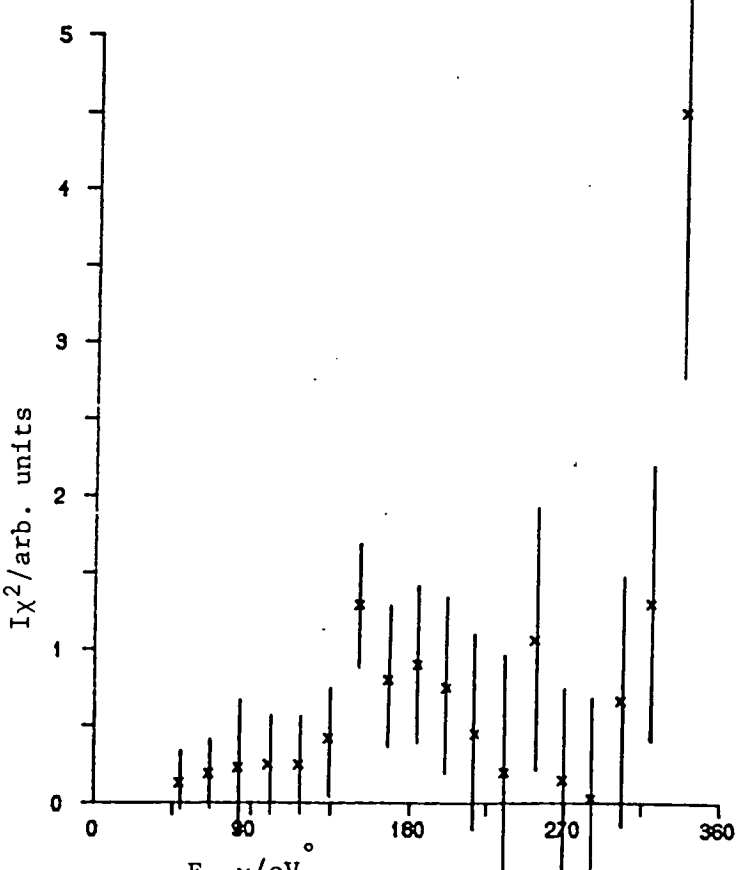


Fig. 3.36: 58.1eV CM, Process 12

$N_2(C^3\pi_u)$

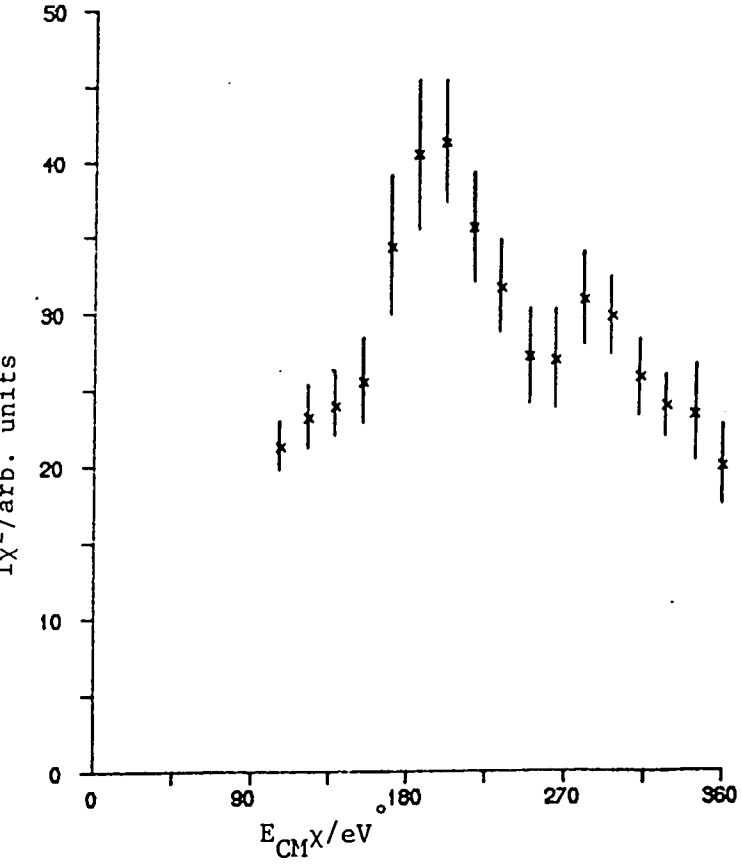


Fig. 3.37: 106.7eV CM, Process 1
Elastic

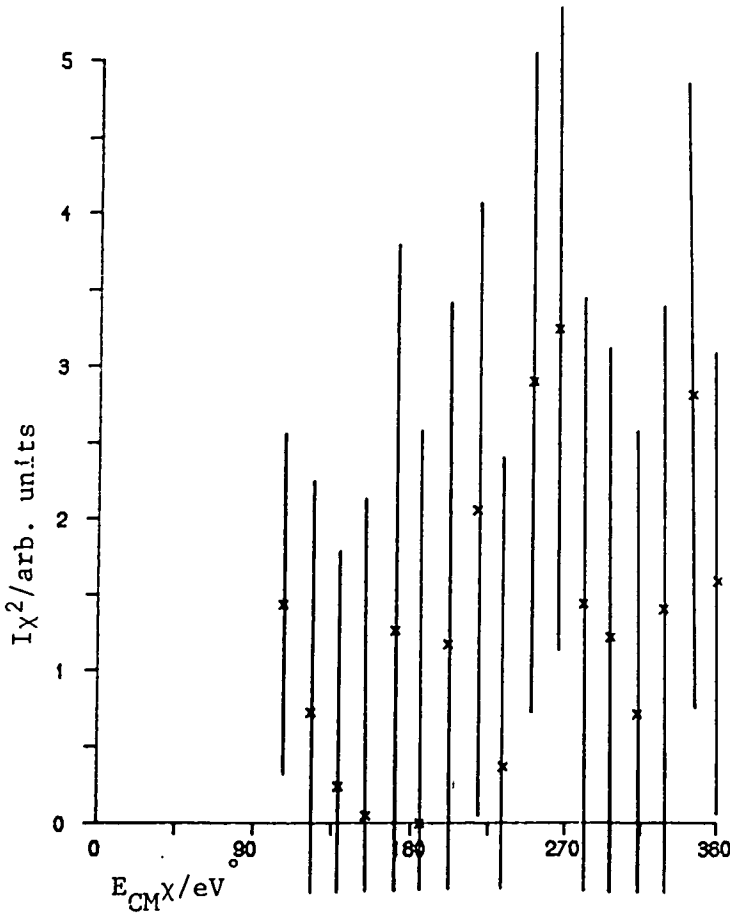


Fig. 3.38: 106.7eV CM, Process 2
Vib. excitation in N-N

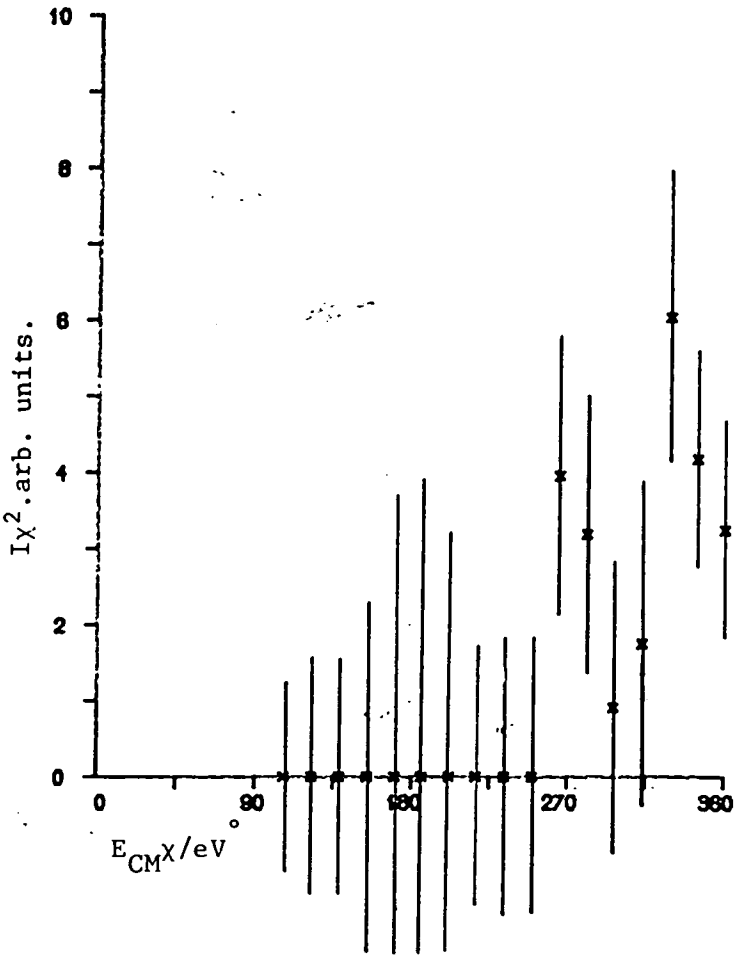


Fig. 3.39: 106.7eV, CM, Process 3
K(4p) early and late

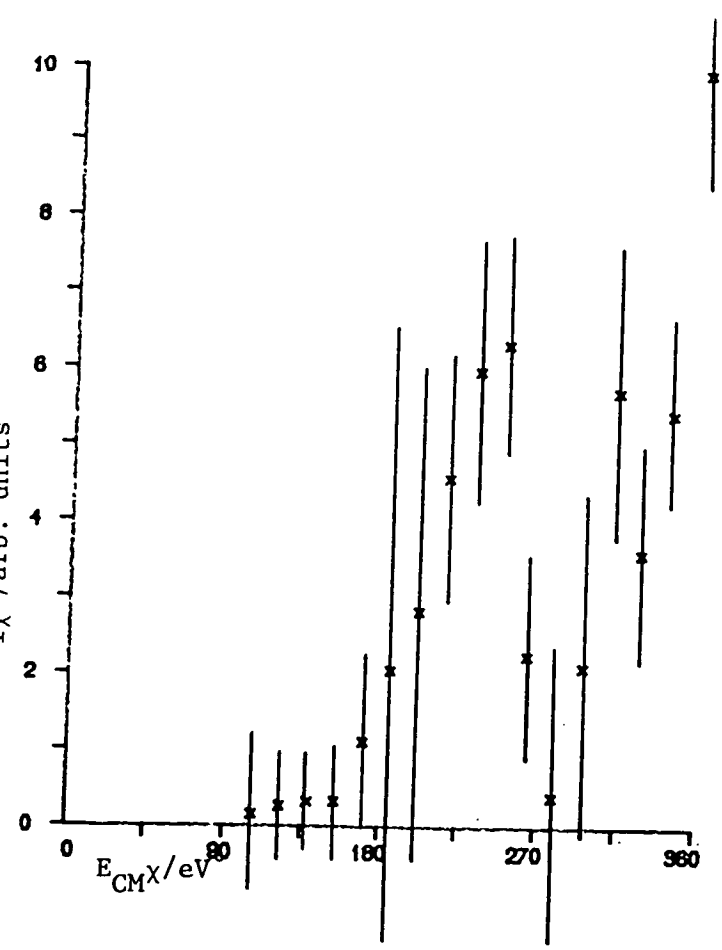


Fig. 3.40: 106.7eV CM, Process 4
K(5s) early and late

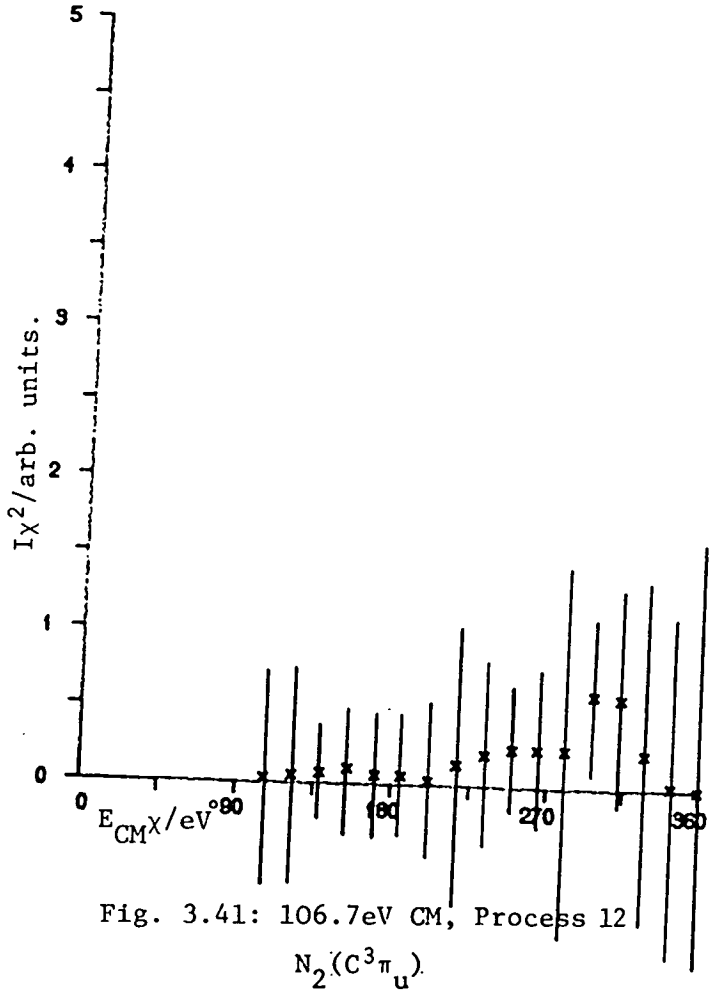


Fig. 3.41: 106.7eV CM, Process 12
$N_2(C^3\pi_u)$

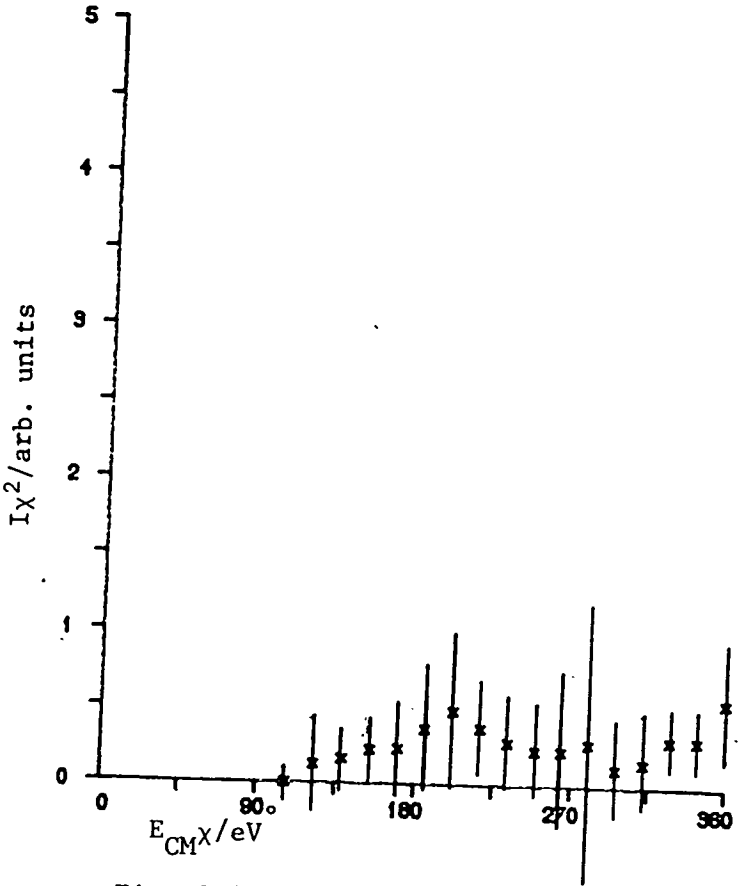


Fig. 3.42: 106.7eV CM, Process 13
$N_2(E^3\Sigma_g^+)$

TABLE 3.4

Observed Energy Losses, $K+N_2$

| Collision Energy | cm/eV | 43.3 | 58.1 | 85.6 | 106.7 | Proposed assignment based on model results (Chap. 6) | Predicted electronic Energy Loss/eV |
|---|---|---|---|---|---|---|---|
| Process No. | 1 | 0 | 0 | 0 | 0 | Elastic | 0 |
| | 2 | 0.6<br>1.5 | 0.8<br>1.4 | 1.1<br>2.2 | 1.9 | vib. energy in N-N bond | 0 |
| | 3a | 2.25 | 2.7 | 2.8 | 3.1 | 4s → 4p | 1.6 (BAC 32) |
| | 3b | 3.0 | | 3.6 | | | |
| | 4a | 3.7<br>4.4 | 3.7<br>4.1 | 4.3<br>5.0 | 4.5 | 4s → 5s | 2.6 " |
| | 5a | 5.0 | 4.6 | | | 4s → 5p | 3.1 " |
| | 5b | 5.6 | 5.5 | 5.5 | | | |

TABLE 3.4 continued.

| Collision Energy cm/eV | | 43.3 | 58.1 | 85.6 | 106.7 | Proposed Assignment | Predicted ΔE/eV |
|---|---|---|---|---|---|---|---|
| Process No. | 6 | 6.4 | 6.5 | | | $X\Sigma_g^+ \rightarrow A^3\Sigma_u^+$ | 6.2 (MIC 83) |
| | 7 | 7.5 | 7.5 | 7.0 | | $X\Sigma_g^+ \rightarrow B^3\pi_g$ | 7.4 " |
| | 8 | 8.0, 8.4 | 8.0 | 8.0 | | $X\Sigma_g^+ \rightarrow B'^3\Sigma_u^-$ | 8.2 " |
| | 9 | 9.0 | 9.0 | | | $X\Sigma_g^+ \rightarrow a^1\pi_g$ | 8.6 " |
| | 10 | 9.7 | 10.2 | | | $X\Sigma_g^+ \rightarrow {}^5\Sigma_g^+$ | 9.7 " |
| | 11 | 10.7 | 10.8 | 10.5 | | $X\Sigma_g^+ \rightarrow {}^1\Sigma_g^+$ | 10.1 |
| | 12 | 11.5 | 12.3 | 12.7 | 12.5 | $X\Sigma_g^+ \rightarrow C^3\pi_u$ | 11.05 " |
| | 13 | 12.3 | - | 14.5 | 15.4 | $X\Sigma_g^+ \rightarrow E^3\Sigma_g^+$ | 11.9 " |
| | | unassigned | 16.0 | 15.6 | 16.2 | | |
| | | | 17.0 | 17.3 | 17.4 | | |
| | | | | 19.0 | | | |
| | | | | 22.0 | | | |
| | | | | 24.0 | 25.0 | | |
| | | | | | 28.3 | | |

average energy losses for each collision process at each collision energy along with proposed assignments, based on the model results in Chapter 6, and electronic excitation energy of these assigned states.

There are two main differences from the potassium - methyl iodide data presented earlier:

a) More excited atomic states are observed - these may be present at low intensities in the potassium - methyl iodide data but obscured by the excitation of molecular electronic states.

b) For the atomic excitations, the accompanying molecular vibrational excitation increases with increasing collision energy for nitrogen but decreases with increasing collision energy for methyl iodide. This will be discussed in detail in Chapter 6.

# CHAPTER 4

# THE MODEL

## 4.1 Aim

A full description of a molecular collision would be provided by close coupled quantum mechanical calculations including all the states of the systems and requiring an accurate knowledge of the potential surfaces and matrix elements. Although advances are being made in the calculation of accurate potential surfaces (e.g. BAL 73, HAB 80), the information is still very scanty especially for electronically excited states and it will still be quite a long while before computing power is great enough to make such full scale calculations feasible, even for simple molecules.

Here it is hoped to develop a simple, classical model, based on the harpoon model, capable of being applied to many collision systems and providing a real physical insight. Such a model should be able to predict the large number of exit channels observed experimentally. In this way it can help the experimenter to gain some intuitive insight into the processes occurring during a collision and aid the interpretation of the experimental data.

It has to be physically plausible and use established knowledge of the system, such as known molecular parameters, so that it remains broadly in agreement with other work.

## 4.2 Background

The Massey criterion is not satisfied under the experimental conditions (NIK 74) so the observed collisional processes fall into the category of the electronically non-adiabatic with a small Massey parameter

$$\xi = \frac{\Delta E}{h\alpha v} \lesssim 1 \qquad (4.1)$$

where $\Delta E$ is the adiabatic splitting of the electronic states at their closest approach

$1/\alpha$ is the characteristic radius of action of the potential

$v$ is the velocity of the projectile.

The transitions from ground to excited state are mainly due to coupling between different electronic states which, at a particular internuclear distance, are degenerate or nearly degenerate. These transitions are highly specific and the Born-Oppenheimer condition for validity that the electronic wavefunctions are slowly varying as a function of the nuclear coordinate is no longer true.

For such transitions the adiabatic potential representation, where the total wavefunction is expanded in a series of electronic wavefunctions which are the eigenfunctions of the electronic Hamiltonian, is not the most natural one to use. The simplest procedure is to choose a set of basis functions which are loosely defined by the requirement that they do not change their character as a function of the nuclear coordinate. According to O'Malley (OMA 71) these wavefunctions define single configuration electronic "diabatic" states which do not diagonalise the electronic Hamiltonian

At a crossing, the diabatic wavefunctions do not change their character - they describe the same electronic configuration to the left and right of the crossing point. The coupling is due to the non-diagonal matrix elements of the electronic Hamiltonian.

Electronically non-adiabatic effects are observed in a large number of fundamental collision processes, including collisional excitation and ionisation (JAN 78), and a number of theoretical approaches to these observed effects have been used.

There are two main types of theoretical approach - the "state based" and "trajectory based" methods. The former, which include close coupling methods (TOP 75) and the Bauer-Fisher-Gilmore (BAU 69) and Franck-Condon (KEN 72) approximations, start from a conventional vibrational state expansion for the total vibrational-translational wavefunction. The latter, surface hopping trajectory methods (TUL 71) rely on the addition or quantum superposition of electronic state-to-state transition probabilities from a spectrum of relevant surface hopping trajectories. There are some good reviews available (e.g. CHI 79, NIK 70, TUL 76).

In fast collisions the surface crossings are localised and many states can be accessed. Under these circumstances the surface hopping trajectory approach is more useful and is the one adopted here.

The experimental results (Chapter 3) show electronically excited states onsetting at very narrow scattering angles. For this to happen there must be an attractive intermediate potential surface linking the ground and excited state potential surfaces. Otherwise the crossing would have to take place high up on the repulsive potential wall, leading to much larger scattering angles. The simplest

attractive intermediate will be ionic in character as in the harpoon model. Fig. 4.1 shows deflection functions corresponding to the above situations.

The harpoon model has been used with both adiabatic and diabatic potential surfaces. Anderson and Herschbach (AND 75) have used the adiabatic formalism to calculate low energy reactive scattering cross sections for various alkali metal halogen molecule systems. The agreement with experiments is excellent but non-reactive scattering data has to be available to obtain the adiabatic potentials.

Aten and Los (ATE 77) have compared the adiabatic and diabatic representations for modelling ion pair formation in $K + Br_2$ collisions. As expected the adiabatic representation was more successful at the lower collision energy (15 eV).

The diabatic formalism has been much more extensively used. The Bauer-Fisher-Gilmore model (BAU 69), mentioned above, and the work of the Amsterdam group (KLE 82) being examples.

The majority of calculations using the harpoon model have involved calculating cross sections for reaction and ion-pair formation in collisions between alkali metals and halogen atoms or halogen containing molecules (GIS 79, LOS 79).

The present work is concerned with cross sections for vibronic excitation and the estimation of the amount of molecular vibrational energy excited in collisions. Where ion pair formation data is available this has also been considered in the model. The reaction channel is excluded as a possible exit by the high collision energy - the fly-by time is too short for the alkali ion formed

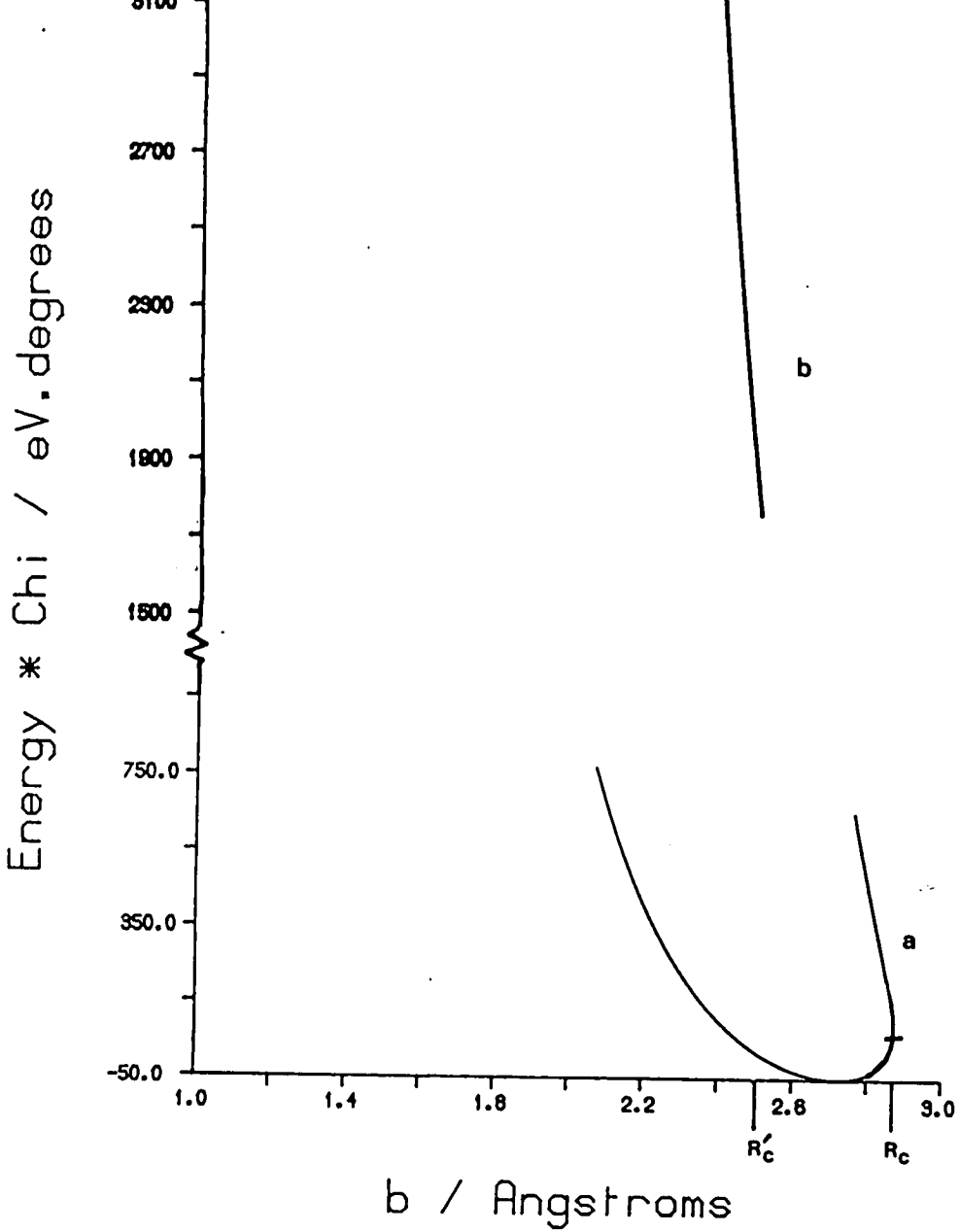


Fig. 4.1: Comparison of Deflection Functions

(a): crossing onto ion-pair curve at $R_c$ (Fig. 4.2) and then onto electronically excited state ($M^*$ + AB) at $R_2$.

(b): crossing onto electronically excited state at $R_c'$

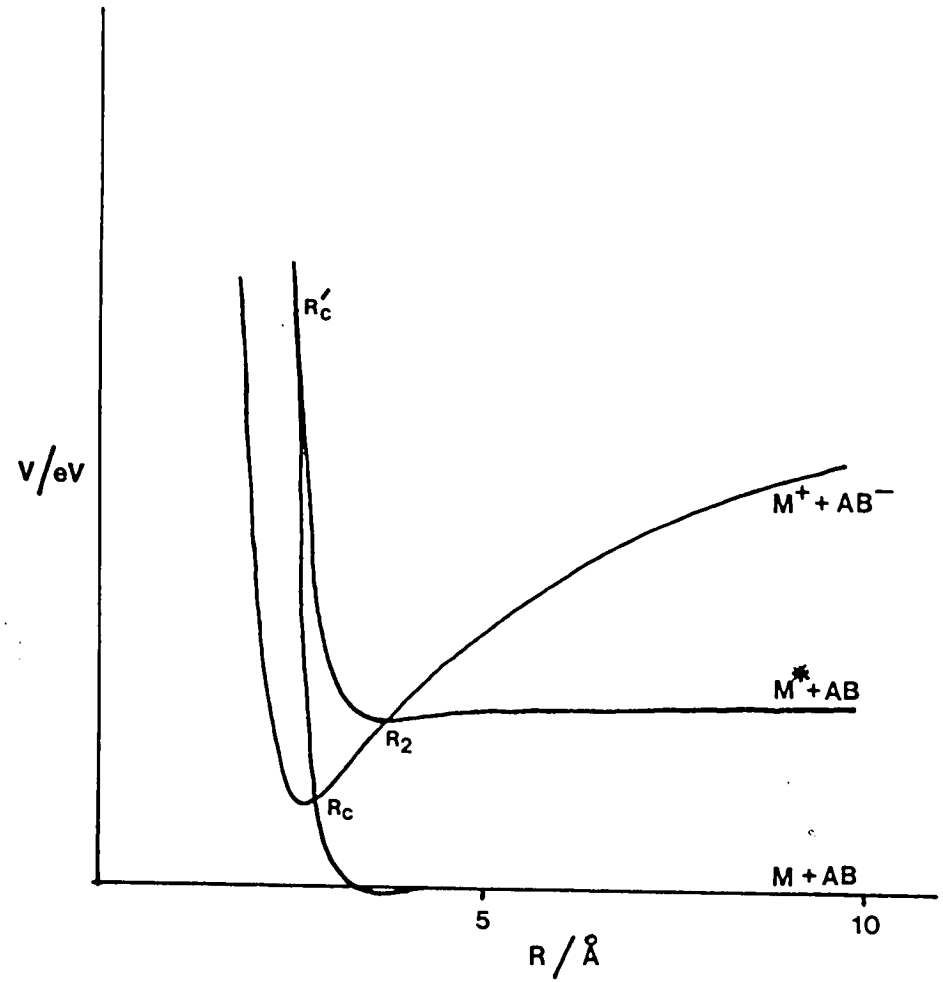


Fig. 4.2: General Potential Scheme for M + AB Collision System

Ground and electronically excited states crossed by ion-pair state.

in the collision to accelerate and capture the negative ion before leaving the ionic surface or escaping from the collision, except in the case of a head on collision.

A general potential scheme is shown in Fig. 4.2 for the ground and first electronically excited covalent surfaces crossed by an ion pair state.

An electron transition is possible both on entering and leaving the interaction region, so that a specified exit channel can be reached via the ionic intermediate in two ways corresponding to either an early or late crossing to the ionic surface.

When the negative molecular ion is formed at the crossing point by a vertical transition, it may be formed in a vibrationally excited state, depending on which kind of orbital the electron has gone into. On crossing back onto a neutral surface the bond length may have changed, thus altering the electron affinity which, in turn, changes the position of the crossing point.

This is shown in Figs. 4.3 and 4.4 for the case of a repulsive molecular negative ion potential. Since, in this case, the molecular ion is formed on the repulsive wall, the molecular bond length will increase with time. The change in the crossing point during the collision depends on the velocity of the incoming metal atom, i.e. on the collision time. For fast collisions there will be little time for the molecular bond to expand, giving rise to only a small amount of vibrational excitation on exit from the collision and a small change in the crossing distance. Slow collisions lead to more vibrational excitation and a greater increase in the crossing distance.

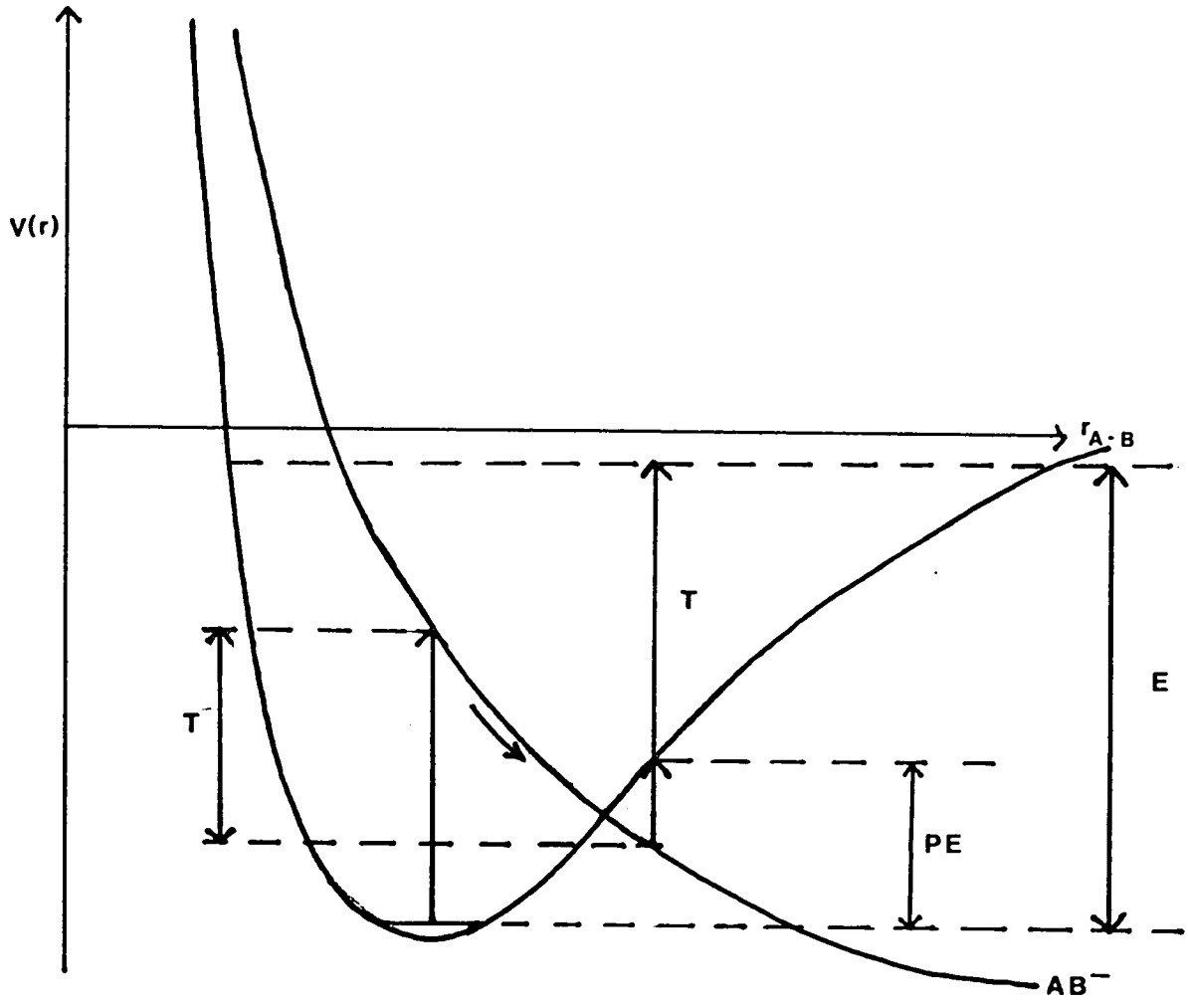


Fig. 4.3: Effect of Bond Stretch

Crossing onto the repulsive molecular ionic surface takes place at $R_c$ (Figs. 4.2 and 4.4). The A - B bond then expands. At the next crossing back onto a neutral surface, the transition takes place conserving position and momentum to yield the neutral molecule AB in a vibrationally excited state. The vibrational excitation, E, is given by PE + T where T is the vibrational kinetic energy of the molecule at the second crossing.

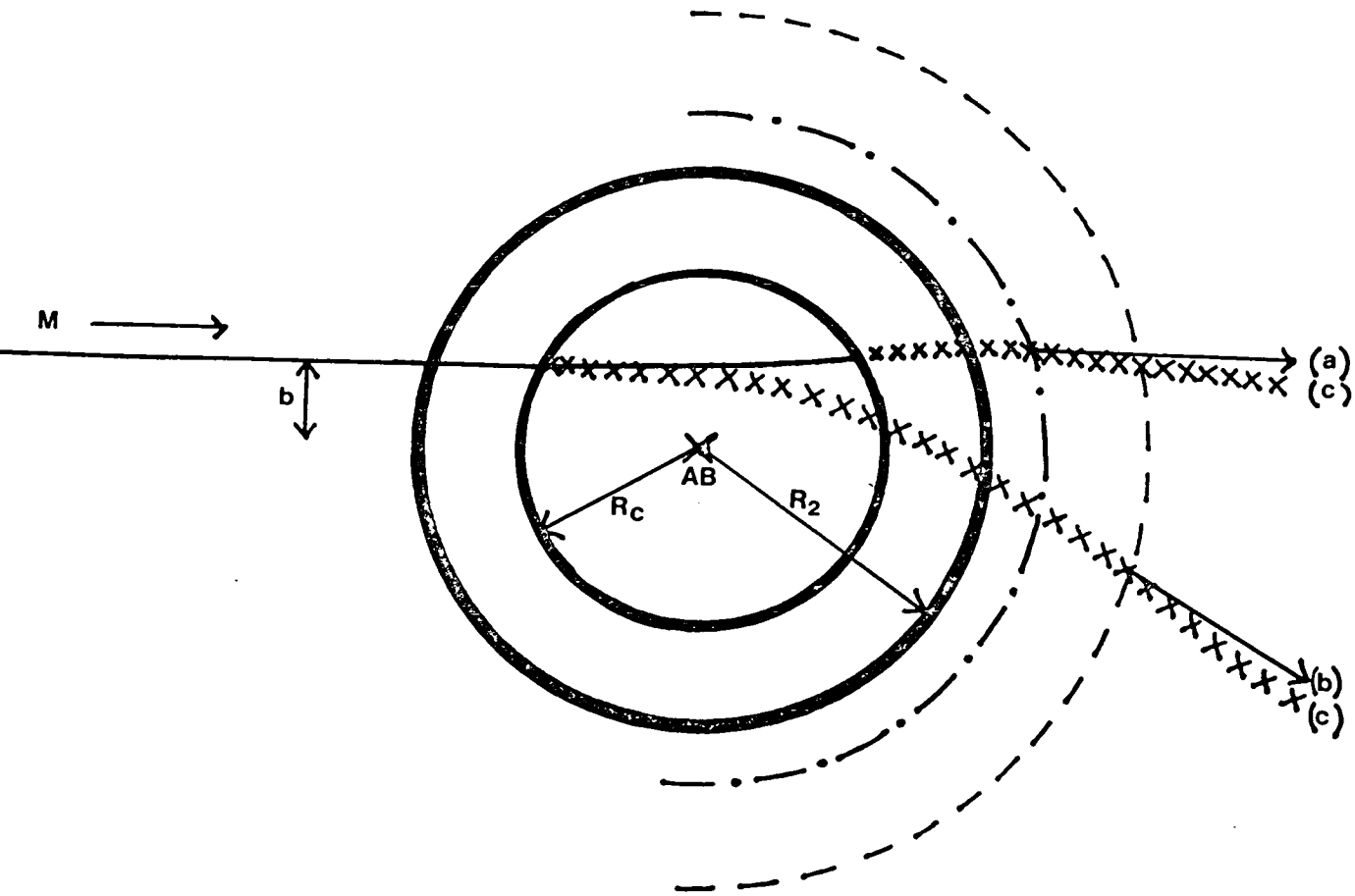


Fig. 4.4: Trajectories involving ion-pair state $M^+ + AB^-$

(a) Crossing onto ion-pair state on way out of collision. Short time on ion-pair state $\Rightarrow$ not much time for A - $B^-$ bond to expand $\Rightarrow$ second crossing only moves out a little bit. Exit as $M^* + AB$.

(b) Crossing onto ion pair state on way into collision $\Rightarrow$ more time for second crossing point to move out. Exit as $M^* + AB$ but with more vib. excitation than case (a).

(c) Exit as $M^+ + AB^-$.

A similar situation exists for the early and late crossing contributions to the scattering, as shown in Fig. 4.4.

In the calculation the motion along the collision coordinate (R) is treated separately from the internal molecular motion (r). The effect of this assumption has been investigated by Aten and Los (ATE 77). They carried out similar calculations for ion pair formation using both adiabatic and diabatic potentials. The calculation with diabatic potentials made the above assumption, whereas the adiabatic calculation contained a coupling term. The introduction of the coupling term slowed down the bond expansion but was significant only for sodium-halogen collisions.

## 4.3 Description of Model

The nuclei are assumed to move classically over any portion of potential surface on the collision path and transition probabilities are calculated at each crossing point encountered en route to find the overall probability of emerging in a given exit channel.

The molecular bond expansion/contraction is determined by calculating the acceleration of the system on the negative molecular ion potential surface.

$$\ddot{r} = -\frac{1}{\mu}\frac{dV(r)}{dr} \qquad (4.2)$$

where $\mu$ is the reduced mass of the molecule.

The experimental measurements are all made in the narrow scattering angle, fast collision regime. The trajectories are therefore approximately linear and of almost constant velocity so that the

dynamical calculation can be considerably simplified. In particular, it is possible to make use of the small angle formula (FLU 73) to calculate the deflection function by summing the contributions of each different section of potential encountered during the collision

$$\chi(b) = \frac{b}{E} \sum_i \int_{Rc_i}^{Rc_{i+1}} \frac{dV}{dR} (R^2 - b^2)^{-\frac{1}{2}} \, dR \qquad (4.3)$$

where i is the number assigned to a particular section of the potential surface

$\chi$ is the angle of deflection

E is the collision energy

b is the impact varameter

and V is the potential.

In the case of inverse power potentials ($V = CR^{-s}$) used throughout the calculations, the contribution of each section can be evaluated analytically using the result:

$$b^s \chi_i(b) = \frac{sC}{E} \int_{\sin^{-1}(b/Rc_i)}^{\sin^{-1}(b/Rc_{i+1})} \sin^s\theta \, d\theta \qquad (4.4)$$

where the substitution $b/R = \sin\theta$ is used.

The classical differential cross section is given by

$$\sigma(\chi) = \frac{b}{\sin\chi \left| d\chi/db \right|} \, . \qquad (4.5)$$

The nonadiabatic transitions are assumed to be localised and vertical and the standard Landau-Zener result (ZEN 32):

$$P_{1,2}(b) = \exp\left(\frac{-2\pi H_{12}^2}{h v_r(b) |s_1 - s_2|_{Rc}}\right) \qquad (4.6)$$

is used for the diabatic transition probability that a system in state 1 will cross into state 2 at the crossing point, Rc, where

$s_1$, $s_2$ are the gradients of the diabatic potentials at the crossing point

$H_{12}$ is the off-diagonal coupling term

and $v_r(b)$ is the radial velocity.

The total deflection along any trajectory, exploring a number of different potential surfaces, is the sum of the individual contributions calculated between successive crossing points using equation (4.4). However, as discussed in section 4.2, the location of the crossing point, $Rc_i$, is a function of the internal target coordinate (bond length) and the $Rc_i$ are revised iteratively as the bond length varies.

The matrix element, $H_{12}$, is parametrised as

$$H_{12}(R'c) = H_{12}(Rc)\exp(0.7(Rc - R'c)) \qquad (4.7)$$

where $R'c$ is the new crossing radius on exit from the ion state. This relation gives an exponential decay with increasing crossing distance as generally suggested (MOU 84).

A flow diagram of the computer program is shown in Fig. 4.5. For computational convenience the program contains only one ionic potential surface, therefore separate calculations must be made for each ion-pair state involved. The calculated intensities for each exit state must therefore be adjusted to take account of this. This is detailed in the following section.

Fig. 4.5 Flow Diagram of Computer Program.

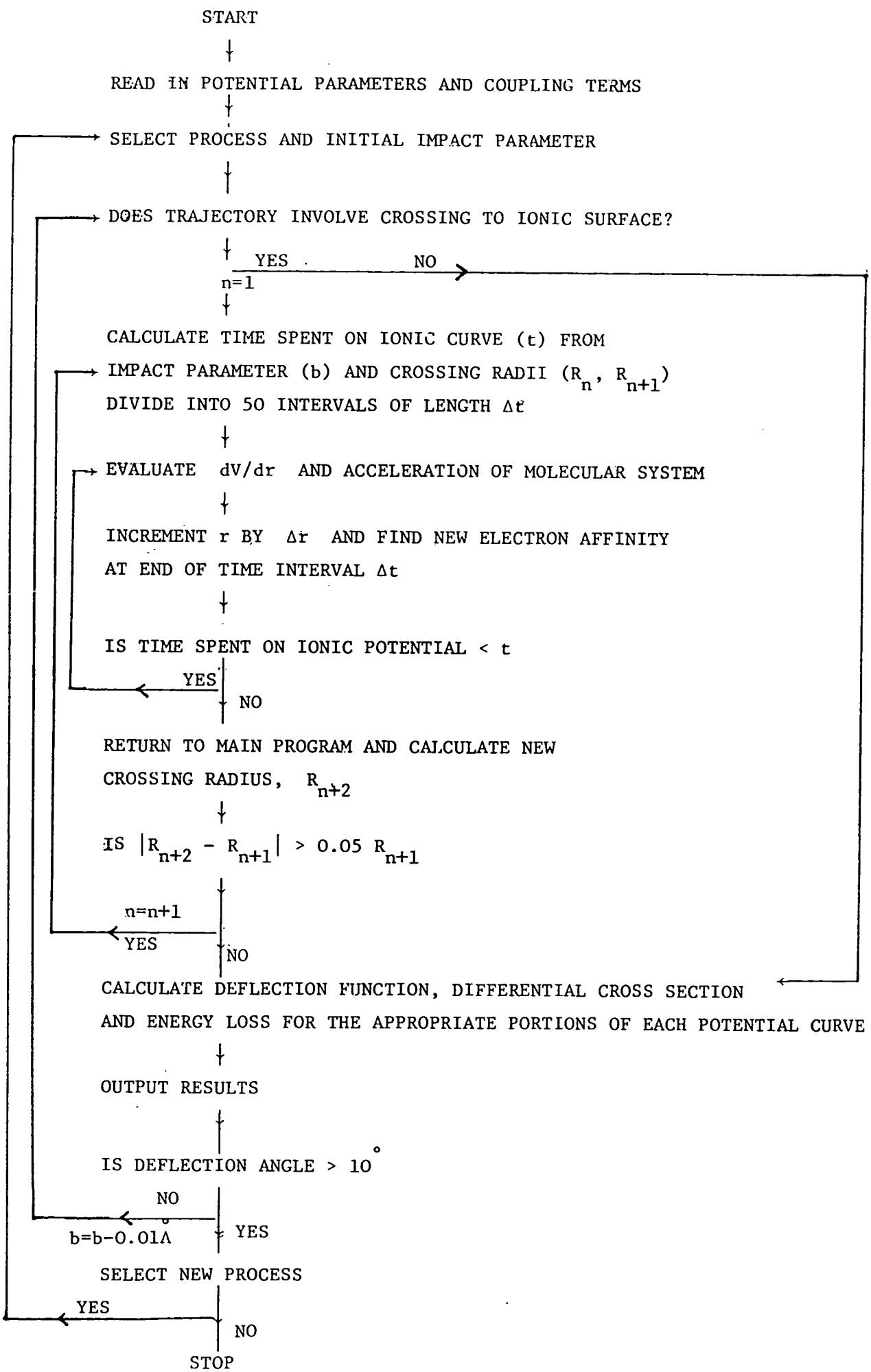

A listing of the model program (for K - $CH_3I$) is given in Appendix A. Sample input and output data are given in Appendices B and C.

The program is very quick to run and results over a range of impact parameters for a given exit channel can generally be obtained in about 30s CPU.

## 4.4 $CH_3I$ Potentials

In the present work the methyl iodide molecule is assumed to be isotropic with the potential parameters appropriate to interaction with the iodine and of the molecule being used - an assumption borne out experimentally (BEU 69).

The K - $CH_3I$ potentials used in the model are shown as a cut through the surface at the molecular equilibrium distance in Fig. 4.6 and Fig. 4.7 shows the intermolecular $CH_3$ - I potentials. The forms of these potentials are given below. The values of all the parameters are given in Tables 4.1 and 4.2.

### 4.4.1 For the M - $CH_3I$, R coordinate (Fig. 4.6)

a) Covalent Potentials

$$V(R) = 4\varepsilon\left(\left(\frac{\sigma}{R}\right)^{12} - \left(\frac{\sigma}{R}\right)^{6}\right) + E_{exc} \qquad (4.8)$$

where $E_{exc}$ is the electronic excitation energy of the atom or molecule.

The potential is based on that used by Evers (EVE 77) for K - $I_2$ collisions.

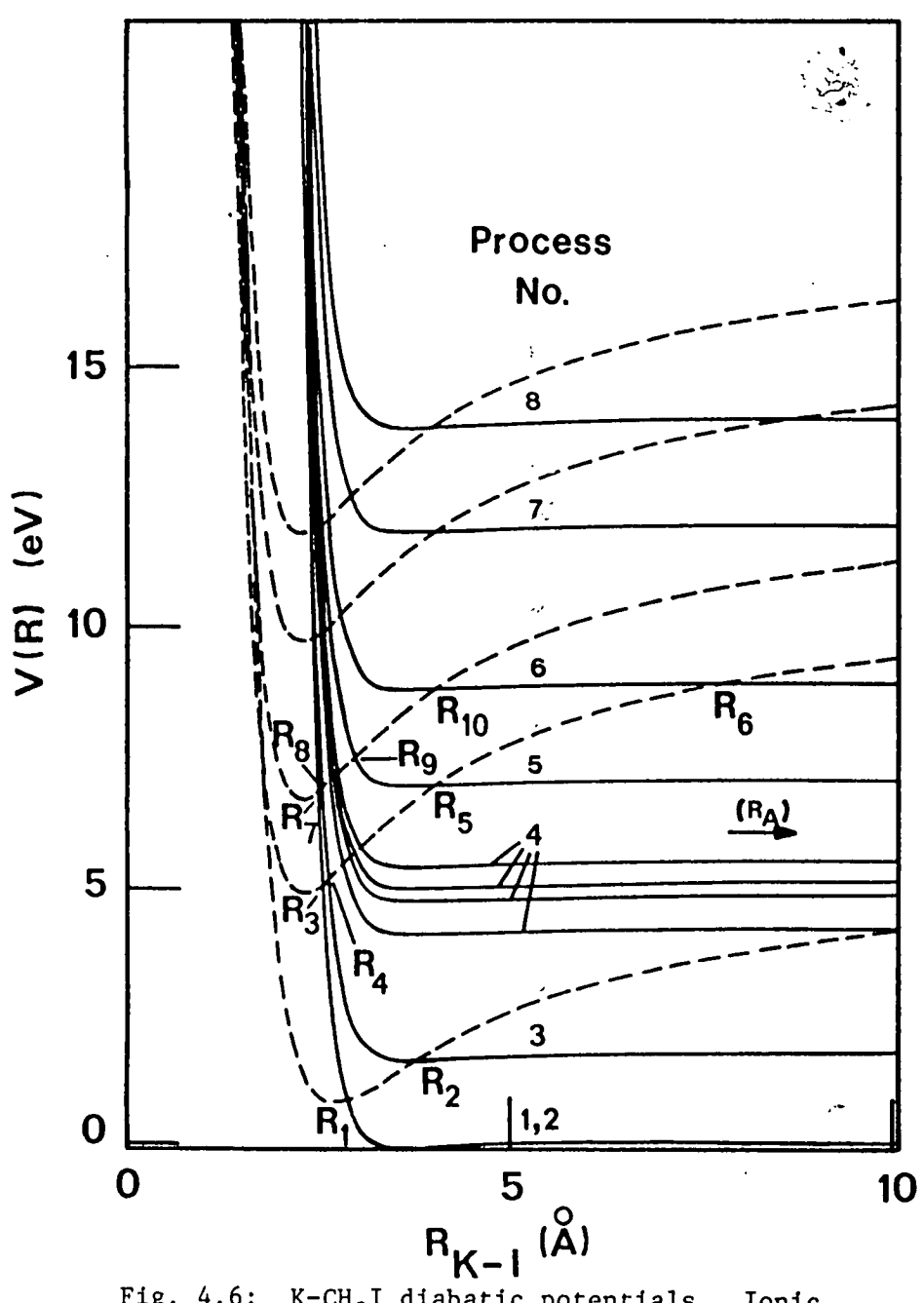


Fig. 4.6: K-$CH_3I$ diabatic potentials. Ionic states are drawn dashed.

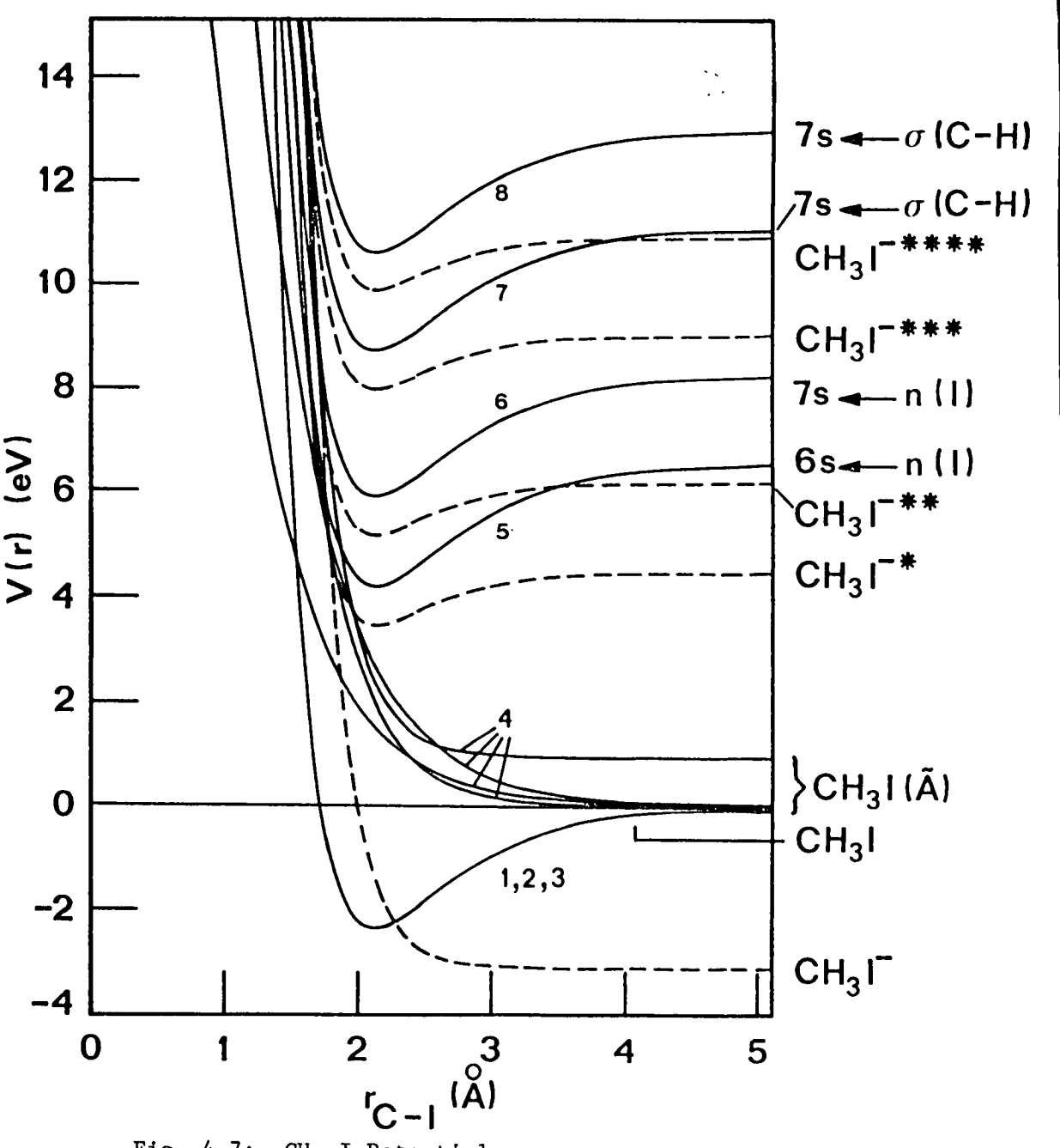


Fig. 4.7: $CH_3$-I Potentials.

b) Ionic Potentials

$$V(R)_{Ground} = A(\frac{Rm}{R})^{s} - 14.4(\frac{\alpha}{R^4} + \frac{1}{R}) + I.P. - EA_{CH_3I} \qquad (4.9)$$

and $$V(R)_{Excited} = A'(\frac{Rm}{R})^{s} - 14.4(\frac{\alpha'}{R^4} + \frac{1}{R}) + I.P. + E'_{exc} \qquad (4.10)$$

where $EA_{CH_3I}$ is the vertical electron affinity of the molecule in the ground state, obtained from Wentworth (WEN 69) and $E'_{exc}$ is the excitation energy at the equilibrium $CH_3I$ distance deduced from energy loss spectra of scattered sodium ions in sodium-methyl iodide collisions reported by Spalburg (SPA 81). The ground ionic potential is based on the one used by Evers (EVE 77).

4.4.2 For the $CH_3$-I, r, coordinate (Fig. 4.7)

a) Covalent Potentials

Their relative position in Fig. 4.7 is appropriate for electron attachment but for the construction of the surface it is convenient to include the molecular excitation in the $M - CH_3I$ interaction.

Covalent with the exception of the $\underline{A}$ states

$$V(r) = D_{cov}(\exp(-2\beta_{cov}(r - r_{eq})) - 2\exp(-\beta_{cov}(r-r_{eq}))) \qquad (4.11)$$

This is the form given by Wentworth (WEN 69) for the ground state of $CH_3$-I.

A States

$$V(r) = A \exp(-B(r - r_{eq})) \qquad (4.12)$$

These are based on the 3 potentials found by Clear et al. (CLE 75) for the A states of HI together with one other potential estimated for the $^3\pi_o$ configuration.

b) Ionic Potentials

$$V(r) = D_{ion} \exp(-2\beta_{ion}(r - r_{eq})) + V^{(3)}(r,R) \qquad (4.13)$$

The repulsive part of the potential $(V(r)_{ground} - V^{(3)}(r,R))$ was found by Wentworth (WEN 69) for the free ion, from electron attachment data.

$V^{(3)}(r,R)$ is a '3-body' potential barrier inserted to constrain the C - I bond expansion. This potential is significant only when the metal ion is close to the molecular ion and is shown in Fig. 5.6

$$V^{(3)}(r,R) = BARR \tanh(4(R_{on} - R))(\tanh(1.8(r-r_{on})) - \tanh(1.8(r - r_{off}))) \qquad (4.14)$$

$$V(r)_{excited} = D'_{ion}(\exp(-2\beta_{ion}(r-r_{eq})) - 2\exp(-\beta_{ion}(r-r_{eq}))) \qquad (4.15)$$

The electronic excitation energy, $E'_{exc}$, is included in the M - $CH_3I$ interaction.

### 4.4.3 Crossing Probabilities

The values of the coupling parameters used in the Landau-Zener expression (equation 4.6) are tabulated in Table 4.3 along with the crossing radii for the molecule at its equilibrium bond length.

TABLE 4.1 M - $CH_3I$ POTENTIAL PARAMETERS

| | K - $CH_3I$ | Cs - $CH_3I$ |
|---|---|---|
| NEUTRAL STATES | | |
| $\varepsilon$/eV | 0.11 (EVE 77) | 0.078† |
| $\sigma$/ Å | 3.2 " | 3.697 |
| I.P./eV | 4.3 (BAC 32) | 3.87 |
| PROCESS No. | $E_{exc}$/eV | |
| 1,2 | 0.0 | 0.0 |
| 3 | 1.6 (BAC 32) | 1.39 |
| 4 | 3.8-5.0 (CLE 75) | Not Modelled |
| 6 | 6.5 (BOS 72) | 6.5 |
| 8 | 8.2 " | 8.2 |
| GROUND IONIC STATE | | |
| A/eV | 0.845† | 1.05† |
| Rm/Å | 3.2 (RIT 51) | 3.697 |
| $\alpha$ /Å$^3$ | 4.0 (BRU 73) | 4.79 |
| s | 5.0 | 4.0 |
| EXCITED IONIC STATES | | |
| A'/eV | 0.75† | 1.05† |
| R'm/Å | 3.2 | 3.697 |
| $\alpha$'/Å$^3$ | 6.25† | 6.60† |
| EA $CH_3I$/eV | 0.94 (WEN 69) | 0.94 |
| s | 5.0 | 4.0 |
| PROCESS No. | $E'_{exc}$/eV | |
| 7 | 5.8 (SPA 81) | 5.8 |
| 9 | 7.5 | 7.5 |

† Values have been adjusted to fit experimental results.

TABLE 4.2 $CH_3$ - I PARAMETERS

| | | |
|---|---|---|
| **NEUTRAL STATES** | | |
| $D_{cov}$/eV | 2.33 | (WEN 69) |
| $\beta_{cov}$/Å$^{-1}$ | 3.4 | " |
| $r_{eq}$/Å | 2.14 | (LAB 73) |
| **A STATES** | | |
| $^1\pi$ A/eV | 2.709† (2.711) | (CLE 75) |
| $^3\pi_1$ A/eV | 1.96 | " |
| $^3\pi_o$ A/eV | 1.5 † | |
| $^3\pi_{o^+}$ A/eV | 1.396 | (CLE 75) |
| $^1\pi$ B/Å$^{-1}$ | 1.9 | " |
| $^3\pi_1$ B/Å$^{-1}$ | 2.85 | " |
| $^3\pi_o$ B/Å$^{-1}$ | 1.9† | |
| $^3\pi_{o^+}$ B/Å$^{-1}$ | 4.1 | (CLE 75) |
| **IONIC STATES** | | |
| $D_{ion}$/eV | 1.65 | (WEN 69) |
| $\beta_{ion}$/Å$^{-1}$ | 2.325 | " |
| $EA_I$/eV | 3.063 | (LAB 73) |
| **$V^{(3)}(r,R)$ term** | | |
| BARR/eV | 1.4 † | |
| $R_{on}$/Å | 10.0 † | |
| $r_{on}$/Å | 2.5 † | |
| $r_{off}$/Å | 3.5 † | |
| **EXCITED IONIC STATE** | | |
| $D'_{ion}$/eV | 1.0† | |
| $\beta_{ion}$/Å-1 | 2.325 | |

†Values have been adjusted to fit experimental results.

TABLE 4.3 COUPLING PARAMETERS

| Crossing Radius as marked on Figs. 4.6 and 4.10 | R1 | R2 | R3 | R4 | R5 | R6 | R7 | R8 | R9 | R10 |
|---|---|---|---|---|---|---|---|---|---|---|
| Crossing Radius at $r_{eq}/\mathring{A}$ | | | | | | | | | | |
| $K/CH_3I$ | 2.868 | 3.80 | 2.564 | 2.637 | 4.060 | 7.748 | 2.509 | 2.561 | 2.981 | 4.060 |
| $Cs/CH_3I$ | 3.195 | 3.76 | 2.857 | 2.917 | 4.257 | 10.00 | 2.801 | 2.846 | 3.229 | 4.256 |
| $K/N_2$ | 2.55 | 3.26 | 4.01 | 4.58 | | | | | | |
| H/ev | | | | | | | | | | |
| $K/CH_3I$ | 0.442 | 0.089 | 0.334 | 0.277 | 0.030 | 0.001 | 0.498 | 0.168 | 0.021 | 0.030 |
| $Cs/CH_3I$ | 0.112 | 0.032 | 0.327 | 0.303 | 0.018 | - | 0.836 | 0.168 | 0.214 | 0.018 |
| $K/N_2$ | 0.75 | 0.45 | 0.32 | 0.25 | | | | | | |

Fig. 4.8 shows these values in comparison with the trend line obtained from other experimentally derived data for one electron transfer processes (MOU 84). They show an exponential decrease with increasing crossing distance but are somewhat smaller. The crossings involving the excited ion-pair states have the larger differences.

The program only contains one ion pair state, one $^1\Sigma$ state and one Rydberg state of the molecule, thus the calculated intensities from the program must be multiplied by the probabilities of crossing the potential surfaces not included in that particular run of the program.

Although there are no neutral inelastic results reported in this thesis for $Cs - CH_3I$ collisions, experimental results have been reported for ion pair formation in these collisions (PRA 83) and the model has been compared with these.

## 4.5 $N_2$ Potentials

The potentials used in the model for the $K - N_2$ interaction are shown as a cut through the surface at the molecular equilibrium distance in Fig. 4.9, with Fig. 4.10 showing the intermolecular $N - N$ interaction. The forms used for the potentials are given below. All parameters are tabulated in Table 4.4. The coupling parameters used in equation (4.6) and the associated crossing radii are included in Table 4.3.

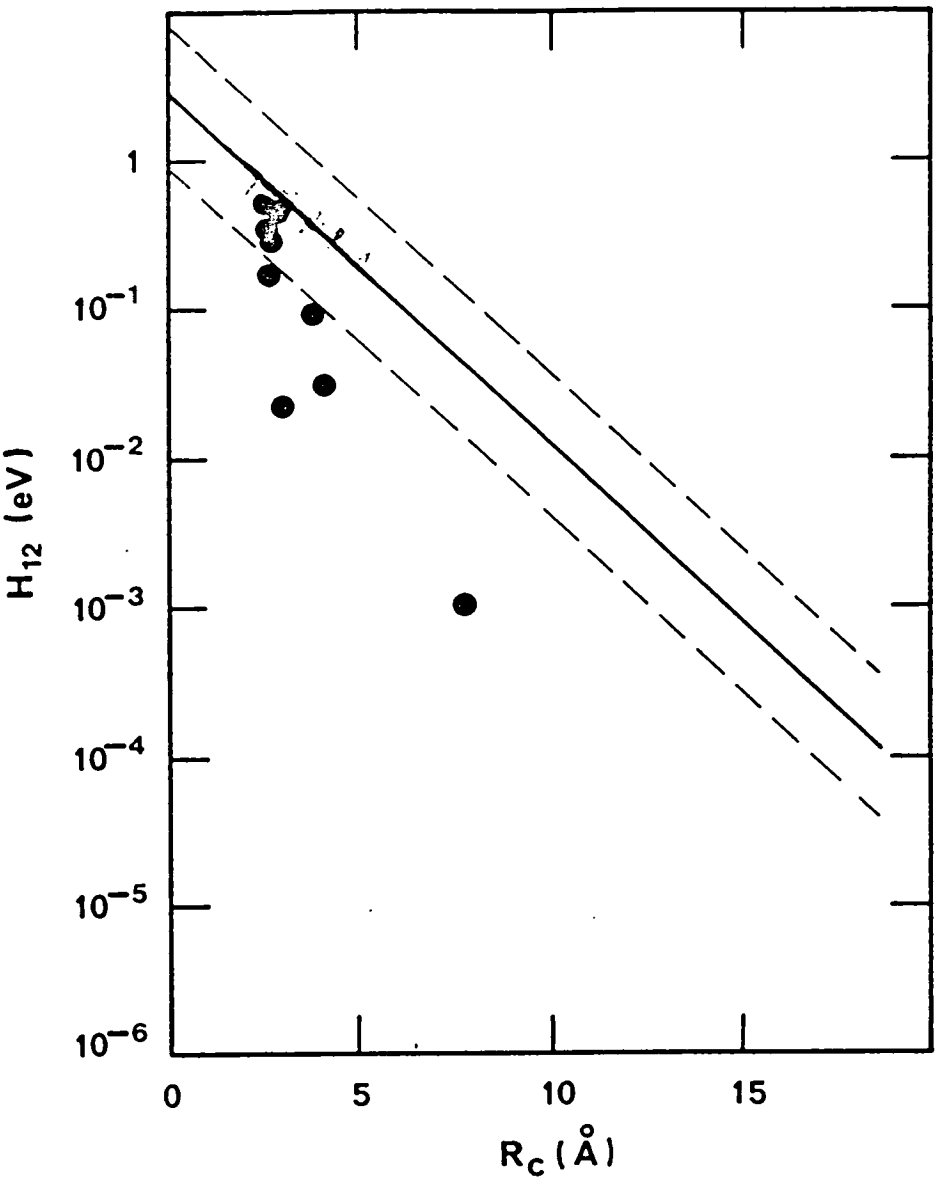


Fig. 4.8: Comparison of K + $CH_3I$ coupling matrix elements with the trend line obtained from other experimentally derived data available for one electron transfer processes (solid line).

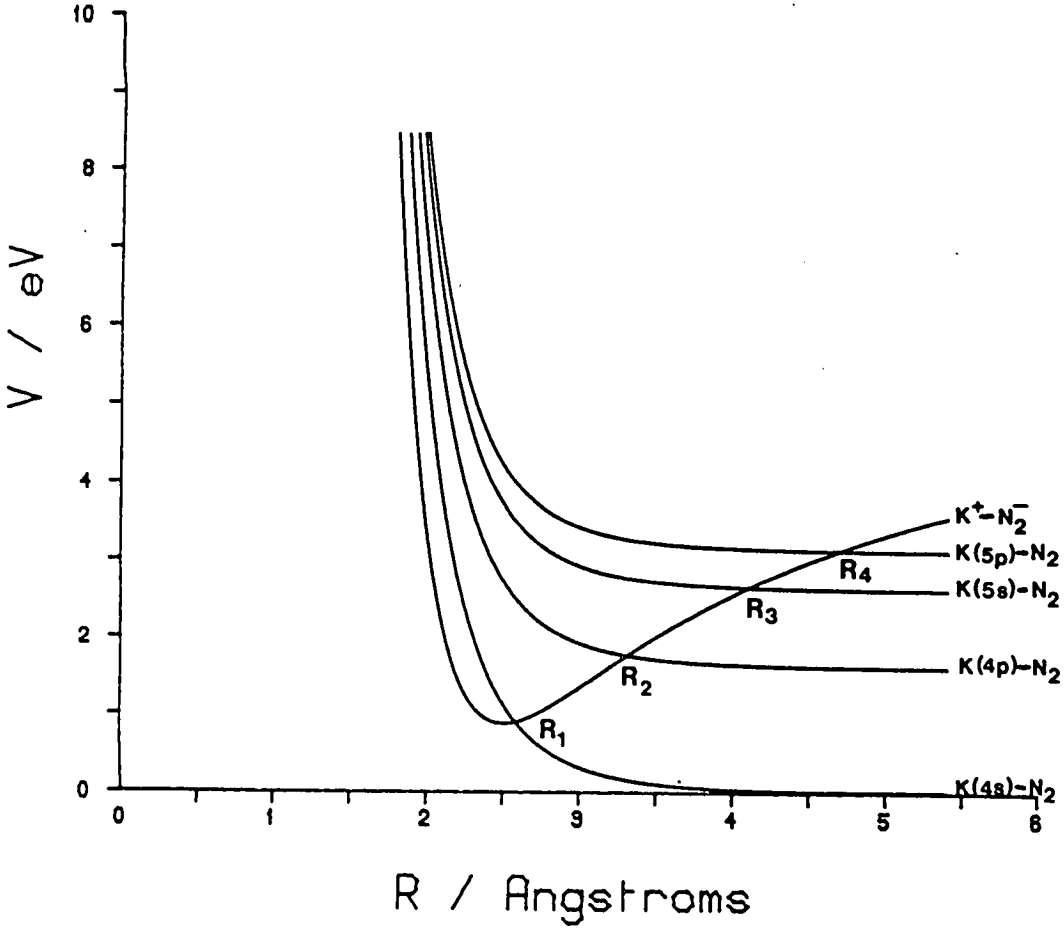


Fig. 4.9: K - $N_2$ diabatic potentials.

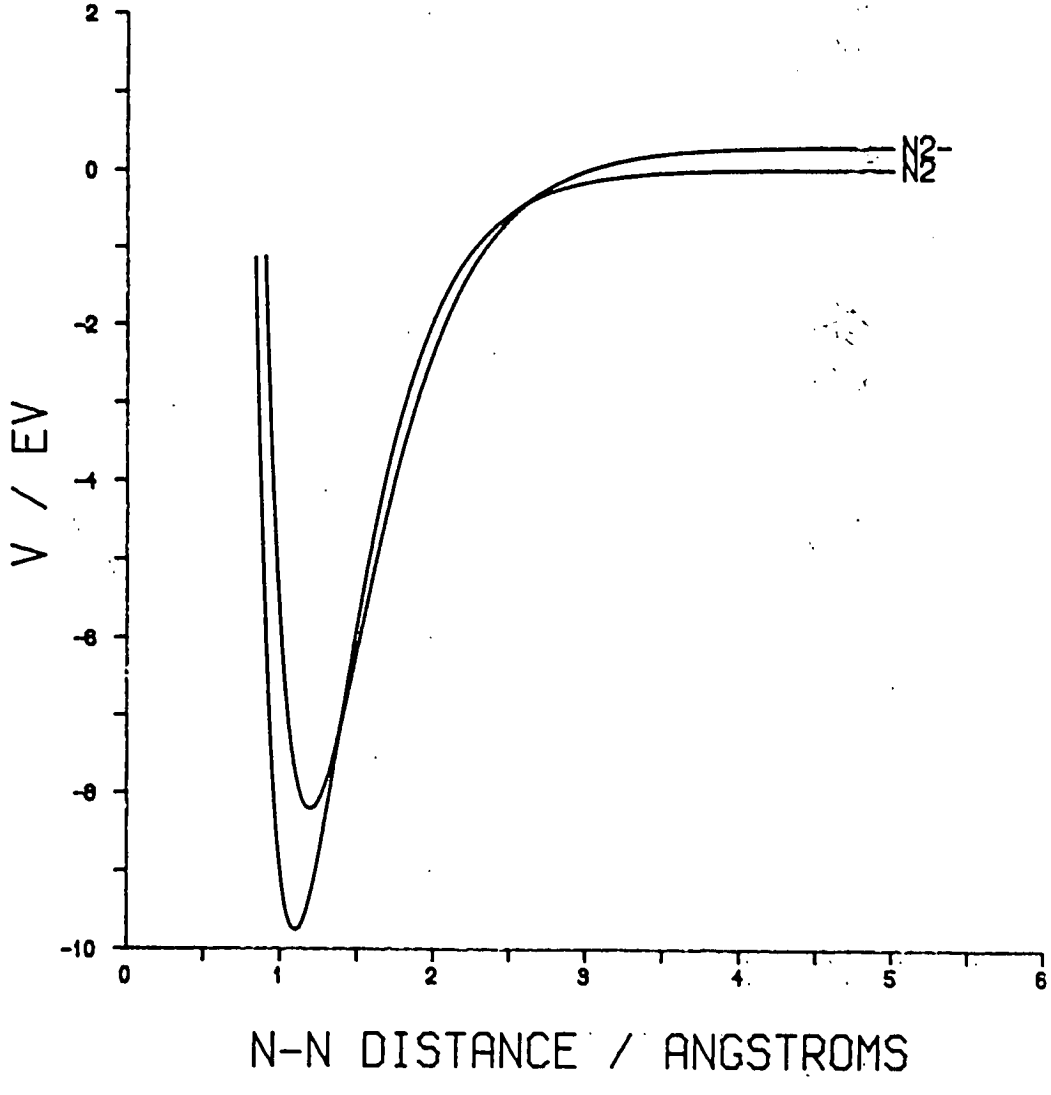


Fig. 4.10: N - N potentials.

4.5.1 For the $K - N_2$, R coordinate

(a) Covalent Potentials

$$V(R) = A\left(\frac{Rm}{R}\right)^{s} + E_{exc} \qquad (4.16)$$

where $E_{exc}$ is the electronic excitation energy of the atom.

b) Ionic Potential

$$V(R) = A'\left(\frac{R'm}{R}\right)^{s} - 14.4\left(\frac{\alpha}{R^4} + \frac{1}{R}\right) + I.P. - EA_{N_2} \qquad (4.17)$$

where I.P. is the ionisation potential of the metal atom and $EA_{N_2}$ is the vertical electron affinity of the ground state molecule.

These potentials are based on ones used by Kempter (KEM 75) and Black (BLA 81) but altered slightly to give a more attractive ionic potential at internuclear distances less than the first crossing point. This is needed to account for the observed differential cross sections. The ionic potential is less steep at $R > R_c$ than that used by Kempter and Black and is closer to the potential used by Ross et al. (ROS 81).

4.5.2 For the N - N, r coordinate

a) Covalent Potential

$$V(r) = D_{cov}(\exp(-2\beta_{cov}(r-r_{eq})) - 2\exp(-\beta_{cov}(r-r_{eq}). \qquad (4.18)$$

TABLE 4.4 $K/N_2$ POTENTIAL PARAMETERS

$K - N_2$

Neutral States

| | | |
|---|---|---|
| $A$/eV | 0.05 | (MAL 77) |
| $R_m$/Å | 3.90 | " |
| $s$ | 7 | " |

| Process No. | $E_{exc}$/eV | |
|---|---|---|
| 1.2 | 0 | |
| 3 | 1.6 | (BAC 32) |
| 4 | 2.6 | " |

Ionic State

| | | |
|---|---|---|
| $A'$/eV | 0.05 | |
| $R'_m$/Å | 4.03 | |
| $s$ | 7 | |
| $\alpha$/Å$^3$ | 2.8 | |

| | | |
|---|---|---|
| IP/eV | 4.34 | (BAC 32) |
| $EA_{N_2}$/eV | 1.9 | (GIL 65). |

$N - N$

Neutral State

| | | |
|---|---|---|
| $D_{cov}$/eV | 9.75 | (GIL 65) |
| $\beta_{cov}$/Å$^{-1}$ | 2.5 | " |
| $r_{eq}$/Å | 1.098 | " |

Ionic State

| | | |
|---|---|---|
| $D_{ion}$/eV | 8.5 | (GIL 65) |
| $\beta_{ion}$/Å-1 | 2.2 | " |
| $r'_{eq}$ /Å | 1.195 | " |

b) Ionic Potential

$$V(r) = D_{ion}(\exp(-2\beta_{ion}(r-r'_{eq})) - 2\exp(-\beta_{ion}(r-r'_{eq}))) \quad (4.19)$$

These potentials were chosen to fit the well established potentials given by Gilmore (GIL 65).

# CHAPTER 5

# DISCUSSION OF K + $CH_3I$ RESULTS

## 5.1 Introduction

The alkali metal - alkyl halide system has been extensively investigated as a paradigm for the electron harpoon mechanism of chemical reaction (HER 79). A large variety of beam techniques have been applied to alkali metal-methyl iodide reactions including product recoil velocity spectra (SHO 76), $CH_3I$ spatial orientation in a refocussing electric field to measure the steric effect (BRO 66, MAR 73) and the measurement of differential cross sections as a function of relative translational energy (SAE 83).

The collective reaction features of $M + CH_3I$ have come to be described as a "rebound" mechanism wherein reaction is favoured for relatively small impact parameter collisions with the iodine end of the $H_3C - I$ bond which scatters the MI product predominantly backwards with a recoil velocity corresponding to a substantial fraction of the total reaction exoergicity. All of these features are consistent with the electron transfer model and the electronic structure of methyl iodide where the lowest unoccupied molecular orbital (LUMO) is a strongly antibonding $\sigma$ orbital localised along the C - I bond. The small negative vertical electron affinity of methyl iodide is consistent with the smaller reactive impact parameters and total reaction cross section relative to the reactions with halogen molecules. The strongly antibonding nature of the LUMO imparts considerable C - I repulsion upon the electron

transfer and accounts for the efficient conversion of reaction exoergicity into recoil energy which is observed.

Collisions at superthermal energies have not been so extensively investigated. Total cross sections for ion pair formation in $M + CH_3I$, $CH_3Br$ collisions are available (MOU 74). The molecular electron affinities were obtained from the thresholds for chemi-ionisation which indicated that negative ions were formed by vertical or near-vertical transitions.

More recently, the angular dependence for ion-pair formation in such collisions has been published (SPA 81, PRA 83). Spalburg (SPA 81) also measured the energy loss spectra of the scattered sodium ions as a function of scattering angle. The results led to the speculation that excited states of the negative molecular ion were involved.

Neutral inelastic differential cross sections for $K + CH_3I$ collisions have been reported by Fluendy et al. (FLU 81) where an ionic doorway state was proposed to account for the collision channels leading to the ground electronic state of the molecule. They also speculated on the existence of excited ion-pair states to explain the low angular onsets of electronically excited states of the molecule.

This chapter aims to show that such speculations are qualitatively correct in the light of the modelling results using the computer model described in Chapter 4. The neutral inelastic scattering data of Fluendy et al. (FLU 81), augmented by the results reported in Chapter 2 for two additional collision energies, and the ion pair formation data of Praxedes et al. (PRA 83) are compared with the model predictions.

The observed processes fall into four main categories: alkali

atom excitation with molecular vibrational excitation; molecular A state excitation; molecular Rydberg excitation and ion pair formation. The model predicts all observed processes except process No. 9 in Table 3.3 which probably involves capture into the $\sigma^*$(C - H) orbital resulting in extension in the C-H coordinate followed by recapture of an electron from the iodine lone pairs. This exclusion necessarily follows from the treatment of - $CH_3$ as a structureless particle.

## 5.2 Vibrational and Alkali Atom Excitation

These processes can extend up to 4.3 eV, the ionisation potential for potassium. However, experimentally only the K($4^2$P) excitation appears to be significant although weaker transitions to the higher alkali states may be concealed by the molecular excitations. The model predicts two exit channels corresponding to electronic excitation of the K($4^2$P) state but with different amounts of vibrational excitation of the molecule corresponding to crossing onto the ground ionic surface on the way into the collision or on leaving it. It also predicts an exit channel corresponding to vibrational excitation of the molecule without electronic excitation (process 2).

At 81 eV CM two sets of energy losses are observed below 1.6 eV (the first electronic excitation energy of potassium) as shown in Fig. 5.1. This features emerges most naturally from the model as a rainbow in the ionic well. The deflection function for exit in the electronic ground states (processes 1 and 2) is shown in Fig. 5.2

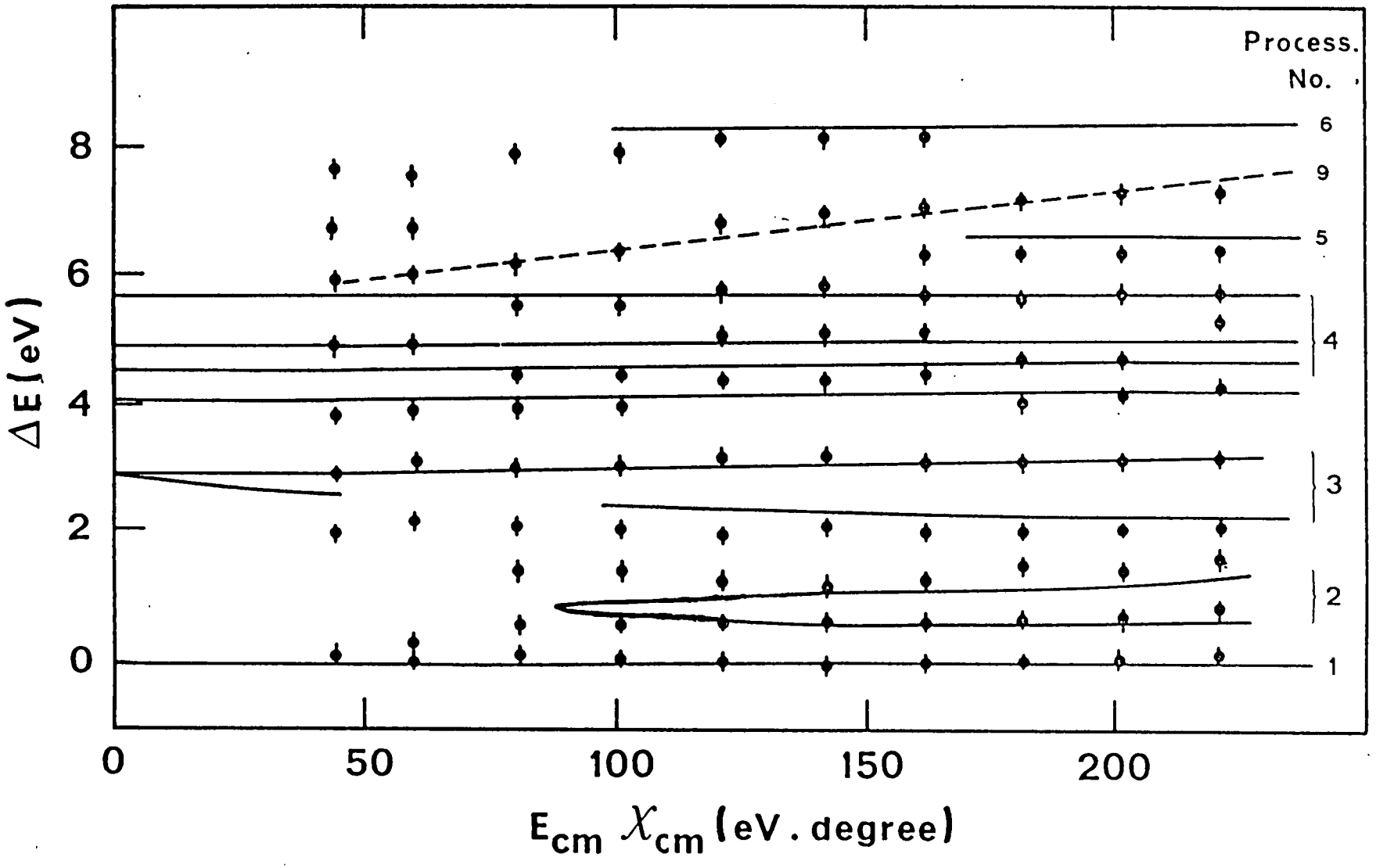


Figure 5.1: Inelastic neutral scattering at 8leV cm. The observed energy losses as a function of scattering angle are compared with the model predictions (solid line). Process 9 (dashed line) is not modelled.

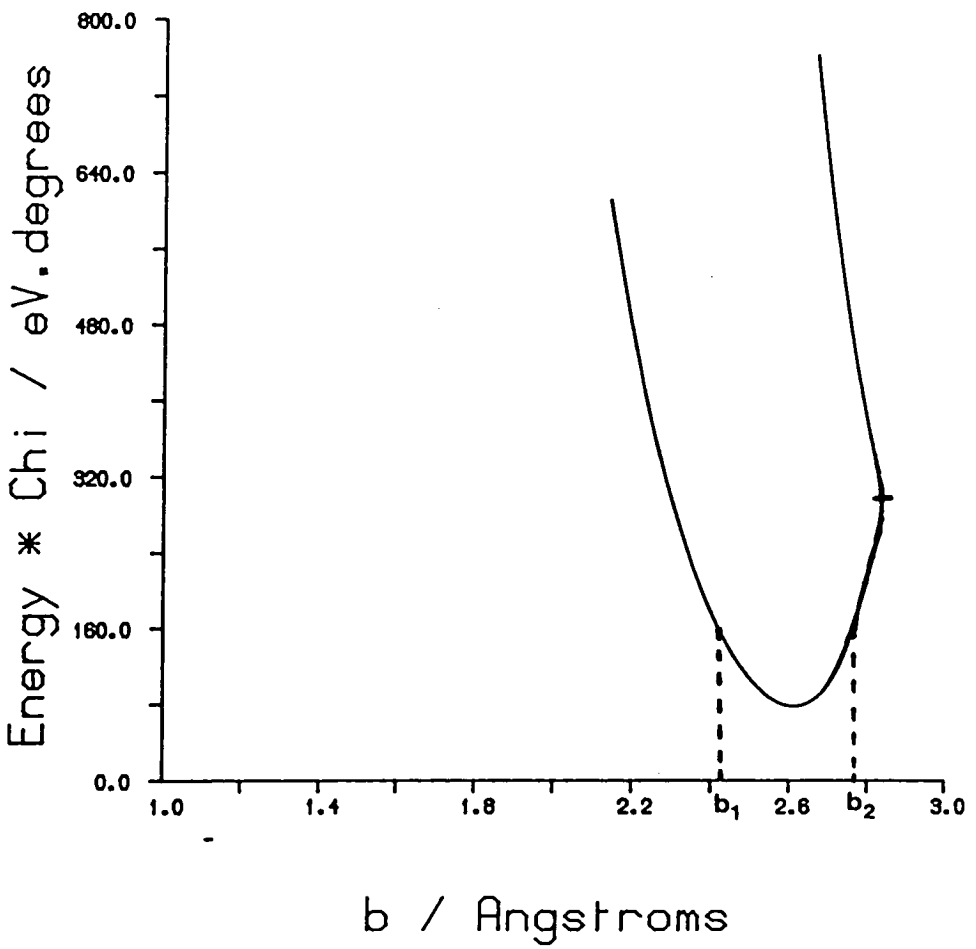


Fig. 5.2: Deflection function for processes 1 and 2.

and clearly shows the rainbowing. The impact parameters corresponding to the same scattering angles (e.g. $b_1$ and $b_2$ in Fig. 5.2) lead to different amounts of time spent on the ionic surface and hence different vibrational energy losses as observed.

This rainbowing also occurs at the other collision energies but is not so obvious in the experimental measurements (e.g. Fig. 5.3). At the higher collision energies, the energy resolution is getting poorer and the vibrational excitation is decreasing, both factors which make the rainbowing difficult to see experimentally.

The model is also successful in predicting the energy losses observed in $K(4^2P)$ formation (Figs. 5.1 and 5.3) The energy losses for most processes are constant over the angular range measured.

Fig. 5.4 shows the observed energy losses averaged over all scattering angles plotted against the inverse of the collision velocity. Here it can be seen that processes 2 and 3, proceeding via the ground ionic surface, show a vibrational excitation that increases with collision lifetime. The solid lines in the figure are the energy losses averaged over scattering angle for each process as calculated by the model. As expected, the vibrational energy loss is monotonic and tends to zero as the collision lifetime tends to zero. This is an effect of the time the C-I bond has to stretch in the ion pair state.

The model energy losses were found to be particularly sensitive to the form of the $CH_3 - I^-$ repulsive potential. It was found necessary to include a 3 body term in the ionic surface ($V^{(3)}(r,R)$ in equation (4.13)) which had the effect of considerably reducing the repulsive strength of the $C-I^-$ interaction when a

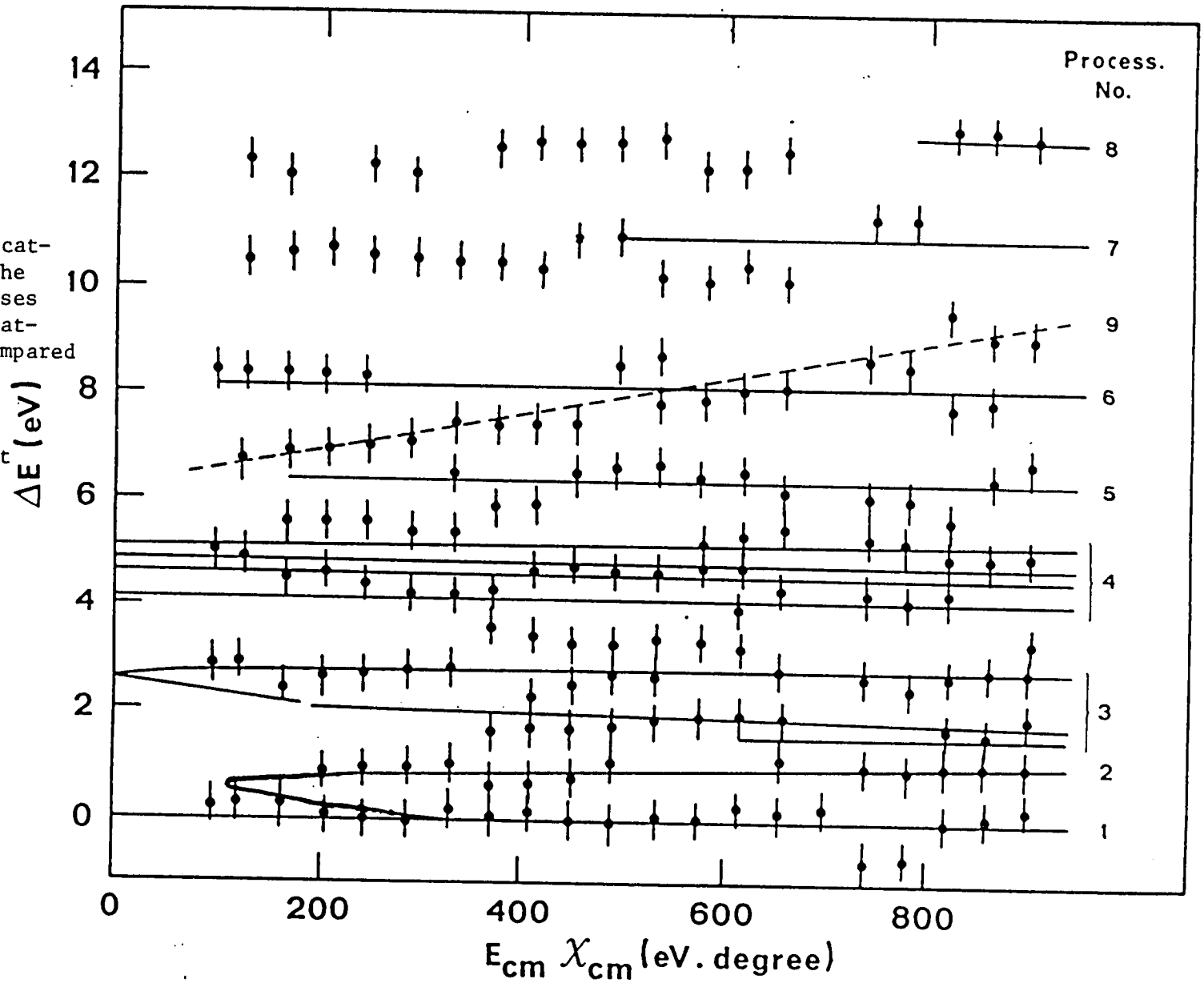


Fig. 5.3: Inelastic neutral scattering at 164eV. The observed energy losses as a function of scattering angle are compared with the model predictions (solid line). Process 9 (dashed line) is not modelled.

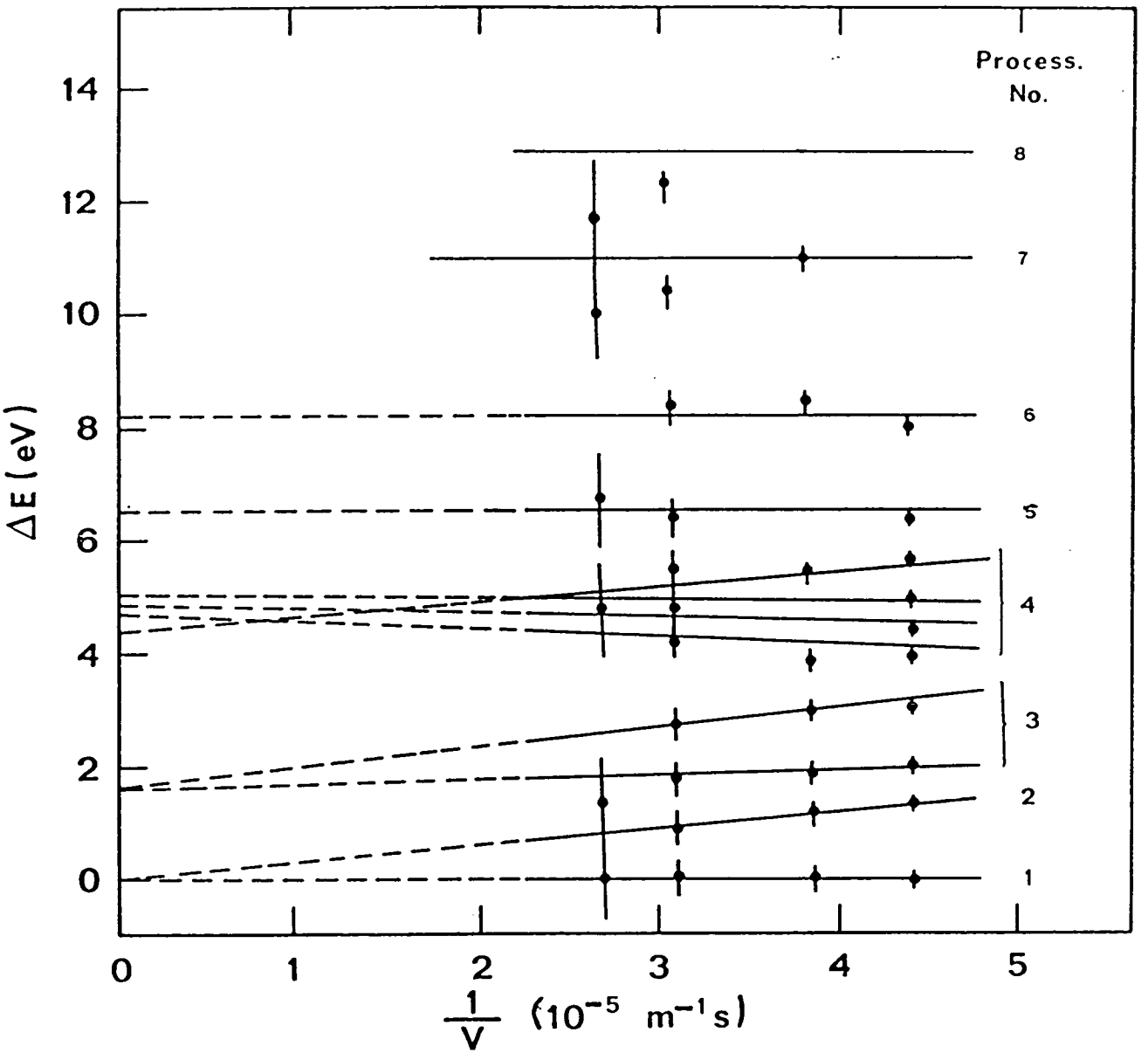


Fig. 5.4: Energy losses averaged over scattering angle as a function of the inverse of the initial collision velocity. The solid lines are the model prediction.

potassium ion was adjacent. This term possibly represents the effect of polarisation in depleting the electron population in the $2\sigma^*$ orbital. In the absence of such a term the model predicted that early electron crossing collisions almost always resulted in dissociation to form $I^-$ ions in contrast to the observed importance of the neutral inelastic channels. Figure 5.5 illustrates this by plotting $CH_3$-I bond length on recrossing to a neutral state against time spent on the ion pair surface for both the free ion potential of Wentworth (WEN 69) and the potential used in the model. The effect of the 3 body term is also shown in Fig. 5.6 where trajectories for the processes involving the ground ion pair state are shown on this potential surface for a collision energy of 81eV CM and an impact parameter of 1.91Å.

Relative differential cross sections for processes 1, 2 and 3 at 164 eV CM collision energy are given in Fig. 5.7. The model predictions are shown by the solid lines. Although these processes are mainly connected to the ground ion state, there is a small contribution to the neutral scattering which samples the higher excited ionic surfaces via an early crossing onto these surfaces on the way into the collision. This is indicated in Fig. 5.7 and is seen to contribute to the structure observed at wide angles in process 1 and narrower angles in process 3.

## 5.3 A State Excitation

The A states of the molecule are repulsive and lead to dissociation of the molecule (RIL 72). Optically these are observed

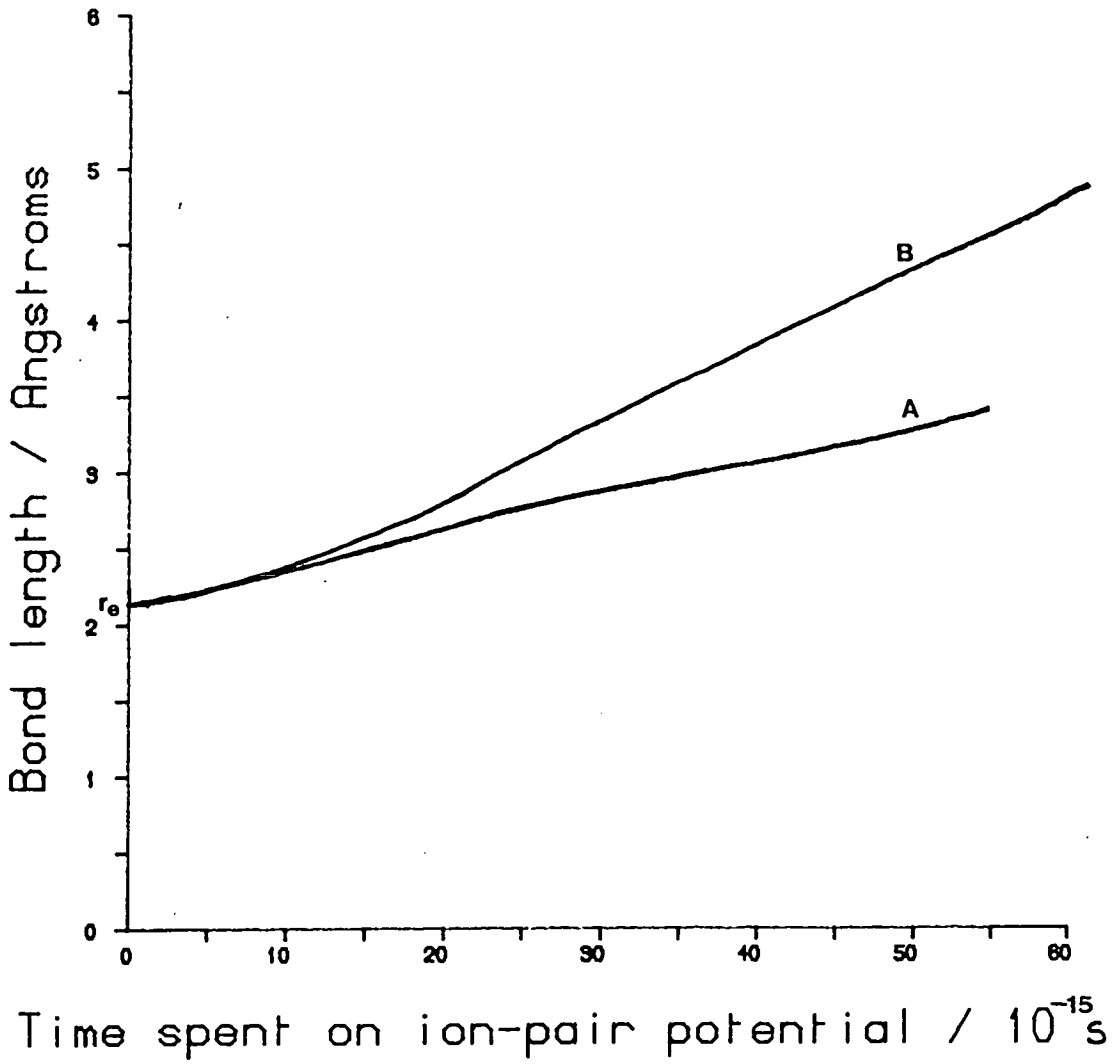


Fig. 5.5: Effect of 3 body potential on expansion of $CH_3$ - I bond

A: with 3 body term
B: free ion potential

The equilibrium bond length of neutral $CH_3I$ is indicated.

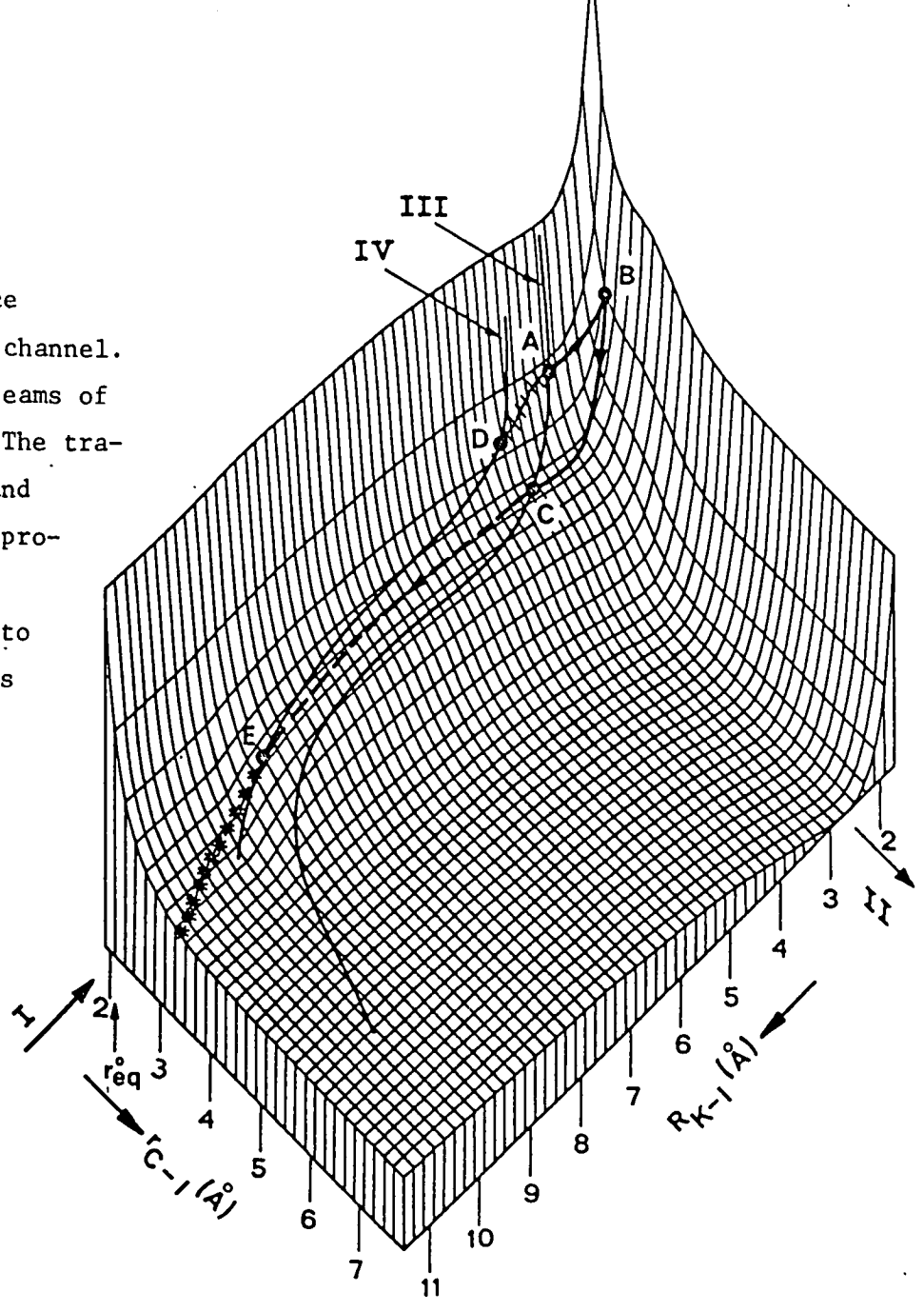


Fig. 5.6: Ground ionic surface showing the effect of the 3 body term in the potential. I; entrance on the ground covalent surface: II reactive channel. The solid lines III and IV are the crossing seams of of $K(4^2S)$ and $K(4^2P)$ to ionic respectively. The trajectories for a collision energy of 81eV cm and impact paremeter 1.91Å are also drawn. The processes 2(⟶⟵), 3, early crossing (— → —) and ion production (***), have an initial jump onto the ionic surface at A. The turning point is B. Process 2 exits at C. Process 3, early crossing exits at E. The ionic trajectory continues on the surface. Process 3, late crossing (xxx) has an initial jump onto the ionic surface at A and exits at D.

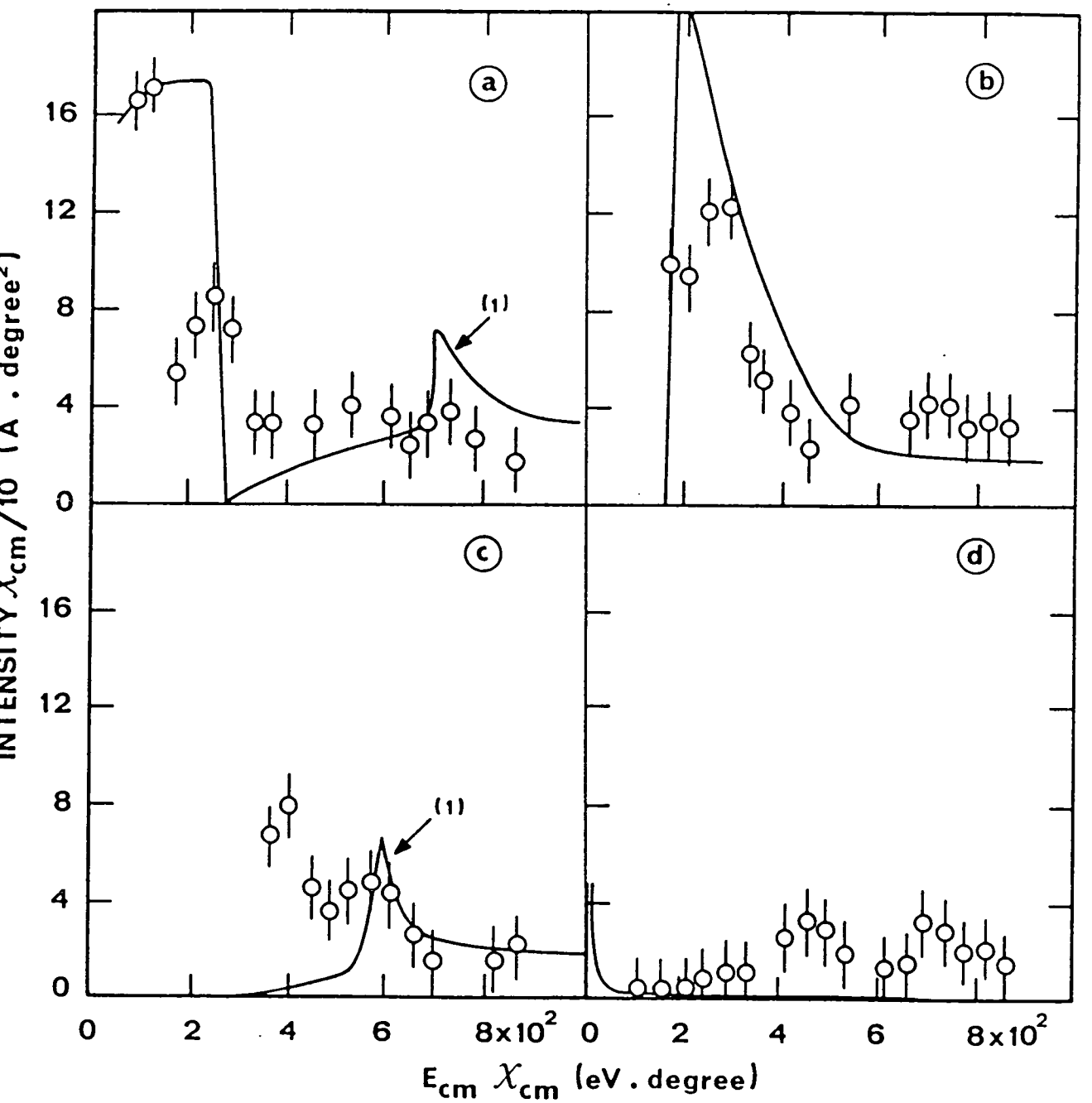


Fig. 5.7: Relative differential cross sections at 164eV cm collision energy. Model prediction is solid line.

(a) Process 1, elastic
(b) Process 2, vib. excitation in $CH_3$-I
(c) Process 3a, late crossing exit as K($4^2$P)
(d) Process 3b, early crossing exit as ($K^2$P)

(1) Contribution from first excited ion state via early crossing at $R_3$ (Fig. 4.6).

to onset in the range 3.5 - 4.5 eV reaching a maximum about 1 eV above onset (HER 66). The continuum observed involves transitions to several states, including those dissociating to $I_{1/2}$ and $I_{3/2}$. Localised collision induced transitions involving rapid electron redistribution would be expected to give discrete energy losses as a result of vertical transitions, in the same way, as described for the excited potassium states. It can be seen from the K - $CH_3I$ potentials in Fig. 4.6 that it is just possible to reach the A states from the ground ionic surface with the molecule in its equilibrium position. The crossing probabilities will, however, be very small since the crossings between the two types of potentials are very far out with the ground ion curve in its equilibrium geometry. In the case of transitions to the bound ground state of $CH_3I$ the electron affinity increases rapidly with C - I stretch. In constrast, the repulsive A states show a decreasing electron affinity depending upon the relative shapes of the ground ionic and A state potential surfaces. In this situation the crossing radius, $R_c$, will decrease during the collision as the C - I bond stretches. This is a natural consequence of the similar electron configurations and potential surfaces in these two states, already remarked by Herschbach (HER 73). Figure 5.8 illustrates the decreasing crossing radius for the four A state potentials used in the model. The mechanism involving crossing from the stretched ground ion pair state offers a plausible route to the population of these states. The model results support this by showing that physically realistic estimates for the potentials account very well for the narrow reduced

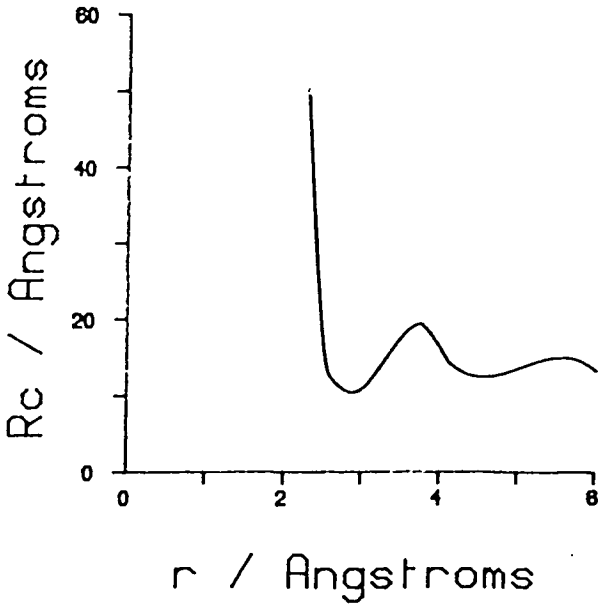


(a) $^1\pi$

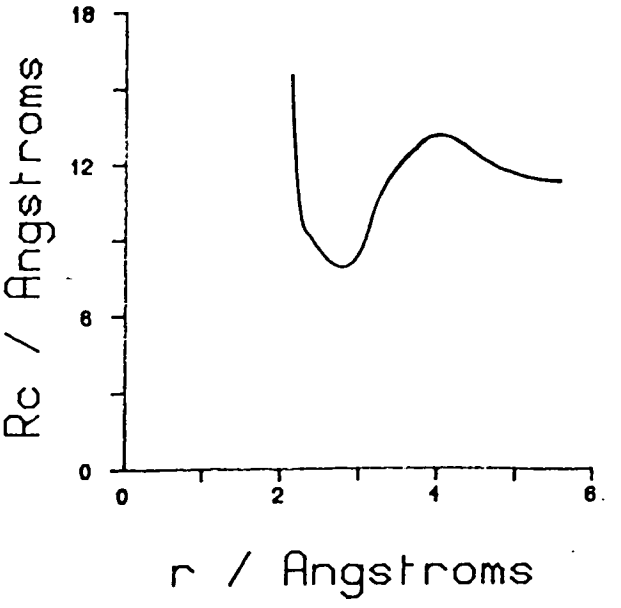


(b) $^3\pi_1$

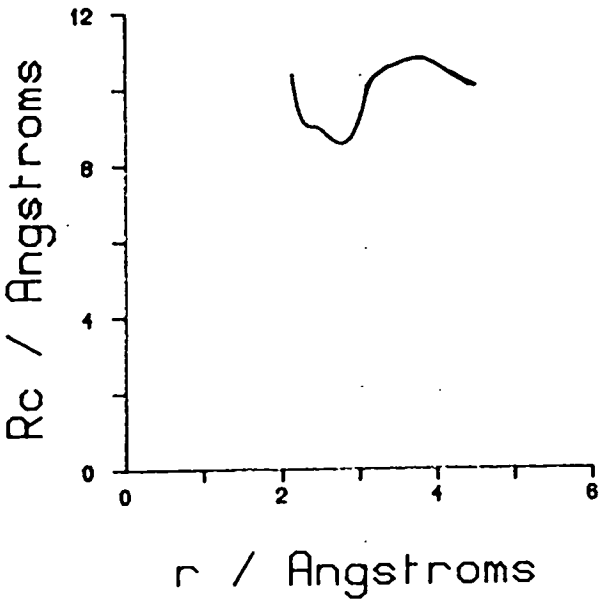


(c) $^3\pi_o$

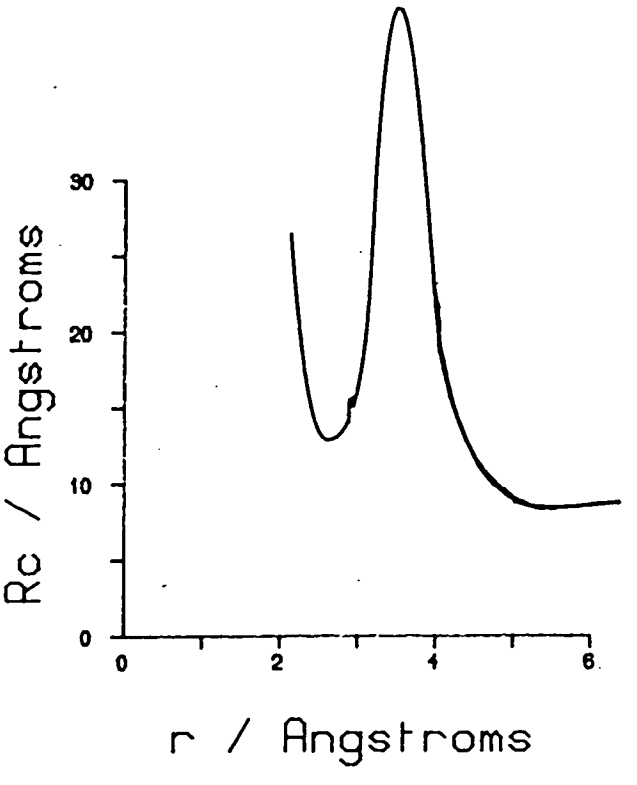


(d) $^3\pi_o^+$ (dissociates to $I_{\frac{1}{2}}$)

Fig. 5.8: Effect of C - I bond length on crossing radius for A states.

scattering angle at which these processes onset as well as accounting for the associated energy losses.

## 5.4 Ion Pair Formation

Differential cross sections for ion production have been measured in Lisbon (PRA 83) and it was reported that at the lowest reduced scattering angles ($\sim$ 60 $eV^{o}$) the time correlation measurements showed the ionic product to be exclusively $I^-$. At larger reduced scattering angles and collision energies however an increasing fraction of $CH_3I^-$ was seen. As the collision energy increased the peak in the cross section was seen to move steadily to wider angles and, in some cases (particularly in Cs + $CH_3I$ collisions), could be seen to be a series of distinct peaks.

The model is of course equally applicable to these channels and predicts a single rainbow for the ground ionic potential as would be expected. The position of this rainbow coincides with the peak seen at the lowest reduced scattering angle in the differential cross sections. The presence of additional peaks suggests that more states must be involved. Introduction of excited ion pair states into the model showed that these additional peaks may also be due to rainbowing. The relative intensity of each rainbow predicted by the model changed rapidly with collision velocity to give, at the experimental resolution, the appearance of a single peak moving in reduced scattering angle as the collision velocity varied. Comparisons of the experimental results with the model predictions are shown in Figs. 5.9 and 5.10

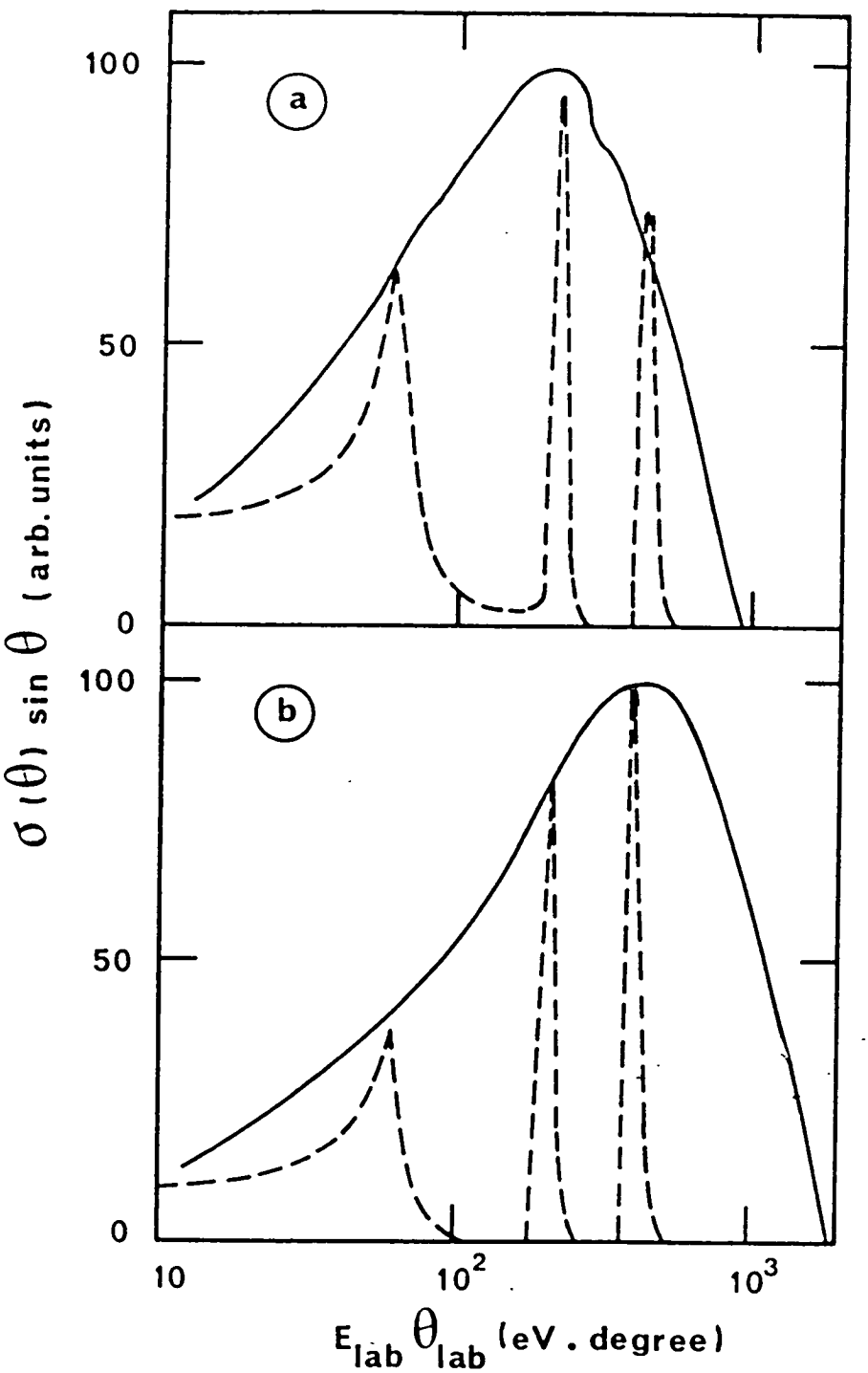


Fig. 5.9: Differential cross sections for ion pair formation, $K + CH_3I$. Experimental solid line, model prediction dashed

(a) 88eV lab. (b) 178eV lab.

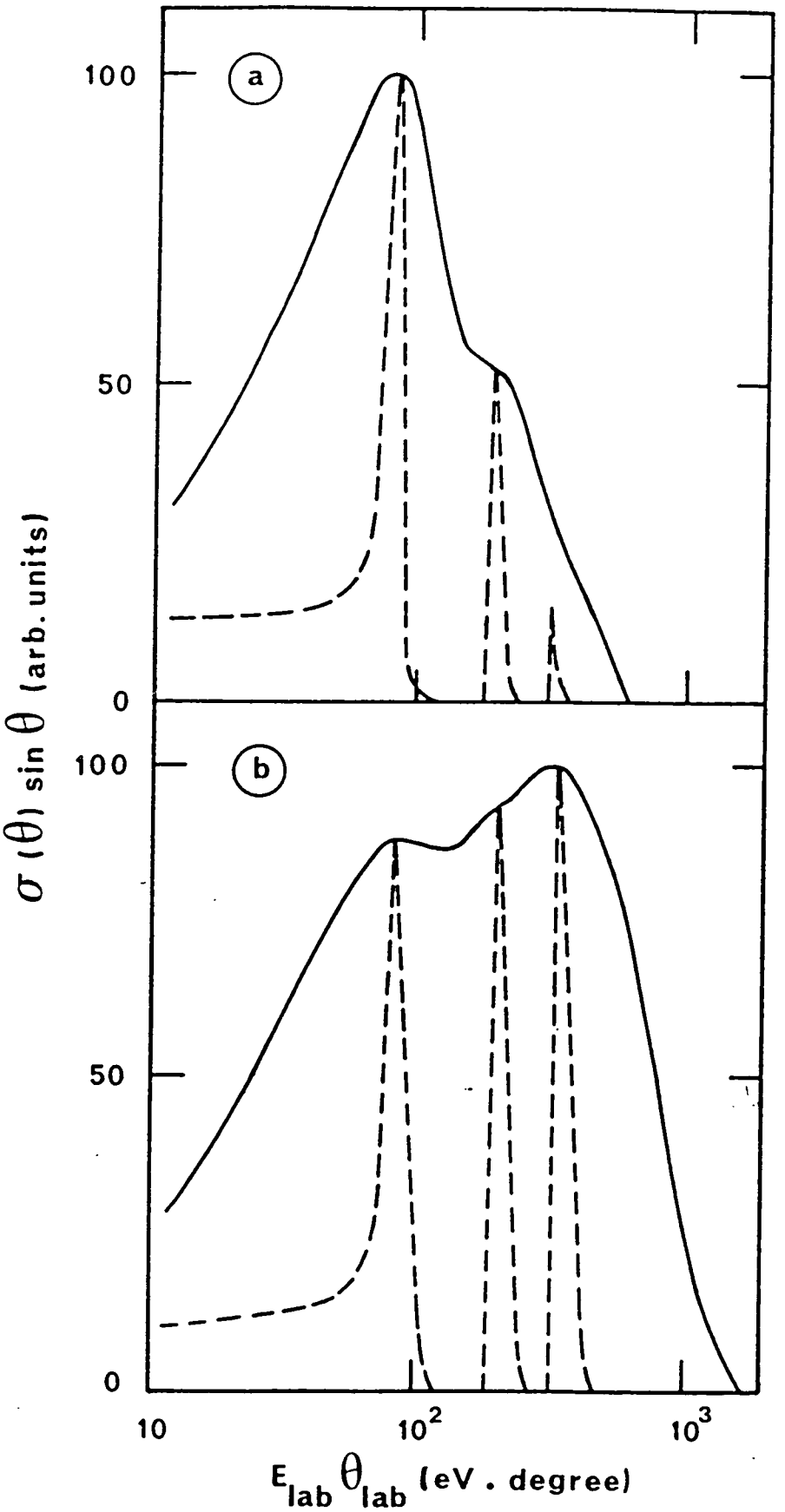


Fig. 5.10: Differential cross sections for ion pair formation, Cs + $CH_3I$. Experimental solid line, model prediction dashed.

(a) 52eV lab. (b) 142eV lab.

for the first three ion pair states used in the model. The experimentally observed peaks seem to be constant in $E\theta$ as the collision energy varies. This implies that they occur at fixed impact parameters and are probably rainbows as the modelling results suggest. There will be infinitely many of these excited ion pair states getting closer together as their energy increases. This implies that the rainbow positions will also get closer together until the individual peaks can no longer be distinguished.

It is possible that the experimentally observed "peaks" could be due to interference effects but if, as we believe, the peaks are occurring at constant $E\theta$ the rainbow explanation is the most likely. We therefore interpret the observed peaks as arising from rainbows in the deflection functions associated with a large number of excited ion pair states. If these excited ion pair states are not dissociative then the model also accounts for the observation of $CH_3I^-$ ions at the wider scattering angles and higher collision energies.

The existence of a number of excited ionic states of $CH_3I$ formed in collision with Na atoms and having excitation energies from about 8eV upwards has already been suggested on the basis of energy loss spectra of $Na^+$ ions (SPA 81). The differential ion production measurements modelled here provide further evidence for these states, the first of the excited levels having an energy of 7.5eV relative to the asymptote of the ground ion.

The lifetime and electron configuration of these excited ion species are unknown but it is likely that a valence or non-bonding electron, probably from the n(I) orbital is promoted, leaving a core vacancy. Since little, or no, vibration excitation is observed

in the lowest molecular Rydberg processes (Figs. 5.3 and 5.4, section 5.5) and $CH_3I^-$ ions are observed, it would seem unlikely that a vacancy in a bonding orbital is created or that the $2\sigma^*$ antibonding orbital is populated. The likelihood is that two active electrons in an excited negative ion (one promoted, one donated by the alkali) are accommodated in molecular Rydberg levels, almost certainly stabilised by the adjacent positive alkali ion which may be within the Rydberg orbitals forming a "quasi-molecule". Such double excited negative ions have been observed in Xe as resonances in the electron scattering (KUY 65). It is known that Xe provides a good model for the excited states of $CH_3I$ (BAI 81, DAG 81).

The three lowest ionic surfaces shown in Figs. 4.6 and 4.7 fit the experimental cross sections very well although no attempt was made to account for the width of the Franck Condon region or the apparatus resolution. The two highest ion pair states shown in Figs. 4.6 and 4.7 were introduced in a more speculative fashion since ion states in this region could provide a gateway to the neutral processes 7 and 8 which probably involve different core vacancies. The experimental ion pair cross-sections do show some evidence for such peaks in the appropriate regions though the resolution is not adequate to permit an unequivocal statement.

Further evidence for the formation of excited negative molecular ions in collisions exists in the form of relative total cross sections for the production of <u>positive</u> molecular ions, presumably formed by autoionisation from the highly excited states formed in the collisions (BRU 84). These cross sections were measured on the same apparatus as the neutral differential cross sections (see section 2.6). The

fragmentation pattern observed corresponded to a minor fraction of $CH_3I^+(X)$, yielding parent ions and the dominant component, $CH_3^+I(A)$ yielding the fragments $CH_3^+$ and $I^+$. The internal energy of the A state was estimated as 12.5 - 13.3 eV and, with less precision, the X state as 10 - 11 eV, both relative to the incident neutral channel. At the collision energies of the neutral experiments both those states occurred with approximately the same intensity.

The excited negative ions formed in the collisions could decay in a number of ways, e.g. by dissociation but are likely to have a high probability of auto-ionisation to yield the molecular positive ion. The observation of such ions under the same experimental conditions, particularly in excited states with appropriate core vacancies (the X state has an iodine non-bonding electron removed, the A state has a vacancy in the C - I bonding orbital) provides strong evidence in favour of the proposed mechanism.

## 5.5 Molecular Rydberg Excitations

The strongest Rydberg transitions observed spectroscopically are to excited s and d orbitals (BOS 72). The lowest s orbital will be 6s and the lowest d orbital 5d (which cannot be distinguished energetically from the 7s orbital in the present experiments). Higher Rydberg states, although available in principle, will have considerably smaller coupling matrix elements due to the larger size of these orbitals and are unlikely to be important. The spin-orbit splitting in these levels is comparable to the energy resolution of the experiments so that an average of the two energy

levels has been used in the calculations. Four excitation processes observed experimentally have been tentatively assigned to Rydberg levels (Table 3.3). All of these processes onset at very low scattering angles (Fig. 5.3), an observation that can be most readily explained by an intermediate in which $dV/dR_{K-I}$ is predominantly positive to scatter the potassium atom in the forward direction. These excited neutral states cannot intersect with the ground ion pair state and the observed excited ion states provide an obvious mechanism. If the electron promoted to a Rydberg level is from a non-bonding n(I) orbital, the C - I force constant and equilibrium distance (HER 66) would be unchanged in both the ion and neutral states. Little or no vibrational excitation would then be expected to occur in conjunction with these transitions. This picture, when incorporated in the model, accounts well for the observations in processes 5 and 6 in Figure 5.3, including the narrow angle onset. It also accounts for the observation of $CH_3I^+(X)$ ions.

It seems possible that the higher neutral excitation processes (7 and 8) almost certainly involving a different core vacancy can be populated in an analogous way by the highest ionic states mentioned in the previous section. It is possible that a vacancy in a $\sigma$(C - H) orbital is responsible, as indicated in Table 3.3. Such states would be expected to show substantial vibrational excitation with a strong dependence on collision lifetime (because of the small reduced mass of the C - H oscillator). There may be some evidence for this in Figure 5.4. A vacancy in the C - I bonding orbital is another candidate and would explain the formation of the $CH_3I^+(\underline{A})$ ions. Unfortunately the different $CH_n^+$ fragments could not be distinguished

in the experiments to detect positive molecular ions. This information would help to assign processes 7 and 8.

## 5.6 Correlation Diagram

A diabatic correlation diagram, drawn according to the Barat rules (BAR 72) for the Xe/K system is shown in Fig. 5.11. As already mentioned, Xe is a good model for the excited states of $CH_3I$. The approximate molecular orbitals for $CH_3I$ and their correlation to the Xe atom for the linear configuration are also shown. The high atomic numbers involved in these systems make the diagram complex but a number of relevant features can be seen. The 4sK(5pσ) orbital has an early crossing with the 7hσ orbital (which correlates to the $2\sigma^*$ $CH_3I$ orbital). Electron transfer to form the ground ion pair state can then be expected in accord with experiment. The 7hσ orbital is strongly promoted so that crossings with a range of excited orbitals can occur. Thus the 5dπ and 6pσ orbitals, correlating to the excited 4p and 5s levels of the atom, are accessible by this route. The 5pσ orbital, either vacant or half full, plunges in energy and is available to create inner vacancies by capture from the core. The production of the excited ions and Rydberg neutral species could be rationalised by the following sequence. An initial electron transfer from K to the 6s Rydberg level of $CH_3I^-$, 4sK → 6sσ, is followed by the production of a core vacancy, 5pπ → 5pσ, 5pσ → 6sσ, to yield $CH_3I^{-*}(5p^56s^2)$. Electron recapture by the $K^+$ ion, 6sσ → 4sK, then yields the neutral Rydberg levels of $CH_3I$.

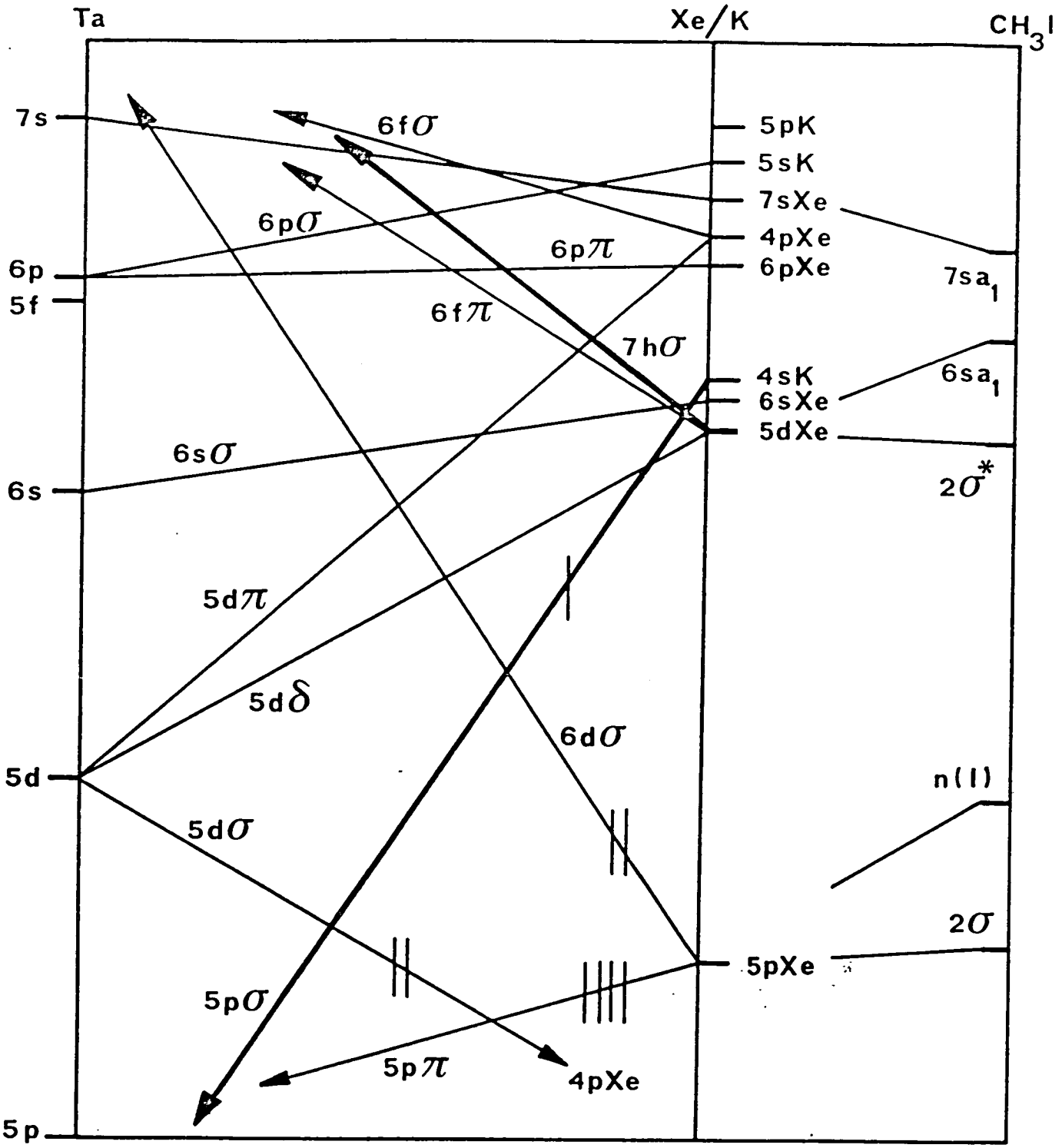


Fig. 5.11: Diabatic correlation diagram for K + Xe. The significant $CH_3I$ orbitals are also shown.

## 5.7 Conclusion

A simple dynamical model involving ground and excited ion pair states to access electronically excited neutral states, and having a minimum of adjustable parameters, has proved to be very successful in predicting experimental data for ion pair production and neutral inelastic scattering over a wide energy and angular range. Comparison of experimental and theoretical results has yielded a greater insight into the electronic rearrangements involved in the collision.

In particular, the importance of an ion pair intermediate as the doorway to atomic excitation, vibrational excitation of $CH_3I$ in its ground electronic state, $CH_3I(\underline{A})$ and $I^-$, $K^+$ ions is confirmed. It has been shown that this intermediate is less repulsive in the C - I coordinate than the free molecular ion - structural information not easily accessible by other methods.

The formation of excited ion pair states is also observed in these collisions. It is suggested that these states are analogous to resonances observed in electron scattering from Xe and involve similar core vacancies. Such states have been shown to provide a plausible mechanism for the production of the highly excited neutral states of methyl iodide which are also produced in the collisions. Experiments in which coincidences are detected between scattered potassium atoms and the positive molecular ions formed from the auto-ionisation of the excited molecules would help in the assignment of the highly excited neutral states observed.

Overall the agreement between model and experimental results is surprisingly good considering the simplicity of the model.

# CHAPTER 6

# DISCUSSION OF K + $N_2$ RESULTS

## 6.1 Introduction

The alkali atom/nitrogen molecule collision system has been of interest for many years (e.g. BRE 82, HER 82). A considerable volume of experimental data is available and there have been several theoretical treatments of the collision dynamics (BAU 69, BOT 77, ARC 83, GIS 81).

The system is of special interest as a relatively simple example of an electronically non-adiabatic molecular collision for which accurate ab initio potential surface data is at least partially available (HAB 80). This system provides an excellent case for the development of a detailed dynamical model for the collision process.

The experimental data available falls into four broad categories:

(a) Excitation processes in which energetic alkali atoms produce vibrational or electronic excitation of the molecule or are themselves electronically excited in the collision.

(b) The quenching process in which an electronically excited atom is quenched to the ground state with concurrent vibrational and translation excitation of the $N_2$.

(c) Intermultiplet quenching of an excited atom, e.g. between the $^2P_{1/2}$ and $^2P_{3/2}$ states during the collision, and

(d) Vibrationally excited $N_2$ being quenched by the atom with concurrent electronic excitation of the atom.

Experiments capable of revealing considerable detail are now possible in all four cases. Excitation measurements, involving the coincidence detection of the alkali atom and the resonant photon emitted from this atom after the collisions, have been made (MAR 79). In favourable cases, measurements of the polarisation of the emitted photon enable the phase as well as the amplitude of the magnetic substates of the excited atom to be determined - information bearing directly on the evolution of the excited atomic orbital, especially during the exit phase of the collision (HAL 84)

Closely related information can be obtained from quenching experiments using oriented or aligned excited alkali atoms (REI 82). With this technique the initial collision orientation can be specified. A direct image can be obtained of the atomic charge cloud and the angluar momentum transferred during the collision.

Additional information is available from studies of the inter-multiplet quenching (MES 82).

A great deal of theoretical effort has gone into understanding the collision dynamics. Martin et al. (MAR 79) carried out classical trajectory calculations to model the differential cross sections for $K(4^2P)$ excitation. They used diabatic potentials and assumed the presence of an ionic intermediate. The quenching process has been modelled on a number of occasions. The first semiquantitative attempts to understand the quenching were made by Bjerre and Nikitin (BJE 67), who recognised that a curve crossing mechanism had to be responsible for the large cross sections. They adopted the harpoon model and treated the remaining dynamical problem in a classical trajectory calculation. The Bauer-Fisher-Gilmore model was the next

step (BAU 69) where each vibrational state of the ionic intermediate as well as the electronic ground state had a separate potential curve. This has been expanded and modified a number of times since then (e.g. BAR 76). Bottcher and Sukumar (BOT 77) treated the problem essentially as scattering of the alkali electron at the quenching molecule, making use of electron scattering data (SCH 73) where low lying $e^-$ + molecule resonances are found. These models all gave reasonably good agreement with experiment for the order of magnitude of the quenching cross sections. The shape, location and width of the final vibrational state populations of the nitrogen molecule were strongly dependent on the form of the potential curves used in the calculations. Very good agreement was obtained by Gislason et al. (GIS 81), where the vibrational motion of the system was treated using a harmonic oscillator wave-packet.

The problem with all of the above calculations was lack of accurate knowledge of the potential surfaces allowing the limited experimental data to be fitted by changes in the potentials and reliance on an ion pair intermediate when there was some doubt as to its validity. There is no well-defined negative nitrogen ion. It is known to exist only as a resonance in electron scattering experiments (SCH 73). Furthermore this state is known to autoionise if the bond length is less than the equilibrium bond length of the ground state neutral molecule (BIR 71).

Habitz has since published accurate <u>ab initio</u> potential surfaces for the $Na + N_2$ system (ground and first electronically excited state) (HAB 80). The potentials are shown in Fig. 6.1 for the most favourable symmetry for quenching, $C_{2v}$, (broadside

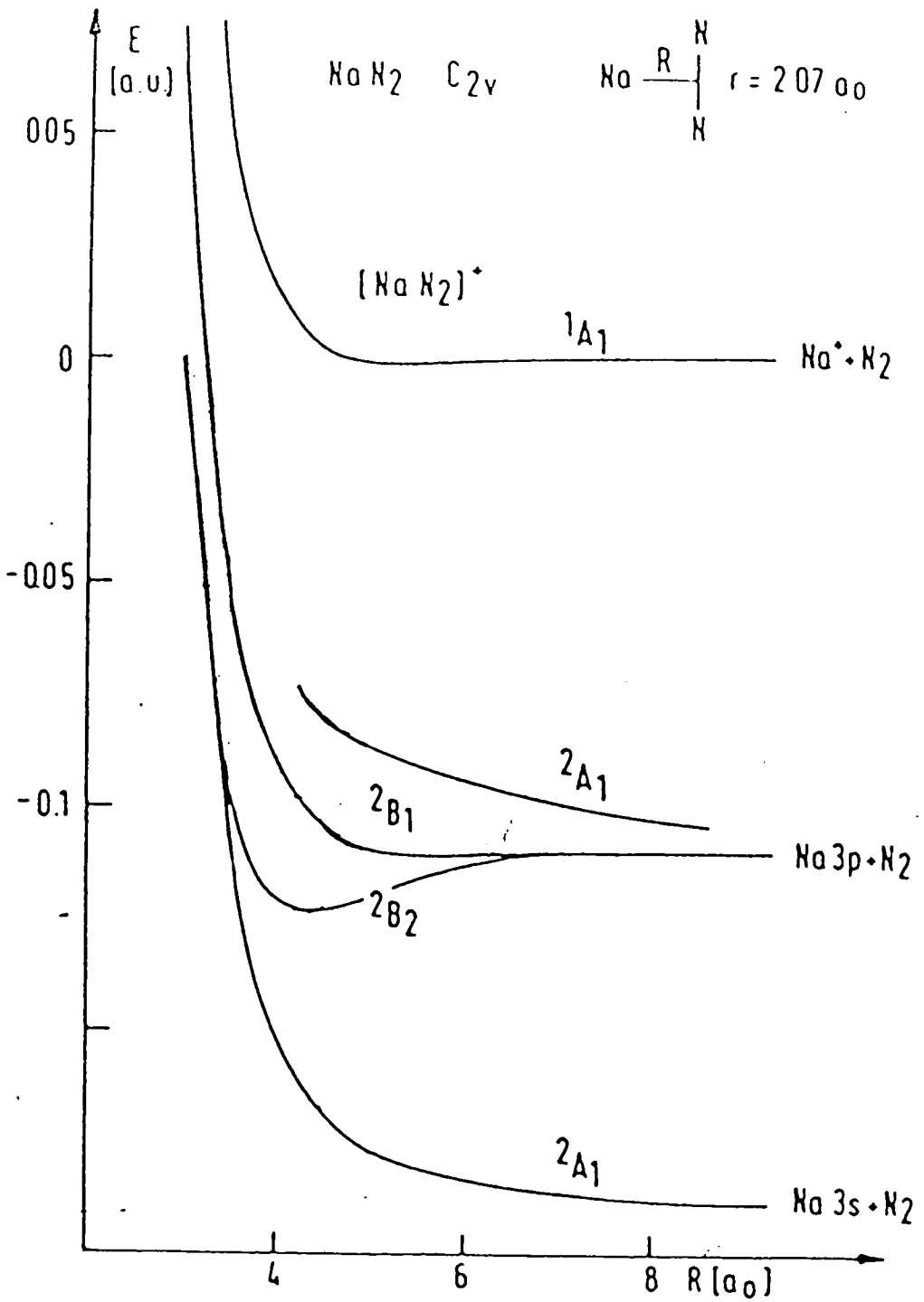


Fig. 6.1: Na - $N_2$ states in $C_{2V}$ symmetry at the $N_2$ equilibrium bond length as calculated by Habitz (HAB 80).

approach) and assume the nitrogen molecule to be in its equilibrium position. As can be seen, the figure still shows remnants of the "ionic intermediate". Partial electron transfer into the $\pi_g(N_2)$ orbital produces a minimum along R in the excited, $V(\tilde{A}^2B_2)$ state and dilutes the $N_2$ bond. This makes the crossing seam energy swing downwards as the partners approach. Archivel and Habitz (ARC 83) used these potentials in classical trajectory calculations to calculate the total and differential cross sections for quenching of $Na(^2P)$ and found very good agreement with experiment.

Ross et al. (ROS 81) scaled the potentials to obtain ones suitable for the $K + N_2$ interaction and used them to investigate the activation threshold for vibrational excitation in such collisions. The potentials are consistent with experimental results.

In this work we have attempted to place more stringent constraints on the model by exploring more processes and hence a larger part of the potential surfaces.

The discussion of the neutral inelastic differential cross sections for $K + N_2$ collisions in this chapter uses diabatic potential surfaces based closely on the adiabatic surfaces used by Ross et al. (ROS 81). The present results involve many more electronically excited states than the above (both atomic and molecular) and, with the collisions at relatively fast collision velocities, the diabatic potential surfaces crossed by a suitable ion pair state should be a fairly good approximation. The results fall into two main categories: electronic excitation of the potassium ion with vibrational excitation of the molecule and electronic (and vibrational) excitation of the molecule. Only the

processes involving electronic excitation of the atom have been compared with model predictions.

## 6.2 Vibrational and Alkali Atom Excitation

Kempter has measured the fluorescence from this system (KEM 73) at energies between 10 and 50 eV CM which revealed predominantly $K(4^2P)$ excitation with the signal from $5^2P' \rightarrow 4^2S$ and $6^2S \rightarrow 4^2P$ yielding populations of these states to be $\sim$ 2% and $\sim$ 0.6% of the $4^2P$ population. We observe $K(4^2P)$, $K(5^2S)$ and $K(5^2P)$ but no $K(6^2S)$, although it does become more difficult, as the electronic excitation approaches the ionisation potential, to unambiguously assign the observed processes. The assignment mentioned above is based on the modelling results. The intensities observed for the higher atomic states were found to be much closer to the intensity of $K(4^2P)$ excitation than found by Kempter.

Gersing et al. (GER 73) did time of flight measurements at collision energies around 50 eV and concluded that the cross section for the excitation of higher lying potassium states should be comparable in magnitude to that for $K(4^2P)$ excitation as observed here. However they analysed their data assuming that no vibrational excitation occurs simultaneously with the electronic excitation which would appear highly unlikely in the light of our results and those of Brieger and Loesch (LOE 77).

In the coincidence experiments of Kempter et al. (MAR 79), which measured the differential cross section of $K(4^2P)$, the apparatus geometry was such that it was not possible to distinguish

any additional energy loss associated with the nitrogen vibrational excitation.

The main feature of the energy loss results for the atomic excitations is illustrated in Fig. 6.2. The vibrational excitation of the molecule which occurs simultaneously with the electronic excitation of the atom is seen to increase with increasing collision energy. This is different from $CH_3I$ and $CH_3NO_2$ (FLU 83) where the vibrational excitation decreases with increasing collision energy. The model predictions are also shown on Fig. 6.2 and are seen to correctly predict the observed trend which is a consequence of the amount of time spent on the ion pair potential surface. When the system crosses onto the ion pair state the $N_2^-$ is formed in a vibrationally excited state; on crossing back onto the neutral surface, the predicted vibrational energy is critically dependent on the phase of the $N_2^-$ vibration. This is illustrated in Fig. 6.3 for process 2 (no atomic excitation, molecular vibrational excitation) where the predicted vibrational energy is plotted against the collision energy. The value of $r_c$, the molecular bond length on crossing back to the neutral potential surface is also indicated.

Using the established potentials the model can predict the energy loss variation with scattering angle fairly well. This is shown in Fig. 6.4 for the lowest collision energy, 43.3eV CM. It is clear from this figure however that there are two sets of energy losses associated with process 2 (as is the case with $CH_3I$) and the model only predicts the higher one. Using a "starting velocity" in the model, i.e. accounting for the motion of the $N_2$

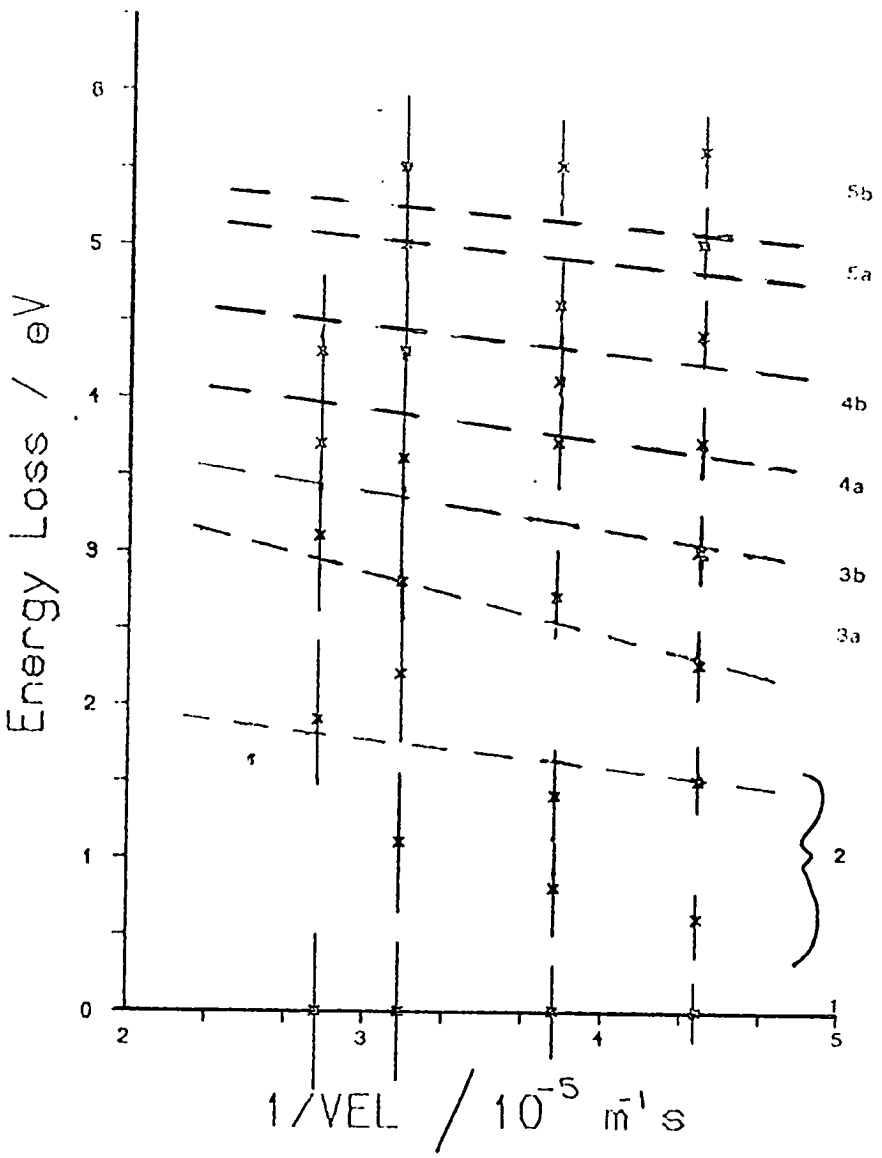


Fig. 6.2: Energy loss vs. $^{1}/_{vel}$ for K excitations. Model prediction is dashed line. Process numbers are indicated.

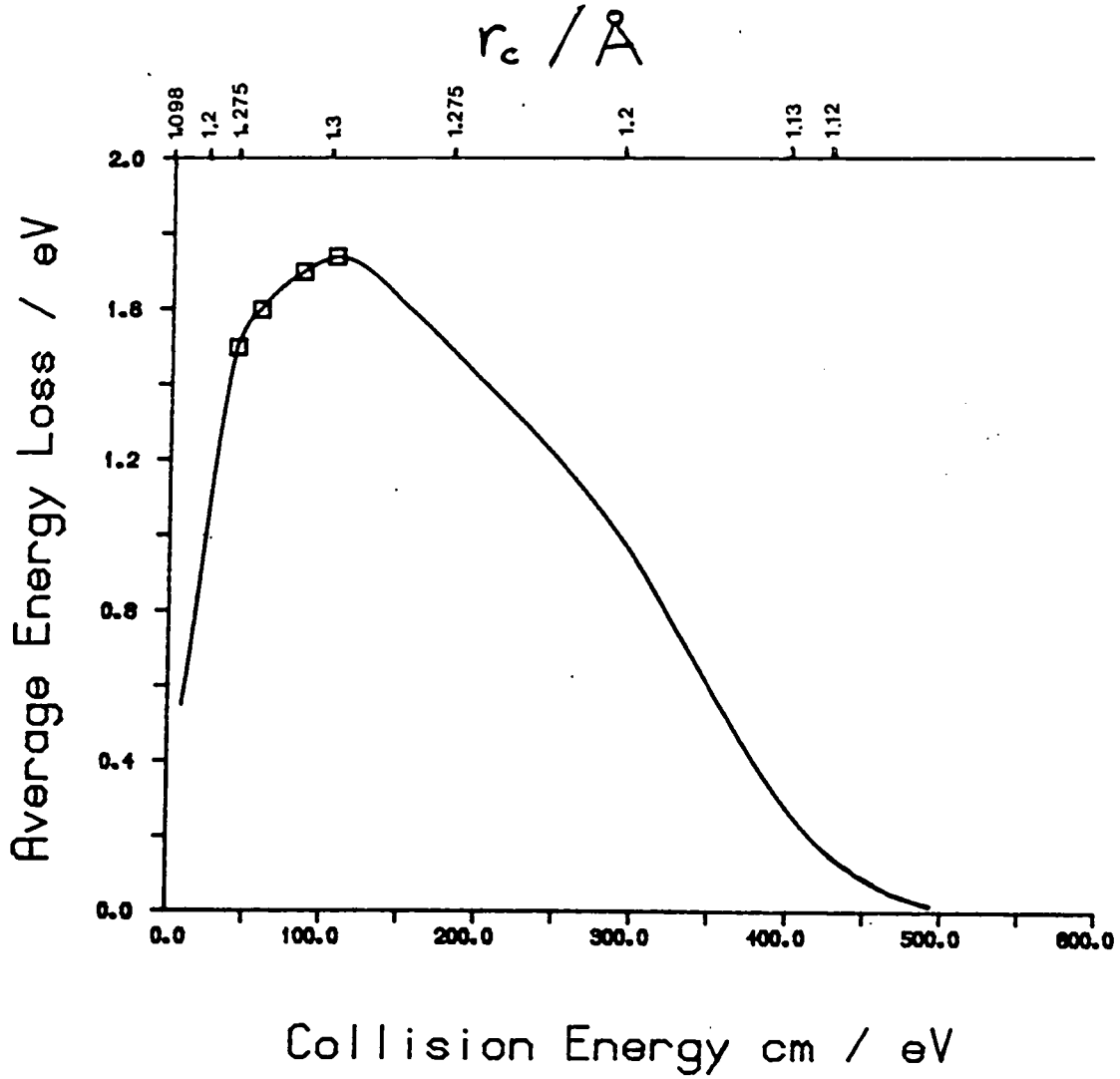


Fig. 6.3: Effect of Bond Stretch and Collision Energy on predicted Vibration Energy Loss Results for process Number 2.

Boxes indicate collision energies for which experimental data is available.

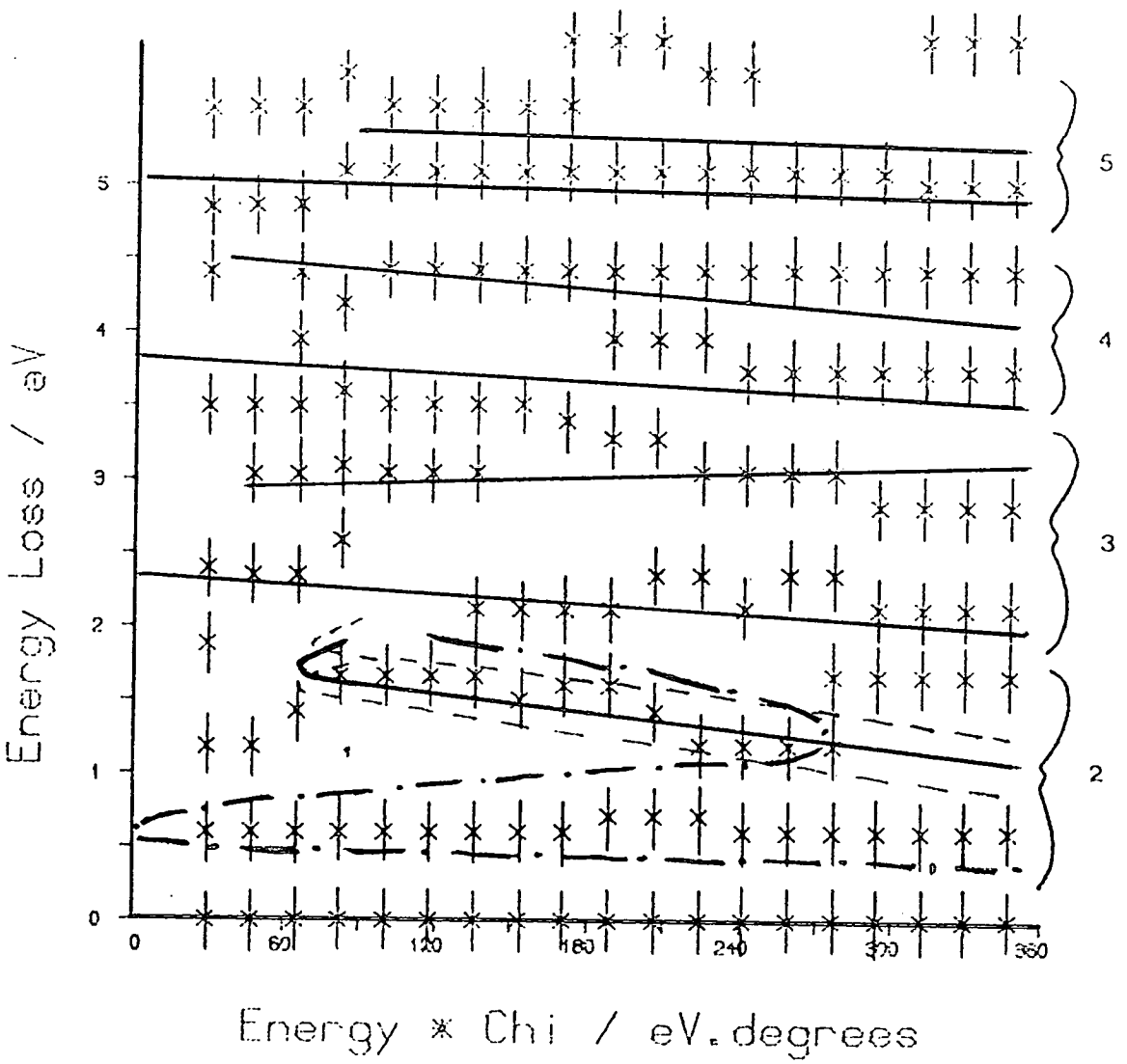


Fig. 6.4: Energy Loss vs. EX · for K excitations.

Model prediction is full line.

- - - model with velocity of $N_2$ taken into account. Upper prediction has $r_{N_2}$ decreasing on jump to $N_2^-$.

— . — . Model prediction with $\alpha = 5.6$ Å$^3$

at the first crossing (expanding or contracting) does not make much difference to the model predictions. This is indicated on Fig. 6.4, and is unlikely to be the cause of the two sets of observed energy losses. Rainbowing (as with $CH_3I$) is another possibility but to obtain the correct energy loss predictions a much more attractive ion pair intermediate is required. This is shown in Fig. 6.5 and was obtained by doubling the polarisation, $\alpha$. This is unlikely to be a realistic picture.

The differential cross sections for the elastic process (process 1) are shown in Fig. 6.6. The model correctly predicts the fall off in intensity at about 300 eV°. This is related to the impact parameter at which the other processes are accessed. The fact that the higher processes onset at reduced scattering angles less than 300eV° indicates that the ion pair state must be more attractive than the ground neutral $K + N_2$ surface. The ion pair potential produced by doubling the polarisation (Fig. 6.5) does not give the correct position for this intensity fall off. There appear to be some interesting oscillations in these differential cross sections which the model does not predict. These oscillations have a period which is decreasing with increasing collision energy. The difference in the value of the impact parameters at the peak positions, $\Delta b$, is given for the three collision energies. It is possible that these peaks are Stueckelberg oscillations. The differential cross sections for processes 2 - 5 may also be showing evidence of oscillations but the large errors in the measurements make a categorical statement difficult.

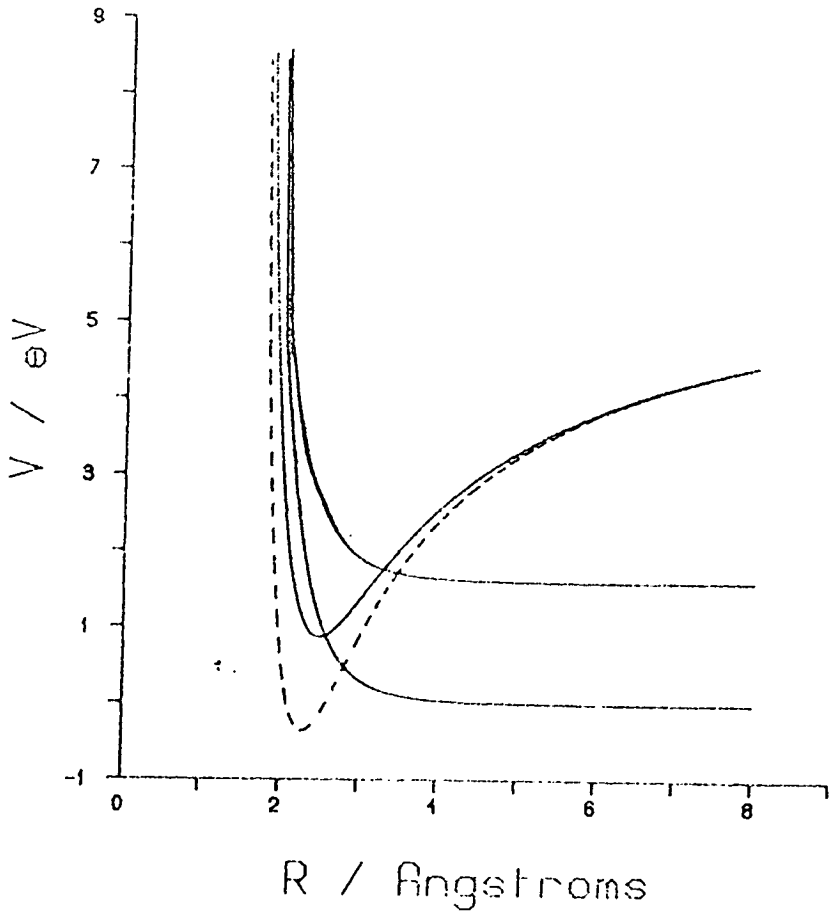


Fig. 6.5: Ion-Pair Potentials.

Dashed line has the polarisability, $\alpha$, doubled to 5.6 $\mathring{A}^3$.

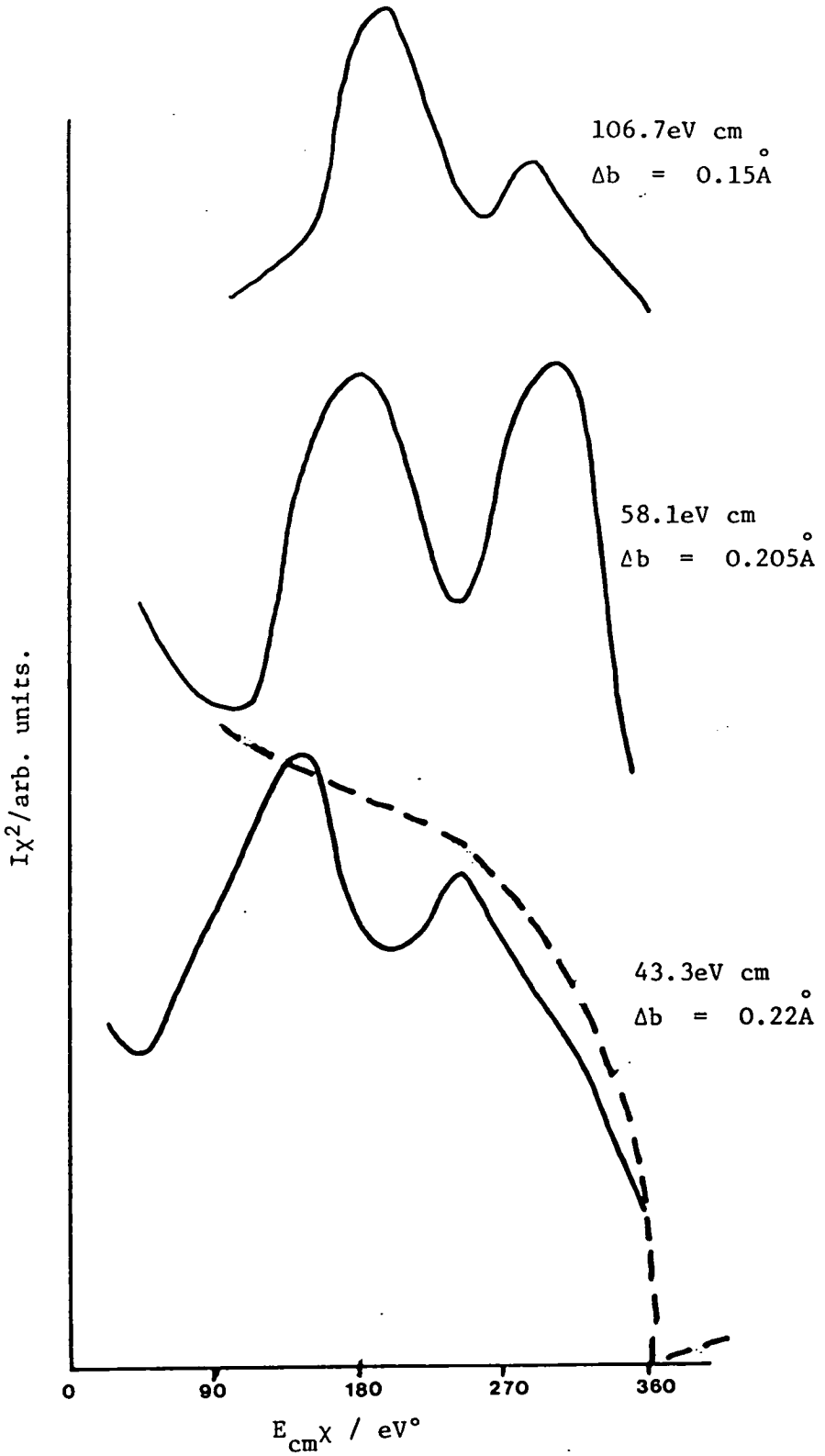


Fig. 6.6: Differential cross sections for process 1 at different collision energies, shifted for clarity. Model prediction is dashed line.

The model can predict the main features of these cross sections as shown in Figure 6.7 for processes 2 and 3 at 43.3 eV CM. A rainbow is responsible for the peak in process 2. The differential cross section for $K(4^2P)$ formation (processes 3a and 3b combined) is similar to that obtained by Kempter (MAR 79) with a steadily increasing intensity from about 50eV° up to about 400eV°.

It should be noted that only the shapes of these differential cross sections have been obtained with the model, their relative intensities have not been matched. The coupling parameters used in the model have been taken directly from the trend line shown in Figure 4.8. To obtain the correct intensities these parameters will have to be systematically varied. A tedious but not impossible task.

## 6.3 Electronic Excitation of the Nitrogen Molecule

The nitrogen molecule has a rich, complex spectrum and has received more attention from spectroscopists than probably any other molecule. A number of reviews have appeared in the literature (LOF 77, MUL 57). An extensive systematic study of the potential energy curves for nitrogen was carried out by Gilmore (GIL 65). These curves were calculated with a numerical RKR method using rotational and vibrational term values from the available literature. A more recent compilation of the potential energy curves for nitrogen, based on available spectroscopic data and extensive calculations for the valence states is that of Michels (MIC 81). The bound states of $N_2$ are shown in Fig. 6.8.

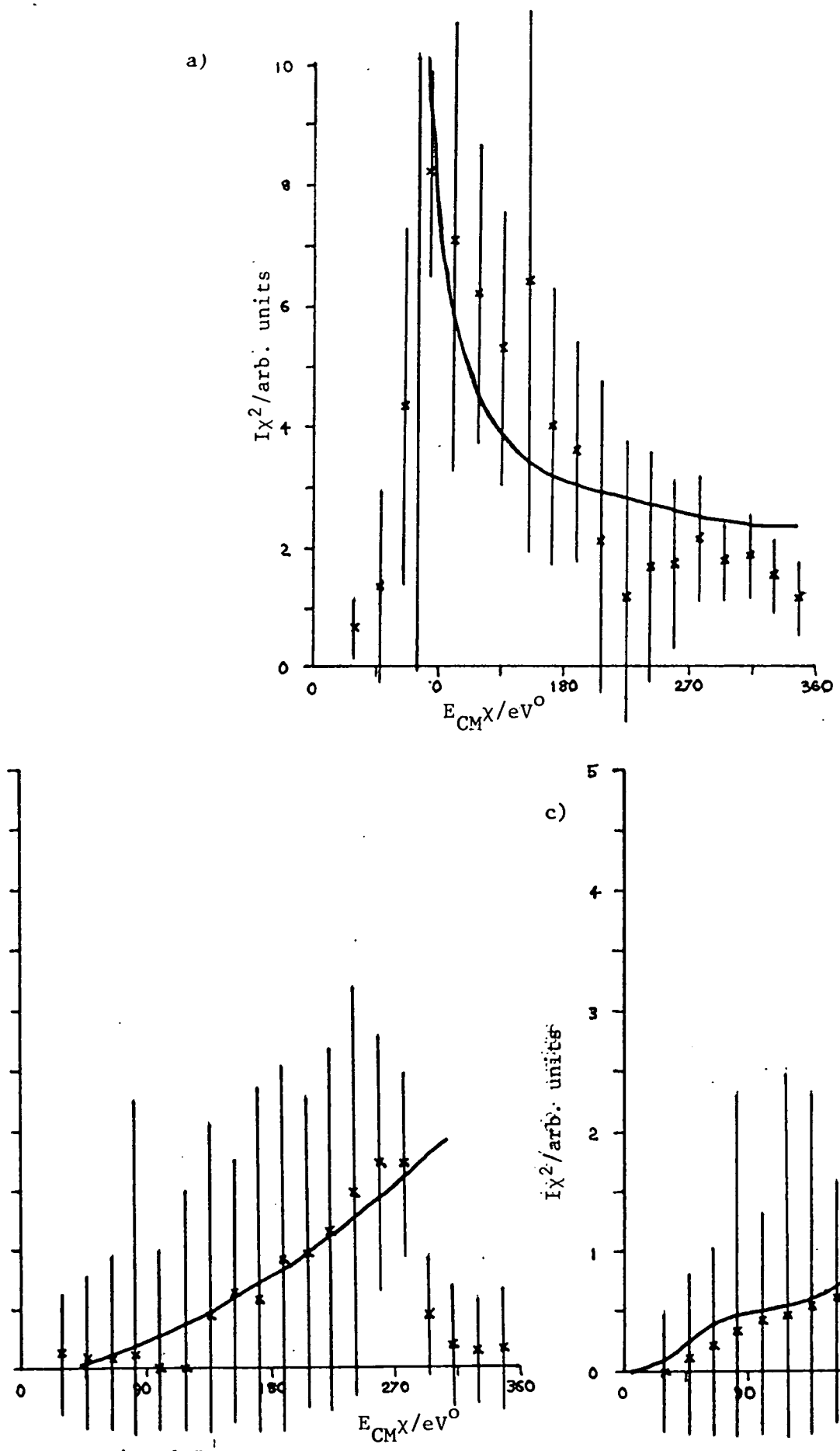


Fig. 6.7: Model Fitting of Differential Cross Sections at 43.3eV.
a) Process 2, vib. excitation in N-N. b) Process 3a, exit as K(4P), early crossing.
c) Process 3b, exit as K(4P), late crossing.
Model Prediction is Solid Line.

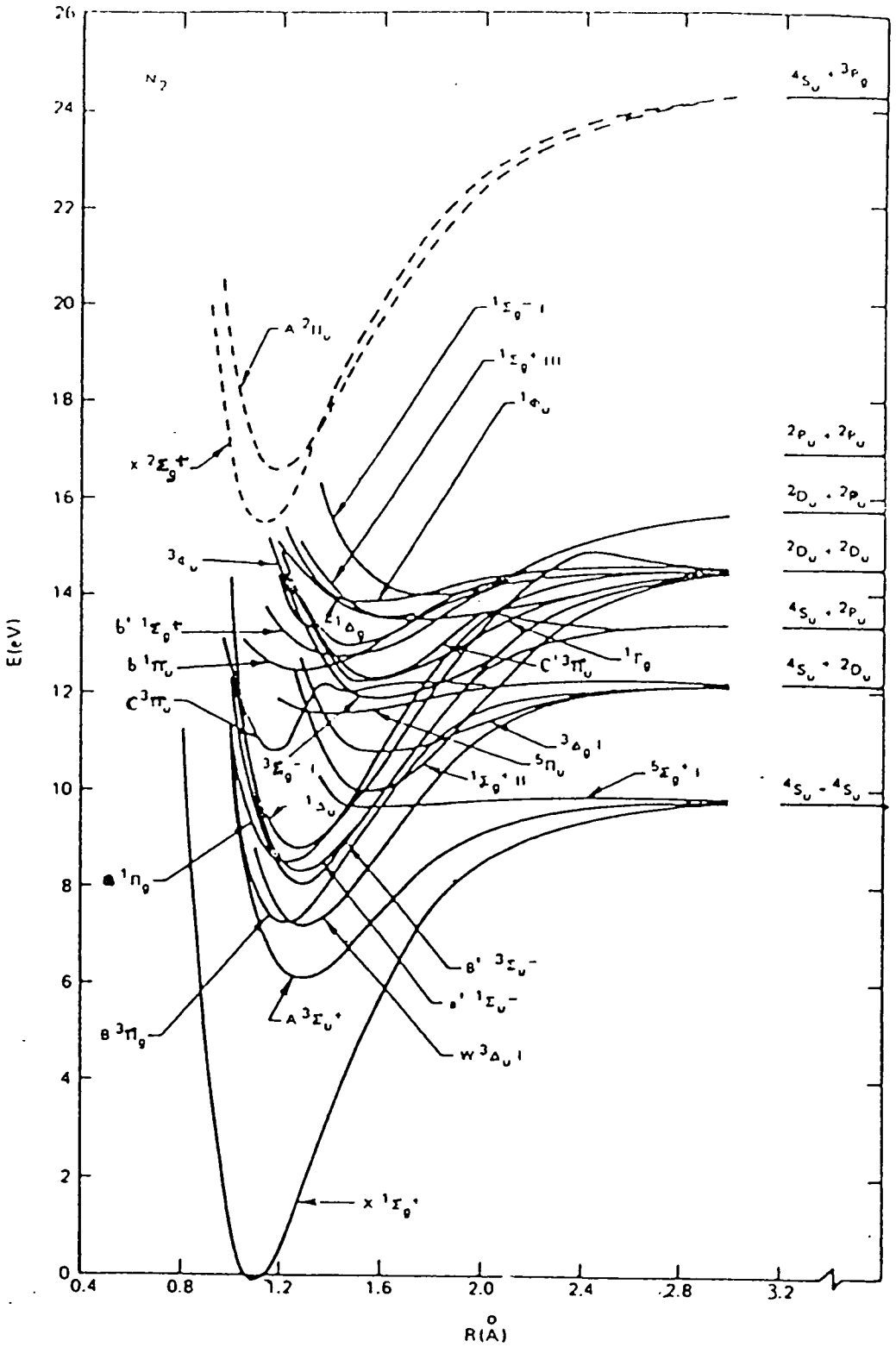


Fig. 6.8: Bound states of $N_2$ (MIC 81).

Fig. 6.9 plots the energy losses, averaged over scattering angle against $\frac{1}{v}$. There seems to be little, or no, vibrational excitation accompanying the electronic excitation for most of these assigned processes. They onset at fairly narrow scattering angles and show a constant energy loss as the scattering angle increases (Fig. 6.10).

The two assigned states that do show increasing energy loss with increasing collision energy are processes 12 and 13 (exit as $C^3\pi_u$ and $E^3\Sigma_g^+$ respectively). These states have equilibrium bond lengths of 1.15Å and 1.12Å (MIC 81) - close to the equilibrium bond length of ground state nitrogen (1.1Å), whereas the other assigned states have bond lengths slightly greater than that of $N_2^-$.

All of these electronically excited states of the nitrogen molecule (with the exception of process 13) have an electron in the $1\pi_g$ orbital which is the highest occupied orbital in the ground state molecular ion. Table 6.1 gives the electron configuration of the assigned states. This would suggest that these states could be accessed via the $K^+ - N_2^-$ ion pair state as are the atomic excitations (section 6.2). In this case the electron recaptured by the potassium ion on leaving the collision is taken from a lower-lying orbital, leaving the receptor orbital occupied and a vacancy in a normally filled position. If the electron recapture occurs round about the outer turning point of the $N_2^-$ vibration, this would explain the energy loss results for processes 6 - 12.

Process 13 ($E^3\Sigma_g^+$) has an electron in the $3s\sigma_g$ orbital

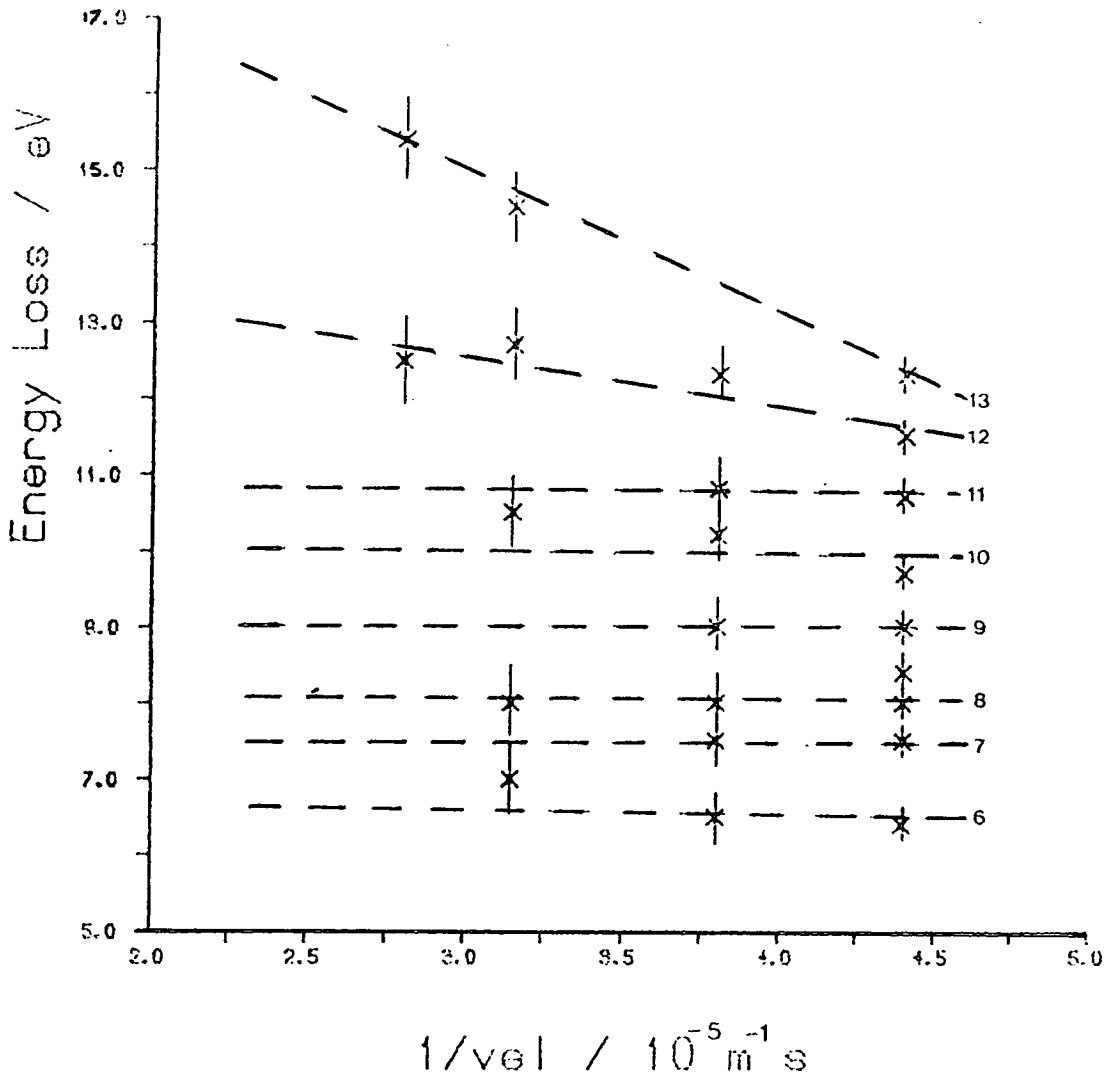


Fig. 6.9: Energy loss vs. $^{1}/vel$ for $N_2$ electronic excitations. Process numbers are indicated.

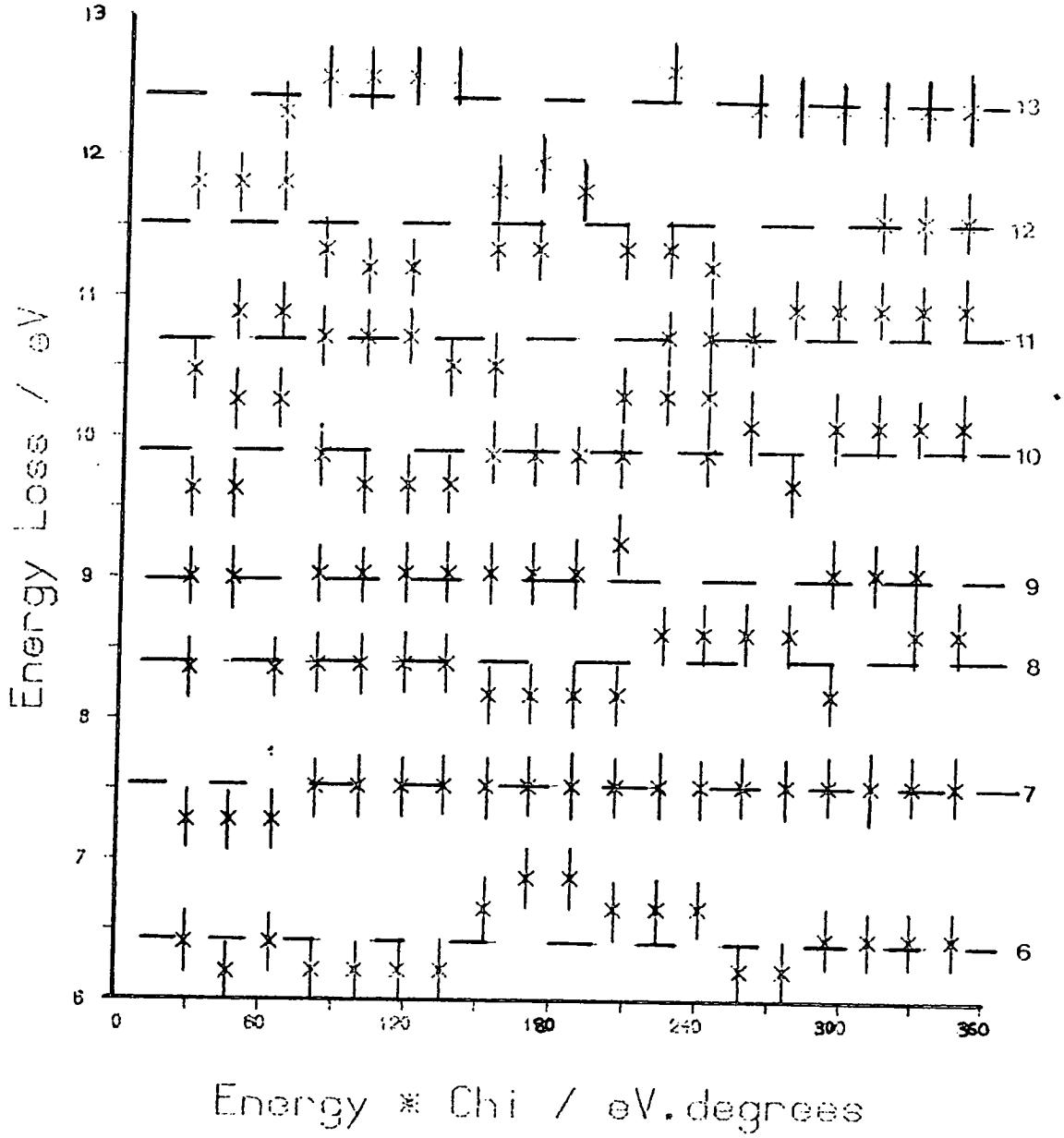


Fig. 6.10: Energy Loss vs. EX for $N_2$ electronic excitations. Process numbers are indicated.

TABLE 6.1

Electron Configurations of Assigned $N_2$ States

| State | Electron Configuration | | | | Excitation Energy/eV |
|---|---|---|---|---|---|
| | $1\pi_u$ | $3\sigma_g$ | $1\pi_g$ | $3\sigma u$ | |
| $X^1\Sigma_g^+$ | 4 | 2 | 0 | 0 | 0.0 |
| $A^3\Sigma_u^+$ | 3 | 2 | 1 | 0 | 6.2 |
| $B^3\pi_g$ | 4 | 1 | 1 | 0 | 7.4 |
| $B'^3\Sigma_u^-$ | 3 | 2 | 1 | 0 | 8.2 |
| $a^1\pi_g$ | 4 | 1 | 1 | 0 | 8.6 |
| $^5\Sigma_g^+$ | 2 | 2 | 2 | 0 | 9.7 |
| $^1\Sigma_g^+$ | 2 | 2 | 2 | 0 | 10.1 |
| $C^3\pi_u$ | 4 | 2 | 1 | $0(-2\sigma_u)$ | 11.05 |
| $E^3\Sigma_g^+$ | 4 | 1 | 0 | $0(3s\sigma_g)$ | 11.9 |

N.B. All states include $(1\sigma_g)^2$ $(1\sigma_u)^2$ $(2\sigma_g)^2$ $(2\sigma_u)^2$ electrons unless otherwise stated.

and would require an excited molecular ion state as intermediate. Feshbach type and shape resonances associated with this Rydberg state of the molecule have been observed in electron impact experiments (SCH 73).

At the higher collision energies, energy losses of more than 16eV are observed with relatively large cross sections (Table 3.4). No attempt has been made to assign these processes; however, resonances have been observed for $N_2$ in the energy range 20 - 24eV (PAV 72). These resonances were interpreted as being associated with doubly excited states of the nitrogen molecule rather than singly excited Rydberg states. Resonances associated with double excited states of atoms (e.g. $2s^2 2p$ in the case of He) are well known. With small systems such as He these resonances are expected to be spaced well apart compared to their width, whereas in systems with more electrons (e.g. $N_2$) there is the possibility of many doubly excited states which are closely spaced, each of which may have an associated compound state. The observed resonances would have two holes in the normally filled shells of $N_2$ and three electrons in vacant orbitals. Such states could provide a means of exciting the above mentioned doubly excited states which we may observe at narrow scattering angles in the neutral scattering experiments.

An alternative explanation of the high energy losses seen in the neutral experiments could be the formation of $N_2^+$ ions. The lowest positive ion state $(X^2\Sigma_g^+)$ lies at 15.6eV above the ground state of the neutral molecule and there are many electronically excited states of the positive ion above that (GIL 65).

Attempts were made to detect any positive molecular ions that may have been formed in the collisions with potassium using the set-up described in Chapter 2. However, due to numerous experimental problems, the results proved to be inconclusive.

The differential cross sections for the energy losses assigned to the electronically excited states of $N_2$ illustrated in Chapter 3, show some signs of oscillations. However, as with the alkali excitations, it is difficult to see a pattern emerging. Data at more collision energies and over a wider range of $E\chi$ would help determine what is happening.

## 6.4 Conclusion

A simple dynamical model has been shown to be a good first approximation to the production of excited alkali atoms in the $K + N_2$ collision system at relatively high collision energies. The ionic model remains predictive in providing information on the topology of the potential surfaces, e.g. position of crossings, at least approximately. It is therefore useful in the absence of *ab initio* surfaces for all states and may actually be more physically realistic. The large number of energy losses observed and their behaviour with changing collision energy can be explained (with the exception of the lowest energy loss assigned to process 2). The next stop should be the development of a quantum mechanical "wave packet" model which could help to clear up the situation with regard to the oscillations observed in the differential cross sections.

The large number of molecular excitations observed have been

assigned and may also be explained by an ion pair intermediate model, although this has not been attempted. Experiments to determine whether any positive molecular ions are formed in the collisions would help to assign the higher energy losses observed.

# CHAPTER 7

# LOCATION SENSITIVE SCATTERED ATOM/ION DETECTOR

## 7.1 Introduction

Location sensitive detectors, able to record scattered intensities at several angles simultaneously, provide a number of important advantages in scattering experiments.

a) Since the measurements at all scattering angles are carried out simultaneously, beam fluctuations are independent of scattering angle and do not contribute to the noise. In typical experiments with long counting times very significant improvements in sensitivity can be realised.

b) Since many angles are measured simultaneously the data rate available for an experiment is greatly increased and the available signal to noise ratio at each angle correspondingly enhanced.

c) Finally, it is possible to envisage the use of the location sensitive detector to encode parameters other than the scattering angle by the use of suitable dispersing elements for mass, spin etc.

The device described here has been designed with a particular requirement in mind. It will be used in the coincident detection of photons and scattered particles from molecular collisions. For this use, the particle detector must have the following features:

(a) An angular range of approximately $0 - 10^{o}$

(b) An angular resolution of $0.1^{o}$

(c) The capability of detecting scattered particles with an energy in the range 10 - 1000 eV.

(d) A time resolution adequate to resolve energy losses of 0.2 eV throughout the initial energy range and to provide coincidence signals with a resolution of $5 \times 10^{-9}$ s.

(e) The capability of handling a dynamic range between the smallest and widest angles of approximately $10^6$ (or as large as possible).

Various techniques have been used for position sensitive particle detectors. Some, such as the charge coupled vaster scan devices are too slow for the present application. Devices based upon channel plates do have the required speed but, as usually constructed, depend upon a charge fractionating technique to determine the position. This limits the response time. Furthermore, the energy resolution required in the planned experiments necessitates flight paths of 1m in length so that to cover the angular range, very large channel plates would be needed or the image of the scattered particles would have to be substantially demagnified.

A device based upon a successfully operating Daley type (DAL 60)single channel particle detector, using a binary coincidence technique to determine the position of an event did not appear to suffer from these limitations and to offer the most economic design for such a detector.

The initial design of the detector, construction of the Pierce gun and lens system and construction of the original fibre optic connections was achieved by a previous research student in the molecular beams group, Colin McGill. He also carried out the trajectory calculations and calculations to

estimate the performance of the detector. The optimisation of the various focussing voltages, improvements in the collection of photons from the scintillator and measurements of the performance sensitivity were carried out by myself. All the work done on the detector has been described here to give an overall view of the device.

## 7.2 Basic Design

A simplified diagram of the detector is shown in Fig. 7.1. It can be used for either the detection of positive ions (which will be the first application) or the detection of energetic alkali atoms. The atoms are detected as ions following their collision with a warm tungsten surface. (In principle, any other ionisation technique could be used at this point). The ions enter a modified Pierce gun (PIE 40), designed to produce a parallel sheet of ions. The entrance slit of the Pierce gun is arranged to intersect a wide range of scattering angles following the collision of the positive ions/atoms with atoms or molecules in a crossed beam experiment. The ions are injected into a region of constant vertical electric field and fall in a parabola onto an $A\ell_2O_3$ plate. Secondary electrons ejected from this plate are focussed through an electric field to form an image of the initial scattering pattern on scintillators. The location of a scattering event in angle and time can then be coded via a bank of photomultipliers multiplexed via optical glass fibres to elements of the scintillator material. If each angular element is connected to two photomultipliers an arrival event, signalled by an electron burst on a specific element, then produces simultaneous

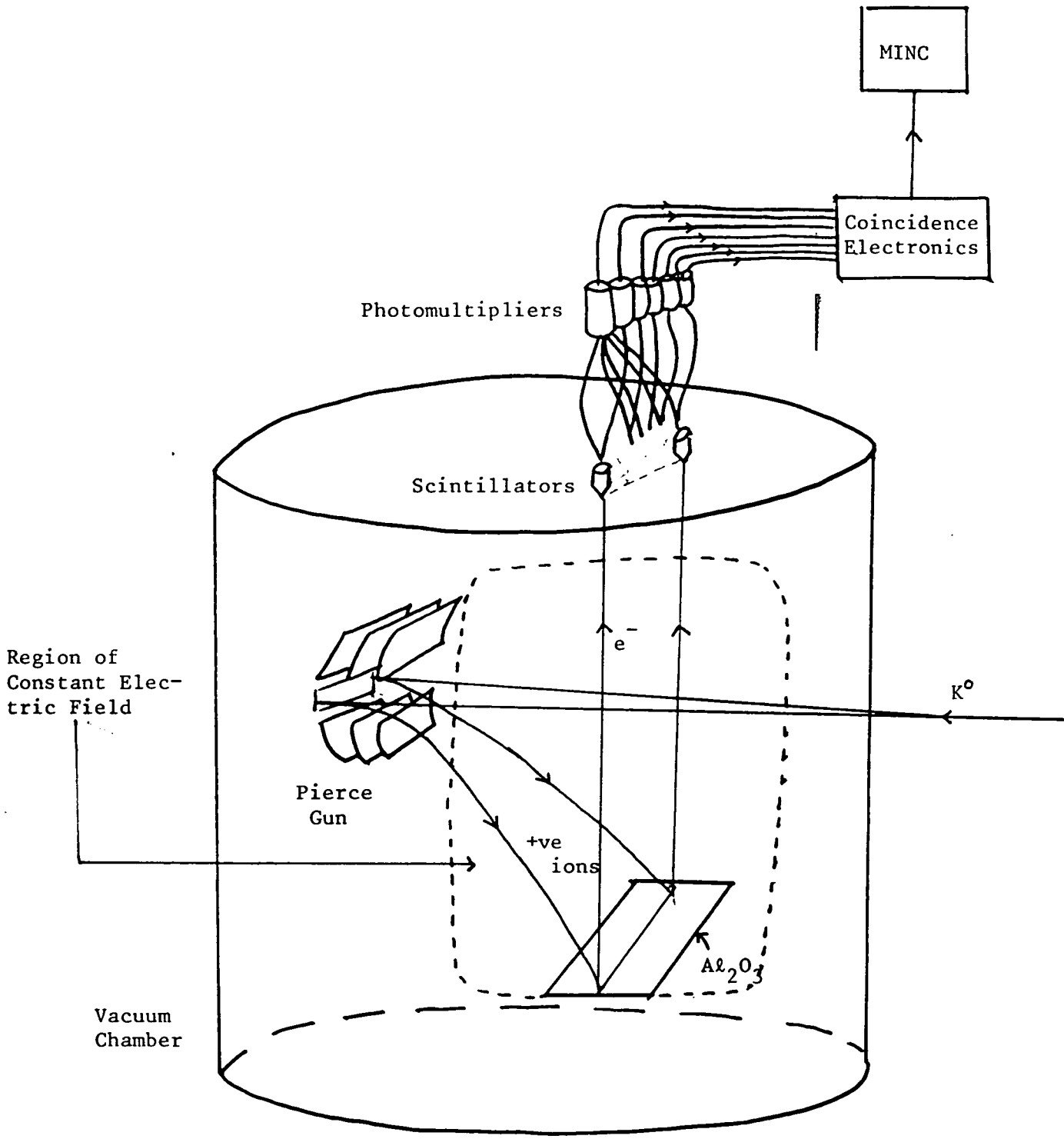


Fig. 7.1: Schematic Diagram of Detector.

signals in each photomultiplier. If this coincidence is detected, the arrival time can be determined directly while the angular location of the event is coded by noting which specific pair of photomultipliers are involved in the coincidence. Thus a bank of 10 photomultipliers could encode by this binary coincidence method $^{2}C_{10}$, i.e. 45 individual angular elements.

The final section of the apparatus thus consists of a network of fibre optic cables which code the individual scintillator elements to a bank of photomultipliers. The signals from these multipliers are processed by a high speed electronic interface (5ns) which detects coincidences between the photomultiplier signals, determines the address of the scintillator element responsible and outputs both time and angular information to a micro computer.

The detector chamber is pumped by an oil diffusion pump (1000 $Ls^{-1}$) and will be separated from the collision chamber by a buffer chamber. There will be a collimating lens system at the entrance to the detector chamber. It is hoped to obtain a working pressure of $\sim 10^{-8}$ torr. in the detector to minimise background noise.

### 7.2.1 Electrostatic Lens System

The construction of the electrostatic lens system is such that it has rectangular symmetry, i.e. the system is independent of the direction along the entrance slit. The behaviour of the ions and electrons is thus independent of scattering angle. There

should be no motion of ions or electrons out of the plane defining the scattering angle (vertical and parallel to the main ion/neutral beam axis). This leads to the requirement for a large number of shimming plates in the region of constant field to maintain the uniformity as shown in Fig. 7.2.

The low initial energy at which the secondary electrons are emitted from the $A\ell_2O_3$ surface ($\sim$ 2eV), coupled with the high field strength in the lens system ensures that any initial motion the electrons have will not lead to loss of angular or time resolution. Similarly, for the detection of atoms, the positive ions formed at the warm tungsten surface have an initial energy of only a few eV.

The whole lens system has to be wide enough to ensure there are no edge effects and mechanical tolerances in the plates ($\pm$ 0.1mm) are such that field inhomogeneities cannot lead to a reduction in performance.

The electrons are always travelling normal to the plates and can be handled by focussing and steering plates. However, the ion path is at a variable angle to the plane of the plates. For plates of finite thickness this leads to defocussing so the slits that the ions pass through have been designed to act as very thin plates. This is illustrated in Fig. 7.3.

With the electrostatic system designed as shown in Fig. 7.2 the path of the ions was calculated with a simple computer program. The potentials in the system are independent of one cartesian coordinate (the horizontal axis which is perpendicular to the beam axis) so that only the potentials in the vertical plane containing the beam axis need be found. A section through the lens system

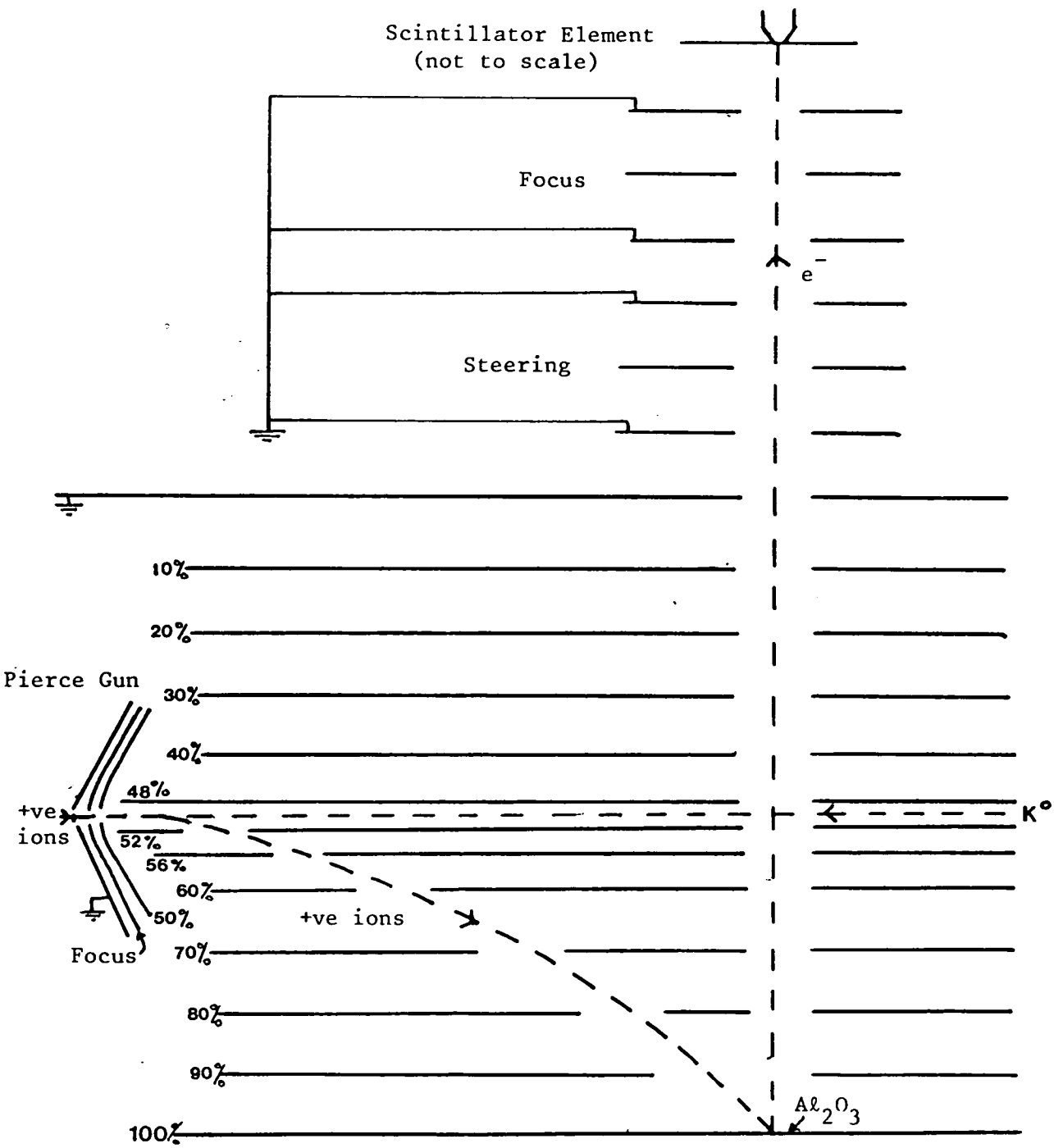


Fig. 7.2: Electrostatic Lens System

was painted on field plotting paper with silver paint, the electrodes were connected up to scaled down potentials and the equipotentials in the paper were found. A grid of numerical potentials was built up and put into a computer data-file. The ions were tracked through this potential grid by calculating the position of the ions at certain time intervals using the Lorentz force equation. These trajectory calculations enabled the geometry of the Pierce gun to be optimised and also showed the effect of having "non-ideal" lens plates. These points are illustrated in Figs. 7.3 and 7.4.

At the nominal design energy of 50 kV it was found that the optimum design could focus the detector 'object' to a line with a standard deviation of 0.5 mm, i.e. 95% of the ion trajectories were found to strike in a 2 mm wide strip on the $Al_2O_3$ plate. The dispersion in flight time then had a standard deviation of 1 ns.

The electron optics were designed to produce a real demagnified image (M = 0.4) of this illuminated strip on the scintillator elements. The design tables of Harting and Read (HAR 76) were used for this purpose. The electron image was predicted to be 1-2 mm wide (after considering aberration effects).

A photograph of the electrostatic lens system is given in Fig. 7.5, as is a general view of the detector.

### 7.2.2 Optical System

In the original design the scintillator was simply a long, thin (2 mm thick) plate which also served as a vacuum seal. The optical fibre 'Y's connecting to each 2 mm × 4 mm element on the

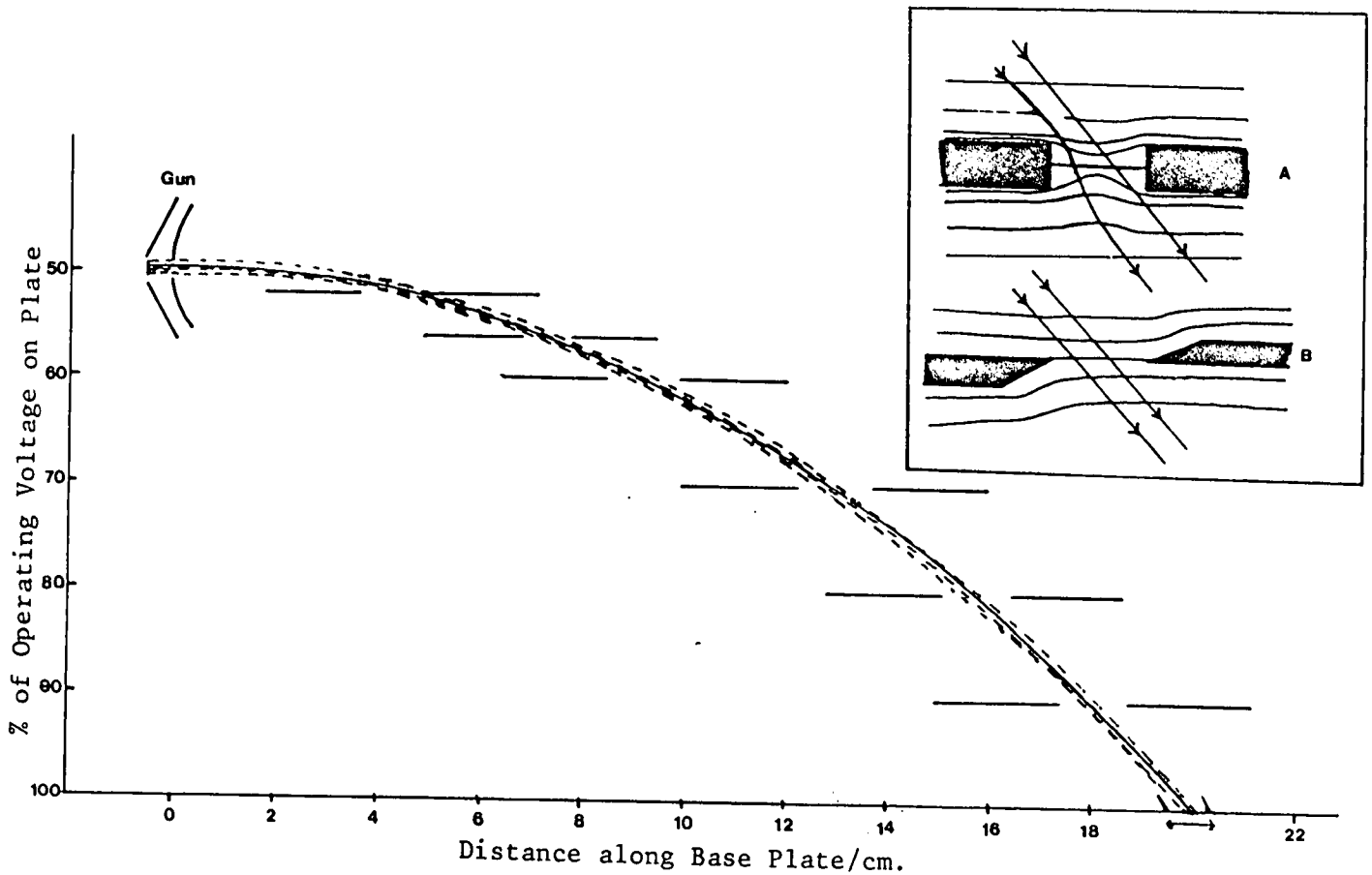


Fig. 7.3: Trajectory calculations to show effect of "non-ideal" lens elements. Trajectories drawn are for Type B plates (see inset). Arrow on x-axis indicates spread with Type A plates.

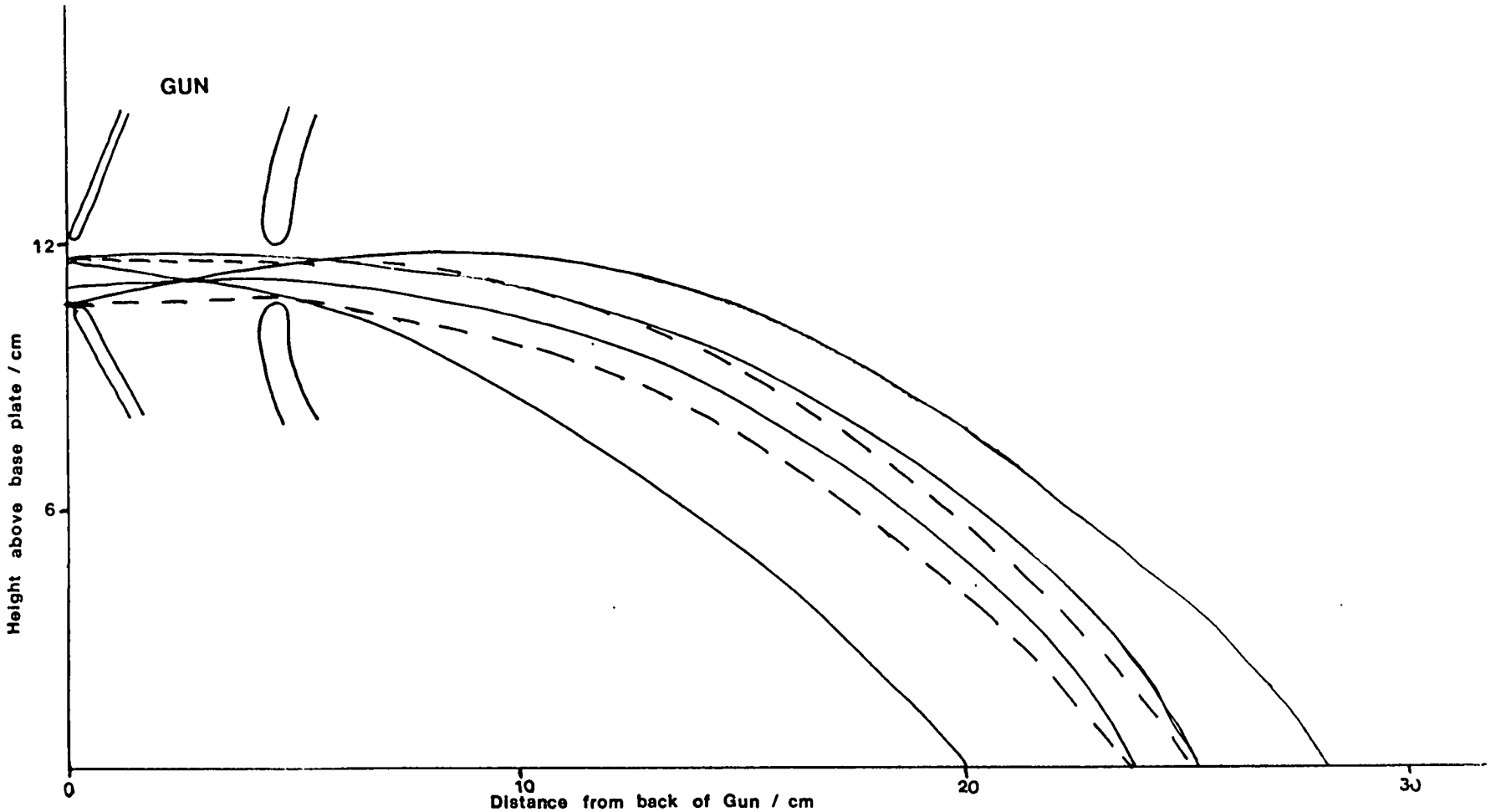


Fig. 7.4: Trajectory calculations to show effect of Pierce Gun Geometry.

Solid lines are trajectories calculated with W filament behind plates.
Dashed lines are calculated for optimum geometry.

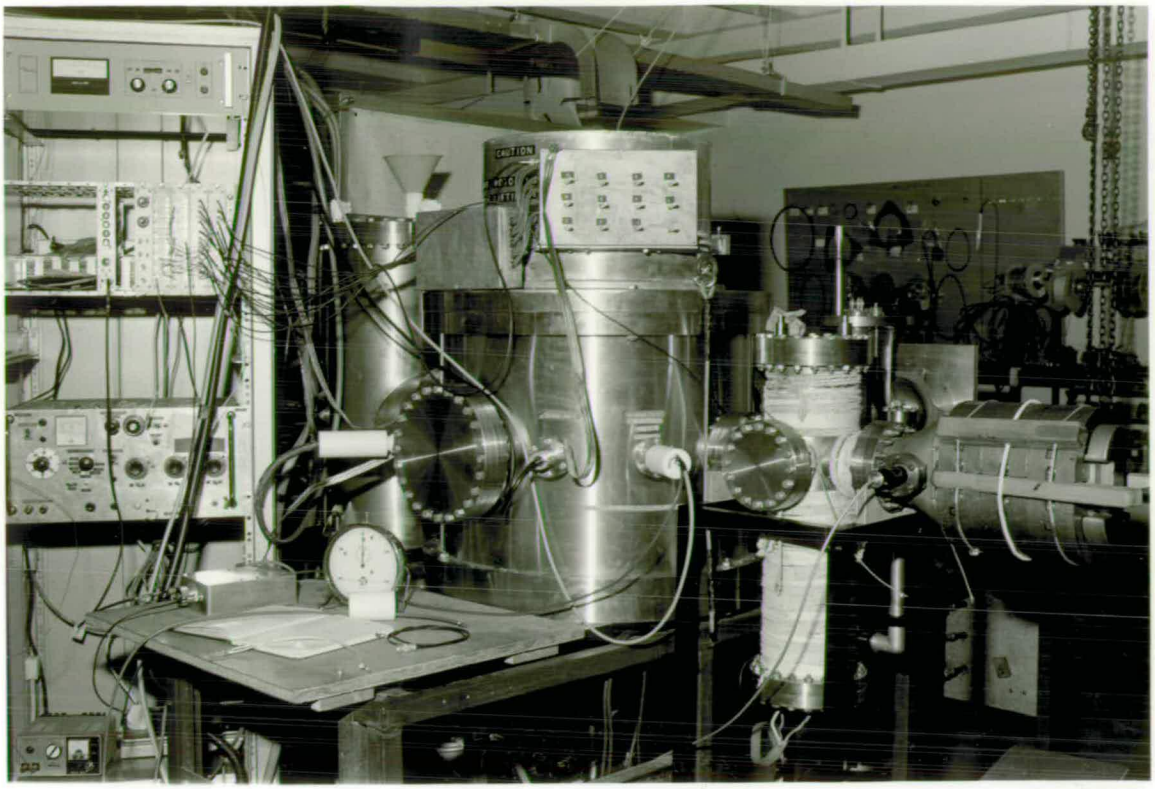

Fig. 7.5(a): General View of Detector.

Electrostatic lens system is located in the large chamber. Scintillators and photomultipliers are at the top of the large chamber under the cover.

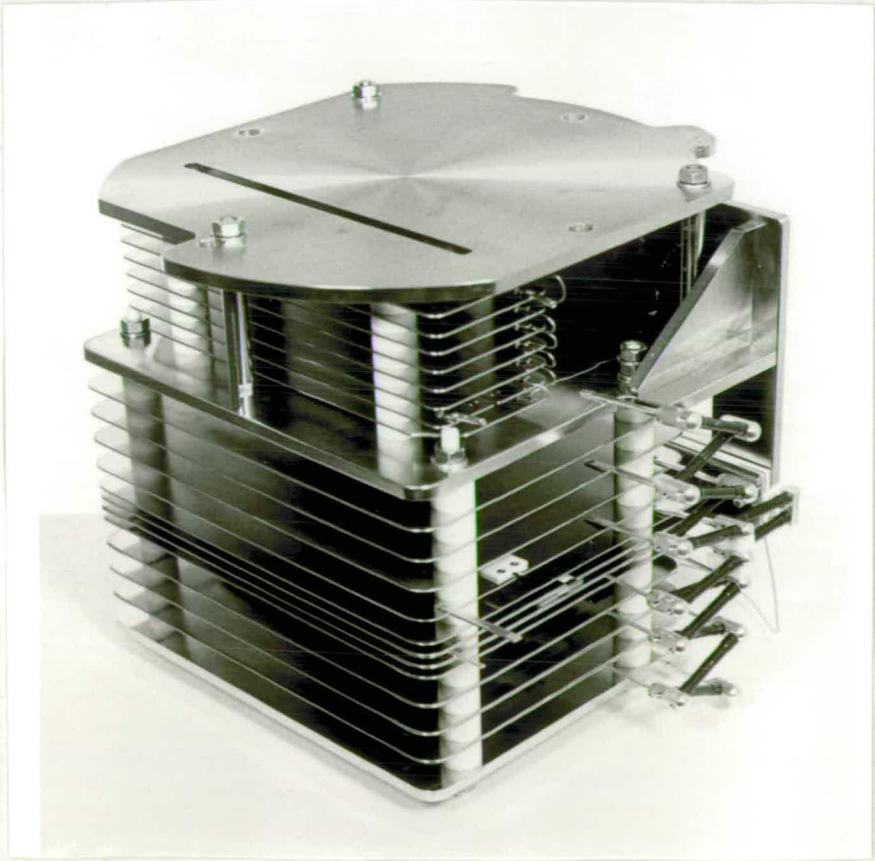

Fig. 7.5(b): View of Electrostatic Elements.

Divider chain and ion injection gun (present gun is four times this size) can be seen at the rear.

scintillator were made in the laboratory. This system proved unsatisfactory and although providing coincidences, was extremely inefficient. The plane scintillator sheet did, however, allow the ion/electron focussing system to be checked since the fluorescence was easily visible to the naked eye.

The design finally adopted was based on commercially available 'Y' optical fibres coupled to individual 'chisel' shaped scintillators which provided a much superior optical performance. The system is shown in Fig. 7.6. The scintillator is NE102 obtained from "Nuclear Enterprises", which outputs light mainly in the blue region ($\sim$ 430 nm).

### 7.2.3 Electronics

The coincidence and decoding interface has been built to perform the following functions:

a) A coincidence event, 'CE', in photomultipliers M and N, signalling an arrival in angle element i, is detected logically as:

$$CE = M.N.(\bar{O} + \bar{P} + \bar{Q} + \bar{R}).(\bar{J} + \bar{T} + \bar{U} + \bar{V} + Hold) \qquad (7.1)$$

where M, N, O, P etc. are the logical signals developed from the separate photomultipliers and 'Hold' is an external logic signal for experimental control purposes. The width in the coincidence window is determined by adjustment of the pulse width from the photomultiplier discriminators (typically 10 ns).

(b) A detected event 'CE' is used to generate a time signal by stopping a 100 MHz clock. This clock is synchronised either to an

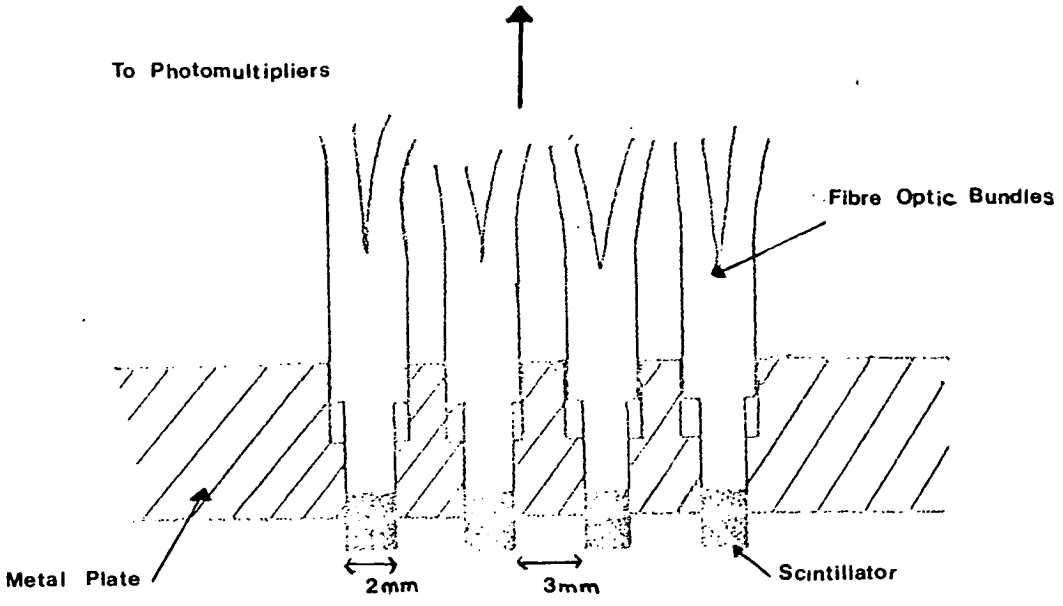


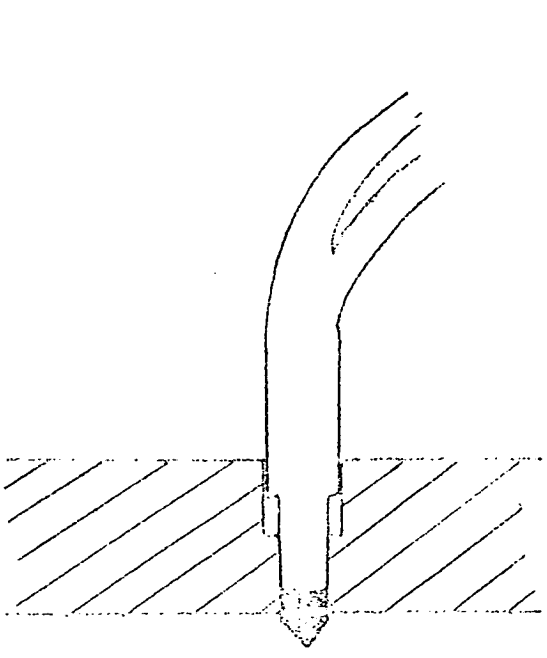


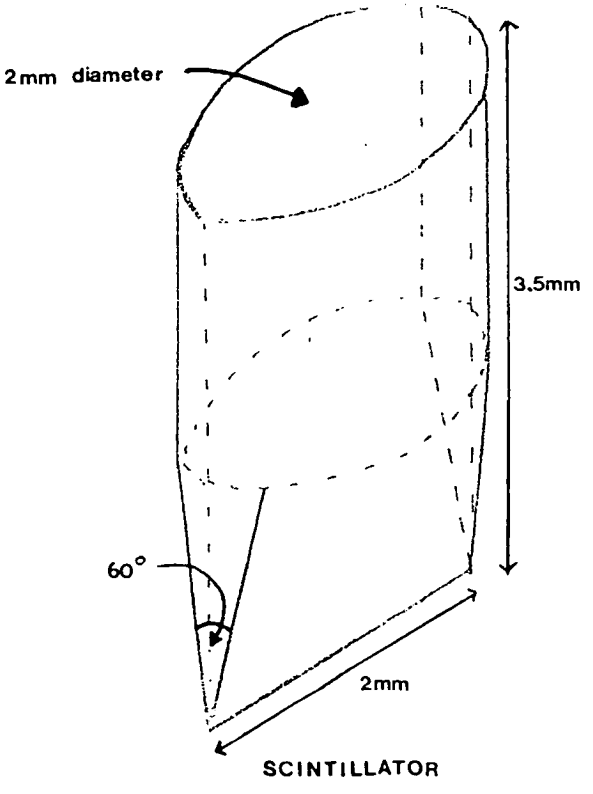


Fig. 7.6 Sketch of Optical System.

external logic signal, e.g. for time of flight experiments or may be triggered by a prior event from another experimental parameter. This facility will allow photon/scattered particle coincidence experiments to be performed.

(c) The event $\langle MN \rangle$ is also decoded to determine the angular location 'i' of the signal, this position then being encoded as a parallel 6 bit address.

(d) The arrivel time, 8 bits, scattered angle, 6 bits, and 2 further bits coding other experimental information are then output to a further device - at present rather slowly to a mini computer but, in due course, more rapidly to a purpose built buffer store.

(e) During the operations (b) - (d) a 'busy' signal is generated. Any coincidence events arriving in this period are counted separately in an overflow channel but are not further processed. Events arriving during the event detection period, (a), are not recorded in any way. The data rate in any experiment must be adjusted so that the overflow count is zero or very small.

### 7.2.4 Data Collection

A DEC Minc computer is used to collect and store the data. A preliminary program has been written in FORTRAN and ASSEMBLER which decodes the angular position information and stores the intensity of counts from each angle in a file. It is also possible to display the data on the terminal screen in the form of a histogram. The software can cope with a count rate equivalent

to a random arrival rate of $10^4$ Hz. This has still to be optimised.

## 7.3 Estimation of Performance

### 7.3.1 Detection Sensitivity

The probability of registering an event by R fold coincidence coding, $P_R$, is

$$P_R = P_c\, t\, \left[1 - (1 - r)^{\ell\gamma P/2}\right]^R \qquad (7.2)$$

where $P_c$ = probability of producing an ion from each incident neutral atom.

$t$ = transmission probability for an ion to the $A\ell_2O_3$ surface.

$\ell$ = transmission probability for an electron from the $A\ell_2O_3$ surface to the scintillator.

$P$ = number of photons produced in the scintillator by each incident electron.

$\gamma$ = number of secondary electrons produced per incident ion, and

$r$ = photomultiplier efficiency × fibre transmission × optical collection efficiency from the scintillator into the fibre.

Estimates of the parameters made to determine the expected performance are given in Table 7.1. The resulting performance curves are shown in Fig. 7.7 as a function of $\gamma P$ (which will vary approximately linearly with accelerating voltage. The anticipated working region is also indicated.

TABLE 7.1

Estimates of Performance Parameters (Equation 7.2)

| Parameter | Value | Comment |
|---|---|---|
| $P_c$ | 0.9 | from previous experience with single channel device |
| t | 0.95 | from trajectory calculation (Section 7.2.1) |
| $\ell$ | 0.95 | from trajectory calculations |
| P | 100-400 | from scintillator specifications |
| $\gamma$ | 5-10 | |
| r | 0.01 | photomultiplier efficiency (0.2) × fibre transmission (0.5) × optical collection efficiency from scintillator (0.1) |

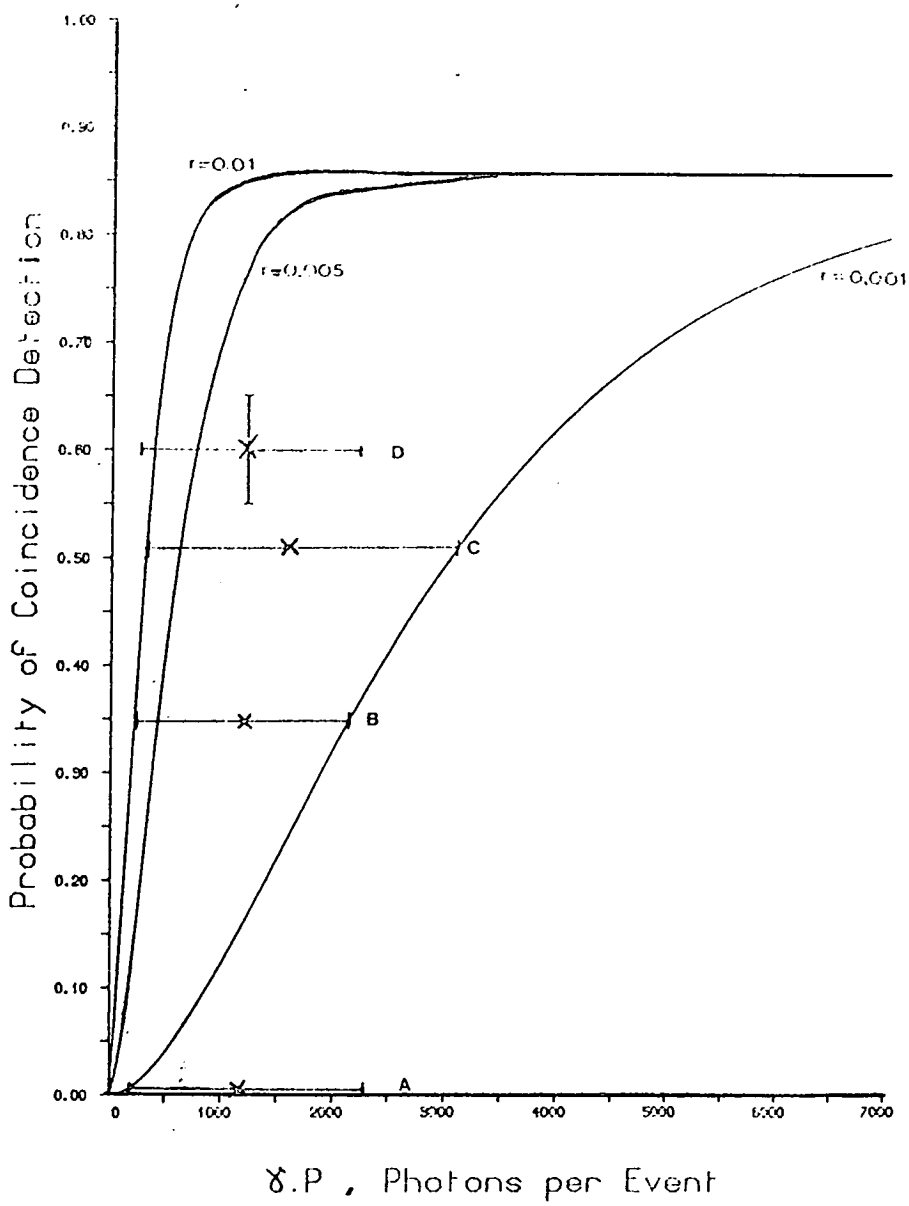


Fig. 7.7: Performance Curves.

A: Plane scintillator home made fibres, no focussing, 50kV

B: Individual non-aluminised scintillators, commercial fibres, 50 kV.

C: Individual non-aluminised scintillators, commercial fibres, 60 kV.

D: Aluminised scintillators, commercial fibres, 50 kV.

### 7.3.2 Noise

The random background noise due to dark current fluctuations in the photomultipliers will be

$$\text{Noise} \simeq N^2 \tau \qquad (7.3)$$

where $\tau$ is the coincidence gate width and $N$ is the dark count rate (at the operational discriminator setting). Since $\tau \simeq 10^{-8}$s and $N \simeq 10 - 100$ the noise contribution from this source, even at the single photon discriminator level, will be quite negligible.

A more important noise source will arise from stray ions originating from thermal or photo-ionisation processes near the detector surface. Experience with the single channel detector has shown that this is a strong function of the background pressure and cleanliness of the system. It can also be minimised by using tight focussing conditions to eliminate noise sources which are not very close to the surface ionising strip.

It is estimated that a noise rate of about 0.01 - 1 Hz may arise in this way.

### 7.3.3 Data Rate

The maximum data rate will be determined by the coincidence resolution time $\tau$ ($\sim$ 10 ns) and the dead time in the decoding interface, following receipt of a coincidence signal, $\tau_I$ ( 40 ns). The maximum rate will be:

$$S_{max} \quad 0.05 \ (\tau + \tau_I)^{-1} \text{ Hz.} \qquad (7.4)$$

In practice the average rate of collection will be determined by the service time of the computer connected to the coincidence interface. This will set a much lower average arrival rate as indicated in Section 7.2.4.

### 7.3.4 Resolution

The angular resolution of the system is inherently limited by the spacing of the scintillator elements. There are 45 elements, 2 mm wide, spread over a 250 mm length. This leads to an angular resolution in the molecular beam apparatus of $\sim 0.1^{\circ}$. The vast majority of secondary electrons produced at the $A\ell_2O_3$ surface have very small initial energies (max. $\sim$ 2 eV) and are given off almost entirely normal to the surface. Taking the worst case of electrons with 2 eV energy given off parallel to the surface, with an accelerating voltage of 50 kV, the deflection of the electrons at the scintillator will be $\sim$ 3 mm. Only electrons given off parallel to the line of scintillators will affect the angular resolution and this will be such a small number as to be negligible. This effect will, however, be increasingly important as the accelerating voltage is decreased, e.g. at 30 kV the deflection will be slightly greater than 4 mm and electrons produced at a position corresponding to one angular element on the $A\ell_2O_3$ surface can produce fluorescence in the neighbouring element.

Inhomogeneities in the electric field could also produce deviations in the electron path as could magnetic fields. It has been estimated that the earth's magnetic field will cause a deviation of 2 mm eastward (i.e. along the scintillator axis)

at 50 kV accelerating voltage. This can be accounted for by fitting Helmholtz coils or by taking the effect into account when assigning angles of deflection to the different scintillator elements since all the electrons will be affected equally.

The time resolution required depends upon the collision energy. We are interested in collisions in the range 10 - 1000 eV and energy losses in the range 0 - 20 eV are likely to be important. The internal energy spread in the beam is $\sim$ 0.15 eV and if this is to be resolved we require, say, 5 points in this energy range. The time resolution required then runs from $2 \times 10^{-7}$s at 10 eV collision energy to $0.3 \times 10^{-9}$s at 1000 eV collision energy. These requirements are shown in Fig. 7.8 along with the possible range of time resolution achievable.

## 7.4 Performance

The main requirement for test purposes is a controlled signal source. Two techniques have been employed. In the first, a fast atom source was mounted in a chamber external to the detector, a collimated beam from this source could then be swept over the detection surface by rotating the source. This method was somewhat inconvenient to use so that for many purposes it was possible to use a hot wire source (W doped with KCℓ) in place of the normal warm W surface. This provided a more easily controllable signal but could not test the critical surface ionisation efficiency for neutral atoms - although this was reasonably well understood from experience with single channel detectors. Some problems were

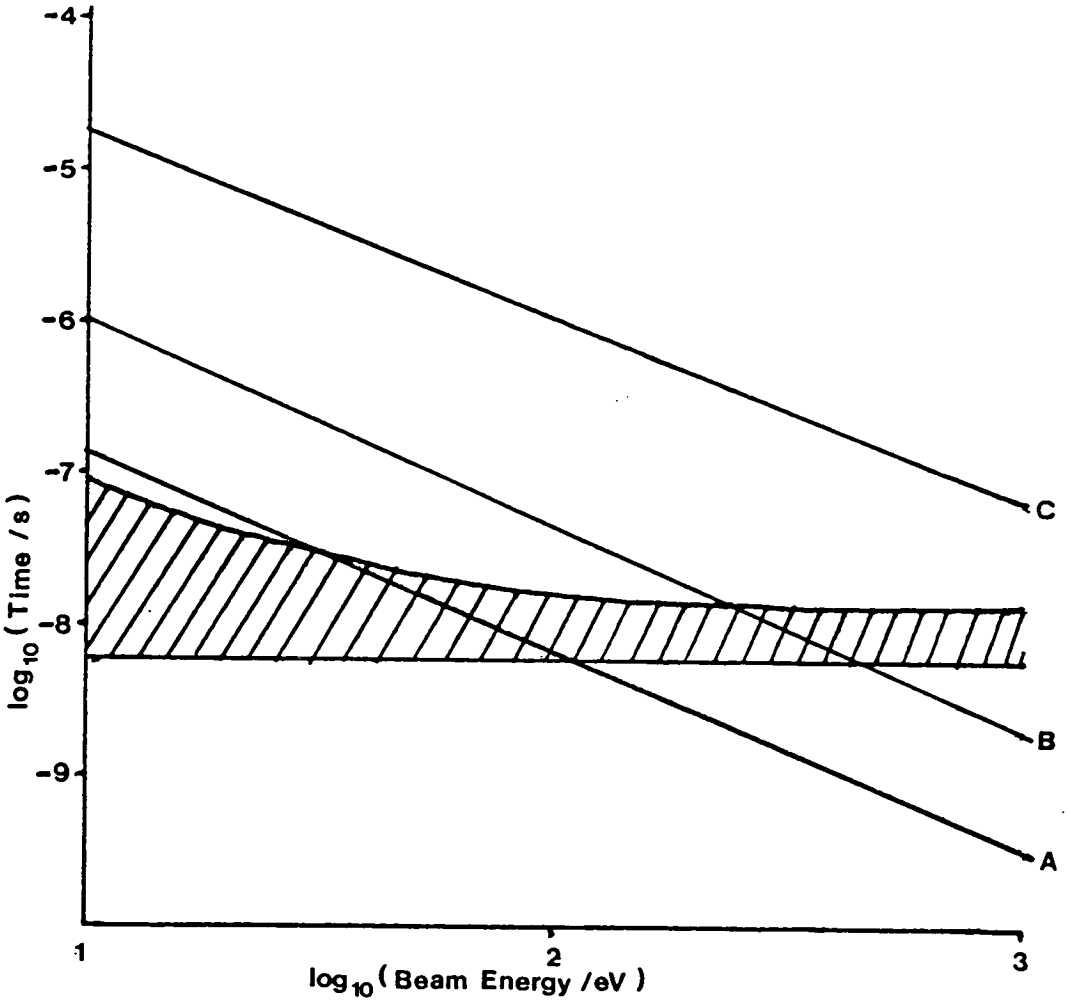


Fig. 7.8: Time Resolution.

A: Ideal time resolution required.

B: Time equivalent to spread in beam energy.

C: Time equivalent to energy loss of interest (2eV).

Shaded area is probable range of time resolution obtainable.

specifically related to the hot wire however, since its position changed in heating and discharges between the high voltage plates in the Pierce gun could sometimes be initiated by the thermal emission. In the course of these tests it was found necessary to rebuild the ion gun at four times the previous scale (without changing the electrostatic properties) to prevent electrical breakdown.

It was also necessary to replace the home-made fibre connectors by commercial items and to replace the flat scintillator sheet by a 'chisel point' design to improve the optical efficiency. The flat scintillator was, however, useful in examining the electrostatic focussing since the final image could be seen by the naked eye.

### 7.4.1 Electrostatics

The observed optimum values obtained for the focussing voltages (gun and electron) by maximising the coincidence count rate at an angle element are shown in Fig. 7.9. It can be seen that the expected linear relationships are obtained for the focussing voltages although, as already mentioned, the filament heating current causes the gun focus to change. This is illustrated in Fig. 7.10. This change is very probably due to mechanical changes in the position of the hot wire in the gun assembly.

The sharpness of the focus obtained with the lenses is shown in Figs. 7.11 and 7.12 for the gun focus and electron focus elements respectively. The trajectory calculations predicted that the gun focus voltage should be $\sim$ 26.5% of the operating voltage. Experimentally the value was found to be $\sim$ 16%. However, as the filament

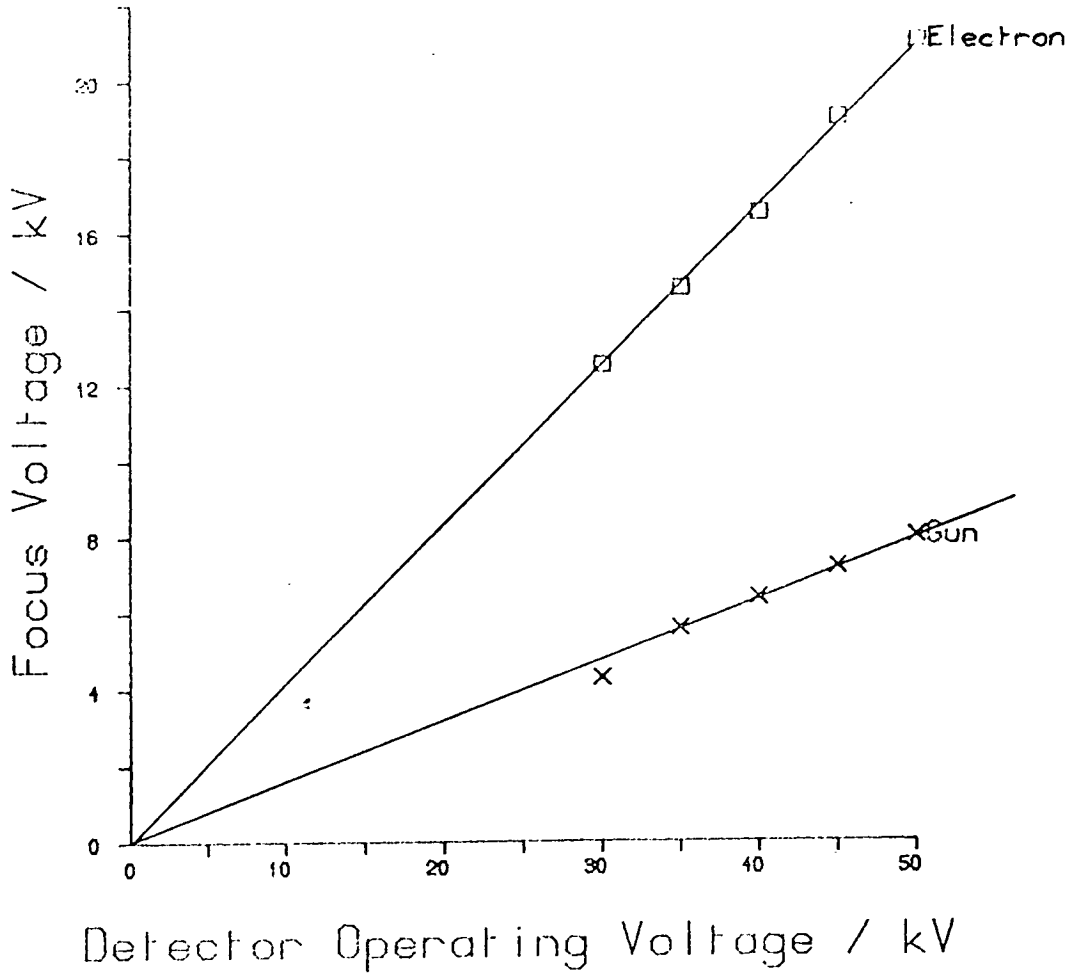


Fig. 7.9: Optimum Values for Gun and Electron Focus.

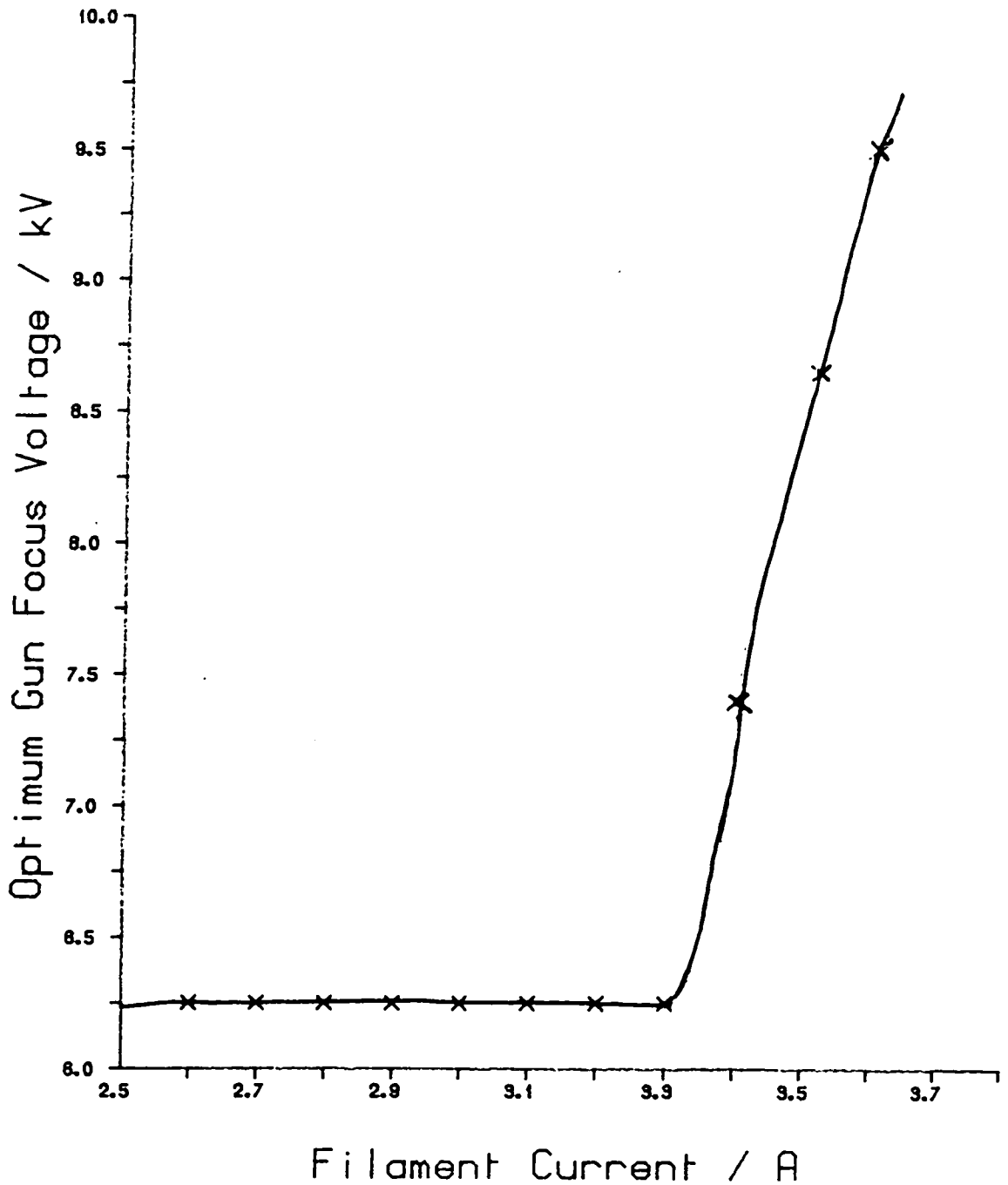


Fig. 7.10: Effect of Filament Current on Optimum Gun Focus Voltage.

Detector operating voltage = 50 kV.

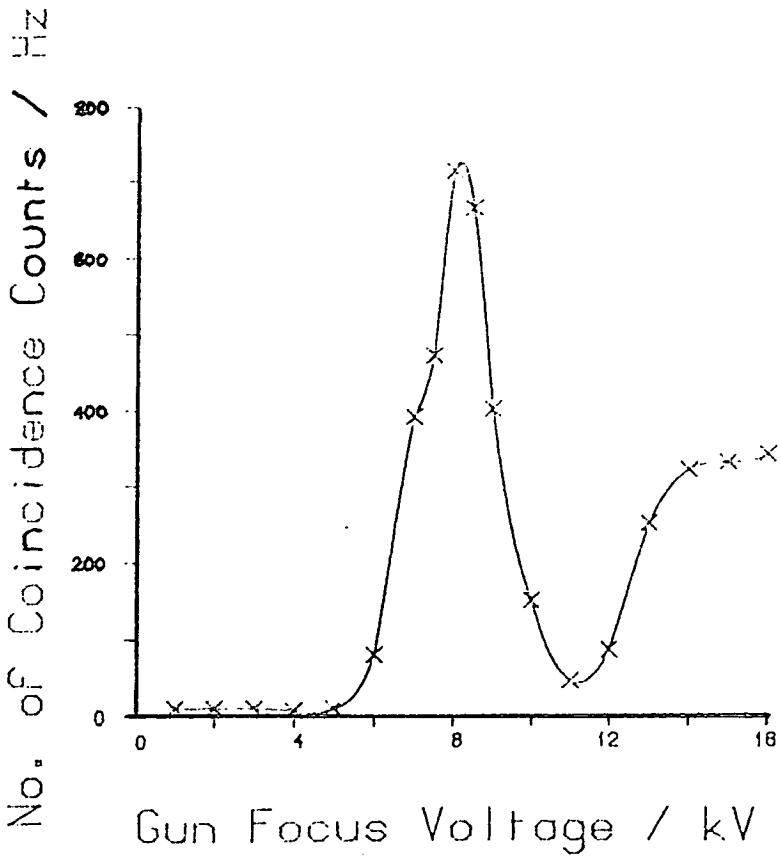


Fig. 7.11: Coincidence Counts vs. Gun Focus Voltage.

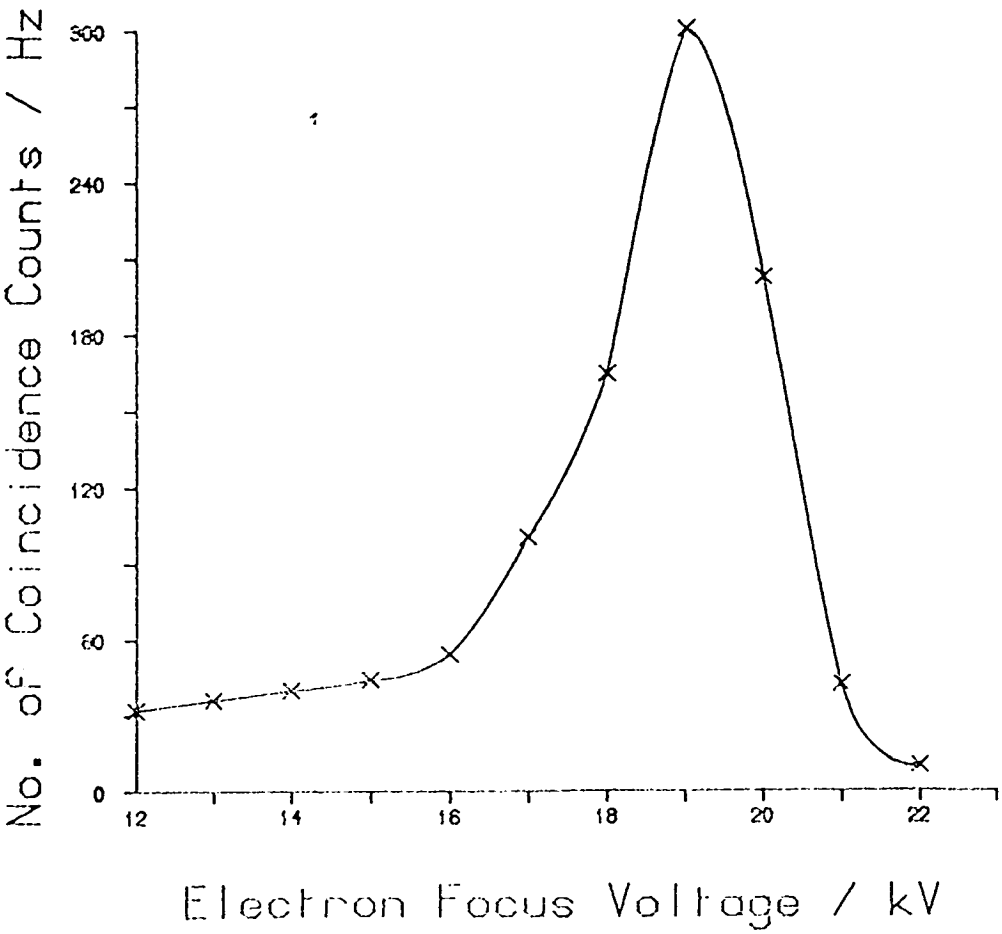


Fig. 7.12: Coincidence Counts vs. Electron Focus Voltage.

wire distorted (approaching closer to the position used in the trajectory calculations?) the gun focus voltage was found to approach the calculated value (Fig. 7.10). An estimate of the electron focus voltage required to produce a magnification of 0.4 at the scintillators was obtained from the tables of Harting and Read (HAR 76). For plates of slightly different thickness and spacing the required voltage was found to be 63% of the operating voltage. The experimentally obtained optimum of $\sim$ 42% is thus seen to have the right order of magnitude.

The electron steering voltage shown in Fig. 7.13 had the expected behaviour. As required, the count rate was not too sharply focussed in the scintillator elements so that small variations in dimension between different angles should not strongly affect the sensitivity.

### 7.4.2 Angular Resolution

The behaviour of the trajectories in the plane orthogonal to the focussing plane, i.e. the angular plane, was checked by inserting a mask immediately in front of the ion injection gun. This mask contained 2 mm wide slits as shown in Fig. 7.14. The coincidence count rates transmitted through the mask are also shown on this figure as a function of angle channel number. These measurements were taken with the plane scintillator sheet with the optical fibres spaced 4 mm apart. As can be seen, the image is reasonably sharp with 10% cross talk between adjacent angles. The measurement has not been repeated with the individual scintillator elements but this arrangement is expected to offer superior angular resolution.

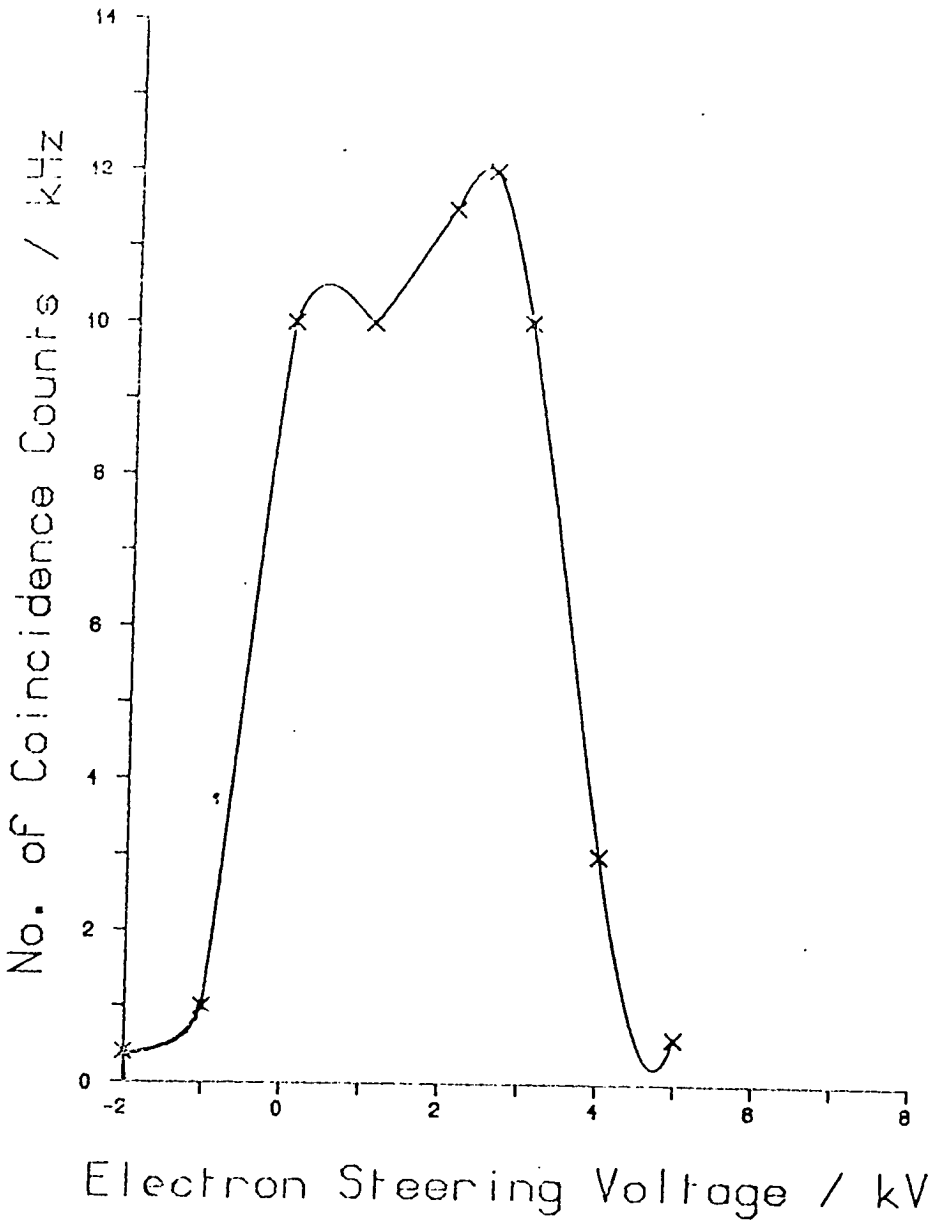


Fig. 7.13: Coincidence Counts vs. Electron Steering Voltage.

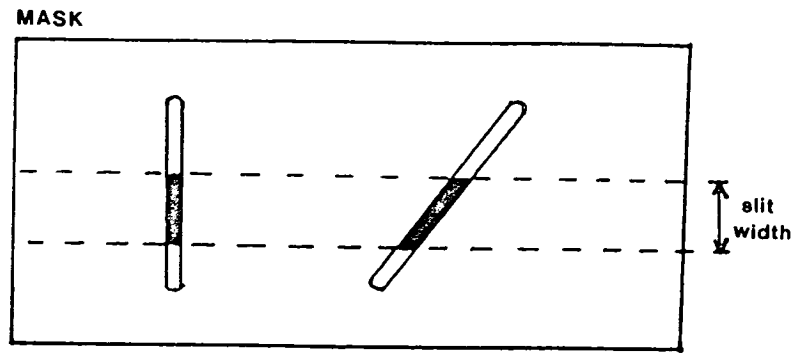


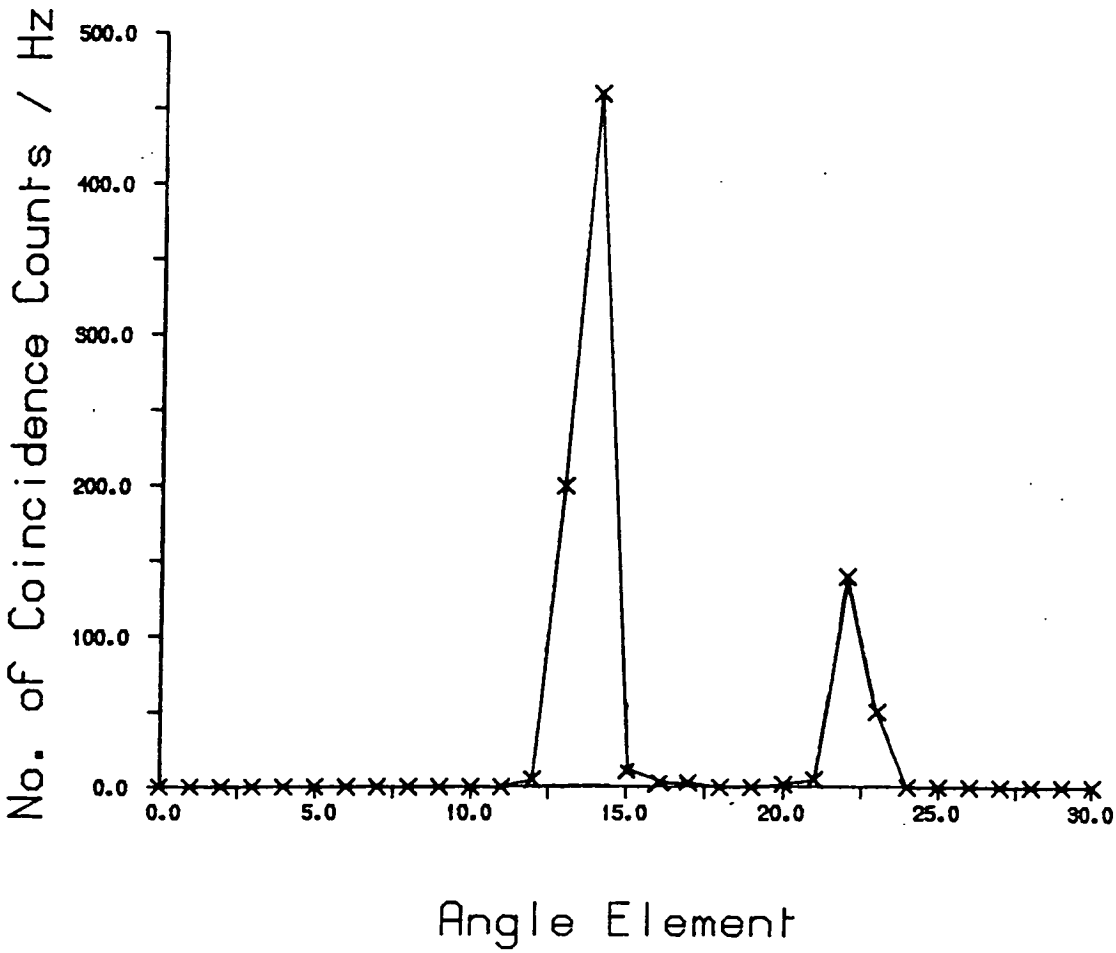


Fig. 7.14: Angular Resolution.

Distance between angle elements and mask dimensions are actual size.

All these measurements could be qualitatively checked by increasing the test signal flux and using the human eye to view the scintillator screen. The focussing and steering elements could all be seen to function as expected. It also appeared that much of the loss of resolution observed in the mask measurements arose in the scintillator itself via multiple reflections. This problem is eliminated in the design now in use.

### 7.4.3 Electron Multiplications

Measurements of the secondary electron gain arising from ion impact on the $A\ell_2O_3$ surface were made by measuring the emitted ion current on a suitably biased gun focus plate. The plate was then biased for normal operation and the electron current measured on a plate inserted in the electron focussing stack. Measurements on several occasions gave results similar to those shown in Figure 7.15. A useful gain is achieved. These measurements also include the transmission efficiency from the gun to the secondary electron plate.

### 7.4.4 Sensitivity

The sensitivity of this device can be checked in two ways - by observing the detection efficiency for fast atoms and comparing the coincidence signal with current measurements on a simple "warm wire" detector. This is the most direct method but depends upon knowledge of the geometric factors between the two detectors.

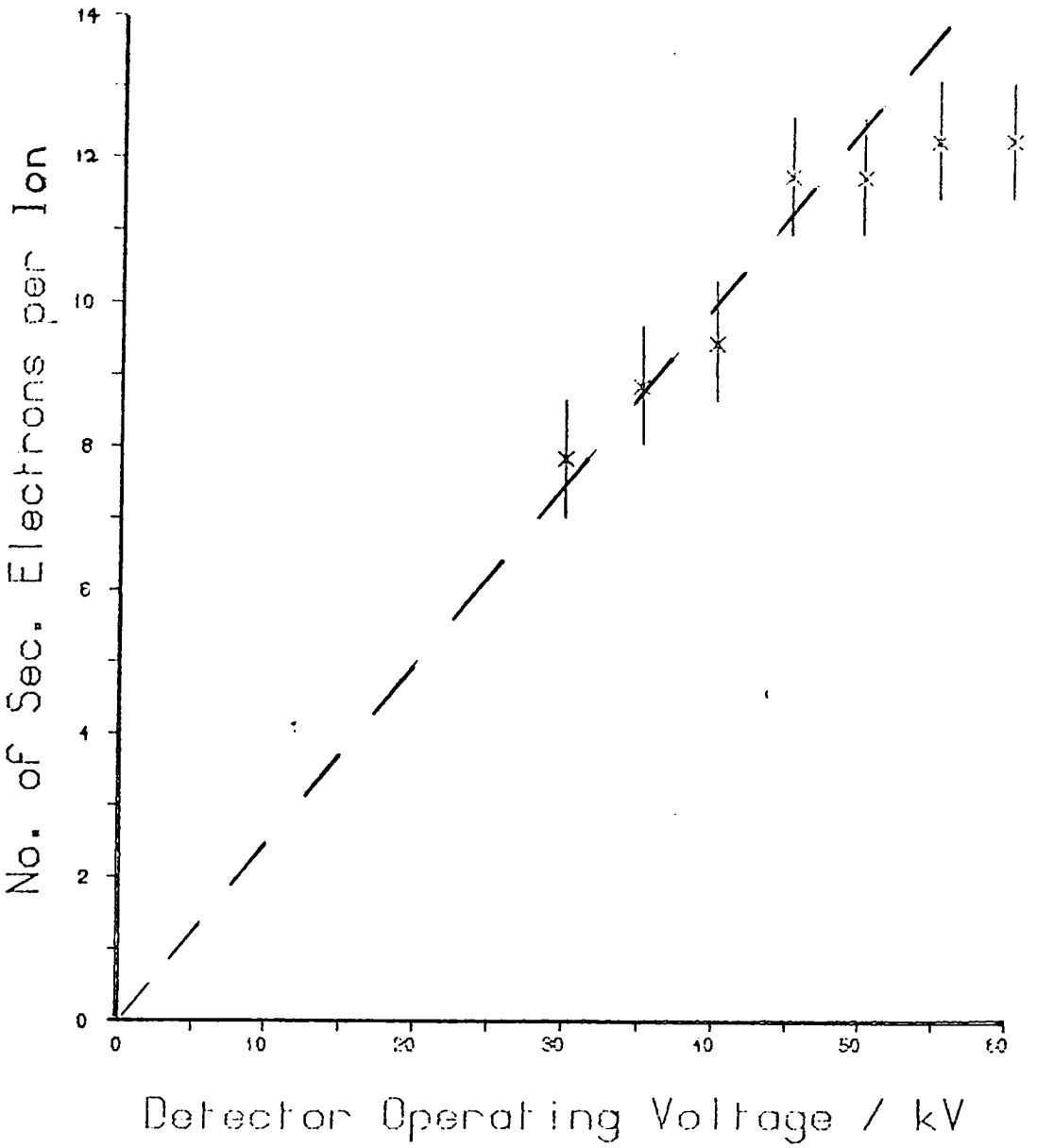


Fig. 7.15: No. of Secondary Electrons obtained per Incident Ion as a function of Device Operating Voltage.

Alternatively, emission from a hot wire in the multi-angle detector itself can be used. In this method the overall efficiency has to be obtained from the ratio of single channel to coincidence counts at a specific angle element, $P_2/P_1$, (R%).

From equation (7.2):

$$P_2/P_1 = \frac{P_c t(1 - (1 - r)^{\ell\gamma P/2})^2}{P_c t(1 - (1 - r)^{\ell\gamma P/2})} \qquad (7.5)$$

$$= \frac{r\ell\gamma P}{2} = \sqrt{\frac{P_2}{P_c t}} \quad .$$

Early measurements at 50 kV, using the fast atom test source and plane scintillator, found $P_2 \simeq 0.02\%$. Measurements with the same arrangement using the $P_2/P_1$ ratio technique found $P_2/P_1 \sim 2\%$. Hence from eq. (7.5) $P_2 = P_c t(P_2/P_1)^2$ and since $P_c t = 0.9 \times 0.95$ (Table (7.1)), this measurement gave $P_2 = 0.03\%$, in good agreement.

The introduction of a focussing lens in the electron field and a perspex light guide shaped so as to increase the optical collection into the fibre gave $P_2/P_1 = 8\%$ or $P_2 = 0.5\%$ at 50 kV - a 25 fold increase in sensitivity.

Further improvements in light collection efficiency by using the individual scintillator elements and new optical fibres yielded $P_2/P_1 = 84\%$ or $P_2 = 60\%$ at 50 kV. This current level of performance has not yet been confirmed by use of the test fast atom source. The various stages in the improvement of the detection efficiency are plotted on Fig. 7.7.

The current performance is illustrated as a function of operating

voltage in Fig. 7.16. As can be seen, the probability of detecting coincidences, $P_2$, is approximately linear with operating voltage. From Fig. 7.7 it is estimated that an increase in the operating voltage to 75 or 80 keV will bring the system onto the desirable plateau region.

The efficiency of various scintillator elements using the same fibres and photomultipliers is compared in Fig. 7.17. The standard deviation of the measurements at the different operating voltages is given on the figure. The difference in scintillator element performance will become less significant as the operating voltage is increased (Fig. 7.7). Interchanging fibres showed a similar stability in behaviour. However, interchange of photomultipliers caused large variations in sensitivity. Nine fibres are connected to the surface of each photomultiplier and it was discovered that the sensitivity of these positions varied considerably. Figure 7.18 plots the mean and standard deviation of the counts from the different surface positions for each photomultiplier. This was improved somewhat by making new connector blocks which had the fibres as close together as physically possible; this data is also shown on the figure. Some modifications in the photomultiplier dynode chains and associated structures may be required to further improve the performance.

### 7.4.5 Long Term Stability

The number of counts detected for a range of angular elements varies considerably and is due to three main factors:

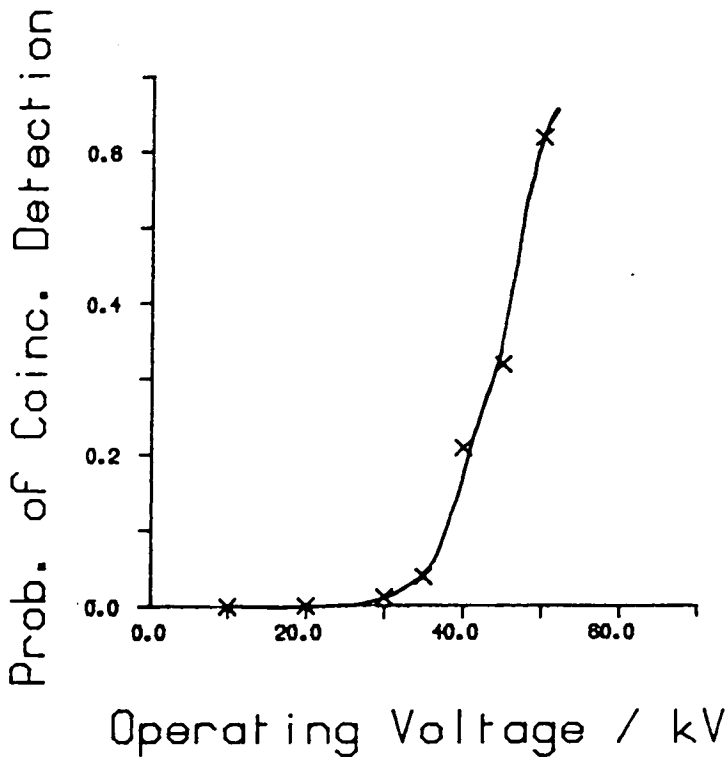


Fig. 7.16: $P_2$ vs. Operating Voltage for One Scintillator Element.

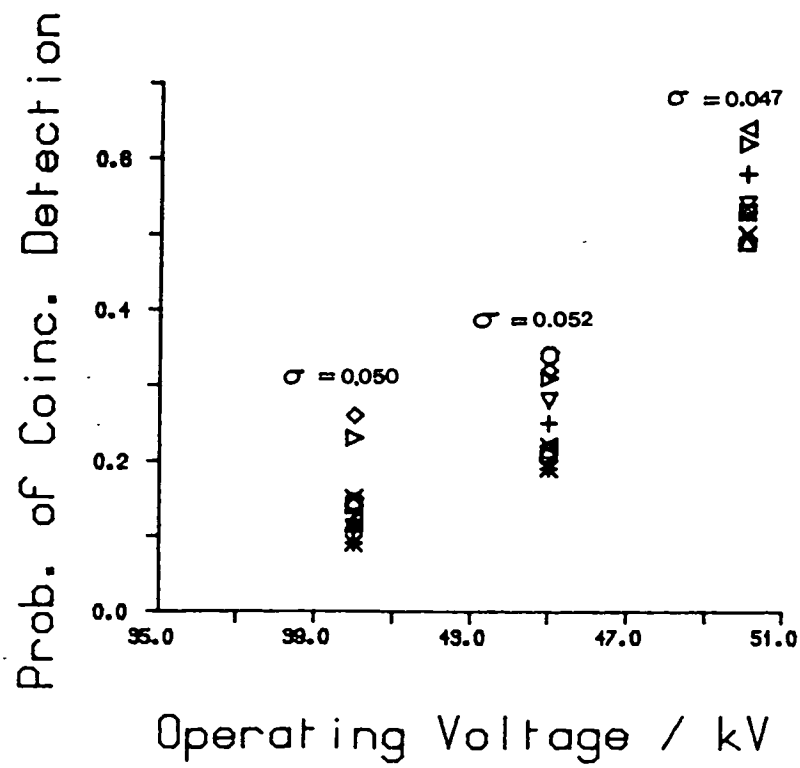


Fig. 7.17: $P_2$ vs. Operating Voltage for Ten Scintillator Elements.
Standard deviation is indicated at each voltage.

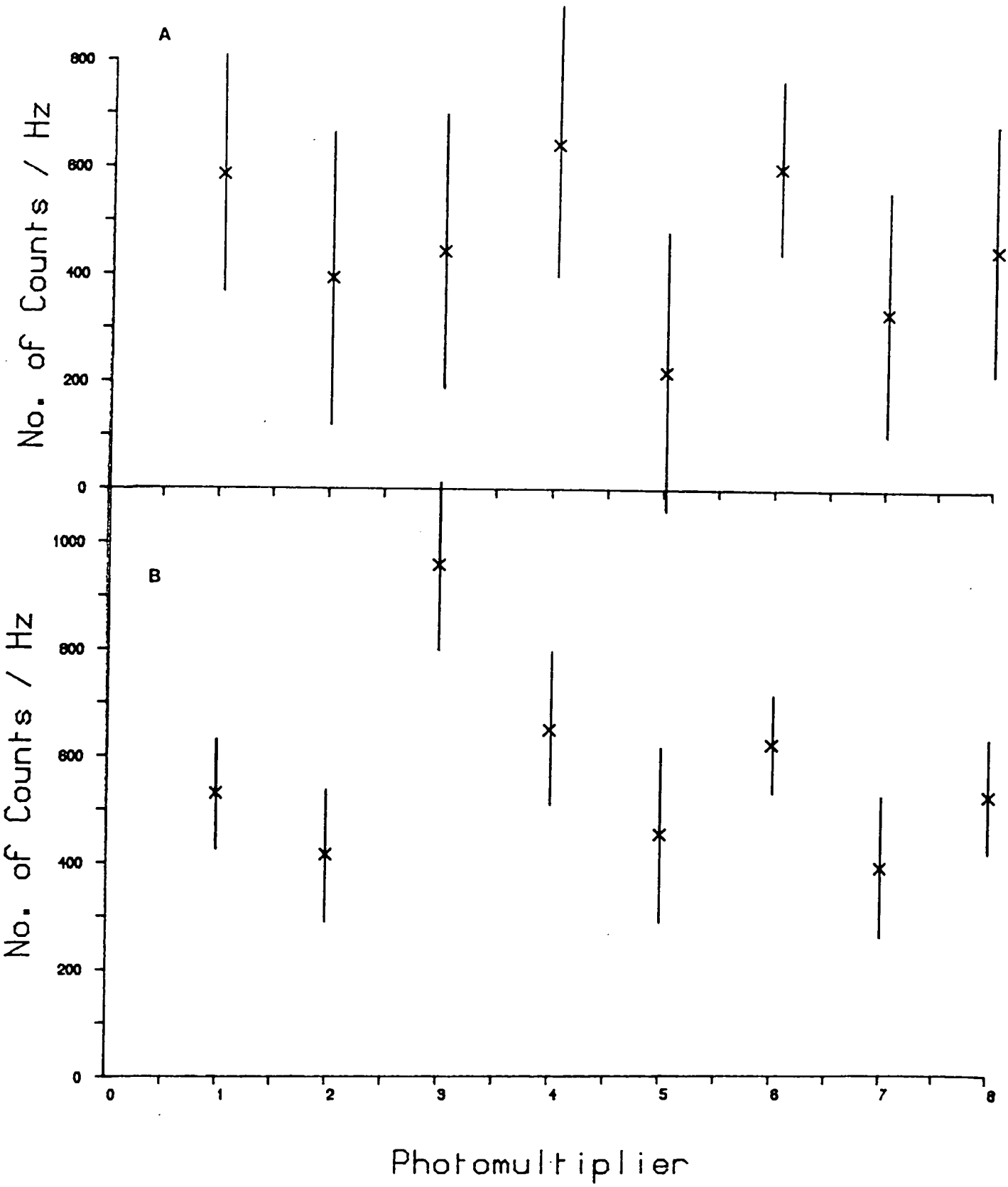


Fig. 7.18: Surface Sensitivity of Photomultipliers.

Number of counts averaged over surface positions for each photomultiplier. A: Old fibre connectors
B: New fibre connectors.
Error bars are 2 standard deviations long.

a) fluctuations in signal from the hot wire source;

b) slight misalignments of some elements;

c) surface sensitivity of photomultipliers.

The means and standard deviations of the counts collected by the computer for all 41 working angles collected over 3 days for a particular operating voltage are shown in Fig. 7.19. To account for factor (a), the data was normalised to give the same total scattering count for each block of data. The time variation of counts from a particular angle element can be shown in a correlogram where the autocorrelation coefficient for observations a distance $k$ apart, $r_k$ is plotted against $k$ (CHA 75).

$$r_k = \frac{\sum_{t=1}^{N-k} (x_t - \bar{x})(x_{t+k} - \bar{x})}{\sum_{t=1}^{N} (x_t - \bar{x})^2} \qquad (7.6)$$

where $N$ is the total number of observations and $\bar{x}$ is the overall mean. This is plotted in 7.20 for some of the angles at two values of the operating voltage. As can be seen, the correlation is improved at the higher operating voltage.

The time variation will mainly be due to factor (b) where any slight fluctuations in focussing and steering voltages will badly affect the performance. Any misalignments in scintillator elements will become less important as the operating voltage is increased and the system becomes less sensitive to such fluctuations. The improvement in the correlation at the higher operating voltage will be due to this.

Factor (c), surface sensitivity of the photomultipliers should not greatly affect the time correlation and can be accounted for by using normalisation.

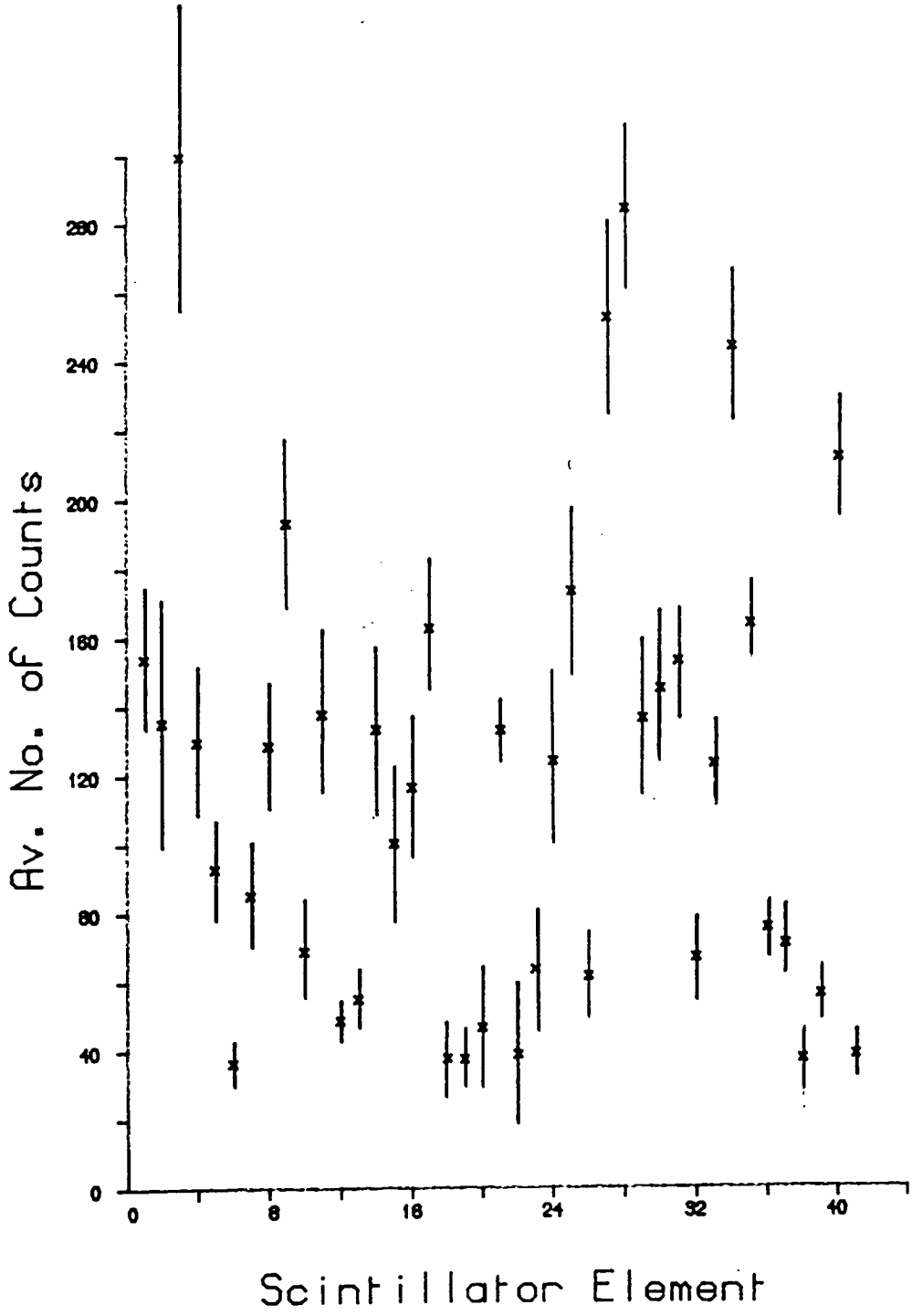


Fig. 7.19: Average number of counts collected per block of data for each element.

Counts collected over 3 days with an operating voltage of 40 kV.
Error bars are 2 standard deviations long.

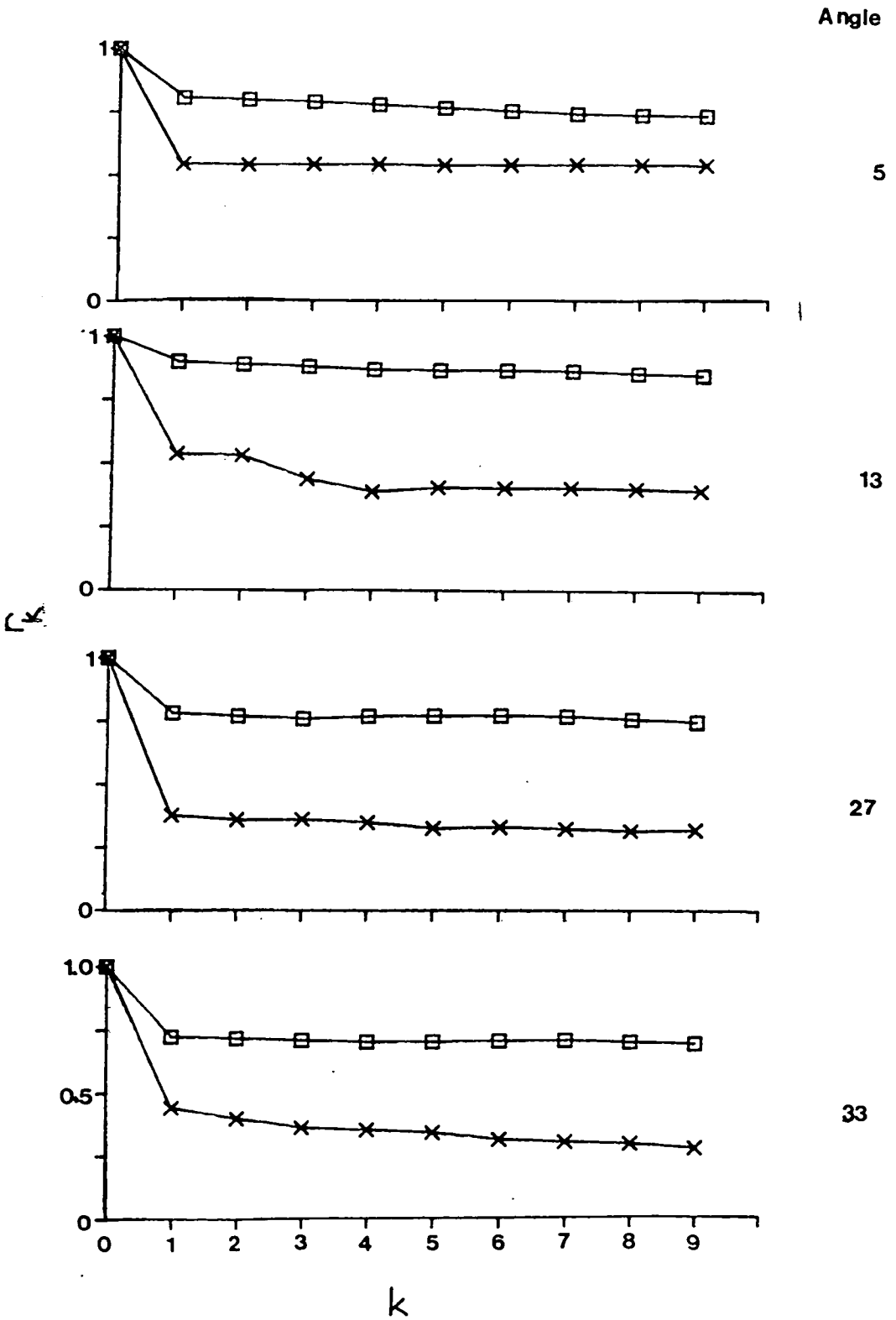


Fig. 7.20: Correlograms for Sample Angle Elements.

□ : 55 kV Op Voltage

× : 40 kV "

## 7.5 Conclusion

A fast multi angle detector providing 45 angle channels distributed over a 250 mm length with a resolution of 2 mm and a response time of 10 ns has been constructed.

41 of the 45 angle channels have been fully implemented and tested. The overall sensitivity is currently 60%. It is anticipated that by operating at higher voltages the sensitivity could be increased to 80 - 85%.

The angular resolution ($\sim 0.1^{o}$), sensitivity (60%) and focussing conditions are shown to accord quite closely with design calculations.

Variation in performance of the different scintillator elements and time correlation are shown to be satisfactory.

Some work remains to be done.

(a) Additional electronic interface cards must be constructed (to a tested design). This is under way.

(b) The photomultiplier dynode chain circuits must be mechanically improved and a number of defective photomultiplier tubes replaced.

(c) To achieve the full data rate a buffer memory unit must be constructed.

(d) Obtain a steady working voltage of $\sim$80 kV (power supply and 100 kV feedthrough is now available).

(e) Time resolution must be tested.

## REFERENCES


AND 75 R.W. Anderson & D.R. Herschbach, J. Chem. Phys., 62, 2666 (1975).

ARC 83 P. Archirel & P. Habitz, Chem. Phys., 78, 213 (1983).

ATE 77 J.A. Aten & J. Los, Chem. Phys., 25, 47 (1977).

BAC 32 R.F. Bacher & S. Goudsmit, "Atomic Energy States", (McGraw-Hill, 1932).

BAE 69 A.P.M. Baede, A.M.C. Moutinho, A.E. de Vries & J. Los, Chem. Phys. Letters, 3, 530 (1969).

BAI 81 M.A. Baig, J.P. Connerade, J. Dagata & S.P. McGlynn, J. Phys. B., 14, 225 (1981).

BAL 73 G.G. Balint-Kurti, Mol. Phys., 25, 393 (1973).

BAR 72 M. Barat & W. Lichten, Phys. Rev., 6, 211 (1972).

BAR 76 J.R. Barker, Chem. Phys., 18, 175 (1976).

BAU 69 E. Bauer, E.R. Fisher & F.R. Gilmore, J. Chem. Phys., 51, 4173 (1969).

BEU 69 R.J. Beuhler & R.B. Bernstein, J. Chem. Phys., 51, 5305 (1969).

BIR 71 D.T. Birtwistle & A. Herzenberg, J. Phys. B., 4, 53 (1971).

BJE 67 A. Bjerre & E.E. Nikitin, Chem. Phys. Letters, 1, 179 (1967).

BLA 80 K.H. Blattmann, B. Menner, W. Schäuble, B. Staudenmayer, L. Zehnle & V. Kempter, J. Phys. B., 13, 3635 (1980).

BLA 81 G.W. Black, Ph.D. Thesis, Edinburgh (1981).

BOS 72 R.A. Boschi & D.R. Salahub, Mol. Phys.,24, 289 (1972).

BOS 74 R.A. Boschi & D.R. Salahub, Can. J. Chem., 52, 1217 (1974).

BOT 75 C. Bottcher, Chem. Phys. Letters, 35, 367 (1975).

BOT 77 C. Bottcher & C.V. Sukumar, J. Phys. B., 14, 2853 (1977).

BRE 82 W.H. Breckenridge & H. Umemoto, Adv. Chem. Phys., 50, 325 (1982).

BRO 66 P.R. Brooks & E.M. Jones, J. Chem. Phys., 45, 3449 (1966).

BRU 73 P. Brumer & M. Karplus, J. Chem. Phys., 58, 3903 (1973).

BRU 84 B.G. Brunetti, M.A.D. Fluendy & R.E. Ryall, Mol. Phys., 53, 1029 (1984).

REFERENCES (Contd.)


BUC 75 U. Buck, Adv. Chem. Phys., 30, 313 (1975).

CHA 75 C. Chatfield, "The Analysis of Time Series", (Chapman & Hall, 1975).

CHI 79 M.S. Child, in "Atom Molecule Collision Theory", ed. R.B. Bernstein, (Plenum Press, New York, 1979).

CLE 75 R.D. Clear, S.J. Riley & K.R. Wilson, J. Chem. Phys., 63 1340 (1975).

DAG 81 J.A. Dagata, G.L. Findley, S.P. McGlynn, J.P. Connerade & M.A. Baig, Phys. Rev. A, 24, 2485 (1981).

DAL 60 N.R. Daly, Rev. Sci. Inst., 31, 264 (1960).

DUC 71 B.S. Duchart, Ph.D. Thesis, Edinburgh (1971).

EVE 77 C. Evers, Chem. Phys., 21, 355 (1977).

FIS 72 E.R. Fisher & G.K. Smith, Chem. Phys. Letters, 13, 448 (1972).

FLU 73 M.A.D. Fluendy & K.P. Lawley, "Chemical Applications of Molecular Beam Scattering", (Chapman & Hall, 1973).

FLU 75 M.A.D. Fluendy, J.H. Kerr, J.M. McCall & D. Munro, in "On-line Computing in the Laboratory", eds. A. Rosner, B.K. Penney & P.N. Clout, (Advance, London, 1975).

FLU 79 M.A.D. Fluendy, K.P. Lawley, J. McCall, C. Sholeen & D. Sutton, Faraday Discuss. Chem. Soc., 67, 41 (1979).

FLU 81 M.A.D. Fluendy, K.P. Lawley, C. Sholeen & D. Sutton, Mol. Phys., 42, 1 (1981).

FLU 83 M.A.D. Fluendy & S.L. Lunt, Mol. Phys., 49, 1007 (1983).

GER 73 E. Gersing, H. Pauly, E. Schadlich & M. Vonderschen, Faraday Discuss. Chem. Soc., 55, 211 (1973).

GIL 65 F.R. Gilmore, J. Quant. Spec. Rad. Transfer, 5, 369 (1965).

GIS 79 E.A. Gislason, in "Alkali Halide Vapours", eds. P. Davidovits & D.L. McFadden, (Academic Press, New York, 1979).

GIS 81 E.A. Gislason, A.W. Kleyn & J. Los., Chem. Phys. 59, 91 (1981).

GRI 75 R. Grice, Adv. Chem. Phys., 30, 247 (1975).

HAB 80 P. Habitz, Chem. Phys., 54, 131 (1980).

REFERENCES (Contd.)

HAL 84 T. Hall, B. Menner, W. Wehrle & V. Kempter, in "Electronic & Atomic Collisions", eds. J. Eichler, I.V. Hertel & N.S. Stolterfoht, ICPEAC XIII, (North-Holland, 1984).

HAR 76 E. Harting & F.H. Read, "Electrostatic Lenses", (Amsterdam, 1976).

HER 61 D.R. Herschbach, G.H. Kwei & J.A. Norris, J. Chem. Phys., 34, 1842 (1961).

HER 66a D.R. Herschbach, Adv. Chem. Phys., 10, 319 (1966).

HER 66b G. Herzberg, "Electronic Spectra of Polyatomic Molecules", (van Nostrand - Rheinhold, 1966).

HER 73 D.R. Herschbach, Faraday Discuss. Chem. Soc., 55, 233 (1973).

HER 77 I.V. Hertel, H. Hofmann & K.A. Rost, Chem. Phys. Letters, 47, 163 (1977).

HER 79 R.R. Herm, in "Alkali Halide Vapours", eds. P. Davidovits & D.L. McFadden, (Academic Press, New York, 1979).

HER 81 I.V. Hertel, Adv. Chem. Phys., 45, 341 (1981).

HER 82 I.V. Hertel, Adv. Chem. Phys., 50, 475 (1982).

HIT 78 A.P. Hitchcock & C.E. Brion, J. Elec. Spec. Rel. Phen., 13, 193 (1978).

JAN 70 P.A. Jansson, J. Opt. Soc. Amer., 60, 184 (1970).

JAN 78 R.K. Janev, Phys. Ionis. Gases, 9, 171 (1978).

KEM 73 V. Kempter, B. Kübler, P. LeBreton, J. Lorek & W. Mecklenbrauck, Chem. Phys. Letters, 21, 164 (1973).

KEM 75 V. Kempter, Adv. Chem. Phys., 30, 417 (1975).

KEN 72 G.M. Kendall & R. Grice, Mol. Phys., 24, 1373 (1972).

KER 75 J.H. Kerr, Ph.D. Thesis, Edinburgh (1975).

KIN 72 J.L. Kinsey, "Molecular Beam Reactions", M.T.P. Int. Rev. Sci., Physical Chemistry, Ser. 1, 9 (1972).

KLE 82 A.W. Kleyn, J. Los & E.A. Gislason, Phys. Reports, 90, 1 (1982).

KUY 65 C.E. Kuyatt, J.A. Simpson & S.R. Mielczarek, Phys. Rev. A, 138, 385 (1965).

LAB 73 R.A. La Budde, P.J. Kuntz, R.B. Bernstein & R.D. Levine, J. Chem. Phys., 59, 6286 (1973).

LAC 80 K. Lacmann, Adv. Chem. Phys., 42, 513 (1980).

REFERENCES (Contd.)

LOE 77 H.J. Loesch & M. Brieger, ICPEAC X, Paris, (1977), Book of Abstracts.

LOF 77 A. Loftus & P.H. Krupenie, J. Phys. Chem. Ref. Data, 6, 113 (1977).

LOS 79 J. Los & A.W. Kleyn, in "Alkali Halide Vapours", eds. P. Davidovits & D.L. McFadden, (Academic Press, New York, 1979).

MAG 40 J.L. Magee, J. Chem. Phys., 8, 687 (1940).

MAR 73 G. Marcelin & P.R. Brooks, Faraday Discuss. Chem. Soc., 55, 318 (1973).

MAR 79 P.J. Martin, E. Clemens, I. Zehnle & V. Kempter, Z. f. Physik A, 289, 373 (1979).

MAS 73 H.S.W. Massey & E.H.S. Burhop, "Electronic & Ionic Impact Phenomena", Vol. 3, (Oxford University Press, 1973).

McC 78 J.M. McCall & M.A.D. Fluendy, J. Phys. E, 11, 631 (1978).

MES 82 J.M. Mestdagh, J. Berlande, J. Cuvellier, P. de Pujo & A. Binet, J. Phys. B, 15, 439 (1982).

MIC 81 H.H. Michels, Adv. Chem. Phys., 45, 225 (1981).

MOU 74 A.M.C. Moutinho, J.A. Aten & J. Los, Chem. Phys., 5, 84 (1974).

MOU 84 A.M.C. Moutinho, personal communication.

MUL 57 R.S. Mulliken, 'The Energy Levels of the Nitrogen Molecule', in "Threshold of Space", (Pergamon, New York, 1957).

NIK 70 E.E. Nikitin, Comments At. Mol. Phys., 1, 166 (1970).

NIK 74 E.E. Nikitin, "Theory of Elementary Atomic & Molecular Processes in Gases", (Oxford, 1974).

OMA 71 T.F. O'Malley, Adv. At. Mol. Phy., 7, 223 (1971).

PAU 78 H. Pauly, Naturwissenschaften, 65, 297 (1978).

PAV 72 Z. Pavlovic, M.J.W. Boness, A. Herzenberg & G.J. Schulz, Phys. Rev. A, 6, 676 (1972).

PIE 40 J.R. Pierce, J. App. Phys., 11, 548 (1940).

POL 32 M. Polanyi, "Atomic Reactions", (Williams & Norris, London, 1932).

PRA 83 A.J.F. Praxedes, M.J.P. Maneira & A.M.C. Moutinho, ICPEAC XIII, Berlin, (1983), Book of Abstracts.

REFERENCES (Contd.)

RED 73 J.F. Reddington, Ph.D. Thesis, Edinburgh (1973).

REI 82 W. Reiland, G. Jamieson, U. Tittes & I.V. Hertel, Z. Phys. A, 307, 51 (1982).

RIL 72 S.J. Riley & K.R. Wilson, Faraday Discuss. Chem. Soc., 53, 132 (1972).

RIT 51 E.S. Rittner, J. Chem. Phys., 19, 1030 (1951).

ROS 81 U. Ross, W. Schepper & D. Beck, Chem. Phys., 61, 95 (1981).

SAE 83 V. Saez-Rabanos, E. Verdasco, A. Segura & A. Gonzalez-Urena Mol. Phys., 50, 825 (1983).

SCH 73 G.J. Schulz, Rev. Mod. Phys., 45, 423 (1973).

SHO 76 C.M. Sholeen & R.R. Herm, J. Chem. Phys., 65, 5398 (1976).

SPA 81 M.R. Spalburg, Doctoral Scriptie, Universiteit van Amsterdam (1981).

SUT 80 D. Sutton, Ph.D. Thesis, Edinburgh (1980).

TOP 75 Z.H. Top & M. Baer, J. Chem. Phys., 66, 1363 (1975).

TUL 71 J.C. Tully & R.K. Preston, J. Chem. Phys., 55, 562 (1971).

TUL 76 J.C. Tully in "Dynamics of Molecular Collisions, Part B", ed. W.H. Miller (Plenum Press, New York, 1976).

WEN 69 W.E. Wentworth, R. George & H. Keith, J. Chem. Phys., 51, 1781 (1969).

ZEN 32 C. Zener, Proc. Royal Soc. A, 137, 696 (1932).

## ACKNOWLEDGEMENTS

Firstly I wish to record my gratitude to Dr. Malcolm Fluendy for supervising this research and for his encouragement and constant optimism throughout. I thank Jimmy "Professor" McKemmie for his technical assistance and good advice and my fellow "beamers"; Stuart Lunt, Rona Ryall and George Keenan who helped in many ways.

My thanks also to the Science and Engineering Research Council for financial support, the University of Edinburgh for laboratory, computing and workshop facilities and Mrs. Chester for turning my scribbles into legible type.

Finally I would like to thank my husband, Iain, for keeping me sane throughout the period of this research.

## APPENDIX A

## Listing of Model Program for K + $CH_3I$

```
!
! THIS PROGRAM CALCULATES ENERGY LOSSES AND DIFFERENTIAL CROSS SECTIONS
! USING CLASSICAL MECHANICS FOR HIGH ENERGY, GRAZING COLLISIONS BETWEEN
! K ATOMS AND CH3I MOLECULES. THE POTENTIAL SURFACES ARE DIABATIC AND THE
! PROBABILITY OF CROSSING BETWEEN SURFACES IS CALCULATED USING THE LANDAU-
! ZENER FORMULA.
! N.B. ONLY ONE ION-PAIR STATE IS PUT INTO THE PROGRAM.
!
!
%REAL %LONG
%BEGIN
%REAL EPS1,EPS2,EPS3,SIG1,SIG2,SIG3,E12,E13,R12,R23,R13R
%REAL E34,EPS4,SIG4,R34,AL2
%REAL B1,B,RIKE,RELVEL,POL,RCDUM,R13,R133,R13D,R23,R23D,R34,R34D,SIGMA
%REAL MU,MU1,VADD,V0,ROCH,DCH,PI,BETA,KIP,AL,AL1,D,RCH,STRETCH
%REAL DFP1,DFP2,DFP3,DFP4,DFP5,DFP6,DFP7,DFP8,KBETA,CBETA
%REAL GDFP1,GDFP2,GDFP3,GDFP4,GDFP5,GDFP6,GDFP7,GDFP8
%REAL G1DFP1,G1DFP2,G1DFP3,G1DFP4,G1DFP5,G1DFP6,G1DFP7,G1DFP8
%REAL EL1,EL2,EL3,EL4,EL5,EL6,EL7,EL8
%REAL ACCADD,DEMT,TF,T,VCI,DT,ACC,DRCH,P1,P2,SP,MORSO,ROCH1
%REAL EXC,MORSO3,ROCH3,THETA1,THETA2,C5,C1,C2,C3,C4,E133
%REAL VAR,V1,V2,V3,V4
%REAL DION,BETAION
%REAL RKE1,KM,RKTM,RON,DUMV,BARR
%INTEGER TRAJ,FLAGA,ES,FLAG1,FLAG2,FLAG3
%INTEGER FLAGEL,FLAGE2,FLAGE1,FLAGE,IRP1,IRP,PATH,I,CHNO,SCSI
%STRING(63) STRING
%ROUTINESPEC ELOSS(%REALNAME DFP,EL)
%ROUTINESPEC OUTPUT(%REALNAME B,DFP,EL,SIGMA,RCH %INTEGER PATH)
%ROUTINESPEC READFILENAME(%STRINGNAME NAME)
%EXTERNALROUTINESPEC DEFINE(%STRING(63) S)
%EXTERNALROUTINESPEC PROMPT(%STRING(255) S)
%REALFNSPEC TANH(%REAL X)
%REALFNSPEC MTCR(%REALNAME R1,B,R2,RSTART %INTEGER PATH)
%REALFNSPEC MORSION(%REALNAME R)
%REALFNSPEC MORSPOT(%REALNAME R,AL)
%REALFNSPEC MORSPOTA(%REALNAME R,AL)
%REALFNSPEC CROSPT(%REALNAME E,EPS1,SIG1,EPS2,SIG2, %REALFN %C
POT1,POT2, %INTEGER FLAGS)
%REALFNSPEC LANZEN (%REALNAME B, %INTEGER PATH)
%REALFNSPEC IONPOT(%REALNAME R,SIG,EPS)
%REALFNSPEC POWPOT(%REALNAME R,SIG,EPS)
%REALFNSPEC DEFION(%REAL B,R1,R2)
%REALFNSPEC DEFPOW(%REAL EPS,SIG,B,R1,R2)
RKTM=50
PI=3.14159
SP=SQRT(PI)
LIS:
TRAJ=0
EXC=0
ES=0
FLAG2=0
FLAG3=0
FLAGE=0
FLAGE1=0
FLAGE2=0
FLAGA=0
SELECTINPUT(1)
```

```
PROMPT("Output ?:")
READFILENAME(STRING)
%IF STRING="TT" %OR STRING="LOCAL" %THEN STRING=".OUT"
DEFINE("ST10,".STRING)
PROMPT("Eps1:")
READ(EPS1)
PROMPT("Eps2:")  ;!POTENTIAL PARAMETERS, EPS1 AND 2 FOR NEUTRAL POTENTIALS
READ(EPS2)  ;!EPS3 FOR IONIC POTENTIAL, SIMILARLY FOR SIG.
PROMPT("Eps3:")
READ(EPS3)
PROMPT("Sig1:")
READ(SIG1)
PROMPT("Sig2:")
READ(SIG2)
PROMPT("Sig3:")
READ(SIG3)
STRETCH=0
PROMPT ("IONISATION POTENTIAL:")   ;!  FOR ALKALI ATOM
READ (KIP)
PROMPT ("METAL EXCITATION:")
READ (E12)
PROMPT("Ion rep pow:")
READ(IRP)
PROMPT("V12:")
READ(H12)         ;!These are reduced coupling parameters used in
PROMPT("V23:")         ;!the Landau-Zener formula
READ(H23)
PROMPT("Red mass:")         ;! Of K-CH3I
READ(MU)
MU=MU*1.6725@-27
PROMPT("RIKE:")         ;!Collision energy in CM
READ(RIKE)
RELVEL=2*RIKE*1.6021@-19/MU
RELVEL=SQRT(RELVEL)
PRINTSTRING("NOW PARAMETERS RELEVANT TO TARGET MOLECULE POTENTIAL")
NEWLINE
PROMPT("Red mass:")         ;!Of CH3I
READ(MU1)
MU1=MU1*1.6725@-27
PROMPT("R0:")      ;! C-I equilibrium bond length
READ(ROCH)
ROCH3=(ROCH+STRETCH)*1@-10  ;!  USED IF PRESTRETCHING OF BOND IS REQUIRED
ROCH=ROCH*1@-10
ROCH1=ROCH
PROMPT("BETA:")
READ(BETA)
%IF BETA>1@-10 %THEN BETA=BETA*1.6021@-19
PROMPT("D0:")
READ(DCH)
%IF DCH>1@-10 %THEN DCH=DCH*1.6021@-19
PROMPT("DION:")
READ(DION)
%IF DION>1@-10 %THEN DION=DION*1.602@-19
PROMPT("BETAION:")
READ(BETAION)
%IF BETAION<1@5 %THEN BETAION=BETAION*1@10
PROMPT("BARRIER:")         ;! max. height of barrier in CH3I- potential
READ(BARR)
BARR=BARR*1.6021@-19
```

```
PROMPT("K BETA:")   ;!   GROUND ION STATE BARRIER POTENTIAL PARAMETERS
READ(KBETA)
PROMPT("CBETA:")
READ(CBETA)
PROMPT("ROP:")
READ(ROP)
PRINTSTRING("ASSYMPTOTIC LIMITS")
NEWLINE
PROMPT("GLW A.L.:")
READ(AL)
PROMPT("IGH A.L.:")
READ(AL1)
%IF AL1>1E-10 %OR AL1<-1E-10 %THEN AL1=AL1*1.60210-19
PROMPT("POL:")  ;!   POLARIZABILITY TERM
READ(POL)
PROMPT("DO YOU WISH TO CONSIDER THE A STATES ?")
SKIPSYMBOL %UNTIL NEXTSYMBOL='Y' %OR NEXTSYMBOL='N'
READSYMBOL(I)
%IF I='Y' %THEN %START
FLAG4=1
->CL1
%FINISH
PROMPT("NO OF EXCITED STATE:")    ;!i.e. GROUND ION PAIR STATE=0, 1ST EXCITED=1
ETC.
READ (ES)
PROMPT("EXC:")   ;!  EXCITATION ENERGY OF EXCITED ION PAIR STATE
READ(EXC)
EXC=EXC*1.60210-19
%IF EXC>0 %THEN %START
FLAG3=1
CL1: PROMPT("EPS4:")  ;!   PARAMETERS FOR A 3RD NEUTRAL POTENTIAL SURFACE
READ(EPS4)     ;!   e.g.  A STATE OR RYDBERG
PROMPT("SIG4:")
READ(SIG4)
PROMPT("V34:")
READ(H34)
PROMPT("AL2:")
READ(AL2)
%FINISH
PROMPT("TRAJ? :")   ;!  IF YOU WISH TO CALCULATE A TRAJECTORY ON THE GROUND ION
PAIR
READ(TRAJ)    ;!  SURFACE GIVE "1" AS REPLY AND DEFINE ST2 AS O/P

C1=-IRP*EPS3*SIG3**IRP/RIKE
C2=4*POL/RIKE
C3=14.4/RIKE   ;!      POTENTIAL "CONSTANTS"
C4=-12/RIKE
C5=6/RIKE

PROMPT("R13:")   ;!   GUESS AT FIRST CROSSING DISTANCE
READ(R13R)
MORS03=MORSPOT(ROCH3,AL)
MORS0=MORSPOT(ROCH,AL)
E133=KIP-(MORS03-MORSION(ROCH3))
E13=KIP-(MORS0-MORSION(ROCH))
PRINTSTRING("E13 = ")
PRINT(E13,4,2)
NEWLINE
```

```
FLAG1=1
ROCH=ROCH
R123=CROSPT(E134,EPS3,SIG3,EPS1,SIG1,IONPOT,POUPOT,FLAG1)
R13=CROSPT(E13,EPS3,SIG3,EPS1,SIG1,IONPOT,POUPOT,FLAG1)
NEWLINE
PRINTSTRING("      R13 = ")
PRINT(R13,6,4)
NEWLINE
D=E13-E12
FLAG1=3
R23=CROSPT(D,EPS4,SIG4,EPS2,SIG2,IONPOT,POUPOT,FLAG1)
PRINTSTRING("      R23 = ")
PRINT(R23,5,3)
NEWLINE
%IF FLAG3=1 %OR FLAGA=1 %THEN %START
E34=RIP-(MORSPOT(ROCH,AL2)-MORSION(ROCH))
%IF FLAGA=1 %THEN %START
E34=RIP-(MORSPOTA(ROCH,AL2)-MORSION(ROCH))
%FINISH
FLAG1=2
R34=CROSPT(E34,EPS3,SIG3,EPS4,SIG4,IONPOT,POUPOT,FLAG1)
FLAG1=3
PRINTSTRING("E34=")
PRINT(E34,4,2)
NEWLINE
PRINTSTRING("      R34=")
PRINT(R34,5,3)
NEWLINE
%FINISH
!
!
!   CALCULATION OF FORM OF POTENTIAL CURVES USED
!
!
PROMPT("Output pots?:")
SKIPSYMBOL %UNTIL NEXTSYMBOL='Y' %OR NEXTSYMBOL='N'
READSYMBOL(I)
%IF I='Y' %THEN %START
PROMPT("Pot1 output:")
READFILENAME(STRING)
%IF STRING="TT" %OR STRING="LOCAL" %THEN STRING=".OUT"
DEFINE("ST12,".STRING)
PROMPT("Pot2 output:")
READFILENAME(STRING)
%IF STRING="TT" %OR STRING="LOCAL" %THEN STRING=".OUT"
DEFINE("ST13,".STRING)
PROMPT("Pot3 output:")
READFILENAME(STRING)
%IF STRING="TT" %OR STRING="LOCAL" %THEN STRING=".OUT"
DEFINE("ST14,".STRING)
%IF FLAG3=1 %THEN %START
PROMPT("POT4 OUTPUT:")
READFILENAME(STRING)
%IF STRING="TT" %OR STRING="LOCAL" %THEN STRING=".OUT"
DEFINE ("ST15,".STRING)
%FINISH
%IF FLAGA=1 %THEN %START
PROMPT("POT4 OUTPUT")
READFILENAME(STRING)
%IF STRING="TT" %OR STRING="LOCAL" %THEN STRING=".OUT"
DEFINE("ST16,".STRING)
%FINISH
```

```
%CYCLE I=1,1,100
VAR=I*0.1
V1=POWPOT(VAR,SIG1,EPS1)
%IF V1>20 %THEN ->PL1
SELECTOUTPUT(12)
PRINT(VAR,5,3)
SPACES(2)
PRINT(V1,5,3)
NEWLINE
PL1:
V2=POWPOT(VAR,SIG2,EPS2)*E12
%IF V2>20 %THEN ->PL2
SELECTOUTPUT(13)
PRINT(VAR,5,3)
SPACES(2)
PRINT(V2,5,3)
NEWLINE
PL2:
V3=POWPOT(VAR,SIG3,EPS3)*E12
%IF V3>20 %THEN ->PL3
SELECTOUTPUT(14)
PRINT(VAR,5,3)
SPACES(2)
PRINT(V3,5,3)
NEWLINE
PL3:
%IF FLAG3=1  %THEN %START
V4=POWPOT(VAR,SIG4,EPS4)*AL2/1.60210-19
%IF V4>20 %THEN ->PL4
SELECTOUTPUT(15)
PRINT(VAR,5,3)
SPACES(2)
PRINT(V4,5,3)
NEWLINE
PL4:
%FINISH
%IF FLAGA=1 %THEN %START
V4=POWPOT(VAR,SIG4,EPS4)*(MORSPOTA(ROCH,AL2)-MORS0)
%IF V4>20 %THEN -> PL5
SELECTOUTPUT(16)
PRINT(VAR,5,3)
SPACES(2)
PRINT(V4,5,3)
NEWLINE
PL5:
%FINISH
%REPEAT
CLOSESTREAM(12)
CLOSESTREAM(13)
CLOSESTREAM(14)
%IF FLAG3=1 %THEN CLOSESTREAM(15)
%IF FLAGA=1 %THEN CLOSESTREAM(16)
PROMPT("Continue:")
SKIPSYMBOL %UNTIL NEXTSYMBOL='Y' %OR NEXTSYMBOL='N'
READSYMBOL(I)
%IF I='N' %THEN %STOP
->LE
%FINISH
!
!
!          START OF CALCULATION
!
!
```

```
16:
PROMPT("IMPACT PARM:")
READ(B)
%IF B<0 %THEN ->LE
!
!
PROMPT("WHICH CHANNEL:")
READ(CHNO)
R23D=R23
R13D=R13
%IF CHNO=1 %THEN %START     ;!     ELASTIC SCATTERING
RCDUM=13
L9:
DFP1=DEFLCT(EPS1,SIG1,B,E,100)
R1=R*1.5-4
RDIFF1=DEL-DW(EPS1,SIG1,R1,R1,100)
RDIFF1=RDIFF1-(RDIFF1-DIFF1)*1.2
RR=R1+ABS(RDIFF1)
EL1=0.000
DFP1=ABS(DFP1)
PATH=1
%IF B<R13 %THEN SIGMA=LAMBLN(B,PATH)*B/(SDFP1*SIN(DFP1))
%IF B>R13 %THEN SIGMA=B/(SDFP1*SIN(DFP1))
OUTPUT(B,DFP1,EL1,SIGMA,RCH,PATH)
%IF DFP1*180/PI>20 %THEN ->L8
B=B-0.01
->L9
%FINISH
!
!
%IF CHNO=2 %THEN %START    ;!   EXIT AS K(4S) AND VIB. EXCITED MOLECULE
FLAGEL=0
PROMPT("OUTPUT ELOSS?:")    ;!    i.e. SEPARATE OUTPUT OF RED. SCATT. ANGLE VS. EN
ERGY LOSS
SKIPSYMBOL %UNTIL NEXTSYMBOL='Y' %OR NEXTSYMBOL='N'
READSYMBOL(I)
%IF I='Y' %THEN %START
FLAGEL=1
PROMPT("OUTPUT?:")
READFILENAME(STRING)
%IF STRING="TI" %OR STRING="LOCAL" %THEN STRING=".OUT"
DEFINE("ST12,".STRING)
%FINISH
L10:
%IF B>R13 %THEN ->L8
VCI=0
DEMT=MTCR(R13,B,R13,RDCH1,2)
D=RIF-(MORSPOT(RCH,AL)-MORSION(RCH))
D=D-(MORSPOT(RCH,AL)-MORS0)
FLAG1=1
RCDUM=CROSPT(D,EPS3,SIG3,EPS1,SIG1,IONPOT,POWPOT,FLAG1)
R13D=R13
%IF FLAGE=0 %THEN %START
L1:
FLAGE2=1
%IF RCDUM-R13D>0.005*R13D %THEN %START
DEMT=MTCR(R13D,B,RCDUM,RCH,3)
D=RIF-(MORSPOT(RCH,AL)-MORSION(RCH))
D=D-(MORSPOT(RCH,AL)-MORS0)
FLAG1=1
R13D=RCDUM
RCDUM=CROSPT(D,EPS3,SIG3,EPS1,SIG1,IONPOT,POWPOT,FLAG1)
%IF FLAGE=0 %THEN ->L1
R13D=RCDUM
```

```
%IF I=1 %THEN %START
!IF(I=1
DEFPOW(EPS1,SIG1,B,B,100)+DEFPOW(EPS1,SIG1,B,B,R13)+DEFION(B,R13,R23D)+DEFPOW(EPS2,SIG2,B,R23D,100)
B1=B+10-4
DEFPOW(EPS1,SIG1,B1,B1,100)+DEFION(B1,B1,R13)+DEFION(B1,B1,R13D)+DEFPOW(EPS1,SIG1,B1,B1,R13D,100)
DEFP2=(DEFP2-B1P2)*1E4
DEF2=ABS(DEFP2)
EL2=DEM1+MORSPOT(RCH,AL)-MORS0
B1P2=ABS(DEFP2)
PATH=2
SIGMA=LIMELOG(B,PATH)*2/(GM*2*1.6E-12)
%IF FLAGEL=1 %THEN %START
PLOSS(DEFP2,EL2)
%FIN%SP
OUTPUT(I,DEFP2,E1,SIGMA,ELOSS,DPATH)
%IF DEF<1E-5/EL2>20 %THEN ELOSS(DEFP2,EL2) %AND->L8
B=B-0.01
FLAGE1=0
FLAGE=0
FLAGE2=0
->L10
%FINISH
!
!
%IF CHAO=3 %THEN %START     ;!   LATE CROSSING TO ION SURFACE, EXIT AS K(AP)+VIB. EXC.
FLAGEL=0
PROMPT("OUTPUT ELOSS?:")
SKIPSYMBOL %UNTIL NEXTSYMBOL='Y' %OR NEXTSYMBOL='N'
READSYMBOL(I)
%IF I='Y' %THEN %START
FLAGEL=1
PROMPT("OUTPUT?:")
READFILENAME(STRING)
%IF STRING="TT" %OR STRING="LOCAL" %THEN STRING=".OUT"
DEFINE("ST12,".STRING)
%FINISH
L11:
FLAGE2=0
VCI=0
DEM1=MICR(R133,B,R23,RCOH3,3)
D=RIP-(MORSPOT(RCH,AL)-MORSION(RCH))-E12
D=D-(MORSPOT(RCH,AL)-MORS0)
FLAG1=3
RCOUM=CROSPT(D,EPS3,SIG3,EPS2,SIG2,IONPOT,POWPOT,FLAG1)
R23D=R23
%IF FLAGE=0 %THEN %START
L2:
%IF RCOUM-R23D>0.025*R23D %THEN %START
FLAGE2=1
DEMT=MICR(R23D,B,RCOUM,RCH,3)
R23D=RCOUM
D=RIP-(MORSPOT(RCH,AL)-MORSION(RCH))-E12
D=D-(MORSPOT(RCH,AL)-MORS0)
RCOUM=CROSPT(D,EPS3,SIG3,EPS2,SIG2,IONPOT,POWPOT,FLAG1)
%IF FLAGE=0 %THEN ->L2
R23D=RCOUM
%FINISH
%FINISH
EL3=DEM1+E12+MORSPOT(RCH,AL)-MORS0
DEF3=DEFPOW(EPS1,SIG1,B,B,100)+DEFPOW(EPS1,SIG1,B,B,R13)+DEFION(B,R13,R23D)+DEFPOW(EPS2,SIG2,B,R23D,100)
B1=B+10-4
```

```
G1DFP3=DEFPOW(EPS1,SIG1,P1,R13,100)+DEFION(P1,P1,R13)+DEFPOW(EPS2,SIG2,P1,R23D,100)
G1DFP3=G1DFP3+DEFION(P1,R13,R23D)+DEFPOW(EPS3,SIG3,P1,R23D,100)
G1FP3=(G1DFP3-DFP3)*184
GDFP3=MOD(G1FP3)
DFP3=MOD(DFP3)
PATH=3
SIGMA=LARZLN(B,PATH)+B/(GDFP3*STDEVDFP3)
%IF FLAGEL=1 %THEN %START
ELOSS(DFP3,EL3)
%FINISH
OUTPUT(B,DFP3,EL3,SIGMA,ITER)
%IF DFP3*180/PI>90 %THEN -> RESTREAM(12) %AND-*L1
RL1:
T=P=0.01
ITER=E1=0
FLAGE=0
-> L11
%FINISH
;
!
%IF CHNO=4 %THEN %START   ;!  EARLY CROSSING TO ION SURFACE, EXIT AS R(4P)=R3B.
EXC.
FLAGEL=0
PROMPT("OUTPUT ELOSS?:")
SKIPSYMBOL %UNTIL NEXTSYMBOL= 'Y' %OR NEXTSYMBOL='N'
READSYMBOL(I)
%IF I='Y' %THEN %START
FLAGEL=1
PROMPT("OUTPUT?:")
READFILENAME(STRING)
%IF STRING="TT" %OR STRING="LOCAL" %THEN STRING=".OUT"
DEFINE ("ST12,".STRING)"
%FINISH
L12:
FLAGE2=0
VC1=0
DENT=ATCR(R13,B,R23,RCH*,4)
D=KIP-(MORSPOT(RCH,AL)-MORSION(RCH))
D=D-E12-(MORSPOT(RCH,AL)-MORSO)
FLAG1=3
RCDUM=CROSPT(D,EPS3,SIG3,EPS2,SIG2,IONPOT,POWPOT,FLAG1)
R23D=R23
L3:
%IF FLAGE=0 %THEN %START
%IF RCDUM-R23D>0.025*R23D %THEN %START
FLAGE2=1
DENT=ATCR(R23D,B,RCDUM,RCP,3)
R23D=RCDUM
D=KIP-(MORSPOT(RCH,AL)-MORSION(RCH))
D=D-E12-(MORSPOT(RCH,AL)-MORSO)
RCDUM=CROSPT(D,EPS3,SIG3,EPS2,SIG2,IONPOT,POWPOT,FLAG1)
%IF FLAGE=0 %THEN ->L3
R23D=RCDUM
%FINISH
%FINISH
EL4=DENT+E12+MORSPOT(R,H,AL)-MORSO
DFP4=DEFPOW(EPS1,SIG1,P,R13,100)+DEFION(B,P,R13)+DEFION(B,P,R23D)+DEFPOW(EPS2,SIG2,B,R23D,100)
B1=B+1E-4
G1DFP4=DEFPOW(EPS1,SIG1,B1,R13,100)+DEFION(B1,B1,R13)
G1DFP4=G1DFP4+DEFION(B1,B1,R23D)+DEFPOW(EPS2,SIG2,B1,R23D,100)
GDFP4=(G1DFP4-DFP4)*184
GDFP4=MOD(GDFP4)
DFP4=MOD(DFP4)
PATH=4
```

```
SIGMA=LANZEN(E,PATH)+B/(1-DFPS+SIN(DFPS))
%IF FLAGEL=1 %THEN %START
ELOSS(DFPS,EL5)
%FINISH
OUTPUT(B,DFPS,EL5,SIGMA,RCH,PATH)
%IF DFPS*180/PI>20 %THEN CLOSESTREAM(12)  %AND->L8
B=B-0.01
FLAGE=0
FLAGE1=0
->L13
```

```
%IF CHNO=6 %THEN %START    !    ION PAIR PRODUCTION, EARLY CROSSING
FLAGEL=0
PROMPT("OUTPUT ELOSS:")
SKIPSYMBOL %UNTIL NEXTSYMBOL='Y' %OR NEXTSYMBOL='N'
READSYMBOL(I)
%IF I='Y' %THEN FLAGEL=1
FLAGEL=1
PROMPT("OUTPUT ELOSS:")
READ(ELOSS)
%IF STRING="TT" %OR  STRING="LOCAL" %THEN STRING=".OUT"
DEFINE("ST12.".STRING)
%FINISH
L14:
FLAGE2=0
VC1=0
DEMT=MTCR(R13,B,R23,RCH1,6)
D=K1P-(MORSPOT(RCH,AL)-MORSION(RCH))-E12
D=D-(MORSPOT(RCH,AL)-MORSO)
FLAG1=3
RCDUM=CROSPT(D,EPS3,SIG3,EPS2,SIG2,IONPOT,POUPOT,FLAG1)
R23D=R23
L5:
%IF FLAGE=0 %THEN  %START
%IF RCDUM-R23D>0.025*R23D %THEN %START
FLAGE2=1
DEMT=MTCR(R23D,B,RCDUM,RCH,3)
R23D=RCDUM
D=K1P-(MORSPOT(RCH,AL)-MORSION(RCH))-E12
D=D-(MORSPOT(RCH,AL)-MORSO)
RCDUM=CROSPT(D,EPS3,SIG3,EPS2,SIG2,IONPOT,POUPOT,FLAG1)
%IF FLAGE=0 %THEN->L5
R23D=RCDUM
%FINISH
%FINISH
EL6=E13+AL1
DFP6=DEFPOW(EPS1,SIG1,B,R13,100)+DEFION(B,B,R13)+DEFION(B,B,100)
B1=B+10-4
G1DFP6=DEFPOW(EPS1,SIG1,B1,R13,100)+DEFION(B1,B1,R13)+DEFION(B1,B1,100)
GDFP6=(G1DFP6-DFP6)*10^4
GDFP6=MOD(GDFP6)
DFP6=MOD(DFP6)
PATH=6
SIGMA=LANZEN(B,PATH)*B/(GDFP6*SIN(DFP6))
%IF FLAGEL=1 %THEN %START
ELOSS(DFP6,EL6)
%FINISH
OUTPUT(B,DFP6,EL6,SIGMA,RCH,PATH)
%IF DFP6*180/PI>20 %THEN CLOSESTREAM(12) %AND->L8
B=B-0.01
FLAGE=0
FLAGE1=0
->L14
%FINISH
!
!
%IF CHNO=7 %THEN %START
FLAGEL=0
PROMPT("OUTPUT ELOSS:")
SKIPSYMBOL %UNTIL NEXTSYMBOL='Y' %OR NEXTSYMBOL='N'
READSYMBOL(I)
%IF I='Y' %THEN %START
FLAGEL=1
```

```
PRINT("OUTPUT?:")
READSYMBOL(STRING)
%IF STRING="TT" %OR STRING="LOCAL" %THEN STRING=".OUT"
DEFINE ("SYS",".STRING)
%FINISH
L12:
FLAGL2=0
UC1=0
DEMT=MTCR(R13,B,R34,RCH1,7)
D=KIP-(MORSPOT(RCH,AL2)-MORSION(RCH))-(MORSPOT(RCH,AL)-MORSO)
%IF FLAGA=1 %THEN %START
D=KIP-(MORSPOTA(RCH,AL2)-MORSION(RCH))-(MORSPOT(RCH,AL)-MORSO)
%FINISH
FLAG1=3
RCDUM=CROSPT(D,EPS3,SIG3,EPS4,SIG4,IONPOT,POWPOT,FLAG1)
R34D=R34
%IF FLAGE=0 %THEN %START
!70:
%IF RCDUM-R34D>0.025*R34D %THEN %START
FLAGL2=1
DEMT=MTCR(R34D,B,RCDUM,RCH,7)
R34D=RCDUM
D=KIP-(MORSPOT(RCH,AL2)-MORSION(RCH))-(MORSPOT(RCH,AL)-MORSO)
%IF FLAGA=1 %THEN %START
D=KIP-(MORSPOTA(RCH,AL2)-MORSION(RCH))-(MORSPOT(RCH,AL)-MORSO)
%FINISH
RCDUM=CROSPT(D,EPS3,SIG3,EPS4,SIG4,IONPOT,POWPOT,FLAG1)
%IF FLAGE=0 %THEN->L70
R34D=RCDUM
%FINISH
%FINISH
EL7=DEMT+MORSPOT(RCH1,AL2)-MORSO
%IF FLAGA=1 %THEN %START
EL7=DEMT+MORSPOTA(RCH1,AL2)-MORSO
%FINISH
DFP7=DEFPOW(EPS1,SIG1,B,B,100)+DEFPOW(EPS1,SIG1,B,B,R13)+DEFION(B,R13,R34D)
DFP7=DFP7+DEFPOW(EPS4,SIG4,B,R34D,100)
B1=B+10-4
G1DFP7=DEFPOW(EPS1,SIG1,B1,B1,100)+DEFPOW(EPS1,SIG1,B1,B1,R13)+DEFION(B1,R13,R34
)
G1DFP7=G1DFP7+DEFPOW(EPS4,SIG4,B1,R34,100)
GDFP7=(G1DFP7-DFP7)*104
GDFP7=MOD(GDFP7)
DFP7=MOD(DFP7)
PATH=7
SIGMA=LANZEN(E,PATH)*E/(GDFP7*SIN(DFP7))
%IF FLAGEL=1 %THEN %START
ELOSS(DFP7,EL7)
%FINISH
OUTPUT(B,DFP7,EL7,SIGMA,RCH,PATH)
%IF DFP7*180/PI>20 %THEN CLOSESTREAM(12) %AND->L8
B=B-0.01
FLAGE=0
FLAGL2=0
->L12
%FINISH
!
!
%IF CHAO=8 %THEN %STAST
FLAGEL=0
PROMPT("OUTPUT ELOSS?:")
SKIPSYMBOL %UNTIL NEXTSYMBOL='Y' %OR NEXTSYMBOL='N'
READSYMBOL(I)
```

```
%IF I = 1 %THEN %STOP
FLAGEL=1
PROMPT("OUTPUT:")
READFILE(STRING)
%IF S[1]=6="TT" %OR S="NIL" %THEN S="LOCAL" %ELSE S=STRING=".DAT"
DEFINE(7,112,",STRING)
%FINISH
L12:
FLAGA=0
VC1=0
DEMT=MTCR(R13,B,R34,ROCH1,8)
D=KIP-(MORSPOT(RCH,AL2)-MORSION(RCH))-(MORSPOT(RCH,AL)-MORSO)
%IF FLAGA=1 %THEN %START
D=KIP-(MORSPOTA(RCH,AL2)-MORSION(RCH))-(MORSPOT(RCH,AL)-MORSO)
%FINISH
FLAG1=3
RCDUM=CROSPT(D,EPS3,SIG3,EPS4,SIG4,IONPOT,POWPOT,FLAG1)
R34D=R34
%IF FLAGE=0 %THEN %START
L80:
%IF RCDUM-R34D>0.025*R34D %THEN %START
FLAGE2=1
DEMT=MTCR(R34D,B,RCDUM,RCH,2)
R34D=RCDUM
D=KIP-(MORSPOT(RCH,AL2)-MORSION(RCH))-(MORSPOT(RCH,AL)-MORSO)
%IF FLAGA=1 %THEN %START
D=KIP-(MORSPOTA(RCH,AL2)-MORSION(RCH))-(MORSPOT(RCH,AL)-MORSO)
%FINISH
RCDUM=CROSPT(D,EPS3,SIG3,EPS4,SIG4,IONPOT,POWPOT,FLAG1)
%IF FLAGE=0 %THEN ->L80
R34D=RCDUM
%FINISH
%FINISH
PRINTSTRING("DEMT = ")
PRINT(DEMT,5,3)
NEWLINE
EL8=DEMT+MORSPOT(ROCH1,AL2)-MORSO
%IF FLAGA=1 %THEN %START
EL8=DEMT+MORSPOTA(ROCH1,AL2)-MORSO
%FINISH
DFP8=DEFPOW(EPS1,SIG1,B,R13,100)+DEFION(B,B,R13)+DEFION(B,B,R34D)+DEFPOW(EPS4,SI
G4,B,R34D,100)
B1=B+10-4
G1DFP8=DEFPOW(EPS1,SIG1,B1,R13,100)+DEFION(B1,B1,R13)+DEFION(B1,B1,R34D)
G1DFP8=G1DFP8+DEFPOW(EPS4,SIG4,B1,R34D,100)
GDFP8=(G1DFP8-DFP8)*10^4
GDFP8=ABS(GDFP8)
DFP8=ABS(DFP8)
PATH=8
SIGMA=LAMBDA*B,PATH)*B/(GDFP8*SIN(DFP8))
%IF FLAGEL=1 %THEN %START
ELOSS(DFP8,EL8)
%FINISH
OUTPUT(B,DFP8,EL8,SIGMA,ROH,PATH)
%IF DFP8-180/PI*20 %THEN FLOAT(STREAM(1),"%N%N") ->L8
D=D-0.01
FLAGE=0
FLAGE1=0
->L18
%FINISH
!
!
L8:
R13D=R13
R23D=R23
```

```
%SELECTOUTPUT(0)
%WRITE("CONTINUE?")
%WHILE %TRUE %DO %START
READSYMBOL(I,
%IF I='Y' %THEN->L6
%IF I='N' %THEN->L1
%FINISH

%REALFN MTCR(%REALNAME R1,B,R2,RSTART %INTEGER PATH)
%REAL RCH1
%IF B>R13 %THEN %RESULT=-999
%IF PATH=2 %THEN %START
TF=2*(SQRT(R1*R1-B*B)*1@-10/RELVEL)
RKE1=SQRT(R1*R1-B*B)
%FINISH
%IF PATH=3 %OR PATH=5 %OR PATH=7 %THEN %START
!   CROSSING TO IONIC CURVE ON WAY OUT
TF=(SQRT(R2*R2-B*B)*1@-10-SQRT(R1*R1-B*B)*1@-10)/RELVEL
RKE1=SQRT(R1*R1-B*B)
%FINISH
%IF PATH=4 %OR PATH=6 %OR PATH=8 %THEN %START
!   CROSSING TO IONIC CURVE ON WAY IN
TF=(SQRT(R1*R1-B*B)*1@-10+SQRT(R2*R2-B*B)*1@-10)/RELVEL
RKE1=SQRT(R1*R1-B*B)
%FINISH
I=0
RCH1=RSTART
!   EQUILIBRIUM C-I BOND DISTANCE
DT=TF/50
!   STEP LENGH FOR CALCULATION OF INCREASE IN C-I BOND
KM=0
!   PATCH TO ALLOW FOR THE INFLUENCE OF THE K+ ION ON THE C- REPULSION
L30:
%IF PATH=3 %OR PATH=5 %OR PATH=7 %THEN %START
RKTM=SQRT((RKE1+KM)*(RKE1+KM)+B*B)
%FINISH
%IF PATH=2 %OR PATH=4 %OR PATH=6 %OR PATH=8 %THEN %START
RKTM=SQRT((RKE1-KM)*(RKE1-KM)+B*B)
%IF TRAJ=1 %THEN %START
SELECTOUTPUT(2)
PRINT(RKTM,5,3)
SPACE
CLOSESTREAM(2)
%FINISH
%FINISH
%IF RKTM>40 %THEN ->M1
!   CROSSING POINT MOVED TO BEYOND 20 ANGSTROMS.  LITTLE
!   POINT IN PROCEEDING FURTHER WITH CALCULATIONS AT THIS IMPACT
!   PARAMETER.  IT ALSO SIDESTEPS THE PROBLEMS CAUSED BY
!   THE EXP ARGUMENT.
%IF ES=0 %THEN %START
ACC=-BETAION*DION*EXP(-BETAION*(RCH1-ROCH1))
ACCADD=DD=CBETA*1@10*BARN*TANH(CBETA*(RON-RBETA))*((TANH(CBETA*(RCH1*1@10-3.5)))**2
%C
-(1.0-TANH(CBETA*(RCH1*1@10-2.5)))**2)
%IF RKTM>RON %THEN ACCADD=0
ACC=ACC+ACCADD
%FINISH
%IF ES>0 %THEN %START
ACC=1.6020-19*(-BETAION*EXP(-BETAION*(RCH1-ROCH1))+BETAION*EXP(-BETAION/2)*(RCH
1-ROCH1)))
%FINISH
ACC=-ACC/AMU1
```

```
DRCH=VC1*DT+0.5*ACC*DT*DT
VC1=VC1+ACC*DT
RCH1=RCH1+DRCH
%IF CHNO=4 %AND TRAJ=1 %THEN %START
SELECTOUTPUT(2)
PRINT(RCH1*1010,5,3)
NEWLINE
CLOSESTREAM(2)
%FINISH
T=T+DT
KM=RELVEL*T*1010
%IF KM>=RKE1 %THEN FLAGE1=1
%IF FLAGE1=1 %AND CHNO=4 %THEN %START
DUMV=IONPOT(RKTM,SIG3.EPS3)+KIP-E12-POWPOT(RKTM,SIG2.EPS2)
DUMV=DUMV-MORSPOT(RCH1,AL)+MORSION(RCH1)
%IF DUMV<0 %THEN DUMV=-DUMV
%IF DUMV<0.05 %THEN FLAGE=1 %AND FLAGE1=0 %AND ->M1
%FINISH
%IF CHNO=4  %OR CHNO=6  %THEN %START
%IF FLAGE2=1 %THEN %START
DUMV=IONPOT(RKTM,SIG3,EPS3)+KIP-E12-POWPOT(RKTM,SIG2,EPS2)
DUMV=DUMV-MORSPOT(RCH1,AL)+MORSION(RCH1)
%IF DUMV<0 %THEN DUMV=-DUMV
%IF DUMV<.05 %THEN FLAGE=1 %AND FLAGE1=0 %AND ->M1
%FINISH
%FINISH
%IF FLAGE1=1 %AND CHNO=2 %THEN %START
DUMV=IONPOT(RKTM,SIG3,EPS3)+KIP-POWPOT(RKTM,SIG1,EPS1)
DUMV=DUMV-MORSPOT(RCH1,AL)+MORSION(RCH1)
%IF DUMV<0 %THEN DUMV=-DUMV
%IF DUMV<.05 %THEN FLAGE=1 %AND FLAGE1=0 %AND ->M1
%FINISH
%IF CHNO=2 %AND FLAGE2=1 %THEN %START
DUMV=IONPOT(RKTM,SIG3,EPS3)+KIP-POWPOT(RKTM,SIG1,EPS1)
DUMV=DUMV-MORSPOT(RCH1,AL)+MORSION(RCH1)
%IF DUMV<0 %THEN DUMV=-DUMV
%IF DUMV<0.05 %THEN FLAGE=1 %AND ->M1
%FINISH
%IF CHNO=3 %OR CHNO=5  %THEN %START
%IF FLAGE2=1 %THEN %START
DUMV=IONPOT(RKTM,SIG3,EPS3)+KIP-E12-POWPOT(RKTM,SIG2,EPS2)
DUMV=DUMV-MORSPOT(RCH1,AL)+MORSION(RCH1)
%IF DUMV<0 %THEN DUMV=-DUMV
%IF DUMV<0.05 %THEN FLAGE=1 %AND ->M1
%FINISH
%FINISH
%IF CHNO=7 %THEN %START
%IF FLAGE2=1 %THEN %START
DUMV=IONPOT(RKTM,SIG2,EPS3)+KIP-POWPOT(RKTM,SIG4,EPS4)
%IF FLAGA=1 %THEN %START
DUMV=DUMV-POPSPOTA(RCH1,AL2)+MORSION(RCH1)
%FINISH
%IF FLAGA=0 %THEN %START
DUMV=DUMV-MORSPOT(RCH1,AL2)+MORSION(RCH1)
%FINISH
%IF DUMV<0 %THEN DUMV=-DUMV
%IF DUMV<0.2 %THEN FLAGE=1 %AND ->M1
%FINISH
%FINISH
%IF FLAGE1=1 %AND CHNO=8 %THEN %START
DUMV=IONPOT(RKTM,SIG3,EPS3)+KIP-POWPOT(RKTM,SIG4,EPS4)
%IF FLAGA=1 %THEN %START
DUMV=DUMV-MORSPOTA(RCH1,AL2)+MORSION(RCH1)
%FINISH
```

```
%IF FLAGA=0 %THEN %START
DUMV=DUMV-MORSPOT(RCH1,AL2)+MORSION(RCH1)
%FINISH
%IF DUMV<0 %THEN DUMV=-DUMV
%IF DUMV<0.2 %THEN FLAGE=1 %AND FLAGE1=0 %AND->M1
%FINISH
%IF CHNO=8 %THEN %START
%IF FLAGE2=1 %THEN %START
DUMV=IONPOT(RKTM,SIG3,EPS3)+KIP-POWPOT(RKTM,SIG1,EPS1)
%IF FLAGA=1 %THEN %START
DUMV=DUMV-MORSPOTA(RCH1,AL2)+MORSION(RCH1)
%FINISH
%IF FLAGA=0 %THEN %START
DUMV=DUMV-MORSPOT(RCH1,AL2)+MORSION(RCH1)
%FINISH
%IF DUMV<0 %THEN DUMV=-DUMV
%IF DUMV<0.2 %THEN FLAGE=1 %AND->M1
%FINISH
%FINISH
%IF T<TF %THEN ->L30
!   MOTION DOWN (CH3I)- CURVE FINISHED
!   NOW CALCULATE CHANGE IN K+/CH3I- CURVE
M1:
RCH=RCH1
P1=MORSION(RCH1)
P2=MORSION(RCH)
%RESULT=P1-P2
%END
%REALFN TANH(%REAL X)
%RESULT=(EXP(X)-EXP(-X))/(EXP(X)+EXP(-X))
%END
%REALFN IONPOT(%REALNAME R,SIG,EPS)
%RESULT=EPS*(SIG/R)**3KP-POL/R**4-14.394/R
%END
%REALFN POWPOT(%REALNAME R,SIG,EPS)
%RESULT=EPS*(SIG/R)**6*((SIG/R)**6-1)
%END
%REALFN CROSF1(%REALNAME E,EPS1,SIG1,EPS2 ,SIG2,%REALFN POT1,POT2  %C
%INTEGER FLAGS)
    %SPEC POT1(%REALNAME R,SIG,EPS)
    %SPEC POT2(%REALNAME R,SIG,EPS)
%REAL R,V1,V2,W1,W2,G,X,Y,EE,HH
%INTEGER FLAG
!   THIS FUNCTION EVALUATES THE CROSSING RADII FOR THE
!   THREE NEUTRAL CURVES AND THE IONIC CURVE.
FLAG = 0
HH =.05
%IF E<0 %THEN%START
    EE = -E/14.394
    W1 = 0; W2 = 1
    R = 2
!   ->L1
    %FINISH
EE = E/14.394
W1 = 0; W2 = 1
%IF FLAGR=1 %THEN %START
R=9
%IF AL2>0 %THEN R=24
%FINISH
%IF FLAGS = 1 %THEN R = 2.8
%IF FLAGS = 2 %THEN R=1
%IF FLAGS = 3 %THEN R = 3
```

```
L1:     V1 = EE+POT1(R,SIG1,EPS1)/14.394
     V2 =POT2(R,SIG2,EPS2)/14.394
%IF V1>=V2 %OR FLAG=1 %THEN->L2
     W1 = V1
     W2 = V2
     R = R+HH
->L1 %UNLESS R>1000
->L3
L2:     X = W1-W2
     Y = V1-V2
     G = -(X-Y)/HH
R = R-HH-X/G
     W1 = V1; W2 = V2
     HH = -(HH+X/G)
     FLAG = 1
->L1 %UNLESS MOD(V1-V2)<1E-3
%RESULT = R
L3:     %RESULT = -10
%END

%REALFN LANZEN(%REALNAME B, %INTEGER PATH)
%REAL P1DD,P1,P1D,P2D,P2DD,P3,P3D,P3DD,P1DDD,VR3,VR1,P2,VR2
!   THIS ROUTINE CALCULATES THE PROBABILITY OF EXITING VIA
!   A GIVEN PATH. R12,R23 AND R34 ARE REDUCED COUPLING PARAMETERS
!   (UNITS ARE 10**6 CM/S)
%IF B>R13 %THEN %START
P1D=1
P2D=0
P1=1
P2=0
->L1
!   NO CHANCE OF INELASTIC BEHAVIOUR
%FINISH
VR1=RELVEL*1E-4*SQRT(MOD(1-B**2/(R13D*R13D)))
P1D=EXP(-R12*EXP(1.4*(R13-R13D))/VR1)
P1DD=EXP(-R12*EXP(1.4*(R23-R23D))/VR1)
P1=EXP(-R12/VR1)
VR2=1E-4*RELVEL*SQRT(MOD(1-B*B/(R23D*R23D)))
P2D=EXP(-R23*EXP(2.5*(R23-R23D))/VR2)
P2=EXP(-R23/VR2)
L1:
%IF PATH=2 %THEN %RESULT=(1-P1D)*(1-P1)
%IF PATH=1 %THEN %RESULT=P1*P1
%IF PATH=3 %THEN %RESULT=P1*(1-P1)*(1-P2D)
%IF PATH=4 %THEN %RESULT=(1-P1)*P1DD*(1-P2D)
%IF PATH=5 %THEN %RESULT=(1-P1)*P1*P2D
%IF PATH=6 %THEN %RESULT=(1-P1)*P1DD*P2D
%IF FLAG3=1 %OR FLAG4=1 %THEN %START
VR3=1E-4*RELVEL*SQRT(MOD(1-B*B/(R34*R34)))
P3=EXP(-R34/VR3)
P2DD=EXP(-R23*EXP(R34-R34D)/VR3)
%IF PATH=7 %THEN %RESULT=P1*(1-P1)*P2DD*(1-P3)
%IF PATH=8 %THEN %RESULT=(1-P1)*P1*P2DD*(1-P3)
%IF PATH=9 %THEN %RESULT=(1-P1)*P1*P2D*P3
%IF PATH=10 %THEN %RESULT=(1-P1)*P1DD*P2D*P3
%FINISH
%END


%REALFN DEFLON(%REAL B,R1,R2)
 %REAL X,X1,X2,Y,Y1,Y2,Z,THETA1,THETA2
     X=B/R1
THETA1=ARCSIN(X)
Y=B/R2
```

```
      THETA2=ARCSIN(Y)
    X1=-0.2*(SIN(THETA1))**4*COS(THETA1)+0.267*(COS(THETA1))**3
    X1=X1-0.8*COS(THETA1)
    X2=0.2*(SIN(THETA2))**4*COS(THETA2)-0.267*(COS(THETA2))**3
    X2=X2+0.8*COS(THETA2)
      %IF R1=100 %THEN X1=0.267-0.8
      %IF R2=100 %THEN X2=-0.267+0.8
    X=X1+X2
    X=C1*X/B**1RP          <- ? should be 5 ?

    Y1=-0.375*SIN(THETA1)*COS(THETA1)-0.25*(SIN(THETA1))**3*COS(THETA1)
    Y1=Y1+0.375*THETA1
    Y2=0.375*SIN(THETA2)*COS(THETA2)+0.25*(SIN(THETA2))**3*COS(THETA2)
    Y2=Y2-0.375*THETA2
      %IF R1=100 %THEN Y1=0
      %IF R2=100 %THEN Y2=0
    Y=Y1+Y2
    Y=C2*Y/B**4

    Z=(C3*(COS(THETA2)-COS(THETA1)))/B
      %IF R1=100 %THEN Z=C3*(COS(THETA2)-1)/B
      %IF R2=100 %THEN Z=C3*(1-COS(THETA1))/B

  %RESULT=X+Y+Z
  %END


  %RE=LFN DEFPOP(%REAL EPS,SIG,B,R1,R2)
    %REAL X1,X2,X,Y1,Y2,Y,THETA1,THETA2
      THETA1=ARCSIN(B/R1)
      THETA2=ARCSIN(B/R2)
    X1=-0.104*(SIN(THETA1))**5*COS(THETA1)-0.13*(SIN(THETA1))**3*COS(THETA1)
    X1=X1-0.195*SIN(THETA1)*COS(THETA1)+0.226*THETA1
    X1=X1-0.375*(SIN(THETA1))**7*COS(THETA1)+0.3*(SIN(THETA1))**5*(COS(THETA1))**3
    X1=X1-0.1125*(SIN(THETA1))**5*(COS(THETA1))**3
    X1=X1-0.083*(SIN(THETA1))**7*(COS(THETA1))**5+0.0417*(SIN(THETA1))**5*(COS %C
(THETA1))**5
    X1=X1-0.009*SIN(2*THETA1)-0.007*SIN(4*THETA1)+0.003*SIN(6*THETA1)-0.0002*SIN(8
*THETA1)
    X2=0.104*(SIN(THETA2))**5*COS(THETA2)+0.13*(SIN(THETA2))**3*COS(THETA2)
    X2=X2+0.195*SIN(THETA2)*COS(THETA2)-0.226*THETA2
    X2=X2+0.375*(SIN(THETA2))**7*COS(THETA2)-0.3*(SIN(THETA2))**5*(COS(THETA2))**3
    X2=X2+0.1125*(SIN(THETA2))**5*(COS(THETA2))**3
    X2=X2+0.083*(SIN(THETA2))**7*(COS(THETA2))**5
    X2=X2-0.0417*(SIN(THETA2))**5*(COS(THETA2))**5
    X2=X2-0.009*SIN(2*THETA2)+0.007*SIN(4*THETA2)-0.003*SIN(6*THETA2)
    X2=X2+0.0002*SIN(8*THETA2)
      %IF R1=100 %THEN X1=0
      %IF R2=100 %THEN X2=0
    X=X1+X2
    X=C4*EPS*SIG**12*X/B**12

    Y1=-0.167*(SIN(THETA1))**5*COS(THETA1)-0.208*(SIN(THETA1))**3*COS(THETA1)
    Y1=Y1-0.3125*SIN(THETA1)*COS(THETA1)+0.3125*THETA1
    Y2=0.167*(SIN(THETA2))**5*COS(THETA2)+0.208*(SIN(THETA2))**3*COS(THETA2)
    Y2=Y2+0.3125*SIN(THETA2)*COS(THETA2)-0.3125*THETA2
      %IF R1=100 %THEN Y1=0
      %IF R2=100  %THEN Y2=0
    Y=Y1+Y2
    Y=C5*EPS*SIG**6*Y/B**6

  %RESULT=X+Y
  %END
```

```
%REALFN MORSION(%REALNAME R)
%REAL X
%REAL VADD
%IF ES=0 %THEN %START
VADD=BARR*TANH(KBETA*(RON-RKTM))*(TANH(CBETA*(R*1@10-2.5))   %C
-TANH(CBETA*(R*1@10-3.5)))
%IF RKTM>RON %THEN VADD=0
X=DION*EXP(-BETAION*(R-ROCH1))+EXC+VADD
%RESULT=(X+AL1)/1.6021@-19
%FINISH
%IF ES >0 %THEN %START
 X=1.602@-19*(EXP(-BETAION*(R-2.14@-10))-2*EXP(-(BETAION/2)*(R-2.14@-10)))
%RESULT=(X+EXC+AL1)/1.6021@-19
%FINISH
%END
%REALFN MORSPOT(%REALNAME R,AL)
%REAL V,R1
R1=R
!
!   SI DOPING
!
V=DCH*(EXP(-BETA*2*(R1-2.139@-10))-2*EXP(-BETA*(R1-2.139@-10)))
%RESULT=(V+AL)/1.6021@-19
%END
%REALFN MORSPOTA(%REALNAME R,AL)
%REAL V,R1
R1=R
V=2.24@-19*(EXP(-4.1@10*(R1-2.14@-10)))
%RESULT=(V+AL)/1.602@-19
%END

%ROUTINE OUTPUT(%REALNAME E,DFP,EL,SIGMA,RCH %INTEGER PATH)
%REAL DFPD
SELECTOUTPUT(10)
WRITE(PATH,2)
SPACE
PRINT(E,5,3)
SPACE
DFPD=DFP*180/PI
PRINT(RCHE*DFPD,4,2)
PRINT(EL,3,2)
SPACE
%IF CHNO=5 %OR CHNO=6 %THEN %START
PRINTFL(SIGMA*SIN(DFP),2)
%FINISH
PRINTFL(SIGMA*DFPD*DFPD,2)
SPACE
PRINTFL(SIGMA,2)
SPACE
PRINT(RCH*1@10,5,3)
SPACE
PRINTFL(RCBUM,3)
NEWLINE
SELECTOUTPUT(0)
%END
```

```
%ROUTINE READFILENAME(%STRINGNAME NAME)
%INTEGER I
NAME = ""
SKIP SYMBOL %WHILE NEXT SYMBOL = '"' %OR NEXT SYMBOL = ' ' %C
%OR NEXT SYMBOL = NL
%CYCLE
READSYMBOL(I)
NAME = NAME.TO STRING(I)
%EXIT %IF NEXT SYMBOL = NL %OR NEXT SYMBOL = '"'
%REPEAT
SKIP SYMBOL %WHILE NEXT SYMBOL # NL
SKIP SYMBOL
%END  !! READ FILE NAME
%RDUTINE ELOSS(%REALNAME DFP,EL)
%REAL DFPD
SELECTOUTPUT(12)
DFPD=DFP*180/PI
PRINT(RIKE*DFPD,4,2)
SPACE
PRINT(EL,3,2)
NEWLINE
%END
LE:
%ENDOFPROGRAM
```

## APPENDIX B

## SAMPLE INPUT DATA FOR K + $CH_3I$

For exit as K(4P), early (Channel No. 4) and late (Channel No. 3) crossing contributions.

```
Command:RUN OS1Ch-1
Output ?:APPEND
Eps1:0.44
Eps2:0.44
Eps3:0.045
Sig1:4.
Sig2:3.2
Sig3:4.
Ion-Ion Potential:4.54
Repulsion:1.6
Jon rep pow:5
V12:1
V23:1
Red mass:30.6
RIKE:164
NOW PARAMETERS RELEVANT TO TARGET MOLECULE POTENTIAL
Red mass:13.4
R0:2.139
BETA:3.4
D0:2.33
DION:1.65
BETAION:4.65
BARRIER:1.4
K BETA:4
CBETA:1.8
ROP:10
ASSYMPTOTIC LIMITS
COV A.L.:0
ION A.L.:-3.01
POL:57.6
DO YOU WISH TO CONSIDER THE A STATES ?N
NO OF EXCITED STATE:0
EXC:0
TRAJ? :0
R13:3
E13 =      5.31

      R13 =        2.8524
      R23 =       3.673
Output pots?:N
IMPACT PARM:2.85
WHICH CHANNEL:3
OUTPUT CLOSS?:N
CONTINUE?:Y
IMPACT PARM:2.85
WHICH CHANNEL:4
OUTPUT CLOSS?:N
CONTINUE?:N
```

## APPENDIX C

## SAMPLE OUTPUT DATA FOR K + $CH_3I$

Exit as K(4P), early and late crossing contributions.

| Channel No. | b | $E_\chi$ | $\Delta E$ | $I_\chi^2$ | | I | | $r_c'$ | $R_c'$ | |
|---|---|---|---|---|---|---|---|---|---|---|
| 3 | 2.850 | 232.48 | 2.02 | [illegible] | | [illegible] | | [illegible] | [illegible] | |
| 3 | 2.840 | 307.36 | 1.99 | [illegible] | | [illegible] | | 2.224 | 3.45[illegible] | 0 |
| 3 | 2.830 | [illegible] | 1.97 | [illegible] | | [illegible] | | 2.218 | [illegible] | |
| 3 | 2.820 | 405.06 | 1.95 | [illegible] | | [illegible] | | 2.214 | [illegible] | |
| 3 | 2.810 | 454.[illegible] | 1.94 | [illegible] | | [illegible] | | [illegible] | [illegible] | |
| 3 | 2.800 | 503.69 | 1.93 | [illegible] | | [illegible] | | [illegible] | [illegible] | |
| 3 | 2.790 | [illegible] | 1.92 | [illegible] | | [illegible] | | [illegible] | [illegible] | |
| 3 | 2.780 | 603.78 | 1.91 | [illegible] | | [illegible] | | [illegible] | [illegible] | |
| 3 | [illegible] | 654.11 | 1.90 | [illegible] | | [illegible] | | [illegible] | [illegible] | |
| 3 | [illegible] | [illegible] | 1.90 | [illegible] | | [illegible] | | [illegible] | [illegible] | |
| 3 | [illegible] | [illegible] | 1.89 | [illegible] | | [illegible] | | [illegible] | [illegible] | |
| 3 | [illegible] | 812.86 | 1.88 | [illegible] | | [illegible] | | [illegible] | [illegible] | |
| 3 | [illegible] | 871.10 | 1.88 | [illegible] | | [illegible] | | [illegible] | [illegible] | |
| 3 | 2.720 | 931.82 | 1.87 | [illegible] | | [illegible] | | [illegible] | [illegible] | |
| 3 | 2.710 | 995.22 | 1.87 | [illegible] | | [illegible] | | [illegible] | [illegible] | |
| 3 | 2.700 | 1061.51 | 1.86 | [illegible] | | [illegible] | | [illegible] | [illegible] | |
| 3 | 2.690 | 1130.87 | 1.86 | [illegible] | | [illegible] | | [illegible] | [illegible] | |
| 3 | 2.680 | 1203.52 | 1.85 | [illegible] | | [illegible] | | [illegible] | [illegible] | |
| 3 | 2.670 | 1279.66 | 1.85 | [illegible] | | [illegible] | | [illegible] | [illegible] | |
| 3 | 2.660 | 1359.52 | 1.84 | [illegible] | | [illegible] | | [illegible] | [illegible] | |
| 3 | 2.650 | 1443.32 | 1.84 | [illegible] | | [illegible] | | [illegible] | [illegible] | |
| 3 | [illegible] | [illegible] | 1.83 | [illegible] | | [illegible] | | [illegible] | [illegible] | |
| 3 | 2.630 | 1623.72 | 1.83 | [illegible] | | [illegible] | | [illegible] | [illegible] | |
| 3 | 2.620 | 1720.84 | 1.83 | [illegible] | | [illegible] | | [illegible] | [illegible] | |
| 3 | 2.610 | 1822.94 | 1.83 | [illegible] | | [illegible] | | [illegible] | [illegible] | |
| 3 | [illegible] | [illegible] | 1.82 | [illegible] | | [illegible] | | [illegible] | [illegible] | |
| 3 | 2.590 | 2043.26 | 1.82 | [illegible] | | [illegible] | | [illegible] | [illegible] | |

| | | | | | | | | | | |
|---|---|---|---|---|---|---|---|---|---|---|
| 4 | 2.850 | 158.25 | 1.96 | 3.86@ | -2 | 4.15@ | -2 | 2.216 | 3.430@ | 0 |
| 4 | 2.840 | 120.86 | 2.03 | 6.19@ | 0 | 1.14@ | 1 | 2.238 | 3.501@ | 0 |
| 4 | 2.830 | 102.09 | 2.08 | 1.83@ | 1 | 4.73@ | 1 | 2.254 | 3.549@ | 0 |
| 4 | 2.820 | 89.22 | 2.10 | 3.16@ | 1 | 1.07@ | 2 | 2.265 | 3.579@ | 0 |
| 4 | 2.810 | 79.55 | 2.13 | 4.50@ | 1 | 1.91@ | 2 | 2.276 | 3.607@ | 0 |
| 4 | 2.800 | 71.95 | 2.14 | 5.84@ | 1 | 3.04@ | 2 | 2.281 | 3.620@ | 0 |
| 4 | 2.790 | 65.84 | 2.15 | 7.24@ | 1 | 4.49@ | 2 | 2.291 | 3.642@ | 0 |
| 4 | 2.780 | 60.86 | 2.16 | 8.77@ | 1 | 6.37@ | 2 | 2.296 | 3.653@ | 0 |
| 4 | 2.770 | 56.81 | 2.18 | 1.05@ | 2 | 8.79@ | 2 | 2.307 | 3.672@ | 0 |
| 4 | 2.760 | 53.52 | 2.18 | 1.28@ | 2 | 1.20@ | 3 | 2.311 | 3.680@ | 0 |
| 4 | 2.750 | 50.88 | 2.19 | 1.57@ | 2 | 1.63@ | 3 | 2.316 | 3.687@ | 0 |
| 4 | 2.740 | 48.81 | 2.20 | 1.99@ | 2 | 2.25@ | 3 | 2.326 | 3.702@ | 0 |
| 4 | 2.730 | 47.25 | 2.21 | 2.69@ | 2 | 3.22@ | 3 | 2.340 | 3.707@ | 0 |
| 4 | 2.720 | 46.15 | 2.21 | 3.97@ | 2 | 5.01@ | 3 | 2.344 | 3.713@ | 0 |
| 4 | 2.710 | 45.48 | 2.21 | 7.33@ | 2 | 9.54@ | 3 | 2.338 | 3.717@ | 0 |
| 4 | 2.700 | 45.20 | 2.22 | 3.75@ | 3 | 4.[illegible]@ | 4 | 2.342 | 3.721@ | 0 |

| | | | | | | | | | | |
|---|---|---|---|---|---|---|---|---|---|---|
| 4 | 2.690 | 45.29 | 2.22 | 1.300 | 3 | 1.210 | 4 | 2.346 | 3.7250 | 0 |
| 4 | 2.680 | 45.73 | 2.22 | 1.290 | 2 | 7.440 | 3 | 2.350 | 3.7260 | 0 |
| 4 | 2.670 | 46.51 | 2.23 | 1.270 | 2 | 4.750 | 3 | 2.354 | 3.7330 | 0 |
| 4 | 2.660 | 47.67 | 2.23 | 1.250 | 2 | 3.460 | 3 | 2.357 | 3.7340 | 0 |
| 4 | 2.650 | 49.04 | 2.23 | 1.240 | 2 | 2.690 | 3 | 2.361 | 3.7350 | 0 |
| 4 | 2.640 | 50.37 | 2.23 | 1.240 | 2 | 2.170 | 3 | 2.364 | 3.7360 | 0 |
| 4 | 2.630 | 52.81 | 2.23 | 1.240 | 2 | 1.800 | 3 | 2.367 | 3.7410 | 0 |
| 4 | 2.620 | 54.14 | 2.23 | 1.240 | 2 | 1.510 | 3 | 2.371 | 3.7420 | 0 |
| 4 | 2.610 | 52.77 | 2.24 | 1.250 | 2 | 1.270 | 3 | 2.374 | 3.7440 | 0 |
| 4 | 2.600 | 56.69 | 2.24 | 1.250 | 2 | 1.160 | 3 | 2.377 | 3.7460 | 0 |
| 4 | 2.590 | 58.51 | 2.24 | 1.430 | 2 | 9.450 | 1 | 2.380 | 3.7470 | 0 |
| 4 | 2.580 | 61.42 | 2.24 | 1.380 | 2 | 8.190 | 2 | 2.383 | 3.7480 | 0 |
| 4 | 2.570 | 63.23 | 2.24 | 1.340 | 2 | 7.160 | 2 | 2.386 | 3.7490 | 0 |
| 4 | 2.560 | 75.64 | 2.24 | 1.310 | 2 | 6.310 | 2 | 2.389 | 3.7490 | 0 |
| 4 | 2.550 | 79.74 | 2.24 | 1.290 | 2 | 5.650 | 2 | 2.392 | 3.7500 | 0 |
| 4 | 2.540 | 84.45 | 2.24 | 1.270 | 2 | 4.990 | 2 | 2.395 | 3.7500 | 0 |
| 4 | 2.530 | 89.46 | 2.24 | 1.260 | 2 | 4.520 | 2 | 2.398 | 3.7500 | 0 |
| 4 | 2.520 | 94.79 | 2.24 | 1.250 | 2 | 4.060 | 2 | 2.401 | 3.7500 | 0 |
| 4 | 2.510 | 100.43 | 2.24 | 1.240 | 2 | 3.690 | 2 | 2.403 | 3.7510 | 0 |
| 4 | 2.500 | 106.40 | 2.24 | 1.230 | 2 | 3.360 | 2 | 2.406 | 3.7510 | 0 |
| 4 | 2.490 | 112.69 | 2.24 | 1.230 | 2 | 3.060 | 2 | 2.409 | 3.7500 | 0 |
| 4 | 2.480 | 119.32 | 2.24 | 1.230 | 2 | 2.820 | 2 | 2.411 | 3.7500 | 0 |
| 4 | 2.470 | 126.29 | 2.24 | 1.230 | 2 | 2.070 | 2 | 2.414 | 3.7500 | 0 |
| 4 | 2.460 | 133.61 | 2.24 | 1.230 | 2 | 1.850 | 2 | 2.417 | 3.7490 | 0 |
| 4 | 2.450 | 141.29 | 2.24 | 1.230 | 2 | 1.650 | 2 | 2.419 | 3.7490 | 0 |
| 4 | 2.440 | 149.33 | 2.24 | 1.230 | 2 | 1.480 | 2 | 2.422 | 3.7480 | 0 |
| 4 | 2.430 | 157.75 | 2.24 | 1.230 | 2 | 1.330 | 2 | 2.424 | 3.7470 | 0 |
| 4 | 2.420 | 166.56 | 2.24 | 1.230 | 2 | 1.200 | 2 | 2.427 | 3.7460 | 0 |
| 4 | 2.410 | 175.76 | 2.24 | 1.240 | 2 | 1.080 | 2 | 2.429 | 3.7460 | 0 |
| 4 | 2.400 | 185.37 | 2.24 | 1.240 | 2 | 9.700 | 1 | 2.431 | 3.7450 | 0 |
| 4 | 2.390 | 195.39 | 2.24 | 1.240 | 2 | 8.740 | 1 | 2.434 | 3.7440 | 0 |
| 4 | 2.380 | 205.84 | 2.23 | 1.240 | 2 | 7.900 | 1 | 2.436 | 3.7430 | 0 |
| 4 | 2.370 | 216.74 | 2.23 | 1.250 | 2 | 7.140 | 1 | 2.438 | 3.7420 | 0 |
| 4 | 2.360 | 228.08 | 2.23 | 1.250 | 2 | 6.460 | 1 | 2.441 | 3.7400 | 0 |
| 4 | 2.350 | 239.90 | 2.23 | 1.250 | 2 | 5.850 | 1 | 2.443 | 3.7390 | 0 |
| 4 | 2.340 | 252.20 | 2.23 | 1.250 | 2 | 5.300 | 1 | 2.445 | 3.7380 | 0 |
| 4 | 2.330 | 265.00 | 2.23 | 1.260 | 2 | 4.810 | 1 | 2.447 | 3.7370 | 0 |
| 4 | 2.320 | 278.30 | 2.23 | 1.260 | 2 | 4.370 | 1 | 2.450 | 3.7360 | 0 |
| 4 | 2.310 | 292.14 | 2.23 | 1.260 | 2 | 3.970 | 1 | 2.452 | 3.7340 | 0 |
| 4 | 2.300 | 306.52 | 2.23 | 1.260 | 2 | 3.610 | 1 | 2.454 | 3.7330 | 0 |
| 4 | 2.290 | 321.47 | 2.23 | 1.260 | 2 | 3.280 | 1 | 2.456 | 3.7310 | 0 |
| 4 | 2.280 | 337.00 | 2.22 | 1.260 | 2 | 2.990 | 1 | 2.458 | 3.7300 | 0 |
| 4 | 2.270 | 353.13 | 2.22 | 1.260 | 2 | 2.720 | 1 | 2.460 | 3.7290 | 0 |
| 4 | 2.260 | 369.88 | 2.22 | 1.260 | 2 | 2.480 | 1 | 2.462 | 3.7270 | 0 |
| 4 | 2.250 | 387.28 | 2.22 | 1.260 | 2 | 2.260 | 1 | 2.464 | 3.7260 | 0 |
| 4 | 2.240 | 405.33 | 2.22 | 1.260 | 2 | 2.070 | 1 | 2.466 | 3.7240 | 0 |
| 4 | 2.230 | 424.08 | 2.22 | 1.260 | 2 | 1.890 | 1 | 2.468 | 3.7230 | 0 |
| 4 | 2.220 | 443.53 | 2.22 | 1.260 | 2 | 1.720 | 1 | 2.470 | 3.7210 | 0 |
| 4 | 2.210 | 463.73 | 2.22 | 1.260 | 2 | 1.570 | 1 | 2.472 | 3.7190 | 0 |
| 4 | 2.200 | 484.68 | 2.22 | 1.260 | 2 | 1.440 | 1 | 2.474 | 3.7160 | 0 |
| 4 | 2.190 | 506.43 | 2.21 | 1.260 | 2 | 1.320 | 1 | 2.476 | 3.7160 | 0 |
| 4 | 2.180 | 528.99 | 2.21 | 1.250 | 2 | 1.200 | 1 | 2.478 | 3.7150 | 0 |
| 4 | 2.170 | 552.40 | 2.21 | 1.250 | 2 | 1.100 | 1 | 2.480 | 3.7130 | 0 |
| 4 | 2.160 | 576.68 | 2.21 | 1.250 | 2 | 1.010 | 1 | 2.481 | 3.7110 | 0 |
| 4 | 2.150 | 601.88 | 2.21 | 1.240 | 2 | 9.240 | 0 | 2.483 | 3.7100 | 0 |
| 4 | 2.140 | 628.03 | 2.21 | 1.240 | 2 | 8.460 | 0 | 2.485 | 3.7080 | 0 |
| 4 | 2.130 | 655.15 | 2.21 | 1.240 | 2 | 7.750 | 0 | 2.487 | 3.7060 | 0 |
| 4 | 2.120 | 683.29 | 2.20 | 1.230 | 2 | 7.110 | 0 | 2.489 | 3.7050 | 0 |
| 4 | 2.110 | 712.49 | 2.20 | 1.230 | 2 | 6.510 | 0 | 2.490 | 3.7030 | 0 |

# APPENDIX D

## PUBLICATIONS

MOLECULAR PHYSICS, 1984, VOL. 52, NO. 5, 1125–1143

# Non-adiabatic processes in alkali metal–alkyl halide molecule collisions

## The electron harpoon

by E. E. B. COWAN†, M. A. D. FLUENDY†,
A. M. C. MOUTINHO‡§ and A. J. F. PRAXEDES‡‖

†Department of Chemistry, University of Edinburgh, West Mains Road, Edinburgh EH9 3JJ, Scotland

‡Centro de Física Molecular das Universidades de Lisboa, Av. Rovisco Pais, Complexo I-IST, 1000 Lisboa, Portugal

(*Received* 17 *February* 1984 : *accepted* 26 *March* 1984)

The mechanism for vibronic excitation and ion pair production in alkali metal–alkyl halide collisions is investigated. A classical trajectory surface hopping model is developed to account for the fourteen exit channels for which data is available. It is shown that the ground ionic intermediate accounts for the observed **A** state excitation in $CH_3I$ as well as the production of excited alkali atoms. It is further shown that the other, more highly excited, processes can be understood on the basis of an electron harpoon to form one of a sequence of strongly ionic doorway states. Each doorway state connecting to a manifold of exit channels. The nature of these doorway states and the role of vacancy production in their excitation is discussed.

---

## 1. INTRODUCTION

The alkali metal–alkyl halide system has been very extensively investigated as a paradigm for the electron harpoon mechanism of chemical reaction [1–3]. In contrast to the otherwise analogous alkali metal halogen molecule systems [4, 5], alkyl halides have a negative vertical electron affinity and the non-adiabatic effects are expected to occur at shorter ranges in these systems. As a consequence the ionic exit channel can only be reached after a sequence of avoided crossings with excited state potential surfaces. A large number of exit channels including electronic, vibrational and ion production channels are thus accessible, via curve crossings, to collisions in the eV range and can yield information on the dynamics of the collision [6]. Energetic collisions scattering at small angles are a particularly convenient probe for the details of the electronically non-adiabatic processes which occur in these systems. In a previous paper [7] one of us reported the results of measurements of the inelastic differential scattering cross sections for the $K + CH_3I$ system and more recently have reported similar data for the K, $Na + CH_3NO_2$ system [8]. In this work we proposed a simple model involving an ionic doorway state to account for the

§ Dept. de Física da Faculdade de Ciencias & Tecnologia (U.N.L.).
‖ Dept. de Física do Instituto Superior Técnico (U.T.L.).

collision channels leading to the ground electronic state of the molecule. We further suggested that various electronically excited states of the alkyl halide might be populated by a similar mechanism involving *excited* doorway states. The main basis for this hypothesis being the comparatively low angular onsets observed for these processes.

In the present paper this hypothesis is tested by comparing the model predictions with *fourteen* distinct exit channels over a significant collision energy range. In particular, recent results for the angular dependence for ion pair production [9] as well as the neutral inelastic channels (including some observations at other energies from those previously reported) are now available. Taken together with information from reactive scattering and other sources of potential data this information provides a stringent test for the basic premises of this model.

## 2. Experimental

The differential cross sections for neutral inelastic scattering were measured in Edinburgh using apparatus that has already been described [10]. The fast alkali beam is produced by charge exchange and pulse modulated for time of flight purposes using a velocity compression technique. The flight time of the scattered alkali atoms is recorded. Measurements have been made for centre of mass collision energies between 81 and 278 eV.

The differential cross sections for ion pair formation were measured in Lisbon at centre of mass energies ranging from 24 to 314 eV. Time of flight measurements as well as time correlation between positive and negative ion species were performed in order to discriminate the possible ionic exit channels $K^+ + CH_3I^-$ and $K^+ + I^-$. The experimental details have been presented elsewhere [9, 11].

## 3. The model

### 3.1. *Algorithm*

The potentials for these systems (as for almost all chemical systems) are not well known, although a variety of fragmentary information is available. In this paper we seek to establish the dynamical mechanism and *not* to invert the data to obtain full potential surface information. Thus a simple model, capable of reproducing the key features in the data with a minimum of adjustable parameters is appropriate.

In these systems the simplest intermediates coupling ground and excited states will be of an ionic character. The attractive Coulomb force will lead to onset of excitation processes at narrow angles as observed experimentally. The potential curves used in this model are shown in figure 1 and the excitation processes considered listed in table 1.

An electron transition is possible both on entering and leaving the interaction region. Thus a specified exit channel can be reached via an ionic intermediiate in two ways corresponding to either an early or late crossing to the ionic surface. The de Broglie wavelength associated with the nuclear motion is small compared to the potential gradient (except in the immediate vicinity of the diabatic crossings) so the nuclear motion can be treated classically. The transition probabilities are calculated at each crossing point encountered

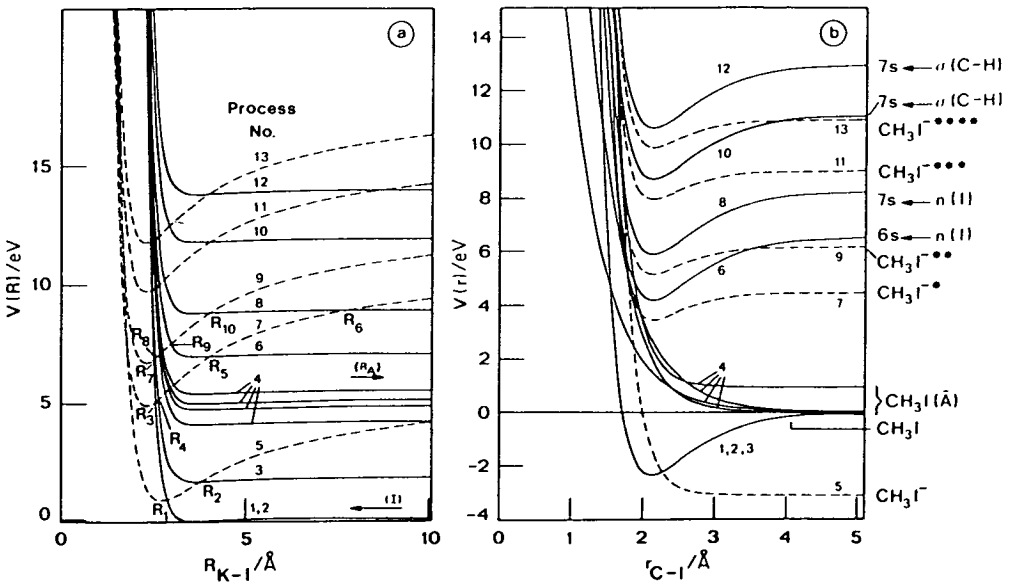


Figure 1. (*a*) K–$CH_3I$ diabatic potentials displayed as a cut through the full surface with the molecule at its equilibrium geometry. The potentials are labelled with the process number specified in table 1. Ionic states are drawn dashed. (I) incident channel. ($R_A$) crossing of **A** state with the ground ionic state. (*b*) $CH_3$–I potentials ; process numbers as in table 1.

Table 1. Modelled processes.

| Process No. | Exit channel | Comments |
|---|---|---|
| 1 | $K(4s)+CH_3I$ | Elastic |
| 2 | $K(4s)+CH_3I(v)$ | Vibrational excitation |
| 3 | $K(4p)+CH_3I(v)$ | Early and late contributions |
| 4 | $K(4s)+CH_3I(\mathbf{A})$ | **A** state excitation (4 states) |
| 5 | $K^+ + (CH_3I)^-$ | Ground ion pair |
| 6 | $K(4s)+CH_3I(6s)$ | Rydberg excitation from ' I ' lone pair |
| 7 | $K^+ + (CH_3I^-)*$ | 1st excited ion pair<br>(Double Rydberg with *n*(I) vacancy) |
| 8 | $K(4s)+CH_3I(7s)$ | Rydberg excitation from ' I ' lone pair |
| 9 | $K^+ + (CH_3I^-)**$ | 2nd excited ion pair<br>(Double Rydberg with *n*(I) vacancy) |
| 10 | $K(4s)+CH_3I(6s)$ | Rydberg excitation from σ(C–H) |
| 11 | $K^+ + (CH_3I^-)***$ | 3rd excited ion pair<br>(Double Rydberg with σ(C–H) vacnacy) |
| 12 | $K(4s)+CH_3I(7s)$ | Rydberg excitation from σ(C–H) |
| 13 | $K^+ + (CH_3I^-)****$ | 4th excited ion pair<br>(Double Rydberg with σ(C–H) vacancy) |

and the overall probability of emerging in a given exit state evaluated. The experimental measurements are all made in the narrow scattering angle, fast collision regime. The trajectories are therefore approximately linear and of almost constant velocity so that the dynamical calculation can be considerably simplified. In particular it is possible to make use of the small angle formula [12] to calculate the deflection function by summing the contributions of each different section of potential encountered during the collision

$$\chi(b) = \frac{b}{E} \sum_i \int_{R_{ci}}^{R_{ci+1}} \frac{dV}{dR} (R^2 - b^2)^{-1/2} \, dR, \tag{3.1}$$

where $i$ is a number of different sections, $\chi$ is the angle of deflection, $E$ the collision energy, $b$ the impact parameter and $V$ the potential. In the case of inverse power potentials ($V = CR^{-s}$) the contribution of each section can be evaluated analytically using the result

$$b^s \chi_i(b) = \frac{sC}{E} \int_{\sin^{-1}(b/R_{ci})}^{\sin^{-1}(b/R_{ci+1})} \sin^s \theta \, d\theta, \tag{3.2}$$

where the substitution $b/R = \sin\theta$ is used. The classical differential cross section is given by

$$\sigma(\chi) = \frac{b}{\sin\chi |d\chi/db|}. \tag{3.3}$$

We assume the non-adiabatic transitions are localized and vertical and use the standard Landau–Zener result [13]

$$P_{12}(b) = \exp \frac{-2\pi H_{12}^2}{\hbar v_r(b) |S_1 - S_2| R_c} \tag{3.4}$$

for the diabatic transition probability that a system in state 1 will cross into state 2 at the point $R_c$ where $S_1$ and $S_2$ are the gradients of the diabetic potentials at the crossing point $R_c$, $H_{12}$ the off-diagonal coupling term and $v_r(b)$ the radial velocity. The matrix element $H_{12}$ is parametrized as :

$$H_{12}(R_c) = H_{12} \exp(0{\cdot}7(R_c - R'_c)), \tag{3.5}$$

where $R'_c$ is the new crossing radius on exit from the ground ion state and this relation gives an exponential decay with crossing distance as generally suggested [14].

In the computation the motion between successive surface crossing points is treated independently in the collision coordinate ($R$) and the internal target coordinate ($r$) (the $CH_3$ group is regarded as structureless). The total deflection along any trajectory, exploring a number of different potential surfaces is then the sum of the individual contributions calculated between successive crossing points using the small angle result, equation (3.1). However, the location of the crossing point $R_{ci}$ is a function of the internal target coordinate (bond length) and the $R_{ci}$ are revised iteratively as the bond length varies. Thus during the collision lifetime typical of these experiments, $10^{-14}$ s, transitions to the ground ionic surface will expand the C–I distance, increase the electron affinity and hence move the related crossing distance, $R'_{ci}$, further out. (The reverse effect appears to occur in the excited **A** states of the molecule and is discussed later.)

The molecular nature of the target is therefore only manifest via the changes in the location of the crossing seams produced by its internal motion.

### 3.2. *Potential surfaces*

In the present work the $CH_3I$ molecule is assumed to be isotropic with the potential parameters appropriate to interaction with the I end of the molecule. Previously [7], some features of the neutral differential cross section, especially the elastic cross section, had been interpreted in terms of molecular anisotropy. In the present model, however, some of these features appear to arise as a result of contributions from an excited ion state and the anisotropy of the molecule now appears to be less significant. The potentials used in the model are shown as a cut through the surface at the molecular equilibrium distance $r_{eq}$ in figure 1 (*a*) and were of the following form :

(*a*) For the K–$CH_3I$, $R$ coordinate.

(i) Covalent potentials

$$V(R)_{K-CH_3I} = 4\epsilon\left[\left(\frac{\sigma}{R}\right)^{12} - \left(\frac{\sigma}{R}\right)^{6}\right] + E_{exc} \tag{3.6}$$

where $E_{exc}$ is the electronic excitation energy of the atom or molecule.

(ii) Ionic potentials

$$V(R)_{K^+-(CH_3I)^-} = A\left(\frac{R_m}{R}\right)^5 - 14{\cdot}4\left(\frac{\alpha}{R^4} + \frac{1}{R}\right) + \text{I.P.} - EA_{CH_3I} \tag{3.7}$$

and

$$V(R)_{K^+-(CH_3I^-)^*} = A'\left(\frac{R_m}{R}\right)^5 - 14{\cdot}4\left(\frac{\alpha'}{R^4} + \frac{1}{R}\right) + \text{I.P.} + E'_{exc}, \tag{3.8}$$

where I.P. is the ionization potential of the potassium atom (4·3 eV), $EA_{CH_3I}$ is the electron affinity of the molecule in the ground state and $E'_{exc}$ is the excitation energy at the equilibrium $CH_3$–I distance.

(*b*) For the $CH_3I$, $r$ coordinate the potential forms are displayed in figure 1 (*b*).

(i) Covalent potentials. Their relative position is appropriate for electron attachment but for the construction of the surface it is convenient to include the molecular excitation in the K–$CH_3I$ interaction.

Covalent with the exception of the **A** states

$$V(r)_{CH_3-I} = D_{cov}(\exp(-2\beta_{cov}(r - r_{eq})) - 2\exp(-\beta_{cov}(r - r_{eq}))). \tag{3.9}$$

**A** states

$$V(r)_{CH_3-I} = A\exp(-B(r - r_{eq})). \tag{3.10}$$

These are based on the 3 potentials found by Clear *et al.* [15] for the **A** states of HI together with one other potential.

(ii) Ionic potentials

Ground ionic

$$V(r)_{CH_3-I^-} = D_{ion} \exp(-\beta_{ion}(r - r_{eq})) + V^{(3)}(r, R) \qquad (3.11)$$

where $V^{(3)}(r, R)$ is the '3-body' potential barrier inserted to constrain the C–I bond expansion. This potential is significant only in the close encounter region.

Table 2. Potential parameters.

| K–$CH_3I$ | | $CH_3$–I | | | | |
|---|---|---|---|---|---|---|
| Neutral states | | Neutral states | | | Ionic states | |
| $\epsilon$/eV | 0·11 (*a*) | $D_{cov}$/eV | 2·33 (*h*) | | $D_{ion}$/eV | 1·65 (*h*) |
| $\sigma$/Å | 3·2 (*a*) | $\beta_{cov}$/Å$^{-1}$ | 3·4 (*h*) | | $\beta_{ion}$/Å$^{-1}$ | 4·65 (*h*) |
| Process no. | $E_{exc}$/eV | $r_{eq}$/Å | 2·14 (*i*) | | $EA_1$/eV | 3·063 (*i*) |
| 1, 2 | 0·0 | *A* states | | | $V^{(3)}(r, R)$ term | |
| 3 | 1·6 (*b*) | $^1\Pi$ | *A*/eV | 2·709(2·711 (*c*))† | BARR/eV | 1·4 |
| 4 | 3·8–5·0 (*c*) | $^3\Pi_1$ | *A*/eV | 1·96 (*c*) | $R_{on}$/Å | 10·0 |
| 6 | 6·5 (*d*) | $^3\Pi_0$ | *A*/eV | 1·5† | $r_{on}$/Å | 2·5 |
| 8 | 8·2 (*d*) | $^3\Pi_{0+}$ | *A*/eV | 1·396 (*c*) | $r_{off}$/Å | 3·5 |
| Ground ionic state | | $^1\Pi$ | *B*/Å$^{-1}$ | 1·9 (*c*) | Excited ionic state | |
| *A*/eV | 0·845(1·5 (*a*))† | $^3\Pi_1$ | *B*/Å$^{-1}$ | 2·85 (*c*) | $D'_{ion}$/eV | 1·0† |
| $R_m$/Å | 3·2 (*e*) | $^3\Pi_0$ | *B*/Å$^{-1}$ | 1·9† | $\beta_{ion}$/Å$^{-1}$ | 4·65 |
| $\alpha$/Å$^3$ | 4·0 (*f*) | $^3\Pi_{0+}$ | *B*/Å$^{-1}$ | 4·1(*c*) | | |
| Excited ionic states | | | | | | |
| *A*′/eV | 0·75† | | | | | |
| $R_m$/Å | 3·2 | | | | | |
| $\alpha'$/Å$^3$ | 6·25† | | | | | |
| $EA_{CH_3I}$/eV | 0·94 (*h*) | | | | | |
| Process no. | $E'_{exc}$/eV | | | | | |
| 7 | 5·8 (*g*) | | | | | |
| 9 | 7·5 (*g*) | | | | | |

† Values have been adjusted to fit the experimental results. Where data is available for these parameters it has been given in brackets after the value used in the model.

(*a*) Fitted to potential of Evers, C., 1977, *Chem. Phys.*, **21**, 355.
(*b*) Bacher, R. F., and Goudsmit, S., 1932, *Atomic Energy States* (McGraw-Hill), p. 245.
(*c*) Clear, R. D., Riley, S. J., and Wilson, K. R., 1975, *J. chem. Phys.*, **63**, 1340.
(*d*) Boschi, R. A., and Salahub, D. R., 1972, *Molec. Phys.*, **24**, 289.
(*e*) Rittner, E. S., 1951, *J. chem. Phys.*, **19**, 1030.
(*f*) Brumer, P., and Karplus, M., 1973, *J. chem. Phys.*, **58**, 3903, [$\alpha = (\alpha_{K^+} + \alpha_{I^-})/2$].
(*g*) Deduced from Spalburg, M. R., 1981, Doctoral Scriptie, Universteit van Amsterdam.
(*h*) Wentworth, W. E., George, R., and Keith, H., 1969, *J. chem. Phys.*, **51**, 1791.
(*i*) LaBudde, R. A., Kuntz, P. J., Bernstein, R. B., and Levine, R. D., 1973, *J. chem. Phys.*, **59**, 6286.

Table 3. Coupling parameters for $K + CH_3I$.

| Crossing radius as marked on figure 1 | R1 | R2 | R3 | R4 | R5 | R6 | R7 | R8 | R9 | R10 |
|---|---|---|---|---|---|---|---|---|---|---|
| Crossing radius/Å (at $r_{eq}$) | 2·868 | 3·800 | 2·564 | 2·637 | 4·060 | 7·748 | 2·509 | 2·561 | 2·981 | 4·060 |
| $H$/eV | 0·442 | 0·089 | 0·334 | 0·277 | 0·030 | 0·001 | 0·498 | 0·168 | 0·021 | 0·030 |

Note. The intensities of processes fed from the two highest excited ion states (11 and 13) have not been fitted to the observed intensities so that the appropriate coupling parameters have not been inferred.

$$V^{(3)}(r, R) = \mathrm{BARR}\tanh(4(R_{on} - R))(\tanh(1{\cdot}8(r - r_{on})) - \tanh(1{\cdot}8(r - r_{off}))). \quad (3.12)$$

Excited ionic

$$V(r)_{(CH_3-I^-)^*} = D'_{ion}(\exp(-\beta_{ion}(r - r_{eq})) - 2\exp(-\tfrac{1}{2}\beta_{ion}(r - r_{eq}))). \quad (3.13)$$

The electronic excitation energy ($E'_{exc}$) is included in the $K$–$CH_3I$ interaction. The values for all the potential parameters are given in table 2. The parameters adjusted to obtain a fit are indicated by a dagger. The values of the coupling parameters used in the Landau–Zener expression (3.3) are given in table 3 along with the crossing radii for the C–I at its equilibrium bond length. The values used for $H_{12}$ are shown in figure 2 in comparison with the trend line obtained from other experimental derived data available for one electron transfer process [14]. They show an exponential decrease with $R_c$ but are somewhat smaller. The crossings corresponding to the excited states have the larger differences.

## 4. Results and discussion

The energy losses observed in the neutral experiments for different collision energies are given in table 4 together with their previous assignment. The model now includes all these observed processes with the exception of process 14 which was provisionally assigned, [7], as $n(I) \rightarrow \sigma^*(C\text{–}H)$ and involved capture into the $\sigma^*$(C–H) followed by recapture of an electron from the iodine lone pairs. This exclusion necessarily follows from our treatment of $-CH_3$ as a structureless particle.

### 4.1. *Vibrational and alkali atom excitation*

These processes can extend up to 4·3 eV, the ionization potential for potassium ; however, experimentally only the $K(4\,^2P)$ excitation appears to be significant. The model predicts two exit channels both corresponding to electronic excitation of the $K(4\,^2P)$ state but with different amounts of vibrational excitation of the molecule corresponding to crossing onto the ground ionic surface on the way into the collision or on leaving it. It also predicts an exit channel corresponding to vibrational excitation of the molecule without electronic excitation (process 2). At 81 eV CM (figure 3) two sets of energy losses are observed below 1·6 eV (the

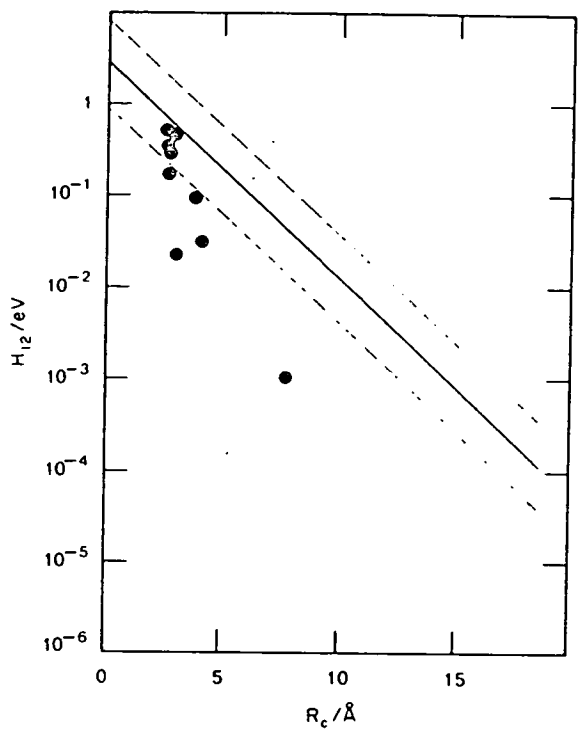


Figure 2. Comparison of coupling matrix elements (table 3) with the trend line obtained from other experimental derived data available for one electron transfer process [14] (solid line). Most of the experimental derived data lie within a factor of 3 (dashed line).

first excitation energy of potassium). This feature emerges naturally from the model as a rainbow in the ionic well. Figure 4 shows the observed energy losses plotted against the inverse of the collision velocity. It can be seen that processes 2 and 3, proceeding via the ground ionic surface, show a vibrational excitation that increases with collision lifetime while the **A** states show no clear trend. The solid lines in the figure are the average energy losses for each process as calculated by the model. The predicted vibrational excitation increases as the collision lifetime allows the C–I bond to stretch.

It was found that the model energy losses were particularly sensitive to the form of the $C–I^-$ repulsive potential. As discussed in the previous paper [7] it is necessary to include a 3 body term in the ionic surface which has the effect of considerably reducing the repulsive strength of the $C–I^-$ interaction when a $K^+$ ion is adjacent. This term possibly represents the effect of polarization in depleting the electron population in the $2\sigma^*$ orbital. In the absence of such a term the model almost invariably predicts that early electron crossing collisions result in dissociation to form $I^-$ ions—in contrast to the observed importance of the neutral inelastic channels.

Table 4. Experimentally observed energy losses. Neutral scattering.

| Model process No. Collision energy cm/eV | Observed energy loss/eV | | | | Proposed assignment | Predicted electronic energy loss/eV |
|---|---|---|---|---|---|---|
| | 81 | 106 | 164 | 218† | | |
| 1 | 0·0 | 0·0 | 0·0 | 0·0 | Elastic | 0·0 |
| 2 | 0·6 | | 1·0 | | Vib. energy in C–I bond | 0·0 |
| | 1·3 | 1·2 | | | | |
| 3 | 2·0 | 1·9 | 1·7 | (1·4) | $4s \rightarrow 4p$ | 1·6 [26] |
| | 3·1 | 3·1 | 2·8 | | | |
| 4 | 4·0 | 4·0 | 4·2 | | | |
| | 4·3 | | 4·8 | (5·0) | $n(\mathrm{I}) \rightarrow \sigma^*(\mathrm{C–I})$ | 3·5–5·5 [17] |
| | 5·0 | | 5·5 | | | |
| | 5·6 | 5·6 | | | | |
| 6 | 6·4 | | 6·4 | (7·0) | $n(\mathrm{I}) \rightarrow 6s$ Rydberg | 6·5 [22] |
| 8 | 8·0 | 8·6 | 8·4 | | $n(\mathrm{I}) \rightarrow 7s$ Rydberg | 8·2 [22] |
| 10 | Higher energy loss processes | 11·3 | 10·4 | (10·2) | $\sigma_p(\mathrm{C–H}) \rightarrow 6s$ Rydberg | 11·0 [27] |
| 12 | obscured by $^{41}$K isotope | 13·4 | 12·4 | | $\sigma_p(\mathrm{C–H}) \rightarrow 7s$ Rydberg | 12·9 [27] |
| (not modelled) | 6–7·2 in $E$ range 40–220 eV° | | 6·4–9·0 in $E$ range 60–900 eV° | | $n(\mathrm{I}) \rightarrow \sigma^*(\mathrm{C–H})$ | ~6·0 [28] |

† At 218 eV collision energy the resolution is insufficient to distinguish the separate contributions.

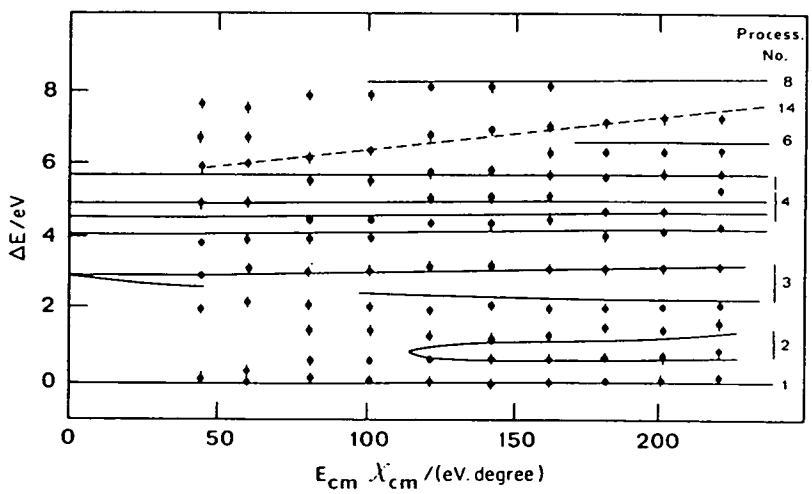


Figure 3. Inelastic neutral scattering at 81 eV cm collision energy. The observed energy losses as a function of scattering angle are compared with the model predictions (solid line). Process 14 (dashed line) is not modelled.

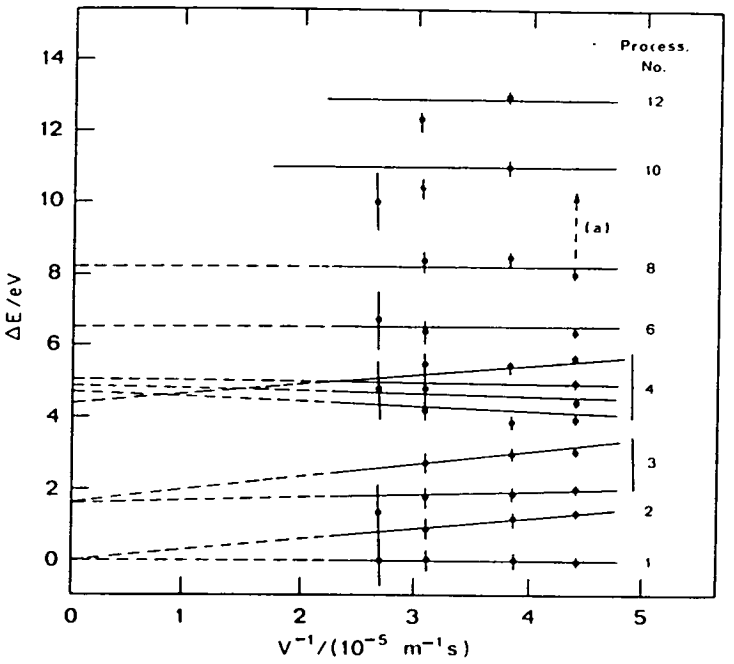


Figure 4. Average channel energy losses as a function of the inverse of the initial collision velocity. The solid lines are the model prediction. (*a*) Higher energy loss processes obscured by isotope.

The ground ionic potential surface required to achieve a satisfactory fit together with a typical trajectory are illustrated in figure 5. It should be noted that the large '*r*' dependence in this barrier is not probed by these experiments. More detailed comparisons between the model and the observations, including energy loss and differential cross sections for the four neutral channels which are populated via the ground ionic surface are shown in figures 6 and 7.

Further information on the ionic surfaces is available from the differential ion production cross section measurements. These are shown for a number of collision energies in figure 8. At the lowest angles (60 eV degree) the time correlation measurements showed the ionic product to be exclusively $I^-$, an increasing fraction of $CH_3I^-$ is however seen at larger $E$ and collision energies [9]. As the collision energy increases, the peak in the cross section moves steadily to wider angles and in some cases (figure 10) can be seen to be a series of distinct angular peaks. The relative intensity of each peak changes rather rapidly with collision velocity to give, at the experimental resolution, the appearance of a single peak moving in angle as the collision velocity varies. Figure 9 illustrates this point and show the model results for the first three ionic states (figure 1). (The other two higher lying ionic states shown in figure 1 will be discussed in a later section.) The observed peaks are seen to be rainbows and provide an excellent probe for the well depth in these states. If these ionic states are not dissociative this model also accounts for the observation of $CH_3I^-$ ions at the wider scattering angles. A similar fit for the $Cs + CH_3I$ system is shown in figure 10.

In general the model, with its limited parametrization, gives excellent agreement in both the neutral and ion channels—confirming the previous picture for these processes.

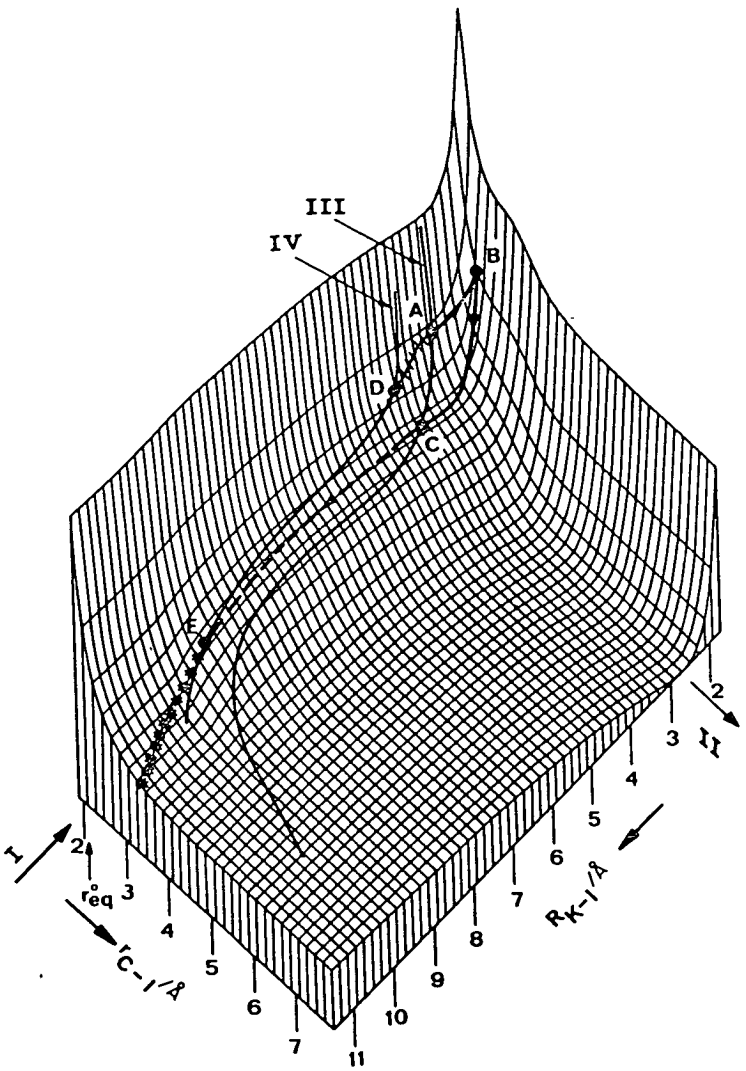


Figure 5. Ground ionic surface showing the effect of the three body term in the potential. I entrance on the ground covalent surface ; II reactive channel. The solid lines III and IV are the crossing seams $K(4\,^2S)$ and $K(4\,^2P)$ to ionic respectively. The trajectories for a collision energy of 81 eV cm and impact parameter of 1·91 Å are also drawn. The processes 2 (→——), 3, early crossing (— → —) and 5 (***), ionic trajectory, have an initial jump into the ionic surface at *A*. The turning point is *B*. Process 2 exists to $K(4\,^2S)$ at *C*. Process 3, early crossing exits $K(4\,^2P)$ at *E*. Process 5, ionic trajectory, continues on the surface. The process 3, late crossing, (× × ×), has an initial jump into the ionic surface at *A* and exits to $K(4\,^2P)$ at *D*.

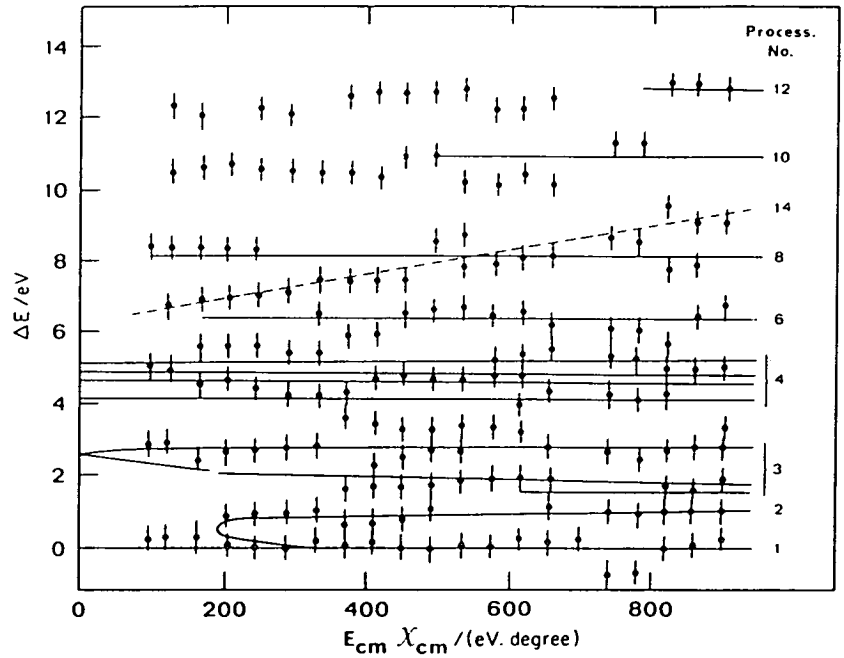


Figure 6. Inelastic neutral scattering as in figure 3 but at 164 eV cm collision energy.

Interestingly it should be noted that although the processes discussed in this section are dominantly connected to the ground ionic state there is nevertheless a small contribution to the neutral scattering which samples the higher excited ionic surfaces. A consequence, which finds some support in the structure seen at wider angles in process 1.

### 4.2. **A** *state excitation*

The **A** states of the neutral molecule are repulsive and lead to dissociation of the molecule [16]. Optically these are observed to onset in the range 3·5–4·5 eV reaching a maximum about 1 eV above onset [17]. The continuum observed involves transitions to several states including those dissociating to $I_{1/2}$ and $I_{3/2}$. Collision induced transitions would be expected to give discrete energy losses as a result of vertical transitions in the same way as described for the excited $K$ states. Inspection of the potential model, figure 1, shows that it is just possible to ' feed ' these states from the ground ionic surface with the molecule in its equilibrium configuration. The crossing of the K–$CH_3I$ (**A**) potentials with the ground ion curve in the equilibrium geometry are very far out, so that the crossing probability would be small. In the case of transitions to the bound, ground state of $CH_3I$ the electron affinity increases rapidly with C–I stretch. In contrast, the repulsive **A** states show a constant or decreasing electron affinity (depending upon the relative shapes of the ground ionic and **A** state potential surfaces). The crossing radius, $R_c$, between the excited molecular **A** states and the ionic surface can thus actually decrease during the collision as the C–I bond stretches : a natural consequence of the similar electron configurations and potential surfaces in these two states already

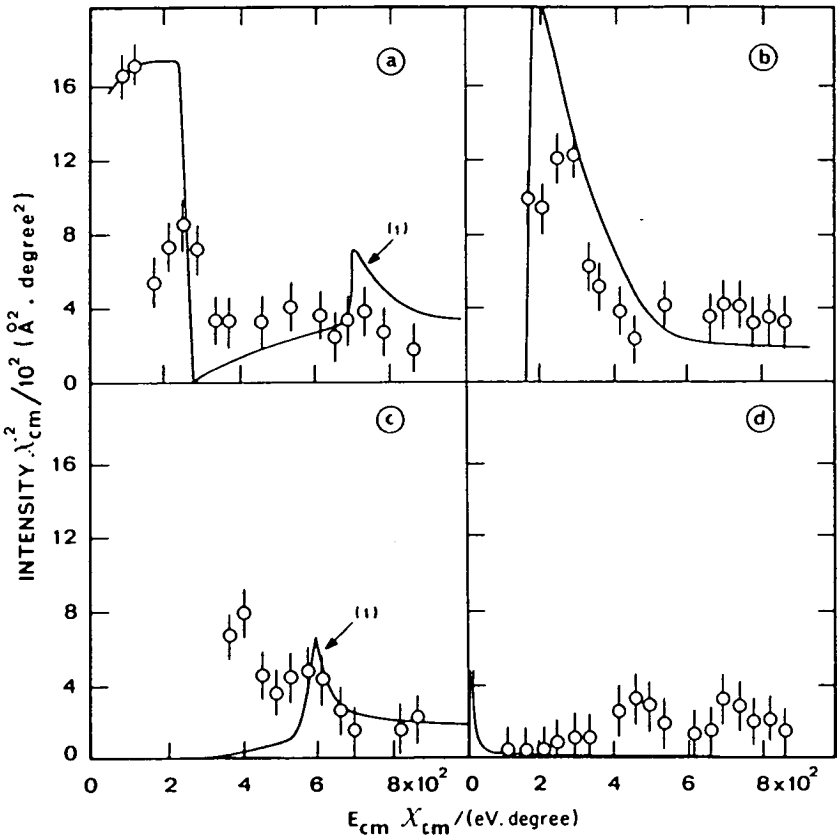


Figure 7. Relative differential cross section for neutral channel at 164 eV cm collision energy. Model prediction is solid line. (*a*) Process 1 Elastic. (*b*) Process 2 Vibrational excitation of $CH_3I$. (*c*) and (*d*) Process 3 late (*c*) and early (*d*) crossing to ionic surface followed by $K(4\,^2P)$ excitation. (1) Contribution from first excited ion state via early crossing at $R_3$ (figure 1 (*a*)).

remarked by Herschbach [18]. This mechanism offers a plausible route to the population of these states. This conjecture is supported by the model results which show that physically realistic estimates for the potentials and coupling terms reproduce the observations rather well and in particular can account for the narrow reduced angle at which these processes onset.

### 4.3. *Excited ionic states*

The existence of a number of excited ionic states of $CH_3I$ formed in collision with Na atoms and having excitation energies from about 8 eV upwards has already been suggested on the basis of energy loss spectra of $Na^+$ ions [19]. The existence of such states was also proposed in our previous paper [7]. The present differential ion production measurements provide further evidence for these states the first of the excited levels having an energy of 7·5 eV relative to the asymptote of the ground ion in the present model.

The lifetime and electron configuration of these species are unknown but it is likely that a valence or non-bonding electron, probably from the $n$(I)

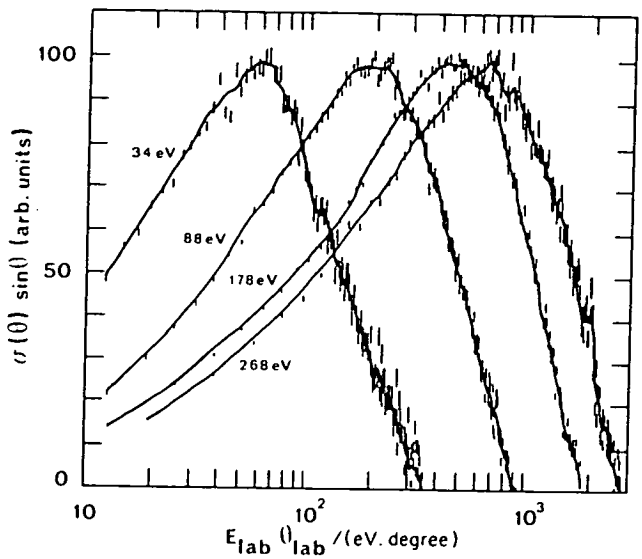


Figure 8. Differential cross sections for ion formation at the indicated laboratory collison energies.

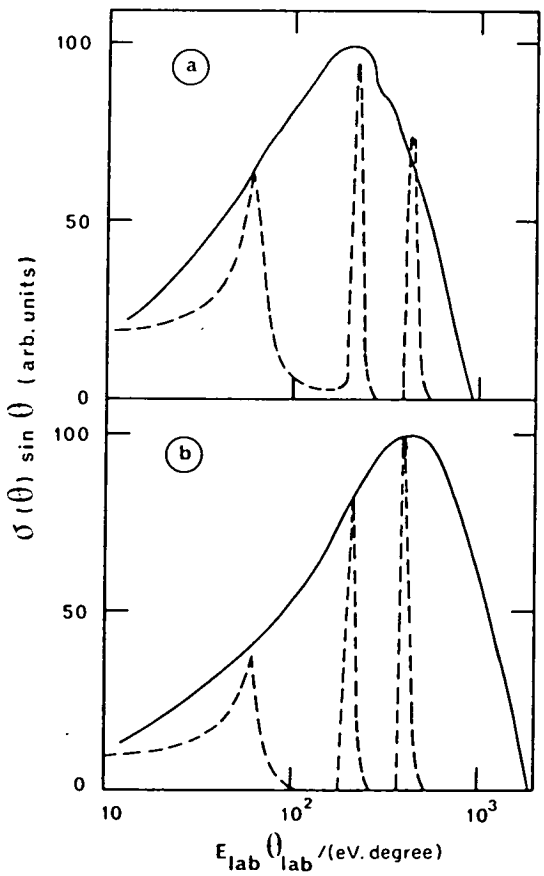


Figure 9. Differential cross sections for ion pair formation, $K + CH_3I$. Experimental solid line, model prediction dashed. (*a*) 88 eV lab. (*b*) 178 eV lab.

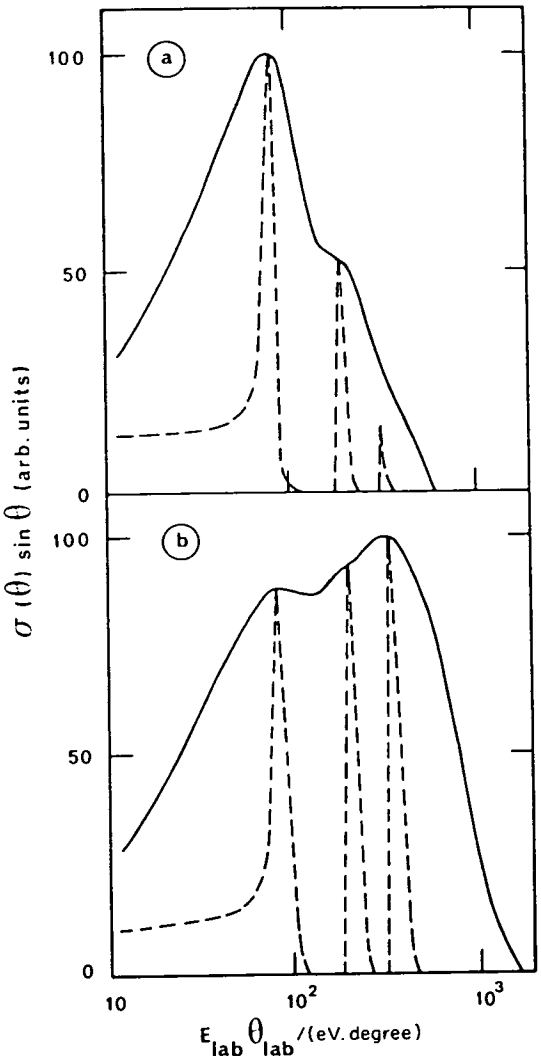


Figure 10. Differential cross section for ion pair formation, $Cs + CH_3I$. Experimental solid line, model prediction dashed. (*a*) 52 eV lab. (*b*) 142 eV lab.

orbital, is prompted to leave a core vacancy. Since little or no vibrational excitation is observed in the molecular Rydberg processes (figures 3 and 6) and $CH_3I^-$ ions are observed it seems unlikely that a vacancy in a bonding orbital is created or that the $2\sigma^*$, antibonding, orbital is populated. We thus hypothesize that the two active electrons in an excited negative ion (one promoted, one donated) are accommodated in molecular Rydberg levels—probably stabilized by the adjacent alkali ions. Such double excited negative ions have been observed in Xe as resonances in the electron scattering [20] and more recently in $He^-$ [21].

As previously described the three lowest ionic surfaces shown in figure 1 have been fitted to the ion pair differential cross sections—though no attempt

has been made to account for the width of the Franck Condon region or the apparatus resolution. The agreement is excellent.

The two highest ion pair states shown in figure 1 were introduced in a more speculative fashion since ion states in this region could provide a gateway to the neutral processes 10 and 12 which probably involve different core vacancies. It is interesting to note that the experimental ion pair cross section shows some evidence for such peaks in the appropriate regions (figure 8) though the resolution is not adequate to permit an unequivocal statement. The production of vacancies in the C–H bonding orbitals would be expected to produce significant vibrational excitation in these ions.

### 4.4. *Molecular Rydberg excitations*

The strongest Rydberg transitions observed spectroscopically are to excited *s* and *d* orbitals [22]. The lowest *s* orbital will be 6*s* and the lowest *d* orbital 5*d* (which cannot be distinguished energetically from the 7*s* orbital in the present experiments). Higher Rydberg states although available in principle will have considerably smaller coupling matrix elements due to the larger size of these orbitals and are unlikely to be important. The spin–orbit splitting in these levels is comparable to the energy resolution of the experiments so that an average of the two energy levels has been used in the calculations. Four excitation processes observed experimentally have been tentatively assigned to Rydberg levels, table 4. All of these processes onset at very low scattering angles (figure 6) an observation that can most readily be explained by an intermediate in which $dV/dR_{K-I}$ is predominantly positive to scatter the K atom into the forward direction. These excited neutral states cannot intersect with the ground ion pair state and the observed excited ion states provide an obvious mechanism. If the electron promoted to a Rydberg level is from a non bonding orbital the C–I force constant and equilibrium distance [17] would be unchanged in both the ion and neutral states. Little or no vibrational excitation would then be expected to occur in conjunction with these transitions. This picture when incorporated in the model accounts rather well for the observations in processes 6 and 8 in figure 6, including the narrow angle onset.

It seems possible that the higher neutral excitation processes (10 and 12), almost certainly involving a different core vacancy can be populated in an analogous way by the highest ionic states tentatively identified in the previous section. These states would be expected to show substantial vibrational excitation with a strong dependence on collision lifetime (because of the small reduced mass of the C–H oscillator). Interestingly, such a trend is observed in processes 10 and 12, figure 4, though we have not attempted to model this effect.

### 4.5. *Correlation diagram*

A diabatic correlation diagram, drawn according to the Barat rules [23], for the Xe/K system is shown in figure 11. Xe provides a good model for the excited states of $CH_3I$ [24, 25]. The approximate molecular orbitals for $CH_3I$ and their correlation to the Xe atom for the linear configuration are also shown. The high atomic numbers involved in these systems make the diagram complex. However a number of relevant features can be seen. Firstly, the $4sK(5p\sigma)$ orbital has an early crossing with the $7h\sigma$ orbital (which correlates to

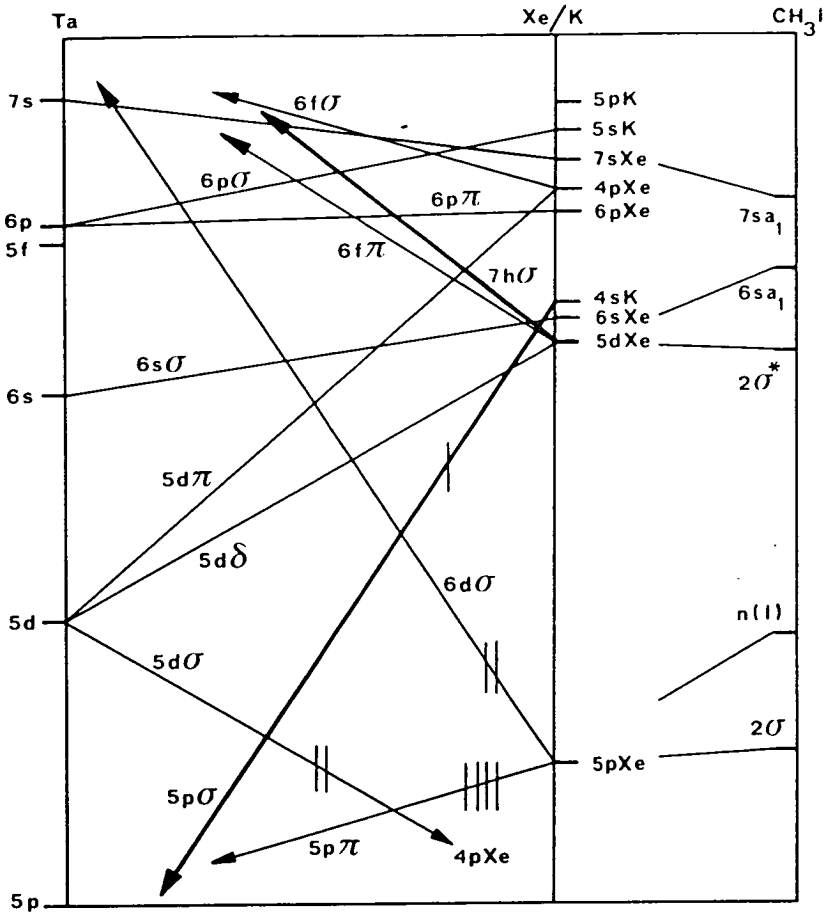


Figure 11. Diabatic correlation diagram for K+Xe. The significant $CH_3I$ orbitals are also shown.

the $2\sigma^*$ $CH_3I$ orbital). Thus electron transfer to form the ground ion pair state is expected in accord with experiment. The $7h\sigma$ orbital is strongly promoted so that crossings with a range of excited orbitals can occur. Thus the $5d\pi$, $6p\sigma$ orbitals correlating to excited $4p$, $5s$ levels of the atom are accessible by this route.

Additionally we note that the $5p$ orbital, either vacant or half-full plunges in energy and is available to create inner vacancies by capture from the core. Thus the production of the excited ions and Rydberg neutral species could be rationalized by the following sequence. An initial electron transfer from K to the $6s$ Rydberg level of $CH_3I^-$, $4sK \rightarrow 6s\sigma$, is followed by the production of a core vacancy, $5p\pi \rightarrow 5p$, $5p\sigma \rightarrow 6s\sigma$, to yield $CH_3I^{-*}$ ($5p^5\,6s^2$). Electron recapture by the $K^+$ ion, $6s\sigma \rightarrow 4sK$, then yields the neutral Rydberg levels of $CH_3I$.

## 5. Conclusions

The combination of experimental data for ion pair production and neutral inelastic scattering over a wide energy and angular range has provided tight constraints on the dynamics of these collisions. Comparison of these results with a simple dynamical model then yields an insight into the electronic rearrangements involved in the collision.

In particular, the importance of an ion pair intermediate as the doorway to atomic excitation, vibrational excitation of the $CH_3I$ (in its ground electronic state), $CH_3I(\mathbf{A})$ and $I^-$, $K^+$ ions is confirmed. It is shown that this intermediate is markedly less repulsive in the C–I coordinate than the free molecular ion–structural information not easily accessible by other methods.

The formation of excited ion pair states is also observed in these collisions. It is suggested that these states are analogous to resonances observed in electron scattering from Xe and involve similar core vacancies. Such states are shown to provide a plausible mechanism for the production of the highly excited neutral states of the alkyl halide which are also produced in these collisions. Finally it is suggested that electron donation *to* the alkali metal plays an important part in the creation of the vacancies in the valence shell required by the proposed mechanism : the whales revenge!

Support from the North Atlantic Treaty Organization for this work is gratefully acknowledged.

## References

[1] Magee, J. C., 1940, *J. chem. Phys.*, **8**, 687.
[2] Herschbach, D. R., 1966, *Adv. chem. Phys.*, **10**, 319.
[3] Herm, R. R., 1979, *Alkali Halide Vapours*, edited by P. Davidovits and D. L. McFadden (Academic Press), p. 189.
[4] Lacmann, K., 1980, *Adv. chem. Phys.*, **42**, 513.
[5] Los, J., and Kleyn, A. W., 1979, *Alkali Halide Vapours*, edited by P. Davidovits and D. L. McFadden (Academic Press), p. 275.
[6] Bernstein, R. B., 1979, *Atom–Molecule Collision Theory* (Plenum Press).
[7] Fluendy, M. A. D., Lawley, K. P., Sholeen, C., Sutton, D., 1981, *Molec. Phys.*, **42**, 1.
[8] Fluendy, M. A. D., and Lunt, S. L., 1983, *Molec. Phys.*, **49**, 1007.
[9] Praxedes, A. J. F., Maneira, M. J. P., and Moutinho, A. M. C., 1983, *13th Int. Conf. on Phys. Electron and Atomic Collision* (ICPEAC).
[10] Fluendy, M. A. D., Lawley, K. P., McCall, J., Sholeen, C., and Sutton, D., 1979, *Faraday Discuss. chem. Soc.*, **67**, 41.
[11] Maneira, M. J. P., Praxedes, A. J. F., and Moutinha, A. M. C., 1982, *Proc. of the 13th Int. Symposium on Rarefied Gas Dynamics.*
[12] Fluendy, M. A. D., and Lawley, K. P., 1973, *Chemical Applications of Molecular Beam Scattering* (Chapman & Hall).
[13] Zener, C., 1932, *Proc. R. Soc.* A, **137**, 696.
[14] Mountinho, A. M. C., *Portgal. Phys.* (to be published).
[15] Clear, R. D., Riley, S. J., and Wilson, K. R., 1975, *J. chem. Phys.*, **63**, 1340.
[16] Riley, S. J., and Wilson, K. R., 1972, *Faraday Discuss. chem. Soc.*, **53**, 132.
[17] Herzberg, G., 1966, *Electronic Spectra of Polyatomic Molecules* (van Nostrand-Rheinhold).
[18] Herschbach, D. R., 1973, *Faraday Discuss. chem. Soc.*, **55**, 233.
[19] Spalburg, M. R., 1981, Doctoral Scriptie, Universiteit van Amsterdam.
[20] Kuyatt, C. E., Simpson, J. A., and Mielczarek, S. R., 1965, *Phys. Rev.* A, **138**, 385.

[21] Buckman, S. J., Hammond, P., Read, F. H., and King, G. C., 1983, *J. Phys.* B, **16**, 4039.
[22] Boschi, R. A., and Salahub, D. R., 1972, *Molec. Phys.*, **24**, 289.
[23] Barat, M., and Lichten, W., 1972, *Phys. Rev.*, **6**, 211.
[24] Baig, M. A., Connerade, J. P., Dagata, J., and McGlynn, S. P., 1981, *J. Phys.* B, **14**, 225.
[25] Dagata, J. A., Findley, G. L., McGlynn, S. P., Connerade, J. P., and Baig, M. A., 1981, *Phys. Rev.* A, **24**, 2485.
[26] Bacher, R. F., and Goudsmit, S., 1932, *Atomic Energy States* (McGraw-Hill), p. 245.
[27] Boschi, R. A. A., and Salahub, D. R., 1974, *Can. J. Chem.*, **52**, 1217.
[28] Hitchcock, A. P., and Brian, C. E., 1978, *J. electron. Spectrosc. rel. Phenom.*, **13**, 193.

XIII ICPEAC, Berlin (1983) Book of Abstracts, p 632

# ADIABATIC PROCESSES IN ALKALI METAL - ALKYL HALIDE MOLECULE COLLISIONS: NEUTRAL EXCITATION AND ION PAIR PRODUCTION CHANNELS

A.M.C. Moutinho and A. Praxedes

Centro de Fisica Molecular des Universidades de Lisboa,
Av. Rovisco Pais, Complexo 1-IST, 100 Lisboa, Portugal.

E. Cowan and M.A.D. Fluendy

Department of Chemistry, University of Edinburgh,
West Mains Road, Edinburgh, EH9 3JJ, Scotland.

Alkali metal/alkyl halide molecular collisions vide convenient systems in which to study non abatic effects in molecular collisions.[1,2] In trast to halogen molecules[3] alkyl halides have a ative vertical electron affinity and curve crossing ects are expected to occur at shorter ranges in these tems. At collision energies in the eV range a large ber of exit channels, including electronic, rational and ion production processes, are open and yield information on the non adiabatic effects.

In this paper measured differential cross sections vibronic excitation[4] and ion production[5] are pared with the predictions of a simple model. At energies of these experiments the trajectories are ost straight so that the deflection of the exit atom ion is a good probe for the atom/ion - molecule ential surface. The vibrational excitation observed the neutral exit channels at small deflections is ilarly sensitive to the intramolecular potential rating during the collisions.

Comparison of these results with the predictions a model based upon diabatic surfaces showed electron nsfer yielding a strongly attractive potential to be essential ingredient, Fig. 1. In the close encounter ion, however, the energy losses observed, Fig. 2, w that the C-I potential is considerably modified m that seen in the free molecular ion.

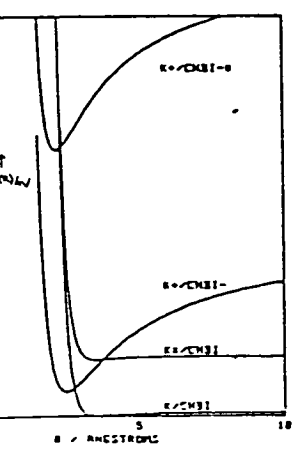

. 1 K-$CH_3I$ Potentials

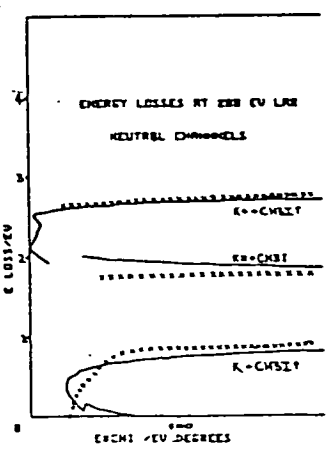

Fig. 2 Comparison of model (solid line) and experiment (XX)

The ion production cross sections, Fig. 3, are consistent with this picture but reveal the involvement of both the ground and an excited ion state, each contributing a rainbow to the observed ion scattering. The nature and possible role of this excited ion state in feeding the observed neutral excited states of the molecule - in an analogous way to the ground ion state - is under investigation.

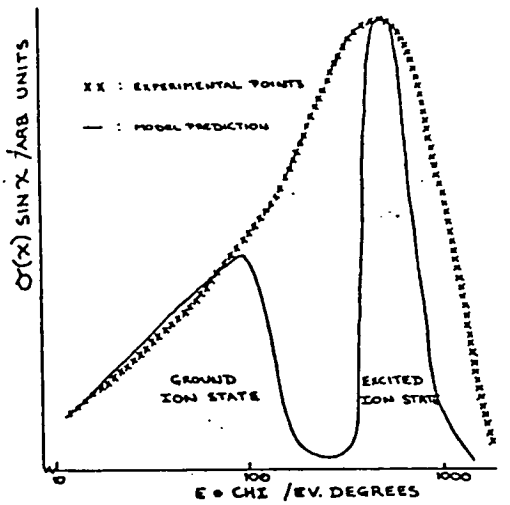


Fig. 3 Differential cross-section at 200 eV LAB Ion pair production channels

References

1. K. Lacmann, Adv. Chem. Phys. 42, 513 (1980).
2. V. Kempter, Adv. Chem. Phys. 30, 417 (1975).
3. P. Davidovits and D.L. McFadden, Alkali Halide Vapours, Academic Press.
4. M.A.D. Fluendy, K.P. Lawley, C. Sholeen and D. Sutton, Mol. Phys. 42, 1 (1981).
5. A.M.C. Moutinho and A. Praxedes, private communication.

FISICA 84 (SOCIEDADE PORTUGUESA DE FISICA)
BOOK OF ABSTRACTS, p219

# PROCESSOS NÃO ADIABÁTICOS EM COLISÕES DE K,Cs COM $CH_3I$

A.J.F.Praxedes**, E.E.B.Cowan≠, M.A.D.Fluendy≠ e A.M.C.Moutinho*+

* Centro de Física Molecular das Universidades de Lisboa ( INIC )
Av. Rovisco Pais, Complexo I - IST 1000 Lisboa, Portugal

≠ Department of Chemistry, University of Edinburgh
West Mains Road, Edinburgh EH9 3JJ, Escócia

** Dep. de Física do Instituto Superior Técnico ( U.T.L. )

*+ Dep. de Física da Fac. de Ciências e Tecnologia ( U.N.L. )

Os sistemas metal alcalino - halogeneto de metilo têm sido extensivamente estudados como exemplos típicos do mecanismo do "electrão arpoador".

Neste trabalho serão apresentados resultados experimentais referentes a canais de saída neutros e iónicos. Secções eficazes diferenciais (fig.1) para a formação de pares de iões foram medidas em Lisboa[1] para energias no centro de massa compreendidas entre 24 e 314 eV, numa versão melhorada do aparelho de feixes moleculares já descrito[2]. As secções eficazes diferenciais para os canais neutros foram realizadas em Edinburgo[3] para energias de colisão no centro de massa entre 81 e 278 eV (fig.2) envolven-

TABELA 1

| Proc. | Canais de saída | | |
|---|---|---|---|
| 1 | $K(4s) + CH_3I$ | elástico | |
| 2 | $K(4s) + CH_3I(\nu)$ | vib. (C-I) | |
| 3 | $K(4p) + CH_3I(\nu)$ | 4s-4p + vib.(C-I) | |
| 4 | $K(4s) + CH_3I(\tilde{A})$ | $n(I) \rightarrow \sigma^*(C\text{-}I)$ | |
| 5 | $K^+ + (CH_3I)^-$ | iónico fundament. | |
| 6 | $K(4s) + CH_3I(6s)$ | $n(I) \rightarrow 6s$ | Estados de Rydberg |
| 7 | $K^+ + (CH_3I^-)^*$ | duplo de n(I) | |
| 8 | $K(4s) + CH_3I(7s)$ | $n(I) \rightarrow 7s$ | |
| 9 | $K^+ + (CH_3I^-)^{**}$ | duplo de n(I) | |
| 10 | $K(4s) + CH_3I(6s)$ | $\sigma_p(C\text{-}H) \rightarrow 6s$ | |
| 11 | $K^+ + (CH_3I^-)^{***}$ | duplo de $\sigma$(C-H) | |
| 12 | $K(4s) + CH_3I(7s)$ | $\sigma_p(C\text{-}H) \rightarrow 7s$ | |
| 13 | $K^+ + (CH_3I^-)^{****}$ | duplo de $\sigma$(C-H) | |
| 14 | $K(4s) + CH_3I^*$ | $n(I) \rightarrow \sigma^*(C\text{-}H)$ | |

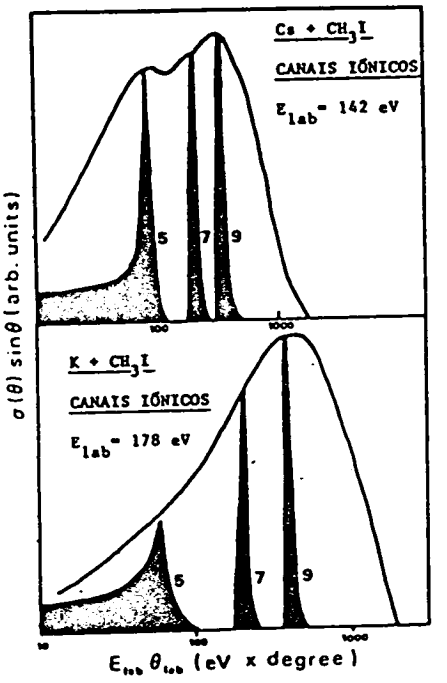


*Fig.1*

■ *modelo não convoluido.*

do perdas de energia até 14 eV.

Os vários processos observados experimentalmente são significativos na zona dos pequenos ângulos de desvio o que se justifica pelo carácter atractivo dos canais iónicos confirmados pelas medidas de pares de iões. Para a análise conjunta dos resultados foi desenvolvido um modelo envolvendo 14 canais de saída ( TABELA 1 ).

Verifica-se que a formação de pares iónicos $K^+I^-$ é fundamental para justificar a excitação atómica K(4p), a excitação vibracional do $CH_3I$ no estado fundamental e do $CH_3I(\tilde{A})$. Para processos de maior perda de energia a formação de estados excitados de pares de iões, acessíveis através de transições não adiabáticas na aproximação, constitui um mecanismo plausível e que explica a produção de estados neutros de Rydberg $CH_3I(6s,7s,...)$. Os estados iónicos excitados envolvem iões negativos com dois electrões em orbitas de Rydberg.

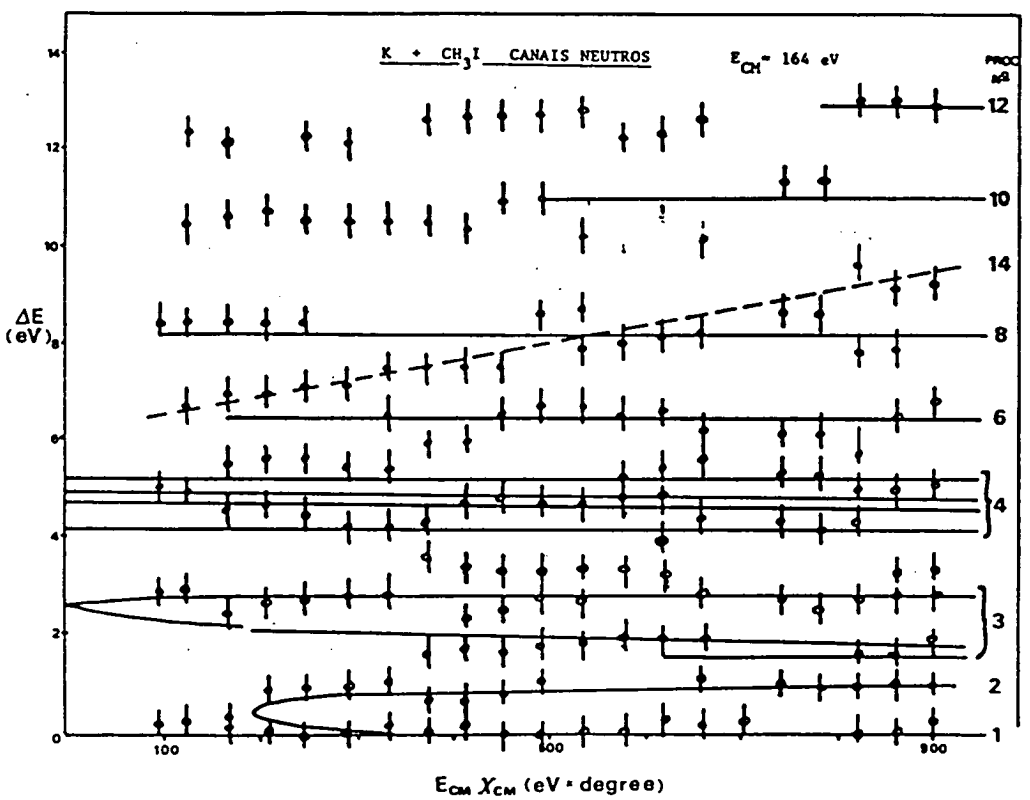


Fig.2 (——) previsões do modelo.


(1) A.J.F.Praxedes, M.J.P.Maneira e A.M.C.Moutinho, Thirteenth Int. Conf. on the Phys. of Elect. and At. Collis. ( XIII ICPEAC ), Berlim (1983)pág.632.

(2) M.J.P.Maneira, A.J.F.Praxedes e A.M.C.Moutinho, Proc. of the 13th Int. Symposium on Rarefied Gas Dynamics, Novosibirsky (1982).

(3) M.A.D.Fluendy, K.P.Lawley, J.McCall, C.Sholeen e D.Sutton, Faraday Discs. Chem. Soc., 67 (1979) 41.

10th Int. Symposium on Molecular Beams, Cannes (1985)
Book of Abstracts

# Vibrational and Electronic Excitation in $K/N_2$ Collisions

E.E.B. Campbell, G.W. Black and M.A.D. Fluendy,
Department of Chemistry, University of Edinburgh,
West Mains Road, Edinburgh EH9 3JJ (U.K.)

Inelastic differential scattering cross sections for the system $K/N_2$ have been measured in the small angle regime for eX in the range 0-600 eV° and at 4 collision energies in the range 43-110 eV CM. Experimental results and preliminary modelling for one collision energy (85.6 eV CM) have already been published [1].

A cross beam time of flight technique was used to measure energy transfer effects occurring in the collision. The apparatus has already been described [2]. The fast alkali beam is produced by charge exchange and pulse modulated for time of flight purposes using a velocity compression technique. The flight time of the scattered atoms is recorded.

Time of flight profiles are produced at a number of angles of deflection and from these the energy loss of the potassium atom is calculated. Such a profile, averaged over all angles of observation, for collisions at 43.3 eV CM is shown in Figure 1. The average energy losses observed for given excitation processes are shown in Figure 2 as a function of 1/V, where V is the relative velocity of the colliding species. Also shown in the figure is a first, tentative assignment of these energy losses.

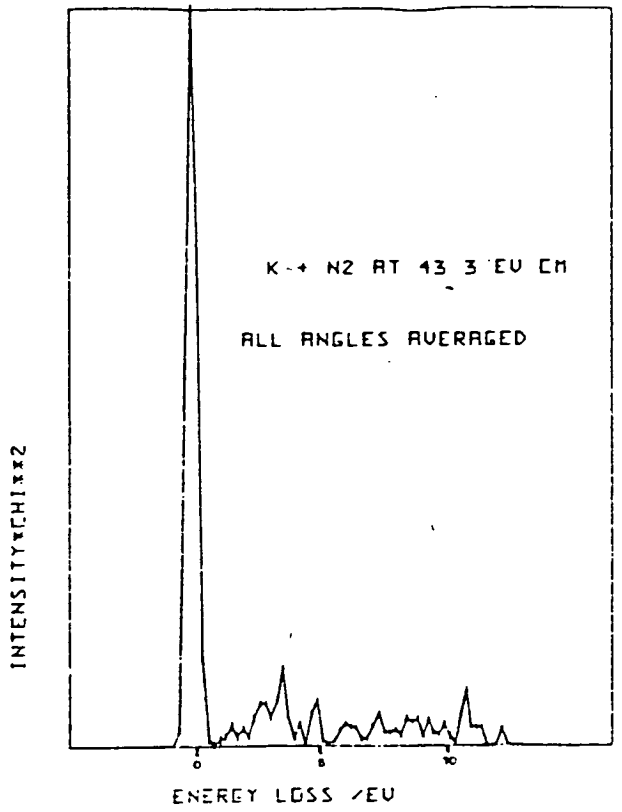


Figure 1 Energy loss spectrum averaged over observations in the 0.5-5.0° range. Bars are two std. devs long

The results will be discussed in detail later but the main features are as follows:

(a) A number of potassium excitations have been observed including K(5P) and K(6S) which were previously observed by Kempter et al [3].

(b) The vibrational excitation observed simultaneously with the electronic excitations of the atom increases as the collision energy increases (Figure 2A). This is in distinction from other systems where the vib. energy tends to zero as the collision tends to the sudden limit.

(c) There appears to be no vibrational excitation associated with most of the observed electronic excitations of the molecule (Figure 2B).

We intend to present a simple classical model for these collisions based on the surface hopping trajectory method. Although quantum mechanics is necessary for a full treatment of this sytem it will be interesting to discover how successful classical physics can be. The proposed model involves an ionic intermediate ($K^+ - N_2^-$) to access electronically excited states of the atom and give vibrational excitation of the molecule. Such a model predicts two exit

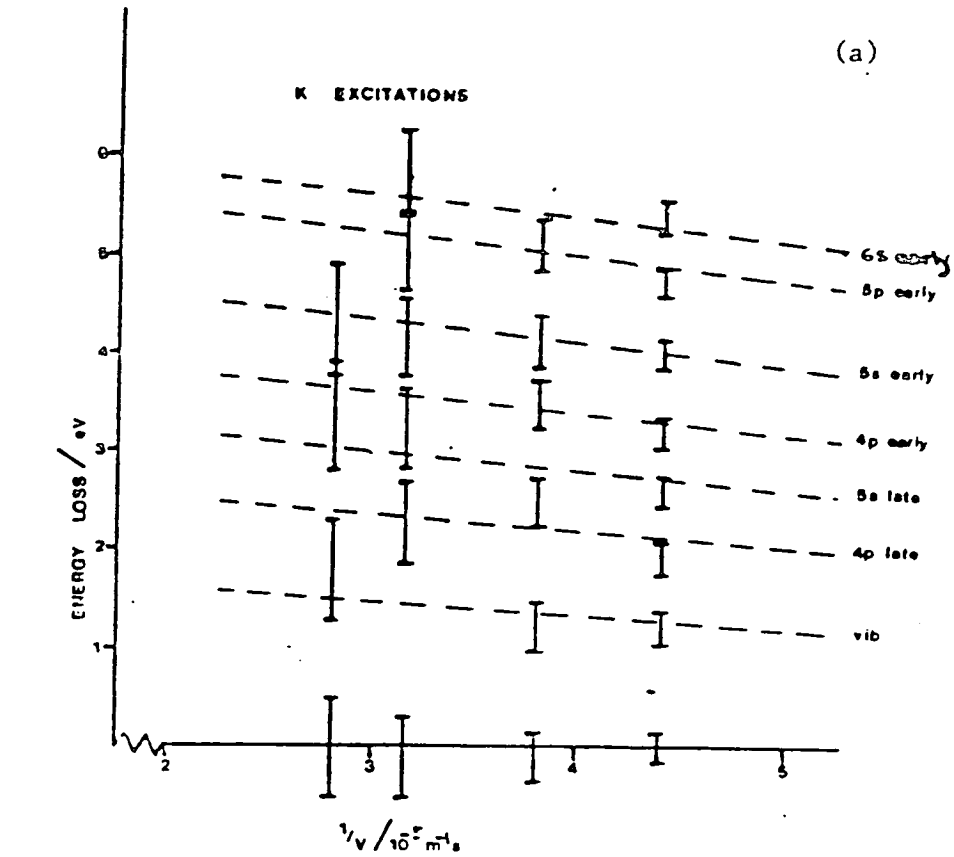


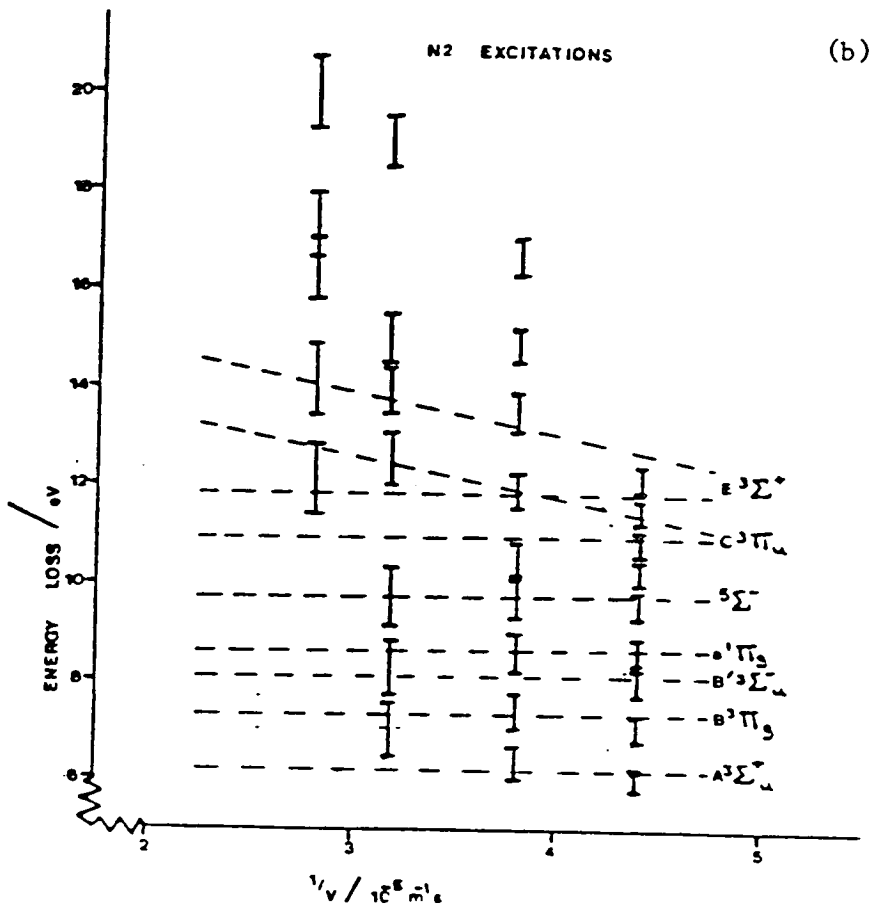


Figure 2 (a) & (b) Observed energy losses plotted against 1/V (the collision lifetime). A tentative assignment is also shown.

channels corresponding to a particular electronic excitation of the atom but with different amounts of vibrational excitation of the molecule corresponding to crossing onto the ionic surface on the way into the collision or on leaving it. A similar model has been described for K-$CH_3I$ collisions [4].


[1] Black, G.W., Fluendy, M.A.D., and Sutton, D.P., Chem.Phys.Letts., 69, 260 (1980).

[2] Fluendy, M.A.D., Lawley, K.P., McCall, J., Sholeen C., and Sutton, D.P., Fara.Disc.Chem.Soc., 67, 41 (1179).

[3] Kempter, V., Kübler, B., LeBreton, P., Lorek J., and Mecklenbrauck, W., Chem.Phys.Letts., 21, 164 (1973).

[4] Cowan, E.E.B., Fluendy, M.A.D., Moutinho, A.M.C. and Praxedes, A.J.F., Mol.Phys., 52, 1125 (1984).